6-22-2018 2:00 PM

Dynamics of the Phase Coupling for Flow, Heat and Mass Transfer in Conjugate Fluid/Porous Domains

Mahmoud Mohamed Mostafa Elhalwagy
The University of Western Ontario

Supervisor
Straatman, Anthony G.
The University of Western Ontario

Graduate Program in Mechanical and Materials Engineering
A thesis submitted in partial fulfillment of the requirements for the degree in Doctor of Philosophy

Abstract

Porous media prevail in industry e.g. heat transfer equipment, drying, food storage and several other applications. Integrated in engineering, they form conjugate Fluid/Porous domains. Physical modelling requires characterizing the microscale heat and mass (moisture) transfer interstitially within porous media and their macroscale counterparts across regional interfaces. Characterizing turbulence and its effects on phase coupling is often needed too. The modeling literature survey shows phase coupling assumptions depending on empiricism, phase equilibrium and lack of generality. Modeling of the dynamic variations for the modes of phase exchanges, i.e. heat, mass and heat accompanying mass exchanges, on both scales and generic turbulent coupling across fluid/porous interfaces are absent. Thus, the objectives of this thesis are to, i) develop a dynamic coupling model for phase heat and mass transfer in conjugate fluid/porous domains, ii) validate the model in terms of interstitial phase exchange, macroscopic interfaces and behaviors in different modes of heat and mass transfer, iii) extend the model to turbulent flows characterizing turbulence correctly for different porosities and permeabilities. The modeling process depends on a finite volume approach. Continuity, momentum, turbulence, energy and mass equations are solved in *point* form for fluid regions. In porous media, a volume averaged version is formulated and solved using one equation per phase e.g. fluid temperature, solid temperature, vapor in fluid mass fraction and liquid in liquid/solid mixture mass fraction. Mathematical conditions are utilised at macroscopic interfaces reconciling the point-volume form differences, to ensure continuity of conservation variables and numerical robustness. Physical phase exchange formulae and numerical implementations for macroscopic interface heat/mass and turbulence treatments are introduced. The model is validated interstitially by comparing to experiments of Coal particles drying, for macroscopic coupling by comparing to experiments and other models of apple and mineral plaster drying, respectively. The results showed good agreement for all the cases. The turbulent coupling model has been tested for a channel with porous obstruction high and low permeability cases and compared well to other studies in the literature. Finally, full turbulent flow, heat and mass

transfer was tested and produced physically correct trends and contours for apple and potato slices drying.

Keywords

Dynamic Coupling, Heat and mass transfer, Computational Fluid Dynamics (CFD), Porous media, Conjugate domains, Turbulence modelling, Low and high Permeability, Enhanced Wall treatment

Co-Authorship Statement

Chapter two is a published manuscript in international journal of heat and mass transfer. The authors are, Elhalwagy, M. M. and Straatman, A.G.

Chapter three is a manuscript that will be submitted to a journal in the area of heat and mass transfer. The authors are, Elhalwagy, M. M. and Straatman, A.G.

In both cases, the writing, research and analysis is carried out by myself, while the guidance and scientific support is provided by Prof. Straatman.

Acknowledgments

I would like to thank GOD for providing me with the courage, patience and stamina to do this work and for all his grants and blessings throughout my entire life.

I would like to express my gratitude and thanks to my supervisor, Prof. Anthony Straatman. He is a true research leader and one of the best supervisors that a student can have. His insight, guidance and continuous support have kept me going through this journey and I always had him backing my steps and strengthening me.

I am grateful to my supervisory committee members, Prof. Eric Savory and Prof. Kamran Siddiqui for multiple discussions and advice about my research topic. I am also grateful to all my past and current colleagues in our CFD research labs for a great environment and technical advice. This includes: Furqan Khan, Nolan Dyck, Shady Ali, Rajeev Kumar and Ahmed Khalil. I also would like to thank Dr. Chris DeGroot for a lot of CFD conversations. Thanks are also due to Professors Chao Zhang and M. Hesham Elnaggar, as well as, the MME graduate coordinator Joanna Blom.

I would like also to take this opportunity to express my deep gratitude to my mother, May she rests in peace, for all the support she gave me and for raising me and making me the man I am now. I also had the care and support of my sisters and brother and for that I am grateful. Special thanks are due to my wife Dina for being my companion through this journey and standing by my side through the bad and the good times and, my children Yusuf and Maryam for filling my life with love.

Finally, Acknowledgement is due to NSERC for the financial support.

Table of Contents

List of Tables

List of Figures

List of Nomenclature

A	area, m^2
A_{fs}	specific interfacial surface area of porous media, m^{-1}
a_i	CFD active coefficient of control volume *i*
a_W	water activity
B	Spalding mass transfer number
Bi	Biot number
b_i	CFD active source term of control volume *i*
c_E	inertia coefficient of porous media
c_p	specific heat at constant pressure, J/kg. K
c_{ps}	specific heat in the solid phase, J/kg. K
C_T, C_m, C_{T1}, C_{m1}	heat and mass transfer correlation constants
$C_k, C_l, C_{1\varepsilon}, C_{2\varepsilon}, C_\mu$	turbulence modelling constants
D	binary diffusivity coefficient, m^2/s
D	Coal particles bed diameter, m
$\boldsymbol{D}$	deformation tensor
d_P	Porous media particle diameter, m
E	integration constant in the turbulent wall log law (=5.0)
$\dot{H}$	Enthalpy phase exchange term, W

H	channel height, m
h	specific enthalpy, J/kg
h	height of porous region, m
h_{fg}	latent heat of vaporization at 0°C, J/kg
h_{fs}	interfacial heat transfer coefficient in porous media, W/m^2.K
h_{fsm}	interfacial mass transfer coefficient in porous media, m/s
$\boldsymbol{I}$	the unit dyadic
i	species counter
$J''_{v_{int.}}$	overall vapor mass transfer flux at fluid/porous interface, kg/m^2.s
k	thermal conductivity, W/m.K, turbulent kinetic energy, m^2/s^2
K	permeability of porous media, m^2
K	phase ratio
L	Porous media length, m
l	REV size, m
M	overall moisture concentration, kg/m^3
m	mass, kg
$\dot{m}$	mass flow rate, kg/s
N	number of neighbors of a CFD cell
$\boldsymbol{n}$	outward normal unit vector

Nu	Nusselt number
P	pressure, Pa
P_i	turbulence production of i
Pr	Prandtl number
Q_{φ_P}	CFD explicit part of the source of φ at control volume P
$q''_{int.}$	overall heat transfer flux at fluid/porous interface, W/m^2
R_i	gas constant of i, J/kg. K
R	mass transfer resistance
Re	Reynolds number
RH	relative humidity
R_{φ_P}	CFD linearized part of the source of φ at control volume P
S	source in a transport equation
Sc	Schmidt number
Sh	Sherwood number
T	temperature, K
$\boldsymbol{t}$	shear unit tangent vector
t	time, s
U	Inlet velocity, m/s
u^*	friction velocity at the wall/interface, m/s

u_{int}	slip shear velocity component at the fluid/porous interface, m/s
$\mathbf{v}$	fluid velocity vector [=(u, v, w)], m/s
V	volume, m^3
x	distance in axial direction, m
x	phase index
y	distance in y-direction , m
Y	mass fraction
α	vaporization energy apportioning factor
α_x	volume fraction of x
β	enhanced vapor diffusion factor
Γ^{φ}	diffusion coefficient of the entity φ
$\delta_{diff.}$	significant liquid diffusion thickness, m
κ	Von-Karman constant (= 0.41)
μ	dynamic viscosity, $N.s/m^2$
μ_t	turbulent eddy viscosity, $N.s/m^2$
ζ	dry solid layer's diffusion resistance altering factor
σ_k	turbulent Prandtl number for k
σ_ε	turbulent Prandtl number for ε
$\boldsymbol{\tau}$	overall fluid stress tensor, Pa

τ	reciprocal of the turbulence time scale, s^{-1}
$\tau_{int.}$	shear stress at the macroscopic interface, Pa
ρ_s	Solid density, kg/m^3
ρ_f	density of fluid mixture, kg/m^3
ϵ_i	turbulence destruction of *i*
ε	Porosity (chapter 2), turbulent energy dissipation (Chapter 3), m^2/s^3
η	dimensionless length scale for calculation of μ_t in enhanced wall treatment
λ_x	thermal conductivity of phase x, W/m.K (only for turbulent flow)
ϕ	porosity (only for turbulent flows)
φ	An entity of interest
$\bar{\varphi}$	time-average of φ
φ'	time fluctuation of φ
$\langle\varphi\rangle$	extrinsic volume-average of φ
$\langle\varphi\rangle^x$	intrinsic volume-average of φ for phase x
$\tilde{\varphi}$	volume deviation of φ
$\langle\bar{\varphi}\rangle$	volume-time-average of φ
ψ_{φ_γ}	Peclet weighting factor for CFD upwind advection scheme

subscripts and superscripts

a	air
$conv.$	convection
$diff.$	diffusion
E	CFD east neighboring cell
e	CFD east integration face
eff	effective property in porous media
f	fluid
fl	fluid side of interface
fs	interfacial
HT	Heat transfer
$interf.$	macroscopic interface
m	mass transfer (subscript), exponent of Reynolds number in heat and mass transfer correlations (superscript)
MT	mass transfer
$macro.$	at fluid/porous interface (macroscpoic interface)
mod,t	modified by turbulence
n	exponent of Prandtl number in heat and mass transfer correlations
nb_{γ}	neighboring CFD cell at face γ

P	control volume (P)
por	porous side of interface
s	solid
sat	saturation
$sol.$	solid particle surface
st	solid matrix
T	Heat transfer
v	vapour
w	water
Γ_i	profile exponent of the dimensionless wall function for equation *i*
γ	general CFD integration face
+	superscript associated with non-dimensional wall function variables

Abbreviations

CFD	Computational Fluid Dynamics
DNS	Direct Numerical Simulations
EWT	Enhanced Wall-like Treatment
LES	Large Eddy Simulations

PIV	Particle Image Velocimetry
RANS	Reynolds-Averaged Navier-Stokes
REV	Representative Elementary Volume
RNG	Re-Normalized Group
RSM	Reynolds Stress Modelling
SAT	Spatial Averaging Theorem
SST	Shear Stress Transport
TKE	Turbulent Kinetic Energy

Chapter 1

1 Introduction

1.1 Background and scope to contribution

This thesis is concerned with the development of a reliable, time efficient and physically dynamic modelling approach that characterizes fluid flow processes around and through porous media, predicting heat and mass transfer locally and globally for different processes, materials and physical conditions.

1.1.1 General Background

Porous media are abundant in everyday life. To name some: particles, grains, sands, soil, fabrics, bricks, metal foams, produce, food stacks, catalytic honeycombs, biological tissues and even liquid mists and sprays are all of porous nature, involving variety of sizes and physical properties. Thus, a wide range of engineering processes and industries are interested in fluid flow, heat and mass transfer around and through these media. Examples include, porous metal foams, porous heat sinks, air conditioning, drying (fabrics, construction materials and foodstuffs, etc.), food cooling and storage, food quality forecasting and ripening, prediction of undersoil smoldering, forest fires, planetary boundary layer through rough terrains and forests, engine catalytic converters and porous burners, some of which are included in Fig. 1.1. This widespread application within these diverse areas of engineering, necessitates a thorough understanding of the different physical processes like fluid flow, heat and mass transfer around and through porous media to facilitate engineering design and analysis and accelerate the process of development.

For the purpose of this work, the term “porous media” refers to structures that are comprised of solid and fluid constituents in a relatively homogeneous distribution such that it may be considered a continuum of both. While a porous material may be permeable or impermeable, the interest herein is directed towards fluid-permeable porous materials, where air, water or some other fluid can pass through the solid structure under the influence of a pressure gradient. Examination of the solid and fluid constituents (or phases) of the porous material leads to the consideration of different important length scales.

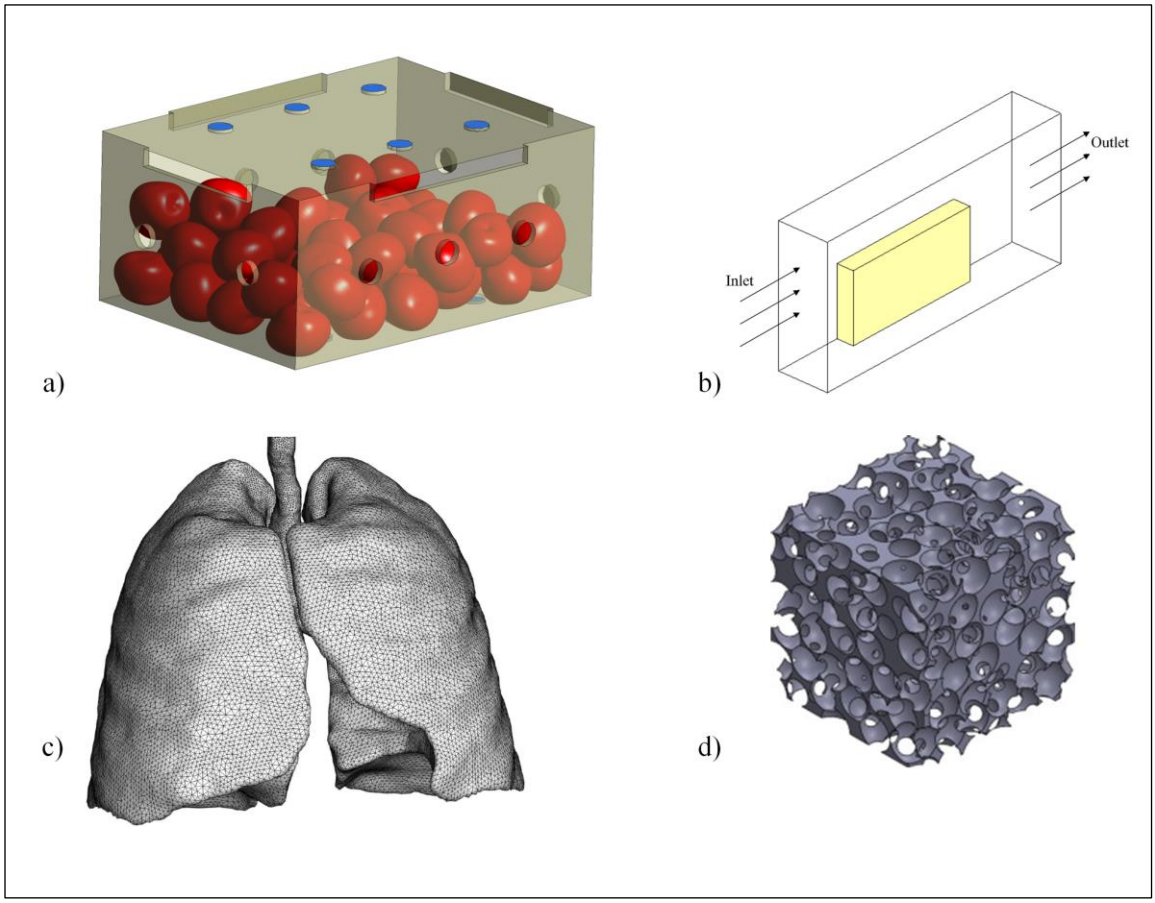

Figure 1.1: Applications of porous media including a) modeling of tomato stacks (taken from Elhalwagy, Dyck and Straatman [1]); b) convective drying of an apple slice; c) modeling of the human lung (taken from DeGroot and Straatman [2]); d) modeling of Graphite foam(taken from Dyck and Straatman [3]).

If one zooms in and considers the internal structure of a porous medium, the length scale of some physical process may be characterized by the distance between two chunks of solid, or the diameter of a pore or void space, or it can be the averaged size or diameter of individual solids (particles, ligaments, etc.), or any other suitable dimension at this microscale. The presence of other forms of matter may also be observed inside what are characterized as the solid or fluid constituents of the porous structure; consider, for example, water vapor in air or liquid water trapped within the solid constituent in tiny interconnected micro-pores (see left panel of Fig 1.2). The presence of temperature

gradients or species concentration gradients between the two phases causes heat and mass transfer on this local (sub-micro) scale as well.

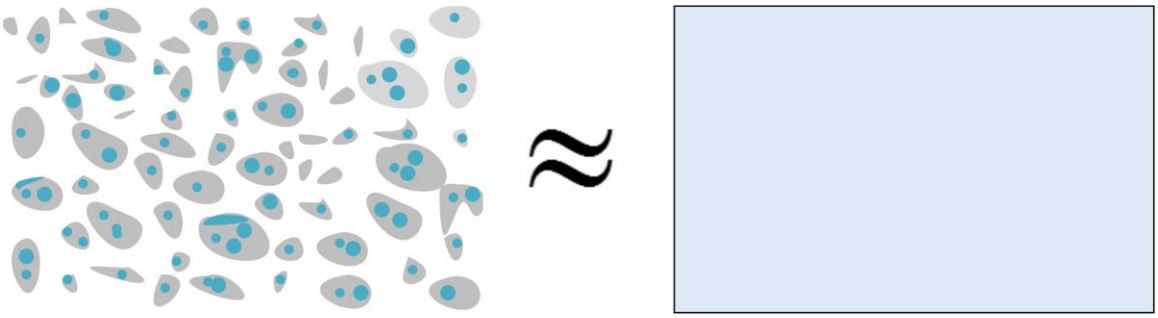

Figure 1.2: Porous media micro- and macroscales. The left panel depicts a microscopic representation of Porous media with liquid trapped inside the solid's micro-pores while the right panel shows the continuum or macroscale equivalent perception.

Depending on the microscale and the geometric nature of the solids or the voids within a porous medium, the physics of the fluid flow or any transfer of heat or mass (e.g. moisture evaporation/condensation) can differ significantly and hence, the resolution of different phenomena is very important on this small scale.

Zooming out, the most prevalent length scale is related to the geometric size of the entire porous medium. On this macroscale, bulk flow variations and pressure drop, and bulk heat and mass transfer is often the goal of net characterization of the physics. Both scales interact considerably and cause different possible behaviors (see Fig 1.2 for porous media scales). Another aspect of interest for physical studies is the different interactions at the interface between the surrounding fluid region and the porous medium; this is often the most difficult part of modelling a process of fluid, heat or mass transfer. The interface is also often complicated by the heterogeneity present in the structure of porous media, i.e. rapid changes in porosity, and the variations of the fluid flow behavior due to shear and obstruction. For heat and moisture transfer, other factors like conduction and diffusion enhancement/inhibition, fluid acceleration/deceleration, phase change, capillarity, surface tension effects, etc., interplay together to pose modelling challenges at interfaces under different conditions. For turbulent flow, the presence of multiple time scales adds to the

already-complicated physics. Instantaneous time-local variations in the flow velocity, temperature or moisture concentration with time are of a small time scale and transient physical phenomena observation (e.g. drying) is of a larger time scale. Hence, in addition to the presence of multiple length scales, processes are affected by multiple time scales as well.

Characterization and study of different phenomena in porous materials often relies on empiricism and is based on some insight into the physical processes. To this end, experimental studies carried out on a bulk scale can quantify the overall drying rate, heat transfer, flow resistance, etc., through a permeable porous material. A more in-depth analysis often depends on numerical simulations based on computational fluid dynamics (CFD) and done at the pore-level. Such analyses can take the place of costly and sophisticated experimentation conducted to resolve the physics inside complex structures subject to multiple length and time scales. Modeling the porous structure at the pore-level depends on resolving the microscale and hence, phenomena is characterized for all voids and particles/ligaments inside the porous material, which can also be prohibitive and time-expensive. A second computational approach is to resolve only the macroscale (i.e. continuum approach) but with upscaling mathematically the microscale information using volume-averaging. Within this approach, with respect to heat and mass transfer, a simple technique is to consider a single temperature and/or mass fraction to characterize a small representative region of porous material, thereby enlisting the assumption of local thermal and mass equilibrium. This equilibrium approach, while successful when this homogeneity is physically acceptable, is of restricted applicability to different classes of problems in which the equilibrium is partially or fully unachieved. Separating the two phases with respect to heat and mass transfer is a solution to this problem and is of an affordable time expense however, it requires a reliable and accurate microscopic phase exchange modeling.

In engineering applications and designs, porous materials are often combined with other solid materials and immersed in a fluid environment to form conjugate domains of fluid/porous/solid regions. Across the clear fluid/porous transition, different modeling approaches have been considered including forcing a gradual change of obstruction between the two regions i.e. porosity gradient, segregate the modeling between both

regions, i.e. either model one region and link it to an empirically estimated effect to the other, or, model one region at a time and obtain the result from this region then use it to carry the interface effect on to the second one (indirect coupling approach). These three approaches are of additional time cost and/or loss of accuracy. The conjugate approach depends on linking the two regions in a single simulation step and ending up with a full characterization of both fluid and porous regions which is time-efficient. While the approach is challenging, considerable success is achieved with room for further development. The process of coupling turbulent flow through both regions in particular is an active area for improvement especially to achieve capability for modeling different ranges of porosity that allow turbulence to penetrate/dissipate into the porous region depending on the level of flow resistance.

1.1.2 Scope

Industrial modelling of general heat and mass transfer and/or drying/rehydration (i.e. heat-affected moisture transfer) in conjugate fluid/porous/solid domains has depended on the above-mentioned design tools and basic CFD studies. Departure from these simple, accuracy-limited, empirical ad-hoc or case-specific techniques has been long under development. It is interesting to mention that to-date (to the best of the author's knowledge) no commercial CFD software contains a generic, accurate, conjugate fluid/porous/solid, time-efficient and physically dynamic; capability for modelling combined flow, heat and mass transfer. The research community is focused on either in-house coding, coupling between different softwares/codes for simulating different regions and is heavily loaded with the different above mentioned empirical or non-generic assumptions. Few studies in the recent years have made progress with conjugate and physically-based CFD for these problems. The present work is a basic step towards the development of a generic, highly-coupled and physically-dynamic approach. The scope herein is directed towards the void areas in CFD literature, as will be shown shortly, where heat and mass exchanges locally (interstitially) and macroscopically (across regional interfaces) are either:

- Overlooked
- Empirically adjusted in a non-generic way that requires case to case calibration
- Coupled with a numerical technique that is conditionally stable or time-consuming

- Formulated with limited reactivity to dynamic physical changes and modes of flow, heat and mass transfer

The approach taken herein is a compromise between very detailed physical modelling for multiple length and time scales, empiricism and time efficiency and it provides alternatives that are capable of solving the above mentioned problems. The resulting work provides a framework that is generic, conjugate, simultaneous for all regions, and physically dynamic with a significant reduction of empiricism which provides a starting point for further development.

The rest of this chapter focuses on reviewing the modelling state of the art, objectives of thesis, research methodology (i.e. averaging techniques, model development background, necessary terminology and numerical discretization) and closes with the thesis outline.

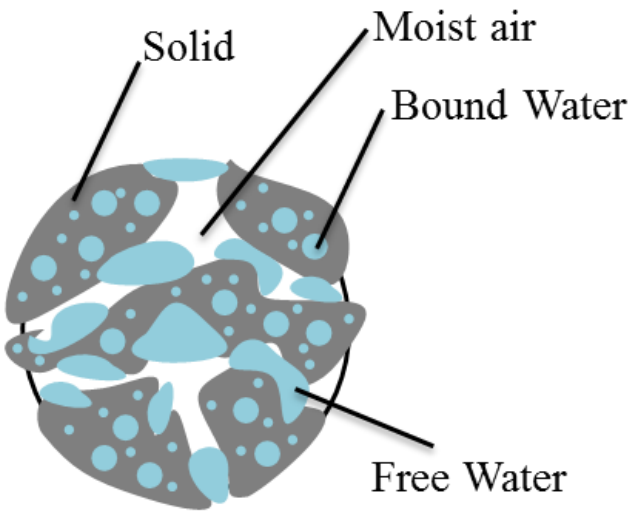

Figure 1.3: Schematic showing a microscopic representation of a moist Porous material.

1.2 Literature survey

1.2.1 Modelling heat and mass transfer of moist porous materials

A moist porous material is a porous material that includes four phases within it. The four phases are, solid matrix or particles, void space including moist air (dry air and water vapor), free liquid water that lies on the surface of the solid constituent and is in contact

with both air and solid phases, and the bound water which is liquid water embedded inside the solid constituent and is not free to move or evaporate (See Fig. 1.3). Drying and rehydration studies are focused on modelling the heat and mass transfer techniques for moist porous materials. One school of practice was established on the work of Luikov [4-5] which tackles the problem from a thermodynamic point of view and does not depend on macroscopic averaging techniques but on a phenomenological approach. It also standardizes the inclusion of the Soret and Dufour effects (i.e. mass and heat transfer due to temperature and species concentration gradients, respectively). This school often refers to moist porous media as capillary-porous and hence it depends highly on characterizing moisture transfer by capillarity. The approach is usually applied in CFD by solving the capillary pressure as a transport variable [6-7] and utilizing a convection term in the liquid transport equations to represent moisture travel macroscopically. The method is of wide use for construction materials. The approach while successful, is non-generic due to its specificity to one certain form of moisture presence (i.e. liquid only) and the fact that it solves the capillary pressure to characterize moisture transfer instead of the mass fraction or species density which are the real conserved variables in this case. Another school of work is Whitaker's [8-9]. His work started by taking the analogy between transport in space and time and coming up with the concept of volume averaging following Reynold's approach for time averaging. The approach ended up by obtaining all the flow, heat and mass transfer volume-averaged forms of conservation equations for the main three phases i.e. air, liquid and solid. The drawback was the very complicated form of the transport equations and the mathematically complex equations of closure [10-11] that need to be solved for a useful utilization of the approach. Closure may also be sought using microscopic data or void level simulations [3, 12]. Special interest has been given to the bound water phase in the literature. Some researchers solved an individual transport equation for this phase separating it from the free liquid phase [13]. Others included them in one equation, but they introduced special terms for diffusion [14] to characterize the different phases e.g. Arrhenius-type expressions or entropy-based approximations to model the gradual freeing of the bound water by heating [15]. Moist porous materials are also categorized to hygroscopic and non-hygroscopic materials [16]. Where a hygroscopic material is defined as a moist porous material that retains moisture and frees it gradually

based on gradual variation of diffusivity or gradual variation of moisture-bond energy e.g. Food [16] while, non-hygroscopic materials are of reduced affinity for moisture. They contain limited amount of free moisture and the moisture-bond to it for the bound phase is very difficult to free i.e. a relatively high diffusivity in the beginning of drying that drops several orders of magnitude in a very short drying time until the material is of nearly neglected diffusivity [6] e.g. some building materials. For both types of materials, the mechanism of moisture transport depends on diffusion, capillarity and surface tension effects [4, 6, 16]. It is also common in the literature to neglect the void phase presence inside the moist porous material and model only liquid and solid phases [17-18]. The approach is again non-generic as it neglects the mechanism of vapor diffusion and the presence of vapor moisture which is not realistic in a lot of cases. Other studies tend to include vapor diffusion mechanism but they incorporate it within a single equation for liquid and vapor [6-7, 14] which is better physically however the segregated species modeling offers more general applicability and it also allows modelling of local phase exchange.

1.2.2 Phase-heat and mass interstitial exchange

Generally, heat and mass transfer inside porous media is categorized to equilibrium and non-equilibrium approaches. An equilibrium approach depends on considering one homogeneous presence of heat and mass transfer for all the phases i.e. one discrete equation for temperature and another for moisture concentration or mass fraction only per each control volume (elaboration will follow in a subsequent section). While non-equilibrium approaches separate each phase’s characterization into one equation i.e. a number of equations equal to the number of phases per control volume. The first approach is widely used in the literature [17-20] however it does not model the phase exchange processes because it considers the transport for the sum of the phases. Our discussion here is relevant to the second approach. Some studies resorted to close the interstitial phase exchange using empirical adjustment [21-22] to account for different modes of heat and mass transfer locally e.g. forcing a mass transfer coefficient of exchange to decrease empirically near the dry out [22]. Studies of packed beds or grain drying [23-27] gave their focus to the microscopic phase exchange area of work. The surface of the solid constituent or the solid

particle has either been assumed as fully saturated with vapor [22], or a thermodynamic equilibrium approach is invoked (more details about thermodynamic equilibrium will follow) to allow a relation between solid surface relative humidity and water activity of the solid particle to form [23-24]. In this approach, the liquid moisture content inside the solid is correlated to the surface vapor concentration on the fluid/solid interface, allowing a driving potential for mass transfer to link both phases using an analogue of Newton's law of cooling [22-24] in which a local interstitial mass transfer coefficient is estimated based on the physics of the flow and the geometric structure of the porous material. This thermodynamic equilibrium expression based on this definition has some limitations close to drying out and does not consider an explicit introduction of the resistance to mass transfer inside the solid constituent. Another problem with the analogue of Newton's law of cooling is that it considers only the diffusive effects in the boundary layer for vapor transport without inclusion of advective effects [17, 22] i.e. Stefan flow. Other studies has considered both a thermodynamic equilibrium approach outside of the solid constituent and a diffusion resistance model on the inside. They either solved an equation inside the solid particle for the solid side's resistance [25-26] or empirically estimated the solid side's resistance from drying kinetics data [27]. Both types of treatments however preserved the thermodynamic equilibrium at the interstitial interface. In a different case, the drying kinetics data were solely used for representation of the phase exchange mass flux without including a fluid side expression [28]. Most of the grain and particle drying studies were applied on one or two dimensional models [13,27-29] mostly because of the complicated local phase coupling approaches, which is not feasible for implementation in cases of high three dimensionality.

The second aspect regarding local phase exchange concerns with the phase exchange energy (i.e. energy accompanying species transport across phases). This energy is mostly representing the latent heat of vaporization for moisture. It is common for applications of evaporative cooling or cases where deviation from thermal equilibrium is minimal [22, 30], to apportion this energy (i.e. withdraw it) completely to the fluid phase. In other cases where the liquid is mostly embedded inside the solid (e.g. packed beds), the practice was to apportion it completely to the solid phase [24, 27-29]. While both assumptions are relevant approximations to their respective cases, they both present a loss of generality.

The physics of vaporization dictates that when liquid is placed at the interface between two phases, it may vaporize and travel between them based on whichever source that can supply the vaporization energy i.e. for free liquid water both phases may contribute to the vaporization heat in different proportions [31].

1.2.3 Coupling across fluid/porous interfaces

Now, the heat and mass transfer coupling between a surrounding fluid region and a moist porous region is reviewed. The fluid/porous regions' linking is achieved either, with an overall empirical/semi-analytical assessment e.g. a drying kinetics technique, a single phase approach which solves single equation of heat and another for mass inside each CFD cell, an uncoupled phase approach that solves the different regions without direct coupling or a conjugate technique that directly couple the different phases. In the first approach, the overall phenomenon is characterized without local variations i.e. no discrete or CFD approach is utilized. This overall behavior is determined based on a drying experiment for a certain specimen of the material of interest and/or a semi-analytical approach that represents an equation for the overall diffusion inside the moist material and its correlation with time or utilizes an Arrhenius-type expression to correlate the kinetic data to overall moisture content and temperature [32-36]. The second category solves only one equation for temperature and one other equation for the overall moisture in the porous region i.e. utilizes an equilibrium approach within the porous media [17-20] (See Fig. 1.4 for a complete description of the different types of CFD regional coupling). While these studies provide a discrete CFD solution, they utilize an empirical estimate of overall heat and mass transfer coefficients at the macroscopic interface i.e. clear fluid/porous interface that carry the effect of the surrounding fluid region on the porous region. These empirical estimates are based mainly on Nusselt and Sherwood number correlations existing in the literature. This single phase approach also provides an overall characterization of the heat and mass transfer however, it is restricted by the applicability, accuracy and case-specificity of these empirical estimations. It may also suffer from the non-equilibrium errors within the porous domain due to the absence of interstitial phase exchange modelling.

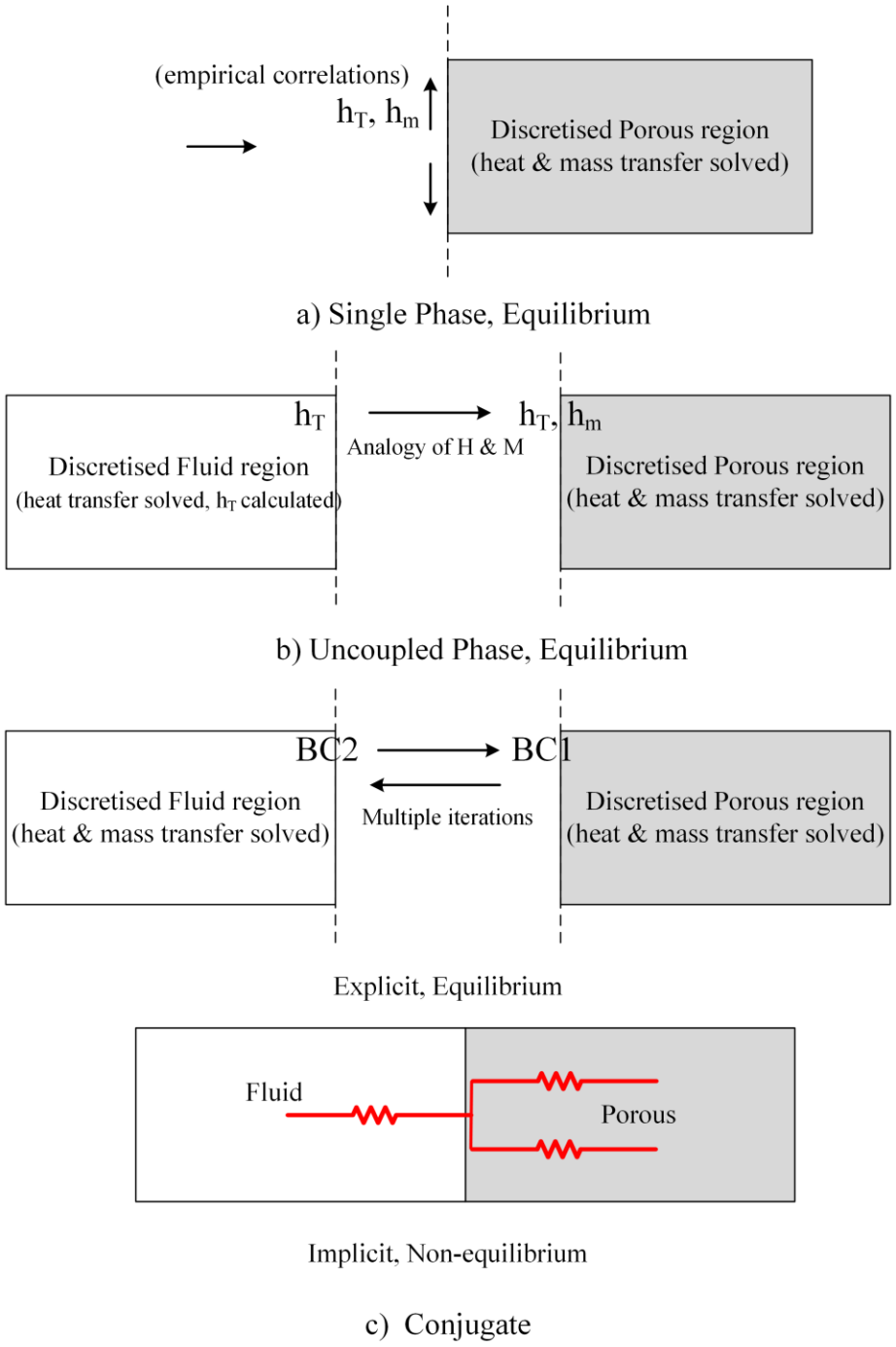

Figure 1.4: Heat and mass transfer coupling in CFD studies of Fluid/Porous domains.

The third group of studies utilize an uncoupled phase technique which means that both, the fluid and porous regions, are discretized and heat and mass transfer are solved

numerically/analytically within them however no interface coupling is present [37-39]. The linking is achieved by using the discrete solution of the fluid region to estimate an interface heat transfer coefficient and utilizing the heat and mass transfer analogy to deduce the corresponding mass transfer coefficient. A convective boundary condition is then set from both transfer coefficients to solve the heat and mass transfer inside the porous region. Figure 1.4 illustrates the process. This technique utilizes equilibrium approaches inside the porous region as well. The last approach for coupling is a conjugate approach in which the full characterization for heat and mass transfer is carried out within both regions. This approach is subdivided to explicit and implicit subcategories. The explicit technique [6, 40] depends on separating the numerical solution of both regions in a way that the interface side coupling is set in the discrete form as a boundary condition and hence multiple iterations or overlapping time steps have to be performed in which multiple explicit updates need to be made for the interface coupling fluxes. A way to reduce these multiple iterations is to reduce the time stepping size so that one update is enough per time step in which the information is carried from the fluid region to the porous region. An obvious disadvantage for this approach is the computational expensiveness and potential stability problems that may require adaptive time stepping to overcome [40]. Few studies have achieved an implicit form of coupling in which both regional equation sets are solved simultaneously. Of these studies a two dimensional approach that is based on using a stream function for the fluid flow is notable [41]. The approach while successful is restricted to two dimensional cases only. A second study achieved this form of coupling with the use of non-equilibrium heat and mass transfer inside porous media however they utilized ad-hoc resistance-altering coefficients for mass transfer coupling at the fluid/porous interface that varied from a simulation to another which is case-specific [30]. The resistances of heat and mass transfer implicit coupling are shown in Fig. 1.4.

1.2.4 Turbulence within porous media

Turbulence plays a major role in heat and mass transfer processes related to porous media hence, it is very important to study the different approaches utilized for modeling within the porous material and across the macroscopic interface. The present section is concerned with the former. One school of work depended on simple modeling techniques [42-43].

The models were single equation models that resolved the turbulent kinetic energy (TKE) and utilized a mathematical expression for its dissipation rate rather than adding another equation. The first version of this expression depended on four empirical constants [42] and the enhanced version eliminated two of them [43]. Generally, the approach simplified the porous media flow modeling by using the Darcy equation with its Forchheimer-added drag resistance with neglecting convection and diffusion transport. It also carried the turbulence effect into heat transfer by using a turbulence intensity-dependent Nusselt number correlation. The main direction of work in the literature focused on two equation modelling, following the direction of volume averaging the time averaged k-ε equations. One group of studies attempted the time-volume-averaging process i.e. Double decomposition (discussion will follow in a subsequent section), based on a definition of TKE that time averaged the square of the volume-averaged velocity fluctuation $\mathbf{v}'$ [44-47]. The definition caused the order of the averaging processes to change the final output for different cases and it also lacked the inclusion of a volume-deviation-time-fluctuation term for the TKE and its dissipation rate. A more general definition was introduced later [48-49] that squared the velocity fluctuation first and then performed the two averaging processes i.e. the double decomposition. This definition included the above mentioned volume-deviation-time-fluctuation term and resulted in an immaterial order of integration. Another introduced definition added to the last one, another term that relates to the porous media dispersion [50-51] to form a TKE equation that resolves the velocity variations macroscopically for time and space integrations. Based on these different definitions for TKE, three different attempts [48, 49, 51] for closure of a k-ε model were performed inside porous media using pore level simulations and ended up successfully adding three different forms of drag terms in the k-ε equations. All three forms are suitable for macroscopic modeling and may be closed for different variations of void level simulations [12]. More advanced modeling have also been carried out. Reynolds stress modeling (RSM) has been utilized [52-53]. While it has been used without any additional change inside porous media for one study [52], macroscopic scaling and closure has been achieved as well [53]. Also, multiple-equation versions of the k-ε model have been created in the literature for cases that added a separate two equations of TKE and its dissipation to characterize dispersive effects [54] and cases that separated macroscopic, microscopic and dispersive TKE and its

dissipation into separate k-ε sets [55]. The three-way splitting approach of k and ε have been developed later into a second moment closure approach as well [56]. A low Reynolds number model have also been developed based on a Lam-Bremhorst version that utilized direct numerical simulations (DNS) inside porous media for validation [57]. Generally, all the turbulence modeling work inside porous media has been successful however, due to the complication of characterizing the additional dispersive and tortuous effects to an already existing random characterization for turbulence for any of the above modeling frames, most of the models were too complex and the multiple equation models were too computationally expensive rendering the standard double decomposed versions of the k-ε model to be the most useful.

In regards to turbulent heat and mass transfer studies, two significant areas of work are concerned with drying and food stacking, respectively. In the first category of work, significant amount of the studies depended on the same assumptions that were utilized inside porous media for laminar flows (see sections 1.2.2 and 1.2.3). They included two equation models of turbulence with standard wall functions to account for boundary layer effects at the macroscopic interface with the exception of few studies. A standard version of k-ε model with standard wall function was utilized by, to name a few, Curcio et al. [58] (parallel flow over food sample, continuity heat and mass transfer flux boundary condition and thermodynamic equilibrium at fluid/sample interface with a non-porous equilibrium approach inside the sample), DeBonis and Ruocco [59] (jet impingement over a general wet protrusion, non-porous approach, non-equilibrium inside the protrusion with lumped vapor/liquid diffusion into a single diffusivity and an Arrhenius expression for macroscopic interface evaporation) and Caccavale et al. [60] (parallel flow over a general wet protrusion utilizing the same approach as [59]). Ateeque et al. [61] utilized a k-ω SST two equation model for modeling the flow around a potato slice based on testing different two equation models for a backward facing step as they considered the separation of the flow and re-attachment as the most significant turbulent behavior for such a kind of flow. For turbulent heat and mass transfer, they considered a non-porous/non-conjugate model that relied on surface transfer coefficients for coupling at the fluid/slice interface. The turbulence effect was incorporated for heat and mass transfer via the flow-spatially dependent surface transfer coefficients, predicting higher values at the upstream face and lower ones at the

downstream one. Another approach for brick drying by Van Belleghem et al. [7], used a realizable *k*-ε model with a low-Reynolds number region at the macroscopic interface instead of a wall function. The heat and mass transfer approach depended on the capillary pressure and incorporating both vapor and liquid transports into one equation inside the drying sample with an empirical specification of the transfer fluxes at the air/brick interface. Studies in this category of work did not consider porosity effects, turbulence inside the drying samples and suffered from the same case-specific empiricism at the macroscopic interface and the time consuming coupling between air heat and mass transfer and the inside of the drying sample and/or equilibrium assumption's inaccuracy. A notable study was conducted by Defraeye et al. [62]. They considered flow around an apple slice and assessed multiple turbulence models in the prediction of drag coefficient, Nusselt number, Separation angle and back reciriculation length. Models included different types of *k*-ε, *k*-ω and RSM. In interface adjacent regions, low Reynolds number modelling as well as standard wall-functions were utilised. They concluded that the *k*-ω SST with low Reynolds number modeling behaves the best in terms of the above mentioned criteria. The drawback was dependence on fine meshes in this case. It is also noted that switching from low-*Re* modeling to standard wall function was a highly pronounced effect on the *k*-ω SST as compared to the same switch for a *k*-ε model.

In the second category of work, porosity inside the food stacks or boxes could not be neglected and hence, turbulence was mostly switched on inside the porous region. To characterize this macroscopic porosity, void level simulations were mainly utilized to provide closure for the macroscopic porous models. The closure path either depended on, empiricism [63], sensitivity analysis for different closure parameters of flow, heat and mass transfer [64], experimental evidence [65] or physical analysis utilizing a representative elementary volume (REV) and averaging the microscopic information through it [66-67]. In these studies the RNG *k*-ε [63, 68], *k*-ω SST [64-67] and RSM [69] were utilized. A choice of a model was mainly based on assessment of different models based on the average error between the experiments and CFD predictions of velocity [66] and temperature [65]. A drawback was that the deviations of different turbulence models near the fluid/porous interface was not considered. One study by Tutar et al. [68] came to a conclusion that the inlet level of turbulence for the flow was not a significant factor for

heat and mass transfer and that other effects like presence of three dimensionality and changing the flow rate are more significant. The disadvantages for this category of studies was the absence of interest in closure of additional porous media terms in the turbulence models and the lack of an investigation of the fluid/porous interface mathematics for coupling turbulence across both regions i.e. all of the above studies depended on the technique that is available in the utilised commerical software ANSYS FLUENT^{TM} [70] plus forcing a switch off for turbulence in some regions (porous and fluid)[63].

1.2.5 Turbulence coupling across macroscopic interfaces

Due to the different natures of the volume averaged equations of porous media and the clear fluid equations, it is important to have a valid coupling approach of turbulence between both regions. Such a process is reliant on an understanding of the physical changes across the transition between both regions. One group of studies focused on utilizing different turbulence models for the macroscopic interface-adjacent layer from the clear fluid side and the free stream region. Such an approach was utilized with a *k-l* model near the interface, a *k-ε* model in the free stream and a compatibility mathematical condition in between [71]. The work utilized a dimensionless fully developed pipe flow around a porous layer and a Brinkman-Forchheimer-extended Darcy equation through it. Another version of the work utilized a Cebecci-smith two-layered turbulence model [72-73] and analyzed the thermal dispersion process inside the porous region [73]. The main disadvantage was relying on a dimensionless analytical expression for the pipe flow, rendering the findings to be case-specific and not generally applicable for other CFD studies. One other study utilized an Analytical wall function [74] for the flow adjacent to a porous region and matched it to an approximation of the Darcy equation solution inside it. Again, this approach was not possible to generalize on other CFD studies. Another work used enough refinement to well capture the viscous layer without modelling and utilized simple turbulence modeling (Prandtl mixing length, Han-Van Driest and Baldwin-Lomax) on the outside region [75] which is considered an over-simplification. Multiple coupling of different models have been utilized by Beyhaghi et al. [76] with a pore-network model (for fluid flow and its moisture coupling) inside the porous region, FLUENT^{TM} [70] for clear fluid region's turbulence modeling and a mass transfer code for the inside mass transfer

process. A no-slip condition was imposed at the macroscopic interface. This group of studies neglected turbulence inside the porous region which is a significant loss of generality.

A second school of work depended entirely on void-level CFD simulations for characterizing the fluid/porous transition. They utilized case specific geometries like group of rods [77] or cubic blocks [78] and their interaction with clear fluid regions with no need for mathematical interface treatments. Sophisticated modeling has been carried out as well in which both a large eddy simulation (LES) or (DNS) is utilized for void level simulations on clear fluid transition to inline/staggered blocks/spheres and continuum approaches for porous media with the same geometry. Jin and Kuznetsov [79] used DNS and volume and time averaged the data to form a basis for comparison to continuum modeling. They concluded that zero equation modeling is enough inside the porous region and turbulence scale is restricted by the pore size. Forcing a gradual change of porosity between the fluid and porous region for the continuum modeling was deemed useful as well [80-81]. The approach enabled using one form of equations for both regions and a turbulence coupling mathematical condition was not necessary. Also, PIV experiments outside the porous region and LES simulations on the inside of it were utilized with the gradual porosity transition technique to develop a four-equation multiscale k-ε model that was successful for analyzing the turbulence within and across the porous region [81]. One may comment that these sophisticated models while capable, they are not general, require extremely fine meshes and have long computational times.

A successful and economic approach for devising a mathematical condition for turbulence across fluid/porous interface was reported [82-83]. The approach utilized a jump condition at the interface for momentum [84] with a continuity condition for k and ε [82] and later another jump coefficient was introduced for k and ε as well [83]. The technique while successful did not provide a general guideline on the estimation of these jump coefficients and was also based on an assumption of a highly permeable media. In cases of low-permeability media like produce e.g. apples and potatoes, the interface condition may not necessarily be valid because of the wall-like blockage and shear in these cases.

1.3 Gaps in the literature and Research Objectives

This section is devoted to presenting the thesis objectives based on the critique for the literature and the knowledge gaps. In view of the literature presented, it has been shown that:

- Modelling of the moisture phase exchange inside porous media has either been, overlooked by the use of equilibrium heat and mass transfer, empirically forced to change near the dry out with an ad-hoc predetermination of a critical moisture content, depended on a surface of solid that is either fully saturated with vapor or was based on a thermodynamic equilibrium expression that is not necessarily accurate near the dry out, or, have been fully resolved analytically/numerically in a complicated technique that is not suitable for three dimensional CFD implementation.

- Energy accompanying the moisture phase exchange has been either fully apportioned to the fluid side for cases relevant to evaporative cooling, or, fully apportioned to the solid side for cases relevant to moisture that is mainly embedded inside the solid. Both cases have a loss of generality.

- Coupling between fluid and porous regions has either been empirically achieved, explicitly achieved in a time consuming technique, or, implicitly achieved with ad-hoc adjustment of the mass transfer resistances in the solid and fluid portions of the porous region.

- Turbulence coupling across fluid/porous interfaces has either been overlooked with assuming laminar flow inside porous region, achieved by assuming the validity of a porous modelling technique across the regions with inclusion of a porosity gradient in the transition region, achieved with a complicated modeling approach like multiscale k-ε models, LES or DNS, or, achieved by using an ad-hoc jump coefficient for k and ε equations.

- Turbulence penetration/dissipation inside a low permeability porous region has not been allowed to develop dynamically and has been forced to be switched off.

In view of these limitations, it is clear that a physically based, fully implicit and simultaneous technique is absent from the literature survey. A technique of this type is developed herein which is referred to as a "Dynamic Coupling" technique. A dynamic coupling technique is defined as a generic, physically-dynamic, implicit, simultaneous, and non-equilibrium technique for phase coupling microscopically (i.e. interstitially) and macroscopically (i.e. across clear fluid/porous interfaces) for conjugate fluid/porous regions. It is characterized as physically dynamic because it allows a numerical reaction to the physics that is dynamically changing based on the different resistances to flow, heat and mass transfer that emerges for different modes and are manifested through space and time. It also allows the tracking of the values of these resistances in a way that needs a reduced level of empiricism or calibration and hence, this enables versatility for vast areas of work and allows an applicability to a wide range of materials and operating conditions and may be considered generic as will be discussed in Chapters 2 and 3. The main objective of the present work is to develop a full flow, heat and mass transfer numerical CFD framework that is capable of achieving a dynamic coupling simulation for the physics of the flow, heat and mass transfer for conjugate domains. Specifically, we may break down this overall goal of work to the following objectives:

1. Develop a dynamic coupling framework that implicitly solves heat and mass transfer for conjugate fluid/porous regions in laminar flows by tracking heat and mass resistances and allow a stable numerical switching between different expressions of different modes for heat and mass transfer, allows a physically based apportioning of the vaporization energy on different phases, and, allows an implicit coupling between fluid and porous regions taking into account the numerical stability, the different species (liquid and vapor) and the two forms (i.e. two resistance legs) of transport of the two phases at the macroscopic interface.

2. Extend the applicability of the dynamic coupling approach to turbulent flows utilizing a technique that allows for penetration/dissipation of turbulence inside porous regions to evolve naturally without any ad-hoc switch off, taking into consideration the computational time and the reflection of turbulence on the flow,

heat and mass transfer inside the porous region and across the macroscopic interface.

3. Develop a capability of characterizing both high and low permeability porous region in turbulence, flow, heat and mass transfer interstitially and macroscopically, taking into consideration the additional blockage and the wall-like shear of low permeability porous media so that a single modeling approach may be able to treat media that is of dynamic porosity and permeability.

1.4 Research Methodology

1.4.1 Volume and time averaging

Before the introduction of our transport equations, we need to shed some light on the different averaging processes in the present work. The porous media modelling herein depends on the theory of volume averaging by Whitaker [85]. Since the presence of solid and fluid phases in the porous region is characterized in an up-scaled manner, an averaging process has to be considered to integrate the microscopic effects that include phase-interaction and small scale spatial variations to the macroscopic scale. So that the volume averaged equations resolve the transport through this macroscopic scale and models the filtered variations in the microscale through closure terms that are introduced to replace the microscale part of the physics. Whitaker [85] defined the macroscale of interest utilizing different scale assumptions, arriving at the concept of a representative elementary volume (REV), which herein we associate a volume V to (see Fig. 1.5). The choice of V is made in a way that it is large enough so that the point value of the volume-averaged quantities is not dependent on value of V but small enough so that it is valid to assume a uniform value of the volume-averaged quantities through it. In our analysis, two types of volume averages are important for any locally-varying entity of interest φ. An extrinsic or superficial average $\langle \varphi_x \rangle$ and an intrinsic or phase-specific average $\langle \varphi_x \rangle^x$. Over the REV, the former is expressed as,

$$\langle \varphi_x \rangle = \frac{1}{V} \int_{V_x} \varphi_x \, d\, V \tag{1.1}$$

while the latter is given by,

$$\langle \varphi_x \rangle^x = \frac{1}{V_x} \int_{V_x} \varphi_x \, d\, V = \frac{\langle \varphi_x \rangle}{V_x / V} \tag{1.2}$$

where x is a phase index and V_x is the volume of phase x inside the REV. One notices that V_x/V represents the porosity (herein as ε) for the fluid phase and the solidity (herein as $(1-\varepsilon)$) for the solid phase. In order to treat transport terms that include the divergence of different quantities, we introduce the spatial averaging theorem (SAT) [85] as,

$$\langle \nabla \cdot \varphi_x \rangle = \nabla \langle \varphi_x \rangle + \frac{1}{V} \int_{A_{xy}} \boldsymbol{n}_{xy} \cdot \varphi_x \, d\, A \tag{1.3}$$

where the first term represents the gradient of the extrinsic quantity of φ through phase x and the second term is the extrinsic average of the amount of φ that crosses from phase y to phase x, $\boldsymbol{n}_{xy}$ is the microscopic local unit normal vector between the two phases and A_{xy} is the interfacial surface area through the REV. The introduction of a spatial deviation to transport quantities for characterizing microscopic spatial variations is often needed when applying volume averaging where the spatial deviation $\widetilde{\varphi_x}$ may be defined as,

$$\widetilde{\varphi_x} = \varphi_x - \langle \varphi_x \rangle^x \tag{1.4}$$

and $\langle \widetilde{\varphi_x} \rangle = 0$. Through the volume averaging process of the transport equations one often needs to transform the volume average of products into the product of volume averages. Utilizing the above definition for deviations, we may cast the volume average of a product of two variables in the following form,

$$\langle \varphi_{x,1} \varphi_{x,2} \rangle = \frac{V}{V_x} \langle \varphi_{x,1} \rangle \langle \varphi_{x,2} \rangle + \langle \widetilde{\varphi_{x,1}} \widetilde{\varphi_{x,2}} \rangle = \frac{V_x}{V} \langle \varphi_{x,1} \rangle^x \langle \varphi_{x,2} \rangle^x + \langle \widetilde{\varphi_{x,1}} \widetilde{\varphi_{x,2}} \rangle \tag{1.5}$$

It is often encountered also in the volume averaging process, the need to close the terms $\frac{1}{V} \int_{A_{fs}} \boldsymbol{n}_{fs} \cdot \mathbf{v} \, d\, A$ and $\frac{1}{V} \int_{A_{fs}} \boldsymbol{n}_{fs} \, d\, A$. The first term is deemed neglected since $\mathbf{v}_{|A_{fs}}$ is neglected to satisfy the no slip condition. For the second term, with the use of the SAT and

the facts that $\langle \nabla (1) \rangle$ is of zero value and $\langle 1 \rangle = \varepsilon$, we may introduce the following equation,

$$\frac{1}{V} \int_{A_{fs}} \boldsymbol{n}_{fs} \, d\, A = \nabla \, \varepsilon \approx 0 \tag{1.6}$$

where in our formulation no spatial or temporal gradient of porosity is considered. Now, we shift our attention to time averaging. It is often needed in the presence of turbulence to express the transport equations in a time averaged framework. In analogy with volume averaging, one may cast the time average of a time-fluctuating entity φ over a period of time Δt as,

$$\bar{\varphi} = \frac{1}{\Delta t} \int_{t}^{t+\Delta t} \varphi \, dt \tag{1.7}$$

where Δt is large enough so that $\bar{\varphi}$ does not depend on its value but small enough so that $\bar{\varphi}$ value does not change through it. Similarly a time fluctuation φ' is defined as,

$$\varphi' = \varphi - \bar{\varphi} \tag{1.8}$$

where $\overline{\varphi'} = 0$. The time averaging approach is used often on a clear fluid domain [86]. Here, it is the applicability of both time and volume averaging to a porous domain that is intricate. The process is termed Double-decomposition [87]. It depends on applying time averaging followed by volume averaging or vice-versa. Since the time change and volume change are not correlated (i.e. there is no shrinkage and volume is rigid and does not change with time), the order of integrals does not affect the final result [87] i.e.$\langle \bar{\varphi} \rangle = \overline{\langle \varphi \rangle}$. Based on the above, one may decompose any locally-varying time-fluctuating fluid entity φ as,

$$\varphi_f = \langle \overline{\varphi_f} \rangle^f + \widetilde{\overline{\varphi_f}} + \langle \varphi_f{}' \rangle^f + \widetilde{\varphi_f}' \tag{1.9}$$

Different other combinations are possible and may be used based on the above equations. It may also be concluded that $\widetilde{\varphi'} = \tilde{\varphi}'$ and $\widetilde{\overline{\varphi'}} = \langle \widetilde{\varphi'} \rangle^f = 0$ [87].

Now, that the averaging processes are introduced, we may introduce the transport equations development.

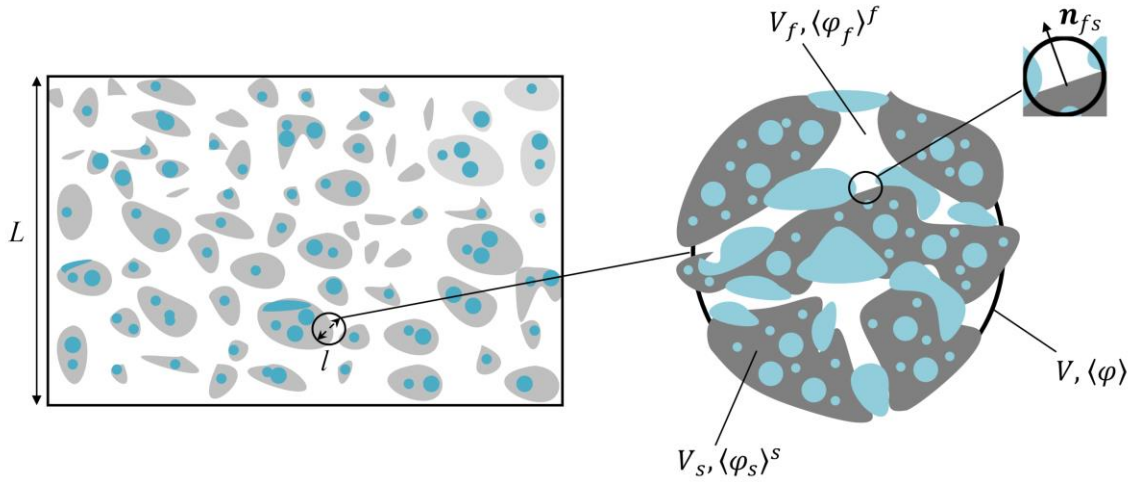

Figure 1.5: Schematic of a representative elemental volume (REV) illustrating the different phases and their volume averages.

1.4.2 Evolution of the transport equations in the present work

Herein, the developed forms for the transport equations that were utilized in chapters 2 and 3, are presented. We utilize an incompressible system of equations. One may cast the equations for continuity and Navier-Stokes for a clear fluid region in their usual forms without inclusion of any external mass or momentum sources [85], as,

$$\frac{\partial \rho_f}{\partial t} + \nabla.(\rho_f \mathbf{v}) = 0 \tag{1.10}$$

$$\frac{\partial (\rho_f \mathbf{v})}{\partial t} + \nabla.\left(\rho_f \mathbf{v}\mathbf{v}\right) = -\nabla P + \mu_f \nabla^2 \mathbf{v} \tag{1.11}$$

We may also give the vapor mass fraction equation [8-9] for a clear-fluid mixture of moist air (dry air and water vapor) by,

$$\frac{\partial(\rho_f Y_v)}{\partial t} + \nabla.\left(\rho_f Y_v \mathbf{v}\right) = \nabla.\left(\rho_f D_f \nabla Y_v\right) \tag{1.12}$$

For the heat transfer equation, we separate the sensible and latent energies in transient, advective and diffusive terms [22]. To elaborate on the development of the equation, we start by considering the sum of the enthalpy equations for species, given in the absence of external sources by,

$$\sum_i \left(\frac{\partial\left(\rho_{f_i} h_i\right)}{\partial t} + \nabla.\left(\rho_{f_i} h_i \, \mathbf{v_i}\right) \right) = k_f \nabla^2 T \tag{1.13}$$

In order to arrive at the final form in chapter 2, we introduce a mass fraction decomposition for species densities $\rho_{f_i} = \rho_f Y_i$ to utilize a fixed overall mixture density ρ_f. We also decompose the total species velocity $\mathbf{v_i}$ with the introduction of species diffusion velocity $\mathbf{v_i} = \mathbf{v} + \mathbf{v_{diff}}_i$. We may also use Fick's law of species diffusion and total enthalpy decomposition by specific and latent heats given by,

$$\rho_{f_i} \mathbf{v_{diff}}_i = -\rho_f D_f \nabla Y_i \qquad , \qquad h_i = c_{p,i} T + h_{fg,i} \tag{1.14}$$

Allowing the use of the next final form,

$$\begin{aligned} \sum_i c_{p,i} \frac{\partial(\rho_f Y_i T)}{\partial t} + \sum_i h_{fg,i} \frac{\partial(\rho_f Y_i)}{\partial t} \\ + \sum_i c_{p,i} \nabla.\left(\rho_f Y_i T \mathbf{v}\right) + \sum_i h_{fg,i} \nabla.\left(\rho_f Y_i \mathbf{v}\right) \\ = k_f \nabla^2 T + \sum_i \nabla.\left[\rho_f D_f \left(\nabla Y_i\right)\left(c_{p,i} T + h_{fg,i}\right)\right] \end{aligned} \tag{1.15}$$

Now that the clear fluid form of equations is presented, the task turns to volume-averaging and arrival at the porous region form of equations. In order to start the volume decomposition process we introduce the relation between different averages of variables and their spatial-deviations. It is considered that $|\langle Y_{i,f} \rangle^f| \gg |\widetilde{Y_{i,f}}|$, $|\nabla \langle Y_{i,f} \rangle^f| \gg$

$|\nabla\widetilde{Y_{i,f}}|$, $|\langle T_f\rangle^f| \gg |\widetilde{T_f}|$ and $|\langle T_s\rangle^s| \gg |\widetilde{T_s}|$ [8-9, 85] while $|\langle \mathbf{v}\rangle^f| \approx |\widetilde{\mathbf{v}}|$ to satisfy the no slip condition at the microscopic interface between fluid and solid phases. It is noted that although the microscopic interface is moisture permeable, it is still considered as a no slip and no penetration surface for overall mixture fluid flow i.e. $\mathbf{v_i} = \mathbf{v_{diff}}_i$ at the microscopic interface. As for the density $|\langle\rho_f\rangle^f|$ it is deemed comparable to $|\widetilde{\rho_f}|$ because of the transfer of moisture at the fluid phase/solid phase interface that is allowed to simulate drying. Utilizing the above assumptions and the different equations of volume averaging in a similar approach to Whitaker's [8-9] we may arrive at the final form of mass conservation. Consideration of the density deviation herein $|\widetilde{\rho_f}|$ instead of Whitaker's assumption of neglecting it [85] results in a mass exchange interfacial term to be present in the continuity equation (i.e. a mass source that emerges due to phase change from liquid inside the solid constituent to vapor inside the fluid mixture). Herein we omit this source term from the continuity equation by utilizing a discretization approach that allows for the update of the density within each non-linear iteration in our in-house code [22]. The final continuity equation form may be cast as,

$$\varepsilon\frac{\partial\langle\rho_f\rangle^f}{\partial t} + \nabla.\left(\langle\rho_f\rangle^f\langle\mathbf{v}\rangle\right) = 0 \tag{1.16}$$

The reflection term of the above-mentioned mass exchange source term of the continuity equation is neglected in the momentum equation allowing a straight forward derivation similar to Whitaker's [85] to arrive at its final closed form cast as [85],

$$\begin{aligned}\frac{\partial\left(\langle\rho_f\rangle^f\langle\mathbf{v}\rangle\right)}{\partial t} + \frac{1}{\varepsilon}\nabla.\left(\langle\rho_f\rangle^f\langle\mathbf{v}\rangle\langle\mathbf{v}\rangle\right) \\ = -\varepsilon\nabla\langle P\rangle^f + \mu_f\nabla^2\langle\mathbf{v}\rangle - \frac{\varepsilon\mu_f}{K}\langle\mathbf{v}\rangle - \frac{\varepsilon\langle\rho_f\rangle^f c_E}{\sqrt{K}}|\langle\mathbf{v}\rangle|\langle\mathbf{v}\rangle\end{aligned} \tag{1.17}$$

The above forms of the continuity and momentum equations are identical to Whitaker's [85]. The mass and heat equations differs herein because of considering only one microscopic interface between the fluid phase and the other phases i.e. the solid and liquid phases are lumped inside one constituent comprising of liquid and solid with defining the liquid water transport equation to represent moisture transport inside this constituent rather

than treating liquid as a separate phase. Utilizing the above assumptions, the volume decomposition equations and the volume average-deviation relations, we arrive at a vapor mass fraction equation of the following form,

$$\begin{aligned}\varepsilon\frac{\partial\left(\langle\rho_f\rangle^f\langle Y_{v,f}\rangle^f\right)}{\partial t}+\varepsilon\nabla.\left(\langle\rho_f\rangle^f\langle Y_{v,f}\rangle^f\langle\mathbf{v}\rangle^f\right)\\ =\nabla.\Bigg(\langle\rho_f\rangle^f\varepsilon D_f\nabla\langle Y_{v,f}\rangle^f+\langle\rho_f\rangle^f D_f\frac{1}{V}\int_{A_{fs}}\boldsymbol{n}_{fs}\cdot\widetilde{Y_v}\,dA\\ -\langle Y_{v,f}\rangle^f\langle\widetilde{\rho_f}\tilde{\mathbf{v}}\rangle-\langle\mathbf{v}\rangle^f\langle\widetilde{\rho_f}\widetilde{Y_v}\rangle-\langle\rho_f\rangle^f\langle\widetilde{Y_v}\,\tilde{\mathbf{v}}\rangle\Bigg)\\ +\frac{1}{V}\int_{A_{fs}}\boldsymbol{n}_{fs}\cdot\rho_f D_f\left(\nabla Y_v\right)dA\end{aligned}\tag{1.18}$$

Arrival at this form was possible by omitting single correlation and triple correlation terms, moving the advective term deviations to the RHS to incorporate them with the elliptic gradient term and neglecting transient gradients of deviation terms. The last term on the RHS represents the mass transfer across the microscopic interface i.e. $\langle\dot{m}_{fs}\rangle$ while the resulting gradient term includes, respectively, a diffusion term which may also include any capillary or surface tension effects, a tortuosity term that represents the deviations of the mass fractions encountered along the tortuous path of the microscopic interface, and three mass dispersion terms coming from double correlation of deviations for ρ_f, Y_v and **v.** The above form for the mass fraction equation needs closure to be useful in CFD simulations. All the gradient transport terms are lumped inside an effective diffusivity $D_{eff,f}$. Now, the equation may be expressed in its final closed form as,

$$\begin{aligned}\varepsilon\frac{\partial\left(\langle\rho_f\rangle^f\langle Y_{v,f}\rangle^f\right)}{\partial t}+\nabla.\left(\langle\rho_f\rangle^f\langle Y_{v,f}\rangle^f\langle\mathbf{v}\rangle\right)\\ =\nabla.\left(\langle\rho_f\rangle^f D_{eff,f}\nabla\langle Y_{v,f}\rangle^f\right)+\langle\dot{m}_{fs}\rangle\end{aligned}\tag{1.19}$$

and in a similar way for the liquid mass fraction, we arrive at,

$$(1-\varepsilon)\frac{\partial\left(\langle\rho_s\rangle^s\langle Y_{w,s}\rangle^s\right)}{\partial t}=\nabla.\left(\langle\rho_s\rangle^s D_{eff,s}\nabla\langle Y_{w,s}\rangle^s\right)-\langle\dot{m}_{fs}\rangle\tag{1.20}$$

Following the same approach for the fluid energy equation, it may be written in this form,

$$\sum_i \varepsilon c_{p,i} \frac{\partial\left(\langle\rho_f\rangle^f \langle Y_{i,f}\rangle^f \langle T_f\rangle^f\right)}{\partial t} + \sum_i \varepsilon h_{fg,i} \frac{\partial\left(\langle\rho_f\rangle^f \langle Y_{i,f}\rangle^f\right)}{\partial t} + \sum_i c_{p,i} \nabla.\left(\varepsilon\langle\rho_f\rangle^f \langle Y_{i,f}\rangle^f \langle \mathrm{T}_f\rangle^f \langle \mathbf{v}\rangle^f\right)$$
$$+ \sum_i h_{fg,i} \nabla.\left(\varepsilon\langle\rho_f\rangle^f \langle Y_{i,f}\rangle^f \langle \mathbf{v}\rangle^f\right)$$
$$= \nabla.\Bigg(\varepsilon k_f \nabla\langle T_f\rangle^f + k_f \frac{1}{V}\int_{A_{fs}} \boldsymbol{n}_{fs} \tilde{T}_f dA$$
$$- \sum_i c_{p,i}(\langle\rho_f\rangle^f \langle Y_{i,f}\rangle^f \langle \tilde{\mathbf{v}}\tilde{T}_f\rangle + \langle\rho_f\rangle^f \langle \mathbf{v}\rangle^f \langle \widetilde{Y_{i,f}}\tilde{T}_f\rangle + \langle Y_{i,f}\rangle^f \langle \mathbf{v}\rangle^f \langle \widetilde{\rho_f}\tilde{T}_f\rangle) - \sum_i (c_{p,i}\langle \mathrm{T}_f\rangle^f + h_{fg,i})(\langle\rho_f\rangle^f \langle \tilde{\mathbf{v}}\tilde{Y}_{i,f}\rangle \quad (1.21)$$
$$+ \langle Y_{i,f}\rangle^f \langle \widetilde{\rho_f}\tilde{\mathbf{v}}\rangle + \langle \mathbf{v}\rangle^f \langle \widetilde{\rho_f}\tilde{Y}_{i,f}\rangle)\Bigg)$$
$$+ \sum_i \nabla.\left(\varepsilon D_f \langle\rho_f\rangle^f \nabla\langle Y_{i,f}\rangle^f \left(c_{p,i}\langle \mathrm{T}_f\rangle^f + h_{fg,i}\right) + D_f\langle\rho_f\rangle^f \frac{1}{V}\int_{A_{fs}} \boldsymbol{n}_{fs}\, \tilde{Y}_{i,f}\left(c_{p,i}\langle \mathrm{T}_f\rangle^f + h_{fg,i}\right) dA\right)$$
$$+ \frac{1}{V}\int_{A_{fs}} \boldsymbol{n}_{fs}.\, k_f \nabla T_f dA + \sum_i \frac{1}{V}\int_{A_{fs}} \boldsymbol{n}_{fs}.\, \rho_f D_f \nabla Y_i (c_{p,i} T_f + h_{fg,i}) dA$$

This form of fluid energy equation was arrived at by omitting single, triple and quadruple correlation terms and following the same assumptions as for fluid species equation derivation. There is two gradient transport terms in this case with the first one related to sensible energy diffusion i.e. conduction and thermal/species energy dispersion and the second one is for latent energy or energy accompanying species transport. The first bracket on the RHS includes respectively, a conduction term, thermal tortuosity term and six component terms of thermal/species energy dispersion depending on six double correlation terms. The second bracket represents, respectively, species energy diffusion and species energy tortuosity. One may utilize an effective conductivity and diffusivity $k_{eff,f}$ and $D_{eff,f}$, respectively, to close the terms in the two brackets. The second last term on the RHS represents sensible energy transfer across the microscopic interface and is closed herein with a local heat transfer coefficient for exchange as $h_{fs}A_{fs}\left(\langle T_s\rangle^s - \langle T_f\rangle^f\right)$. The last term on the RHS is the latent energy exchange based on mass exchange and by looking at its composition, one notices that it includes the mass exchange closure term within it and hence it may be closed as $\dot{H}_{fs}^{mass} = \sum_i \langle\dot{m}_{fs}\rangle_i\, h_{i_{fs}}$where $h_{i_{fs}}$is the enthalpy

of species i at the microscopic interface as it crosses between phases. Chapters 2 and 3 include a technique of calculating the value for this enthalpy for drying processes and another one that reconciles the form of this term with the unique approach utilized for discretization that omits the mass exchange term from the continuity equation as mentioned earlier and thus, this process has a reflection on the fluid energy equation discretization as well. Based on the above decomposition and for a similar treatment of solid energy equation, the energy equations in their final forms are cast as,

$$\begin{aligned}\sum_i \varepsilon c_{p,i}\frac{\partial\left(\langle\rho_f\rangle^f\langle Y_{i,f}\rangle^f\langle T_f\rangle^f\right)}{\partial t}+\sum_i \varepsilon h_{fg,i}\frac{\partial\left(\langle\rho_f\rangle^f\langle Y_{i,f}\rangle^f\right)}{\partial t}\\ +\sum_i c_{p,i}\nabla.\left(\langle\rho_f\rangle^f\langle Y_{i,f}\rangle^f\langle T_f\rangle^f\langle\mathbf{v}\rangle\right)\\ +\sum_i h_{fg,i}\nabla.\left(\langle\rho_f\rangle^f\langle Y_{i,f}\rangle^f\langle\mathbf{v}\rangle\right)\\ =k_{eff,f}\nabla^2\langle T_f\rangle^f\\ +\sum_i \nabla.\left[\langle\rho_f\rangle^f D_{eff,f}\nabla\langle Y_{i,f}\rangle^f\left(c_{p,i}\langle T_f\rangle^f+h_{fg,i}\right)\right]\\ +h_{fs}A_{fs}\left(\langle T_s\rangle^s-\langle T_f\rangle^f\right)+\dot{H}_{fs}^{mass}\end{aligned} \tag{1.22}$$

$$\begin{aligned}\sum_i(1-\varepsilon)c_{ps,i}\frac{\partial\left(\langle\rho_s\rangle^s\langle Y_{i,s}\rangle^s\langle T_s\rangle^s\right)}{\partial t}\\ =k_{eff,s}\nabla^2\langle T_s\rangle^s+\sum_i\nabla\left[\langle\rho_s\rangle^s D_{eff,s}\nabla\langle Y_{i,s}\rangle^s\left(c_{ps,i}\langle T_s\rangle^s\right)\right]\\ -h_{fs}A_{fs}\left(\langle T_s\rangle^s-\langle T_f\rangle^f\right)-\dot{H}_{fs}^{mass}\end{aligned} \tag{1.23}$$

In regards to the turbulent version of these transport equations which is presented in chapter 3, a full mathematical treatment may be found for clear fluid region by Wilcox [86], and for Porous media by De Lemos [87]. Herein, the major features only are discussed. Regarding the *point* continuity equation, both a time averaged version for $\bar{\mathbf{v}}$ or a time-fluctuation version for $\mathbf{v}'$ may have the same form as an instantaneous version for $\mathbf{v}$ after carrying out the time averaging. In regards to the Navier-Stokes equations, the main difference arises from the turbulent stresses (i.e. double correlation fluctuation terms

arising from time-averaging of the instantaneous advective transport term, which are analogous to the above dispersive terms for laminar porous media modeling). Herein, our work depends on the Boussinesq approach [86] which incorporates the turbulent stresses inside a diffusion term and closes them using an eddy viscosity μ_t. A similar approach is used for heat and mass transfer analogous terms as well in which an eddy conductivity and diffusivity are linked by analogy to the eddy viscosity using a turbulent Prandtl Pr_t and Schmidt Sc_t numbers. The turbulent fluctuation terms may all be represented as,

$$\mu_t = C_\mu \overline{\rho_f} \frac{k^2}{\varepsilon} \;\; , -\overline{\rho_f}\;\overline{\mathbf{v}'\mathbf{v}'} = \mu_t\, 2\overline{D} - \frac{2}{3}\overline{\rho_f}\, k\, \boldsymbol{I} \;, -\overline{\rho_f}\overline{\mathbf{v}'\mathrm{T}'} = \frac{\mu_t c_{p,f}}{Pr_t} \nabla \bar{T}$$
$$-\overline{\rho_f}\overline{\mathbf{v}' Y_\iota'} = \frac{\mu_t}{Sc_t} \nabla \bar{Y}_\iota \tag{1.24}$$

where herein the eddy viscosity is given by the standard *k*-ε model approximation wherein C_μ is a constant **,** $\overline{D}$ is the fluid deformation tensor estimated by, $\overline{D} = (\nabla \bar{\mathbf{v}} + (\nabla \bar{\mathbf{v}})^T)/2$, k is the turbulent kinetic energy which is given as, $\overline{\mathbf{v}'\mathbf{v}'}/2$, $\boldsymbol{I}$ is the unit dyadic and ε is the turbulence energy dissipation which is estimated by, $\mu_f(\overline{\nabla \mathbf{v}' : \nabla \mathbf{v}'^T})/\rho_f$. The turbulent diffusion terms are all lumped inside the main diffusion term where the eddy diffusivities act as an enhancement to the molecular diffusion while the term $-(2\overline{\rho_f}\, k/3)\, \boldsymbol{I}$ is incorporated with the pressure term to form the kinematic pressure in the momentum equation as it represents normal turbulent stresses. As for the k-equation, the classic approach for arriving at its mathematical form depends on multiplying the time-averaged Navier-Stokes equations by $\mathbf{v}'$ and then redo the time averaging on the product to obtain a turbulent stress transport equation [86]. k-equation is simply obtained by taking the trace of the turbulent stress equations and carrying out some mathematical manipulations. The ε-equation is obtained by subtracting the time averaged momentum equation from the instantaneous counterpart and differentiating the result with respect to space followed by some mathematical manipulations. The interested reader may turn to Celik [88] for details. Due to the presence of multiple double and triple correlation terms, the exact form of the equations is not utilized and closure is sought in this case. Additional diffusion utilizing the eddy diffusivity, a turbulent kinetic energy Prandtl number σ_k and a dissipation Prandtl

number σ_ε is introduced for closure of some diffusive higher-order correlation terms. Both equations are characterized with their production and destruction or dissipation source/sink terms which represent the main turbulence transport mechanism that converts inertia to turbulent kinetic energy and dissipates it to the molecular viscosity. For k-equation, the production and dissipation are given by,

$$P_k = -\overline{\rho_f}\ \overline{\mathbf{v}'\mathbf{v}'} : \nabla \bar{\mathbf{v}} = \mu_t(\nabla \bar{\mathbf{v}} + (\nabla \bar{\mathbf{v}})^T) : \nabla \bar{\mathbf{v}}\ , \quad \epsilon_k = \overline{\rho_f}\,\varepsilon \tag{1.25}$$

It should be mentioned that the turbulent energy dissipation term is added as a source to the energy equation since it is a loss of kinetic energy that is transformed by viscosity to internal energy. In order to close the production and destruction for ε-equation, one should utilize the local scale equilibrium assumption for turbulence. The assumption indicates that P_k and ϵ_k are of comparable orders of magnitude and shares the same time and length scales that are assumed dependent on location only. While the assumption has its restrictions, it has shown decent success for a wide class of problems in which free stream effects are not as powerful as local effects which indicates that local scales govern the turbulence. It follows from this assumption that $P_\varepsilon\, \alpha\, \frac{P_k}{1/\tau}$ and $\epsilon_\varepsilon\, \alpha\, \frac{\epsilon_k}{1/\tau}$ where $1/\tau$ is a turbulence time scale that is estimated by dimensional analysis as $\frac{k}{\varepsilon}$. It also follows from these expressions that,

$$P_\varepsilon = C_{1\varepsilon}\, P_k \frac{\varepsilon}{k} \quad , \quad \epsilon_\varepsilon = C_{2\varepsilon}\, \overline{\rho_f}\, \frac{\varepsilon^2}{k} \tag{1.26}$$

where $C_{1\varepsilon}$ and $C_{2\varepsilon}$ are constants.

In regards to turbulence in porous media, a volume averaged version of the above-described turbulence equations is sought. Several additional fluctuation-deviation correlation terms are emerged however the closure path is identical to the laminar one in most cases [87]. Most of the turbulent quantities are transformed to their intrinsic averages resulting in a porosity multiplier (herein as ϕ) in several terms. The turbulent eddy viscosity is utilized to enhance diffusion to include the turbulent stresses for momentum herein as well. Instead of utilizing different turbulent Prandtl or Schmidt numbers for heat

and mass transfer, the turbulent fluxes and dispersion terms are all added inside $\lambda_{eff,f}$ and $D_{eff,f}$. $\langle k \rangle^f$ is defined by $\langle \overline{\mathbf{v}'\mathbf{v}'} \rangle^f / 2$ [87] since the definition is deemed inclusive to all necessary terms and is also not depending on the order of the double decomposition [87]. While the turbulence dissipation $\langle \varepsilon \rangle^f$ takes the form $\mu_f \langle \overline{\nabla \mathbf{v}' : \nabla \mathbf{v}'^T} \rangle^f / \langle \overline{\rho_f} \rangle^f$. The forms for $\langle k \rangle^f$ and $\langle \varepsilon \rangle^f$ equations are very similar to their *point* counterparts with intrinsic averaged production and dissipation terms. All of the present formulation equations described for turbulence are presented in their final forms in Chapter 3 and are omitted here for brevity.

The above discussion concludes this section for transport equations' development. The following section is concerned with Conjugate domains and non-equilibria.

1.4.3 Conjugate domains and non-equilibria

In Chapters 2 and 3, the terms of conjugate domains, thermal, mass and thermodynamic non-equilibria are mentioned. In the present section, we elaborate on the meanings and consequences of each of these terms.

Thermal non-equilibrium

A thermal equilibrium approach of study for a porous region implies that at each and any point through the region, the phase specific temperatures are equal i.e. through each REV, the intrinsic temperatures are equal to each other and to the superficial temperature $\langle T_f \rangle^f = \langle T_s \rangle^s = \langle T \rangle$. Consequently, one energy equation for $\langle T \rangle$ is enough to characterize heat transfer inside the domain. Such an equation may be derived by summing the earlier-presented two phase-specific energy equations of $\langle T_f \rangle^f$ and $\langle T_s \rangle^s$. Resulting in the cancellation of the interfacial exchange closure terms, the $\langle T \rangle$ equation is not capable of modeling or quantifying the local phase energy exchange. Another result would be the representation of diffusion inside all the phases utilizing a single effective diffusivity. The approach is widely used in the literature [17-20] due to its simplicity. For a number of reasons, the deviation from thermal equilibrium becomes significant in a lot of porous media heat transfer problems. The fact that the $\langle T \rangle$ equation is the sum of the phase-specific equations falsely gives an impression that the heat transfer conservation achieved is

physically accurate or that characterizing the exchange between phases is not required. That false impression is the reason behind the over or under prediction of the overall heat transfer characteristics that results from such an assumption because any local non-equilibrium effect magnifies through discretization and integration. In cases where the two phases are of considerable difference in respect to conductivity and heat capacity, this local deviation from equilibrium and the consequent error on the overall heat transfer are further magnified. One famous example is the case of porous metal foam in which the two phase conductivities are orders of magnitude different. For a very transient phase exchange phenomenon such as drying, the vaporization energy withdrawal from different phases and its apportioning becomes very important. Because the enthalpies of liquid water and water vapor are very different in their orders of magnitudes, the non-equilibrium effect becomes more pronounced even for small differences in conductivities. Such a problem cannot be overcome unless by estimating the heat exchange accompanying mass exchange. Since the heat and mass transfer processes are also highly coupled in such a case, the error in overall predictions of drying rates and heat transfer becomes even higher because it is reflected on both equations and further magnified. For the above reasons, a thermal non-equilibrium approach is deemed necessary in the present work.

Mass non-equilibrium

The mass or moisture equilibrium approach is analogous to the thermal equilibrium one however in the present framework the equilibrium does not mean equality of both phase mass fractions because of the occurring phase change (i.e. liquid to vapor or vice versa) and the difference in definitions and magnitudes between both of them. Herein, the meaning of equilibrium mass transfer is the capability of representing the total superficial averaged moisture fraction inside an REV using only one transport equation that carries the two phases' moisture in it i.e. $\langle M \rangle$ (kg moisture/m^3 of PM) $= \varepsilon \langle \rho_f \rangle^f \langle Y_{v,f} \rangle^f + (1 - \varepsilon) \langle \rho_s \rangle^s \langle Y_{w,s} \rangle^s$. Arrival to such an equation is obtained in analogy to heat transfer by summing the two phase-specific moisture equations. Herein as well, the process results in cancellation of the moisture exchange terms and the lack of their modeling capability plus the aggregation of diffusion terms and being able to close them with a single diffusivity. The approach has been widely used in the literature [17-20] and is often accompanied by

neglecting the gaseous phase, considering the drying material as a wall. Assigning a single physical state of water to the moisture i.e. liquid for all the moisture present locally is another loss of generality that often accompanies this approach. The approach suffers from accumulation of error due to the heterogeneity of the distributed moisture mass inside a porous medium (i.e. affinity for moisture is different between fluid and solid phases) that is assumed homogenous in this case i.e. the mass transfer profiles are more diffusive. It also produces overall mass transfer and drying rate inaccuracy and has its effect reflected on heat transfer for the same logical reasons as in the above discussed case of thermal equilibrium. Since it often neglects the presence of vapor, a main mechanism for transport that is important in simulations of construction materials moisture removal is absent [6-7]. To avoid all of the above, the present work models both moisture phases.

Thermodynamic non-equilibrium

Is a different type of non-equilibrium that is often encountered in drying processes. The origin of the term thermodynamic equilibrium herein is relevant to the state at which an equal chemical potential (i.e. Gibbs free energy) exists between the liquid water and its adjacent vapor layer. In such a situation, if we think of the evaporation/condensation as a chemical equilibrium reaction, this reaction will no longer change the mixture composition i.e. when chemical potential is equal for both water phases, no more detectable phase change occurs [16]. The term is of more relevance to hygroscopic materials (e.g. fruits and vegetables), which are materials that have considerable room or allowance to absorb moisture and retain it. For these materials, present vapor and liquid are adjacent and hence, the vapor pressure is fully exerted on the liquid and the energy required to allow any more vaporization/condensation is of dependence on it. In cases where the liquid is embedded or partially bound from vapor, the vapor pressure in its classical definition is not directly related to chemical potential. In thermodynamic equilibrium situations, liquid and vapor are directly in contact and it follows from the above discussion that vapor pressure in the moist air is correlated to the liquid concentration in the liquid/solid solution according to Raoult's and Henry's laws. In order to further simplify this equal chemical potential assumption, the water activity a_W is defined. Where water activity is the relative humidity that corresponds to a specific liquid concentration during thermodynamic equilibrium [16].

In short, if thermodynamic equilibrium condition is achieved, $a_W = RH$ at the liquid/vapor surface i.e. solid/fluid microscopic interface. As, Gibbs free energy is also function of temperature, the water activity a_W is function of both the liquid water concentration or mass fraction and temperature. This dependence of a_W allows it to be correlated to liquid mass fraction alone at a fixed temperature i.e. a sorption isotherm [16]. The expression of the mass transfer driving potential based on RH and a_W is also often referred to as thermodynamic equilibrium expression for moisture transfer. This expression could be written when combined with our thermal non-equilibrium assumption as [17],

$$\langle Y_v \rangle^{fs} - \langle Y_{v,f} \rangle^f = \frac{1}{R_v \langle \rho_f \rangle^f} \left(\frac{a_W P_{sat.s}}{\langle T_s \rangle^s} - \frac{RH\ P_{sat.f}}{\langle T_f \rangle^f} \right) \tag{1.27}$$

A deviation from thermodynamic equilibrium occurs in such a situation where the bulk liquid and bulk vapor are partially or no longer in contact, which occurs when the drying out is imminent and the liquid is shrinking inside the solid constituent of the porous material as per our formulation since we do not allow vapor to entrain where solid shrinkage happen i.e. we do not consider shrinkage of the solid/liquid material mass. We also do not allow the presence of liquid water to be zero through the dry layer that forms between the wet core of the solid constituent and the fluid mixture (i.e. a volume averaging restriction) which is another reason for this deviation from equilibrium to occur. It is also worth mentioning that even if these model assumptions were overcome, eventually near to the dry out, the thermodynamic equilibrium assumption in its current form becomes less valid due to the dominance of the liquid diffusion mechanism of mass transfer within the solid with its capillary and surface tension effects that alter the definition of chemical potential and makes it deviate from the classical one. In our frame work, for mathematical convenience and based on our model assumptions of no shrinkage and no complete dry out, the thermodynamic non-equilibrium expression for mass transfer is switched on as soon as it becomes rate-limiting and a mass transfer liquid-in-solid diffusion potential is utilized as explained in Chapter 2.

Conjugate Domains

The conjugate domains are domains that contain fluid/porous/solid regions (see Fig. 1.6). A fluid/porous/solid region may contain a clear fluid and/or porous and/or void-less solid regions with multiple possible macroscopic interfaces between them (i.e. CFD integration faces that separate two cells of different regions). The conjugacy here is based on CFD simulations i.e. conjugate domain approach. All transport equations through all regions and their interface treatments are solved simultaneously without deferral or explicit coupling. The term conjugate is different from coupled in the sense that it is simultaneous. It is also different from conjugate heat and mass transfer as the latter expresses the coupling between heat and mass transfer equations and not the simultaneous coupling of both and each of them through the different regions. It is also worth mentioning that a conjugate domain approach does not utilize any convective boundary conditions at any of the macroscopic interfaces. Different other approaches utilized this boundary conditions and either provided the information for coupling from empirical correlations or segregated the different region solutions and performed iterative updates between them. The merits of the conjugate domain approach over this approach are: the fact that its accuracy is not constrained by the accuracy of empirical estimates and its time-to-solution is not affected by an explicit iterative update between regions.

The above discussion concludes this section for conjugate domains and non-equilibria. The following section is concerned with discretization.

1.4.4 Numerical discretization and solution

The discretization in the present work follows the finite volume approach by Patankar [89]. In order to discuss the discrete form of different terms for our transport equations, one

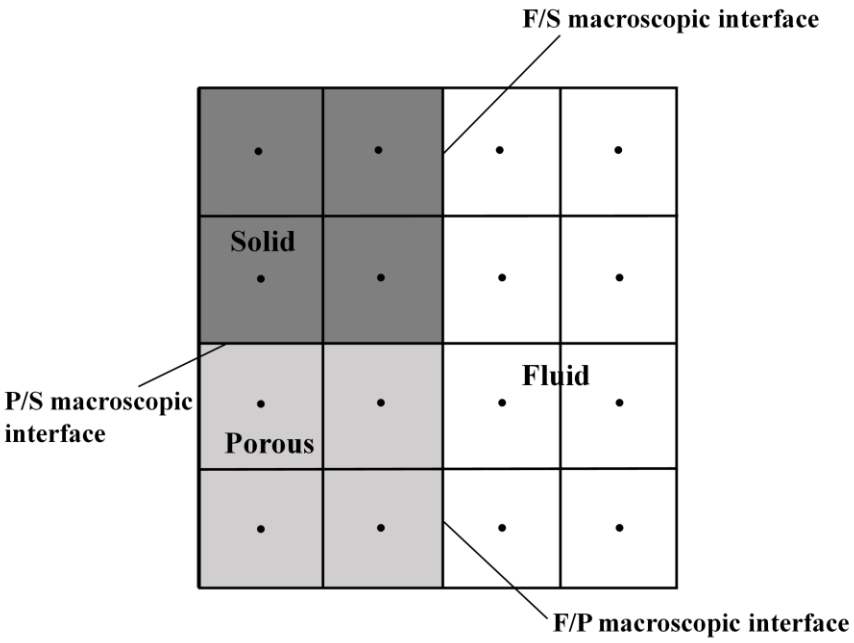

Figure 1.6: Conjugate Fluid/Porous/Solid domains.

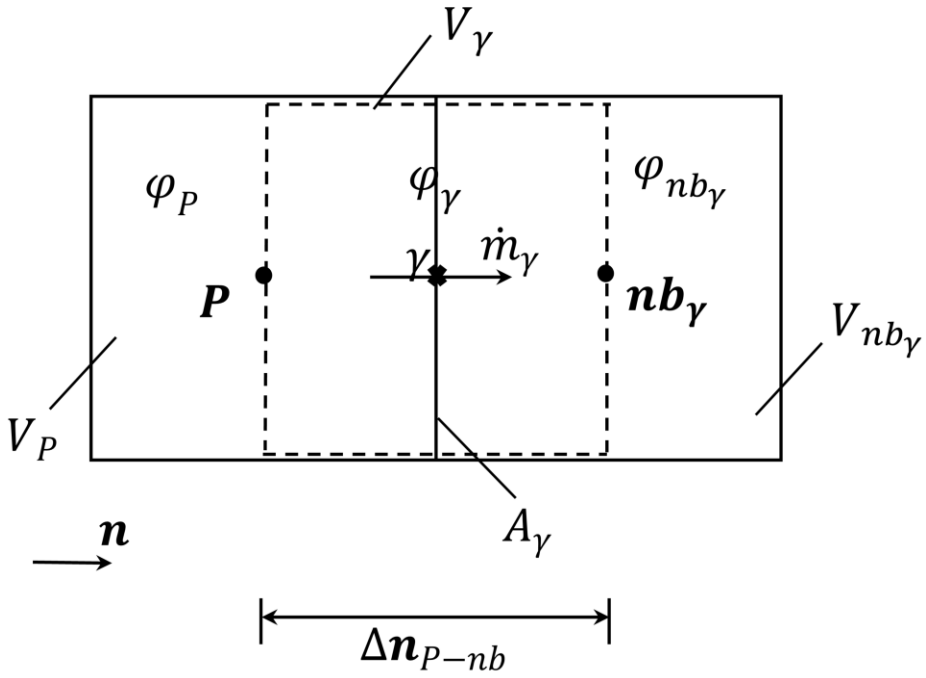

Figure 1.7: Finite volume CFD discretization in structured orthogonal frameworks.

introduces a partial differential equation (PDE) for a generic conserved entity of interest φ in an incompressible fluid flow field, cast as,

$$\frac{\partial(\rho_f \varphi)}{\partial t} + \nabla.\left(\rho_f \varphi \mathbf{v}\right) = \nabla\left(\Gamma^{\varphi} \nabla \varphi\right) + S_{\varphi} \tag{1.28}$$

where the terms from left to right are the unsteady, advective, diffusive and source, respectively. All transport equations may be represented in the above form with suitable substitutes for φ (e.g. $\varphi = 1$ for continuity equation), its diffusion coefficient Γ^{φ} and its source term S_{φ}. The utilized finite volume approach depends on integrating the PDEs in time over a period Δt using an implicit time integration approach and in space over a CFD cell of a control volume V_P containing a node (P) located in its geometric center and has a number of integration faces N that links it to N neighboring control volumes (See Fig. 1.7). Herein also, the continuity equation, multiplied by a reference value of φ (often chosen as φ_P), is subtracted from all other φ-equations in order to reduce the dependence of a φ-equation convergence on the mass conservation. Utilizing an orthogonal and structured framework while applying this integration process on a φ-equation, we arrive at,

$$\frac{V_P \rho_{f,P}^{o}(\varphi_P - \varphi_P^{o})}{\Delta t} + \sum_{\gamma}^{N} \dot{m}_{\gamma}\left(\varphi_{\gamma} - \varphi_P\right) = \sum_{\gamma}^{N} \Gamma^{\varphi}\left(A \frac{\partial \varphi}{\partial \boldsymbol{n}}\right)_{\gamma} + V_P S_{\varphi_P} \tag{1.29}$$

where the mass flux at each integration face γ is defined as $\dot{m}_{\gamma} = \rho_{f_{\gamma}} A_{\gamma}\, \hat{\mathbf{v}}_{\gamma}$. Noting that $\hat{\mathbf{v}}_{\gamma}$ is the advecting velocity, φ_{γ} is the advected value of φ from cell (P) to the neighboring cell (nb_{γ}) and $(\frac{\partial \varphi}{\partial \boldsymbol{n}})_{\gamma}$ is the spatial gradient of φ at face γ in the perpendicular direction. The aim of the discretization process is to cast the above equation in the following form,

$$a_P\, \varphi_P = \sum_{\gamma}^{N} a_{nb_{\gamma}}\, \varphi_{nb_{\gamma}} + b_P \tag{1.30}$$

where the above equation is incorporated with the counterparts of other cells to form a sparse non-symmetric system of algebraic linear equations to be preconditioned and iteratively solved. When the active coefficients a_P, $a_{nb_{\gamma}}$ and active source b_P are functions of φ_P and $\varphi_{nb_{\gamma}}$, the system of equations is linearized by considering the φs explicitly inside

and reiterating using the above equation and hence, we break the non-linear problem into a sequence of linear ones. This process of linearization is done inside each time step where multiple iterations may be required to reach convergence i.e. an inner non-linear CFD loop inside the outer time CFD loop. The advection and diffusion terms are cell coupling terms and hence they have to be implemented implicitly. To that end, starting with the advection term, we estimate φ_γ using a first order upwind approach, as it is the most stable, as,

$$\varphi_\gamma = \frac{1}{2}\left(1 + \psi_{\varphi_\gamma}\frac{\dot{m}_\gamma}{|\dot{m}_\gamma|}\right)\varphi_P + \frac{1}{2}\left(1 - \psi_{\varphi_\gamma}\frac{\dot{m}_\gamma}{|\dot{m}_\gamma|}\right)\varphi_{nb_\gamma} \tag{1.31}$$

where ψ_{φ_γ} is a factor that may or may not be utilized to hybridize the upwind scheme based on a local Peclet number estimate and make it depend on both the two adjacent cell values of φ. This choice is made as needed for different φs and is standardized for ρ_{f_γ}. Whenever a Fluid/Porous interface advection condition or a different advection scheme is implemented i.e. QUICK, CDS, second order upwind or limited upwinding, to preserve stability, we implement an explicit difference between the above implicit implementation and the corresponding scheme which is known as the deferred correction approach of Khosla and Rubin [90]. Turning attention to the diffusion term, the estimate of the gradient of φ at the integration face is given by,

$$\left(\frac{\partial\varphi}{\partial \boldsymbol{n}}\right)_\gamma = \frac{\varphi_{nb_\gamma} - \varphi_P}{\Delta \boldsymbol{n}_{P-nb}} \tag{1.32}$$

This is a straight forward estimate that is very useful for orthogonal frameworks. In cases of non-linearly varying diffusion i.e. Γ^φ is a variable, one utilizes the harmonic mean formulation by Patankar [89, 91] to force the continuity of fluxes given by,

$$\Gamma^\varphi_P\left(\frac{\varphi_\gamma - \varphi_P}{\Delta \boldsymbol{n}_{P-\gamma}}\right) = \Gamma^\varphi_{nb_\gamma}\left(\frac{\varphi_{nb_\gamma} - \varphi_\gamma}{\Delta \boldsymbol{n}_{\gamma-nb}}\right) \tag{1.33}$$

as,

$$(\Gamma^{\varphi}\frac{\partial \varphi}{\partial \boldsymbol{n}})_{\gamma} = \frac{\varphi_{nb_{\gamma}} - \varphi_{P}}{\frac{\Delta \boldsymbol{n}_{P-\gamma}}{\Gamma^{\varphi}_{P}} + \frac{\Delta \boldsymbol{n}_{\gamma-nb}}{\Gamma^{\varphi}_{nb_{\gamma}}}} \tag{1.34}$$

The source terms S_{φ} are either constants or φ-dependent. Sources and transient terms are often apportioned between implicit and explicit implementation. In a constant source term a full explicit implementation is easy to converge. For a φ dependent source term, the apportioning is defined as,

$$S_{\varphi_P} = Q_{\varphi_P} + R_{\varphi_P}\varphi_P \tag{1.35}$$

where R_{φ_P}has to be negative for implicit implementation into a_P while Q_{φ_P} is explicit. For sink terms, we often stabilize the solution by a fully implicit implementation as,

$$Q_{\varphi_P} = 0 \quad , \quad R_{\varphi_P} = S_{\varphi_P}/\varphi_P \tag{1.36}$$

Which is often useful for phase exchange and turbulent dissipation terms. For highly non-linear source terms, they are decomposed as,

$$Q_{\varphi_P} = S_{\varphi_P} - (\frac{\partial S_{\varphi}}{\partial \varphi})_P\, \varphi_P \qquad , \qquad R_{\varphi_P} = (\frac{\partial S_{\varphi}}{\partial \varphi})_P \tag{1.37}$$

The last aspect of implementation concerns the pressure-velocity coupling. Herein, we utilize the collocated approach by Rhie and Chow [92]. The approach utilizes two different definitions for the two velocities inside the momentum equation advection term $\nabla.(\rho_f \mathbf{vv})$. One is $\mathbf{v}_{\gamma}$ which is known as the advected velocity and is estimated using an advection scheme as explained above. The second one is used inside the mass flux $\dot{m}_{\gamma}$ which is known as $\hat{\mathbf{v}}_{\gamma}$ or the advecting velocity. The pressure velocity coupling depends on expressing $\hat{\mathbf{v}}_{\gamma}$ in a form that includes pressure dependence and hence the continuity and momentum equations may be closed as now they both include pressure and velocity dependences. If an imaginary control volume V_{γ} is to be centered at γ integration face, an active coefficient equation for $\hat{\mathbf{v}}_{\gamma}$ may be cast as,

$$a_\gamma \, \hat{\mathbf{v}}_\gamma = \tilde{\mathbf{v}}_\gamma - \left(\frac{\partial P}{\partial \boldsymbol{n}}\right)_\gamma V_\gamma \tag{1.38}$$

where $\left(\frac{\partial P}{\partial \boldsymbol{n}}\right)_\gamma V_\gamma$ is the pressure source term and $\tilde{\mathbf{v}}_\gamma$ is given as, $\sum_P^{N_\gamma} a_{nb}\, \mathbf{v}_{nb} + b_\gamma$ for control volume γ. The above equation is simplified to alter its form from the classic discretized momentum equation (i.e. a special momentum equation) and several interpolations are introduced to link $\tilde{\mathbf{v}}_\gamma$, a_γ and V_γ to their P and nb_γ counterparts, arriving finally at,

$$\hat{\mathbf{v}}_\gamma = \mathbf{v}_\gamma^{approx.} - \frac{V_\gamma}{a_\gamma}\left[\left(\frac{\partial P}{\partial \boldsymbol{n}}\right)_\gamma - \left(\frac{\partial P}{\partial \boldsymbol{n}}\right)_\gamma^{approx.}\right] \tag{1.39}$$

where $\mathbf{v}_\gamma^{approx.}$ may be a central differencing or inverse distancing approximation for $\mathbf{v}$ in clear fluid cells. The second term is a fourth-order correction to the first term including pressure gradients to damp any unconstrained mode of convergence. The above form for $\hat{\mathbf{v}}_\gamma$ is implemented so that $\mathbf{v}_\gamma^{approx.}$ and $\left(\frac{\partial P}{\partial \boldsymbol{n}}\right)_\gamma$ are implicit while $\left(\frac{\partial P}{\partial \boldsymbol{n}}\right)_\gamma^{approx.}$ is deferred explicitly. For porous media cells and Fluid/Porous interface coupling, the above equations for pressure-velocity coupling are valid but they include different approximations for pressure, pressure gradients and interpolated velocity terms [91]. Herein, the approach for solving the continuity and momentum equations is a direct coupled approach. All other equations for temperature and species are directly coupled between phases as well similar to the continuity/momentum coupling while the turbulence equations are segregated. It is also worth mentioning that the turbulence equations solution has a lead over the rest of the equations to improve the stability of convergence by updating turbulence-related terms in the rest of the equations before solving them.

With the pressure-velocity coupling, the discretization discussion is concluded.

1.5 Thesis Outline

Next chapters in this thesis focus on carrying out the work necessary to accomplish the thesis objectives. Description of each chapter is provided as:

- Chapter 2: presents the development of a dynamic coupling model for laminar flow, heat and mass transfer inside porous media and through the fluid/porous transition. Introduction of the work is presented followed by the model formulation including the transport equations in the point form for clear fluid region and their volume averaged counterparts in porous region. This is followed by mathematical coupling conditions across the macroscopic interface and the formulation of novel physical dynamic coupling models interstitially and new resistance networks for coupling across the macroscopic interface. Three verification cases that were selected carefully to provide a spectrum of applicability for the model that shows its viability and usefulness are presented next. The three cases represent a coal particle study to show the interstitial coupling technique's efficacy and two different cases for conjugate fluid/porous coupling that represent a porous material of material-side mass transfer resistance domination (i.e. drying of an apple slice) and another material of convective mass transfer resistance domination (i.e. dehydration of mineral plaster). The model produced very good agreement with reported experimental data. The overall purpose of this chapter is to present this generic approach for treatment of different materials and its flexibility for dealing with different physical cases. This chapter is the basis of work in the whole thesis and the following chapter builds on it for achieving the rest of the objectives for turbulent flows.

- Chapter 3: extends the dynamic coupling approach to include turbulent flows within porous media and across the transition between clear fluid and porous regions and formulates a novel technique for turbulence coupling across the macroscopic interface that is capable of treating both high and low permeability porous materials. The introduction was followed by a detailed description of the formulation enhanced with the turbulence equations and their reflection on other transport equations followed by the mathematical conditions at the fluid/porous interface including turbulence coupling. Next, an extension of the dynamic modeling to turbulent flows is presented including the novel formulation for interface coupling that includes an enhanced wall-like treatment for the

macroscopic interface that is of relevance to low permeability porous materials. A two dimensional test case for flow around and through a porous obstruction was presented to show the efficacy of the model for turbulence coupling in different permeability materials including properties of apple (moderately permeable) and potato slice (low permeability). This is followed by a full flow, heat and mass transfer verification for both produce slices including analysis for the different behaviors of heat and mass transfer in both cases. The technique predicts accurate trends for drying and affirms the applicability of the dynamic coupling approach for turbulent flows as well as proving that an interface coupling approach for turbulence is not capable alone to treat a low permeability material and an enhanced wall-like treatment is required.

- Chapter 4: is the last chapter of the thesis, providing summary of the work, original thesis contributions and future recommendations.

References

[1] Elhalwagy, M., Dyck, N. & Straatman, A. (2017). Numerical simulation of gas respiration in produce processing and storage applications. *Proceedings of the 25th. annual conference of the CFD society of Canada*, Windsor, Canada.

[2] DeGroot, C. T., & Straatman, A. G. (2016). A Conjugate Fluid–Porous Approach for Simulating Airflow in Realistic Geometric Representations of the Human Respiratory System. *Journal of Biomechanical Engineering*, *138*(3), 034501.

[3] Dyck, N. J., & Straatman, A. G. (2015). A new approach to digital generation of spherical void phase porous media microstructures. *International Journal of Heat and Mass Transfer*, *81*, 470-477.

[4] A.V. Luikov. (1966) Heat and Mass Transfer in Capillary Bodies. Pergamon Press, Oxford, England.

[5] Liu, J. Y., & Shun, C. (1991). Solutions of Luikov equations of heat and mass transfer in capillary-porous bodies. *International Journal of Heat and Mass Transfer*, *34*(7), 1747-1754.

[6] Defraeye, T., Blocken, B., & Carmeliet, J. (2012). Analysis of convective heat and mass transfer coefficients for convective drying of a porous flat plate by conjugate modelling. *International Journal of Heat and Mass Transfer*, *55*(1-3), 112-124.

[7] Van Belleghem, M., Steeman, M., Janssen, H., Janssens, A., & De Paepe, M. (2014). Validation of a coupled heat, vapour and liquid moisture transport model for porous materials implemented in CFD. *Building and Environment*, *81*, 340-353.

[8] Whitaker, S. (1977). A Theory of drying. *Advances in heat transfer*, *13*, 119-203.

[9] Whitaker, S. (1998). Coupled transport in multiphase systems: a theory of drying. *Advances in heat transfer*, *31*, 1-104.

[10] M. Quintard, M. Kaviany, S. Whitaker, Two-medium treatment of heat transfer in porous media: numerical results for effective properties, Adv. Water Resour. 20 (1997) 77–94.

[11] DeGroot, C. T., & Straatman, A. G. (2011). Closure of non-equilibrium volume-averaged energy equations in high-conductivity porous media. *International Journal of Heat and Mass Transfer*, *54*(23-24), 5039-5048.

[12] Khan, F. A., & Straatman, A. G. (2016). Closure of a macroscopic turbulence and non-equilibrium turbulent heat and mass transfer model for a porous media comprised of randomly packed spheres. *International Journal of Heat and Mass Transfer*, *101*, 1003-1015.

[13] Zhang, K., & You, C. (2011). Experimental and numerical investigation of lignite particle drying in a fixed bed. *Energy & Fuels*, *25*(9), 4014-4023.

[14] Younsi, R., Kocaefe, D., Poncsak, S., & Kocaefe, Y. (2007). Computational modelling of heat and mass transfer during the high-temperature heat treatment of wood. *Applied thermal engineering*, *27*(8), 1424-1431.

[15] Lu, T., Jiang, P., & Shen, S. (2005). Numerical and experimental investigation of convective drying in unsaturated porous media with bound water. *Heat and mass transfer*, *41*(12), 1103-1111.

[16] Keey, R. B. (1972). Drying: Principles and Practice, International Series of Monographs in Chemical Engineering, vol. 13.

[17] Islam, M. R., Ho, J. C., & Mujumdar, A. S. (2003). Convective drying with time-varying heat input: Simulation results. *Drying technology*, *21*(7), 1333-1356.

[18] Hussain, M. M., & Dincer, I. (2003). Two-dimensional heat and moisture transfer analysis of a cylindrical moist object subjected to drying: a finite-difference approach. *International Journal of Heat and Mass Transfer*, *46*(21), 4033-4039.

[19] Younsi, R., Kocaefe, D., Poncsak, S., & Kocaefe, Y. (2006). Thermal modelling of the high temperature treatment of wood based on Luikov's approach. *International Journal of Energy Research*, *30*(9), 699-711.

[20] Chourasia, M. K., & Goswami, T. K. (2007). CFD simulation of effects of operating parameters and product on heat transfer and moisture loss in the stack of bagged potatoes. *Journal of Food Engineering*, *80*(3), 947-960.

[21] De Bonis, M. V., & Ruocco, G. (2008). A generalized conjugate model for forced convection drying based on an evaporative kinetics. *Journal of Food Engineering*, *89*(2), 232-240.

[22] Khan, F. A., Fischer, C., & Straatman, A. G. (2015). Numerical model for non-equilibrium heat and mass exchange in conjugate fluid/solid/porous domains with application to evaporative cooling and drying. *International Journal of Heat and Mass Transfer*, *80*, 513-528.

[23] Ilic, M., & Turner, I. W. (1986). Drying of a wet porous material. *Applied mathematical modelling*, *10*(1), 16-24.

[24] Sitompul, J. P., Istadi, & Sumardiono, S. (2003). Modelling and simulation of momentum, heat, and mass transfer in a deep-bed grain dryer. *Drying Technology*, *21*(2), 217-229.

[25] Saastamoinen, J. J. (2005). Comparison of moving bed dryers of solids operating in parallel and counterflow modes. *Drying technology*, *23*(5), 1003-1025.

[26] Zhonghua, W., & Mujumdar, A. S. (2007). Simulation of the hydrodynamics and drying in a spouted bed dryer. *Drying Technology*, *25*(1), 59-74.

[27] Stakić, M., Stefanović, P., Cvetinović, D., & Škobalj, P. (2013). Convective drying of particulate solids–Packed vs. fluid bed operation. *International Journal of Heat and Mass Transfer*, *59*, 66-74.

[28] Messai, S., El Ganaoui, M., Sghaier, J., Chrusciel, L., & Slimane, G. (2014). Comparison of 1D and 2D models predicting a packed bed drying.*International Journal for Simulation and Multidisciplinary Design Optimization*, *5*, A14.

[29] Stakić, M., & Tsotsas, E. (2004). Modeling and numerical analysis of an atypical convective coal drying process. *Drying technology*, *22*(10), 2351-2373.

[30] Khan, F. A., & Straatman, A. G. (2016). A conjugate fluid-porous approach to convective heat and mass transfer with application to produce drying. *Journal of Food Engineering*, *179*, 55-67.

[31] Y.A. Cengel and M.A. Boles. Thermodynamics an Engineering Approach: Sixth edition. New York, McGraw Hill Company, 738-747, 2008.

[32] Sarsavadia, P. N., Sawhney, R. L., Pangavhane, D. R., & Singh, S. P. (1999). Drying behaviour of brined onion slices. *Journal of Food Engineering*,*40*(3), 219-226.

[33] Menges, H. O., & Ertekin, C. (2006). Mathematical modeling of thin layer drying of Golden apples. *Journal of Food Engineering*, *77*(1), 119-125.

[34] Karoglou, M., Moropoulou, A., Maroulis, Z. B., & Krokida, M. K. (2005). Drying kinetics of some building materials. *Drying technology*, *23*(1-2), 305-315.

[35] Zhang, M., Jiang, H., & Lim, R. X. (2010). Recent developments in microwave-assisted drying of vegetables, fruits, and aquatic products—Drying kinetics and quality considerations. *Drying Technology*, *28*(11), 1307-1316.

[36] Perazzini, H., Freire, F. B., & Freire, J. T. (2013). Drying kinetics prediction of solid waste using semi-empirical and artificial neural network models.*Chemical Engineering & Technology*, *36*(7), 1193-1201.

[37] Kaya, A., Aydın, O., & Dincer, I. (2006). Numerical modeling of heat and mass transfer during forced convection drying of rectangular moist objects.*International journal of heat and mass transfer*, *49*(17), 3094-3103.

[38] Mohan, V. C., & Talukdar, P. (2010). Three dimensional numerical modeling of simultaneous heat and moisture transfer in a moist object subjected to convective drying. *International Journal of Heat and Mass Transfer*, *53*(21), 4638-4650.

[39] Esfahani, J. A., Majdi, H., & Barati, E. (2014). Analytical two-dimensional analysis of the transport phenomena occurring during convective drying: Apple slices. *Journal of Food Engineering*, *123*, 87-93.

[40] Erriguible, A., Bernada, P., Couture, F., & Roques, M. (2006). Simulation of convective drying of a porous medium with boundary conditions provided by CFD. *Chemical Engineering Research and Design*, *84*(2), 113-123.

[41] Lamnatou, C., Papanicolaou, E., Belessiotis, V., & Kyriakis, N. (2010). Finite-volume modelling of heat and mass transfer during convective drying of porous bodies–Non-conjugate and conjugate formulations involving the aerodynamic effects. *Renewable Energy*, *35*(7), 1391-1402.

[42] Alvarez, G., Bournet, P. E., & Flick, D. (2003). Two-dimensional simulation of turbulent flow and transfer through stacked spheres. *International Journal of Heat and Mass Transfer*, *46*(13), 2459-2469.

[43] G. Alvarez, D. Flick, Modelling turbulent flow and heat transfer using macroporous media approach used to predict cooling kinetics of stack of food products, *J. Food Eng.* 80 (2) (2007) 391–401.

[44] K. Lee, J.R. Howell, Forced convective and radiative transfer within a highly porous layer exposed to a turbulent external flow field. In: Proceedings of the 1987 ASME-JSME Thermal Engineering Joint Conf., vol. 2, 1987, pp. 377–386.

[45] H. Wang, E.S. Takle, Boundary-layer flow and turbulence near porous obstacles, Bound. Layer Meteorol. 74 (1–2) (1995) 73–88.

[46] B.V. Antohe, J.L. Lage, A general two-equation macroscopic turbulence model for incompressible flow in porous media, Int. J. Heat Mass Transfer 40 (13) (1997) 3013–3024.

[47] Getachew, D., Minkowycz, W. J., & Lage, J. L. (2000). A modified form of the κ–ε model for turbulent flows of an incompressible fluid in porous media. *International Journal of Heat and Mass Transfer*, *43*(16), 2909-2915.

[48] A. Nakayama, F. Kuwahara, A macroscopic turbulence model for flow in a porous medium, *J. Fluids Eng.* 121 (2) (1999) 427–433.

[49] M.H. Pedras, M.J. de Lemos, Macroscopic turbulence modeling for incompressible flow through undeformable porous media, *Int. J. Heat Mass Transfer* 44 (6) (2001) 1081–1093.

[50] F.E. Teruel, Rizwan-uddin, A new turbulence model for porous media flows. Part I: Constitutive equations and model closure, *Int. J. Heat Mass Transfer* 52 (19) (2009) 4264–4272.

[51] F.E. Teruel, Rizwan-uddin, Numerical computation of macroscopic turbulence quantities in representative elementary volumes of the porous medium, *Int. J. Heat Mass Transfer* 53 (23) (2010) 5190–5198.

[52] J. Moureh, M. Tapsoba, D. Flick, Airflow in a slot-ventilated enclosure partially filled with porous boxes: Part II–Measurements and simulations within porous boxes, *Comput. Fluids* 38 (2) (2009) 206–220.

[53] Mößner, M., & Radespiel, R. (2015). Modelling of turbulent flow over porous media using a volume averaging approach and a Reynolds stress model. *Computers & Fluids*, *108*, 25-42.

[54] M. Drouin, O. Grégoire, O. Simonin, A consistent methodology for the derivation and calibration of a macroscopic turbulence model for flows in porous media, *Int. J. Heat Mass Transfer* 63 (2013) 401–413.

[55] Kuwata, Y., Suga, K., & Sakurai, Y. (2014). Development and application of a multi-scale k–ε model for turbulent porous medium flows. *International Journal of Heat and Fluid Flow*, *49*, 135-150.

[56] Y. Kuwata, K. Suga, Modelling turbulence around and inside porous media based on the second moment closure, *Int. J. Heat Fluid Flow* 43 (2013) 35–51.

[57] Kundu, P., Kumar, V., & Mishra, I. M. (2014). Numerical modeling of turbulent flow through isotropic porous media. *International Journal of Heat and Mass Transfer*, *75*, 40-57.

[58] Curcio, S., Aversa, M., Calabrò, V., & Iorio, G. (2008). Simulation of food drying: FEM analysis and experimental validation. *Journal of Food Engineering*, *87*(4), 541-553.

[59] De Bonis, M. V., & Ruocco, G. (2014). Conjugate heat and mass transfer by jet impingement over a moist protrusion. *International Journal of Heat and Mass Transfer*, *70*, 192-201.

[60] Caccavale, P., De Bonis, M. V., & Ruocco, G. (2016). Conjugate heat and mass transfer in drying: A modeling review. *Journal of Food Engineering*, *176*, 28-35.

[61] Ateeque, M., Mishra, R. K., Chandramohan, V. P., & Talukdar, P. (2014). Numerical modeling of convective drying of food with spatially dependent transfer coefficient in a turbulent flow field. *International Journal of Thermal Sciences*, *78*, 145-157.

[62] Defraeye, T., Verboven, P., & Nicolai, B. (2013). CFD modelling of flow and scalar exchange of spherical food products: Turbulence and boundary-layer modelling. *Journal of Food Engineering*, *114*(4), 495-504.

[63] Chourasia, M. K., & Goswami, T. K. (2007). Steady state CFD modeling of airflow, heat transfer and moisture loss in a commercial potato cold store. *International Journal of Refrigeration*, *30*(4), 672-689.

[64] Ambaw, A., Verboven, P., Defraeye, T., Tijskens, E., Schenk, A., Opara, U. L., & Nicolai, B. M. (2013). Porous medium modeling and parameter sensitivity analysis of 1-MCP distribution in boxes with apple fruit. *Journal of Food Engineering*, *119*(1), 13-21.

[65] Delele, M. A., Ngcobo, M. E., Opara, U. L., & Meyer, C. J. (2013). Investigating the effects of table grape package components and stacking on airflow, heat and mass transfer using 3-D CFD modelling. *Food and Bioprocess Technology*, *6*(9), 2571-2585.

[66] Delele, M. A., Schenk, A., Tijskens, E., Ramon, H., Nicolaï, B. M., & Verboven, P. (2009). Optimization of the humidification of cold stores by pressurized water atomizers based on a multiscale CFD model. *Journal of food engineering*, *91*(2), 228-239.

[67] Delele, M. A., Vorstermans, B., Creemers, P., Tsige, A. A., Tijskens, E., Schenk, A., Opara, U. L., Nicolai, B. M., Verboven, P. (2012). Investigating the performance of thermonebulisation fungicide fogging system for loaded fruit storage room using CFD model. *Journal of food engineering*, *109*(1), 87-97.

[68] Tutar, M., Erdogdu, F., & Toka, B. (2009). Computational modeling of airflow patterns and heat transfer prediction through stacked layers' products in a vented box during cooling. *International Journal of refrigeration*, *32*(2), 295-306.

[69] Moureh, J., Tapsoba, M., & Flick, D. (2009). Airflow in a slot-ventilated enclosure partially filled with porous boxes: Part I–measurements and simulations in the clear region. *Computers & Fluids*, *38*(2), 194-205.

[70] ANSYS Fluent Theory Guide (2015). ANSYS Inc., Canonsburg, PA.

[71] Kuznetsov, A. V. (2004). Numerical modeling of turbulent flow in a composite porous/fluid duct utilizing a two-layer k–ε model to account for interface roughness. *International journal of thermal sciences*, *43*(11), 1047-1056.

[72] Kuznetsov, A. V., & Xiong, M. (2003). Development of an engineering approach to computations of turbulent flows in composite porous/fluid domains. *International journal of thermal sciences*, *42*(10), 913-919.

[73] Kuznetsov, A. V., Cheng, L., & Xiong, M. (2002). Effects of thermal dispersion and turbulence in forced convection in a composite parallel-plate channel: investigation of constant wall heat flux and constant wall temperature cases. *Numerical Heat Transfer: Part A: Applications*, *42*(4), 365-383.

[74] Suga, K., & Nishiguchi, S. (2009). Computation of turbulent flows over porous/fluid interfaces. *Fluid dynamics research*, *41*(1), 012401.

[75] Fetzer, T., Smits, K. M., & Helmig, R. (2016). Effect of turbulence and roughness on coupled porous-medium/free-flow exchange processes. *Transport in Porous Media*, *114*(2), 395-424.

[76] Beyhaghi, S., Xu, Z., & Pillai, K. M. (2016). Achieving the Inside–Outside Coupling During Network Simulation of Isothermal Drying of a Porous Medium in a Turbulent Flow. *Transport in Porous Media*, *114*(3), 823-842.

[77] Prinos, P., Sofialidis, D., & Keramaris, E. (2003). Turbulent flow over and within a porous bed. *Journal of Hydraulic Engineering*, *129*(9), 720-733.

[78] Yang, G., Weigand, B., Terzis, A., Weishaupt, K., & Helmig, R. (2018). Numerical Simulation of Turbulent Flow and Heat Transfer in a Three-Dimensional Channel Coupled with Flow Through Porous Structures. *Transport in Porous Media*, 1-23.

[79] Jin, Y., & Kuznetsov, A. V. (2017). Turbulence modeling for flows in wall bounded porous media: An analysis based on direct numerical simulations. *Physics of Fluids*, *29*(4), 045102.

[80] Breugem, W. P., & Boersma, B. J. (2005). Direct numerical simulations of turbulent flow over a permeable wall using a direct and a continuum approach. *Physics of fluids*, *17*(2), 025103.

[81] Suga, K. (2016). Understanding and modelling turbulence over and inside porous media. *Flow, Turbulence and Combustion*, *96*(3), 717-756.

[82] Silva, R. A., & de Lemos, M. J. (2003). Turbulent flow in a channel occupied by a porous layer considering the stress jump at the interface. *International Journal of Heat and Mass Transfer*, *46*(26), 5113-5121.

[83] De Lemos, M. J. (2009). Turbulent flow around fluid–porous interfaces computed with a diffusion-jump model for k and ε transport equations. *Transport in porous media*, *78*(3), 331-346.

[84] Ochoa-Tapia, J. A., & Whitaker, S. (1995). Momentum transfer at the boundary between a porous medium and a homogeneous fluid—I. Theoretical development. *International Journal of Heat and Mass Transfer*, *38*(14), 2635-2646.

[85] Whitaker, S. (1997). Volume averaging of transport equations. *International Series on Advances in Fluid Mechanics*, *13*, 1-60.

[86] Wilcox, D. C. (1998). Turbulence modeling for CFD (Vol. 2, pp. 103-217). *La Canada, CA: DCW industries*.

[87] De Lemos, M. J. (2012). Turbulence in porous media: modeling and applications.

Elsevier.

[88] Celik, I. B. (1999). Introductory turbulence modeling. *Western Virginia University*.

[89] Patankar, S. (1980). Numerical heat transfer and fluid flow. *CRC press*.

[90] Khosla, P. K., & Rubin, S. G. (1974). A diagonally dominant second-order accurate implicit scheme. *Computers & Fluids*, *2*(2), 207-209.

[91] Betchen, L., Straatman, A. G., & Thompson, B. E. (2006). A nonequilibrium finite-volume model for conjugate fluid/porous/solid domains. *Numerical Heat Transfer, Part A: Applications*, *49*(6), 543-565.

[92] Rhie, C. M., & Chow, W. L. (1983). Numerical study of the turbulent flow past an airfoil with trailing edge separation. *AIAA journal*, *21*(11), 1525-1532.

Chapter 2

2 Dynamic Phase Coupling for laminar flows in Fluid/Porous domains*

2.1 Introduction

Studies that involve heat and mass exchange in porous media are of significant practical interest and involve various applications. The importance of the subject has grown over the past decade and the computational fluid dynamics (CFD) capability of treating the microscopic heat and mass exchanges between the different phases of porous materials in an accurate and timely fashion is an active research topic. It is also necessary to develop rigorous techniques to couple porous materials to the surrounding moist air for computational modeling of heat and mass transfer. Such macroscopic coupling techniques should ensure accuracy and robustness as well as be computationally efficient. This will assist in the design of dryers and storage facilities for moist materials as well as enabling better forecasting for the quality of stored foodstuffs, processing of building materials and the study of packed bed dryers, among other applications.

The modeling interest here is directed towards moist porous materials. A moist porous material is considered to contain a solid matrix, liquid water and void or moist air space i.e. (dry air and water vapor) [1-2]. Two sources of liquid water exist within the porous material: free liquid water that occupies the interconnected pores, and bound water within the solid constituent's closed micro-pores. As the moist material loses its moisture content, the closed pores open up and the bound water gradually becomes free. This process is correlated to changes in temperature and suggests the use of activation energy-type models [3-5]. Whether the material is hygroscopic (i.e. exhibits a high degree of moisture retention and gradual variation of moisture diffusivity, like most food stuffs) or non-hygroscopic (i.e. not considered to have a significant affinity for moisture and involves more sharp drops in moisture diffusivity, like most building materials) [6], moisture transport within a porous material involves factors like vapor diffusion, liquid capillary forces and surface

* This chapter with the title, "Dynamic Coupling of Phase-Heat and Mass Transfer in Porous Media and Conjugate Fluid/Porous domains" has been published in *International Journal of Heat and Mass Transfer 106* (2017) 1270-1286.

tension effects [7-8], and all of these factors are functions of moisture content and temperature. Adding the difficulty of coupling clear fluid regions with the porous material itself, and the dynamic nature of the changes in moisture content near the macroscopic interfaces, physical modelling becomes a significant challenge, and a compromise must be struck between the microscopic and macroscopic scale information to avoid making simulation models too computationally expensive.

The current state of the literature for the coupling of clear fluid and porous regions in these types of problems varies across: drying kinetics, single-phase, uncoupled-phase and conjugate coupling of phases (See reference [9] for a detailed literature review on the topic). In the first category, an overall drying curve is determined for the moist material by either experimentally and/or semi-analytically utilizing the concept of overall drying effective diffusivity and Arrhenius-type drying expressions. Thus, by this approach, it is the overall phenomenon that is modelled, as opposed to discrete solutions of heat and mass transfer [10-14]. Models in the second category solve for discrete quantities, but use single-phase values to describe the presence of moisture or temperature in a CFD cell. Such models are not capable of resolving the liquid to vapor exchanges or the solid phase to fluid phase energy flux. This category of modelling is referred to as the *Equilibrium approach for heat and mass transfer* [15-18]. By this approach, a specified boundary flux for the fluid to porous regions is empirically assigned utilizing correlations for Nusselt and Sherwood numbers available in the literature. This method is capable of characterizing the overall heat and mass transfer, but is case specific and is dependent on empirical estimates of the fluxes assigned at the boundaries. For the uncoupled-phase approach, the local solution inside the porous material is still based on an equilibrium model, in which a single transport equation characterizes the two phases. As for the macroscopic interface treatment, both the clear fluid region and the porous region are discretized and solved, however, they are uncoupled from one another. The fluid side solution is utilized to evaluate an interface heat transfer coefficient and through the Chilton-Colburn heat and mass transfer analogy, a mass transfer coefficient is obtained. These coefficients are then utilized as boundary conditions for the porous side solution [19-21]. The conjugate category of models mainly uses a non-simultaneous technique that solves each phase on its own, and then couples them explicitly by updating the fluxes at the boundaries at each time step [8],[22]. This

technique is effective, but similar to the uncoupled approach, computationally time-consuming due to its explicit nature. In addition, most of the work in the conjugate category either simplifies the porous material to a non-porous material – i.e. the technique typically neglects the gas transport inside the porous region – or is an equilibrium-type model that solves one entity to characterize the two phases. Implicit conjugate coupling has also been achieved. Lamnatou et al. [23] have used a simultaneous conjugate coupling technique for two dimensional convective drying simulations using a stream function formulation. This, however, restricts its application to two-dimensional simulations. Most recently, Khan and Straatman [9], presented an implicit conjugate approach for the simulation of produce drying. The model considers non-equilibrium heat and mass transfer, however, the macroscopic interface treatment involves empirical coefficients to characterize the changes in liquid and vapor mass transfer resistances, which are simulation dependent, i.e. changes with change of boundary conditions.

Local exchanges of heat and mass between the phases of porous materials have also been studied, however, generally they have been ignored in equilibrium-type models, or they are empirically adjusted for non-equilibrium models [24-25]. Particle and grain packed-bed studies have given the subject more practical interest mainly in terms of the dynamic nature of the change in mass transfer resistances that is more pertinent in these studies [26-30]. The state of the art in the literature is either to treat the surface of the solid constituent as fully-saturated with water vapor, i.e. 100 % relative humidity [25], or to define water activity for the moist material. Where water activity is defined as the thermodynamic equilibrium value of the relative humidity at the surface of a wet particle, which is based on the particle's liquid moisture content and temperature [6],[15]. The driving potential for mass transfer is then usually determined based on the surface-to-fluid vapor concentration difference, and local mass transfer coefficients that are functions of the nature of the flow and internal geometry of the porous material; and such models do not usually take the solid-side resistance to mass exchange into account [15],[25]. Another drawback is that these models only consider the diffusive effects in the fluid side resistance without consideration of advective effects, which are important in cases where the porosity and thus the evaporation rate can be high. The solid-side mass transfer resistance has been considered in different ways in the literature however, it mostly involves intensive empirical

calibration of the resistance and is dependent on data from thin-layer or single-particle kinetics' experiments [30-32]. The assumption of thermodynamic equilibrium, i.e. depending entirely on water activity to represent the solid side potential for mass transfer, is also utilised in different studies [27],[30],[33]. Whenever the surface of the solid constituent becomes relatively dry – i.e. when drying out becomes imminent – a liquid moisture front starts shrinking inside the solid constituent forming a dry layer at the solid surface. In these situations the thermodynamic equilibrium assumption is no longer valid, specifically in a macroscopic model that characterizes the local solid constituent moisture content with one moisture fraction value. In such a case it is not possible to split the solid constituent to a dry part and a wet part. It is also a common weakness in packed-bed drying models to have phase exchange techniques that are too complicated for time-efficient implementation in three dimensional models, i.e. such models are mainly one-dimensional [30],[31],[33]. Another aspect to shift attention to the phase exchange processes is the moisture-accompanied heat exchanges, i.e. mass flux enthalpy exchange between the phases. The amount of heat that is withdrawn is the heat of vaporization associated with the mass transfer. Some existing models in the literature withdraw this energy entirely from the void (air-vapour mixture) constituent [9],[25]. Such studies have been modeling evaporative cooling processes or cases that do not involve high temperature variation. Other cases – especially in packed beds, and problems with high thermal non-equilibrium – withdraw this energy entirely from the solid portion, since it is assumed that the liquid is mostly either bound inside the solid portion or due to high solid conductivity compared to the fluid side, both liquid and solid constituents are in thermal equilibrium [27],[30],[32]. This is another loss of generality as the physics of the process of evaporation dictates the withdrawal of vaporization energy from both phases in different proportions [34].

The present paper describes a computational technique for characterizing dynamic coupling of the phases in porous media applications which, to the best of the authors' knowledge, has not yet been achieved. Herein, we define 'Dynamic Coupling' as an implicit, simultaneous, non-equilibrium approach for characterizing microscopic (interstitial) and macroscopic interfaces. In this manner, the interstitial heat and mass exchanges between the solid and fluid phases of the porous medium are captured, as well as those between the fluid and porous cells at macroscopic interfaces that separate fluid

and porous regions of conjugate domains. The key to the approach is that interface heat and mass transfer resistances are formulated to vary locally and dynamically in response to changes that occur during the physical process under consideration. This approach removes the need for ad-hoc or empirical specification of the fluxes at the interfaces and nearly eliminates case-to-case calibration. In the remaining sections of the paper, the general formulation is first presented for the clear fluid and porous regions, followed by the approach developed for dynamic coupling at microscopic and macroscopic interfaces. The presence of a macroscopic interface has a strong influence on the heat and mass transfer phenomenon as it is often rate-determining, especially in low porosity materials like food stuffs or building materials, and requires special attention in the formulation. Different cases for modeling dynamic coupling at the fluid/porous interfaces are then presented, followed by verification cases that demonstrate the viability of the formulation under various drying conditions.

2.2 Model formulation

The governing equations and mathematical conditions relevant to the conjugate modeling of fluid and porous regions as well as the interstitial and macroscopic phase coupling approaches are presented in this section. A simple depiction of a conjugate fluid-porous domain is given in Fig. 2.1 to illustrate what is meant by fluid region, porous region and macroscopic interface. The porous region of the domain is comprised of solid and void (fluid) constituents, which interact via microscopic interfaces. The general formulation is adopted from the work of Khan et al. [25] with improvements and modifications discussed in the relevant subsections. The fluid in the present formulation is assumed to be comprised of a mixture of dry air (i.e. includes all the dry gas species of atmospheric air) and water vapor and is referred to as ‘moist air’. The flow is considered to be density-varying due to the change in the local vapor moisture content and the moisture transport phenomenon under study, characterized by the local vapor moisture mass fraction in the moist air (Y_v). Expressions utilized for the mixture density ρ_f and vapor moisture fraction Y_v are,

$$\rho_f = \rho_a + \rho_v = \frac{P - (RH \cdot P_{sat})}{R_a T} + \frac{RH \cdot P_{sat}}{R_v T} \tag{2.1}$$

$$Y_v = \frac{RH \cdot P_{sat}}{\rho_f R_v T} \tag{2.1}$$

where ρ_a is the dry air density, ρ_v is the vapor moisture density, P is the local pressure, RH is the local relative humidity, P_{sat} is the saturation vapor pressure at the local temperature, R_a and R_v are the gas constants for dry air and water vapour, respectively, and T is the local temperature of the fluid volume.

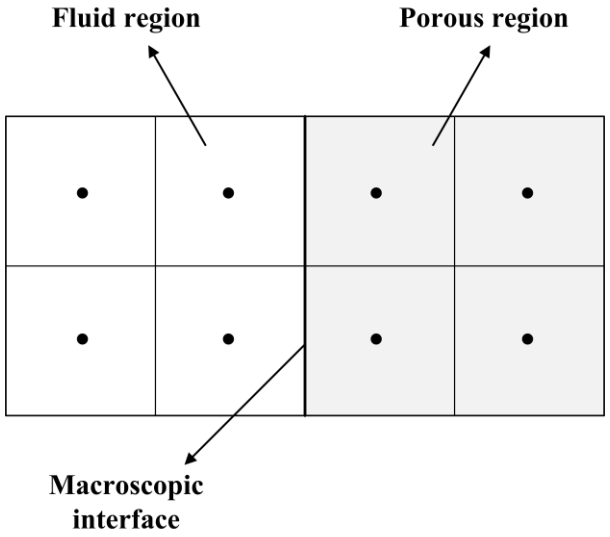

Figure 2.1: A discrete conjugate Fluid-Porous domain.

2.2.1 Fluid Region

To fully characterize the fluid flow and heat and mass transfer in the fluid region, vapor (moisture) mass fraction (Y_v) and energy equations are solved in addition to the Navier-Stokes and conservation of mass equations. In the absence of external forces, mass or heat sources, the equations of mass and momentum conservation, vapor moisture and fluid energy are given, respectively, as,

$$\frac{\partial \rho_f}{\partial t} + \nabla . \left(\rho_f \mathbf{v}\right) = 0 \tag{2.2}$$

$$\frac{\partial (\rho_f \mathbf{v})}{\partial t} + \nabla . \left(\rho_f \mathbf{v}\mathbf{v}\right) = -\nabla P + \mu_f \nabla^2 \mathbf{v} \tag{2.3}$$

$$\frac{\partial(\rho_f Y_v)}{\partial t} + \nabla.\left(\rho_f Y_v \mathbf{v}\right) = \nabla.\left(\rho_f D_f \nabla Y_v\right) \tag{2.4}$$

$$\begin{aligned}\sum_i c_{p,i}\frac{\partial(\rho_f Y_i T)}{\partial t} + \sum_i h_{fg,i}\frac{\partial(\rho_f Y_i)}{\partial t} \\ + \sum_i c_{p,i}\nabla.\left(\rho_f Y_i T \mathbf{v}\right) + \sum_i h_{fg,i}\nabla.\left(\rho_f Y_i \mathbf{v}\right) \\ = k_f \nabla^2 T + \sum_i \nabla.\left[\rho_f D_f \nabla Y_i (c_{p,i} T + h_{fg,i})\right]\end{aligned} \tag{2.5}$$

Here, i represents a counter of species, $c_{p,i}$ is the specific heat of species i and is calculated with a reference at 0°C for vapor mositure, and $h_{fg,i}$ accounts for the latent heat of vaporization at a reference temperature of 0°C, which is of zero value for dry air. The formulation accounts for the sensible and latent portions of the mixture energy in separate terms for both the transient and advective terms [25]. This approach provides a means for reducing non-linearity that is not needed in cases where the specific heat accounts for both types of energy. It is also a method that enables the control of convergence using different time steps [25]. We also include two terms for the energy diffusion: a conductive term and a term that accounts for the species energy diffusion or the species energy transfer accompanying mass transfer. This term is of special importance at macroscopic interfaces.

2.2.2 Porous Region

The general framework of the porous model is based on the theory of *volume-averaging* for flow, heat and mass transfer by Whitaker [2]. In this framework, every representative elementary volume (REV) for the porous material includes a fluid or void phase, a solid phase, and a liquid phase with multiple microscopic interfaces between them. Following the approach by Khan et al. [25], a simplification is introduced in which only a single microscopic interface is considered between the moist air (void part) and the solid matrix which holds the liquid water. Thus, in this simplification, we consider bound water. We also consider the free water by allowing the variation of the effective liquid-in-solid diffusivity to account for transport of both types of water. Figure 2.2 gives a schematic of

a representative elemental volume (REV) showing how the phases are characterized in the present formulation.

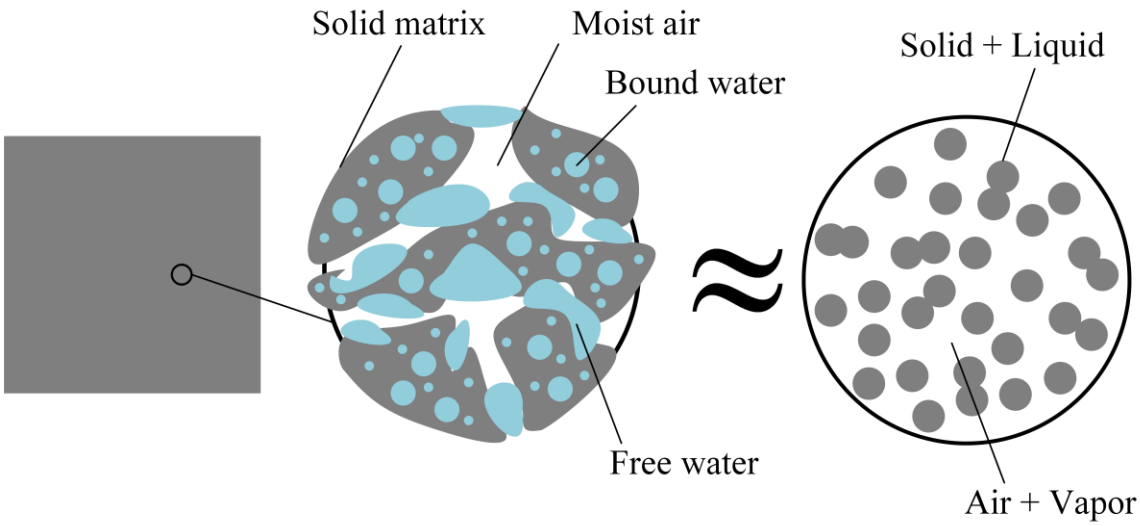

Figure 2.2: Illustration showing the different constituents in the porous region and the simplification of the problem.

Two types of volume averages are useful for porous media models; an intrinsic average, which is the averaged value of a property φ over a specific phase volume within an REV, and an extrinsic average defined as the average value of φ over the total volume of the REV. The expressions for both averages are, respectively, given by,

$$\langle \varphi_x \rangle^x = \frac{1}{V_x} \int_{V_x} \varphi_x \, d\, V \tag{2.7}$$

$$\langle \varphi_x \rangle = \frac{1}{V} \int_{V_x} \varphi_x \, d\, V \tag{2.8}$$

where x represents the phase index, V_x is the volume of phase x within the REV and V is the total volume of the REV. The following expression is also useful for linking the two averages for fluid phases,

$$\langle \varphi_f \rangle = \varepsilon \langle \varphi_f \rangle^f \tag{2.9}$$

with ε indicating the porosity defined by the void volume over the total volume of the moist material. All the quantities solved for in the porous region are intrinsic averages except for the velocity as it is useful to obtain an extrinsic average to characterize the averaged fluid flow. In the absence of external forces and external heat and mass sources, the volume-averaged form of the Navier-Stokes equations for the continuity, momentum, moisture mass fractions and energy for the relevant phases are cast, respectively, as,

$$\varepsilon \frac{\partial \langle \rho_f \rangle^f}{\partial t} + \nabla . \left(\langle \rho_f \rangle^f \langle \mathbf{v} \rangle \right) = 0 \tag{2.10}$$

$$\begin{aligned} &\frac{\partial \left(\langle \rho_f \rangle^f \langle \mathbf{v} \rangle \right)}{\partial t} + \frac{1}{\varepsilon} \nabla . \left(\langle \rho_f \rangle^f \langle \mathbf{v} \rangle \langle \mathbf{v} \rangle \right) \\ &\qquad = -\varepsilon \nabla \langle P \rangle^f + \mu_f \nabla^2 \langle \mathbf{v} \rangle - \frac{\varepsilon \mu_f}{K} \langle \mathbf{v} \rangle - \frac{\varepsilon \langle \rho_f \rangle^f c_E}{\sqrt{K}} |\langle \mathbf{v} \rangle| \langle \mathbf{v} \rangle \end{aligned} \tag{2.11}$$

$$\begin{aligned} &\varepsilon \frac{\partial \left(\langle \rho_f \rangle^f \langle Y_{v,f} \rangle^f \right)}{\partial t} + \nabla . \left(\langle \rho_f \rangle^f \langle Y_{v,f} \rangle^f \langle \mathbf{v} \rangle \right) \\ &\qquad = \nabla . \left(\langle \rho_f \rangle^f D_{eff,f} \nabla \langle Y_{v,f} \rangle^f \right) + \langle \dot{m}_{fs} \rangle \end{aligned} \tag{2.12}$$

$$(1 - \varepsilon) \frac{\partial \left(\langle \rho_s \rangle^s \langle Y_{w,s} \rangle^s \right)}{\partial t} = \nabla . \left(\langle \rho_s \rangle^s D_{eff,s} \nabla \langle Y_{w,s} \rangle^s \right) - \langle \dot{m}_{fs} \rangle \tag{2.13}$$

$$\begin{aligned} &\sum_i \varepsilon c_{p,i} \frac{\partial \left(\langle \rho_f \rangle^f \langle Y_{i,f} \rangle^f \langle T_f \rangle^f \right)}{\partial t} + \sum_i \varepsilon h_{fg,i} \frac{\partial \left(\langle \rho_f \rangle^f \langle Y_{i,f} \rangle^f \right)}{\partial t} \\ &\qquad + \sum_i c_{p,i} \nabla . \left(\langle \rho_f \rangle^f \langle Y_{i,f} \rangle^f \langle T_f \rangle^f \langle \mathbf{v} \rangle \right) \\ &\qquad + \sum_i h_{fg,i} \nabla . \left(\langle \rho_f \rangle^f \langle Y_{i,f} \rangle^f \langle \mathbf{v} \rangle \right) \\ &\qquad = k_{eff,f} \nabla^2 \langle T_f \rangle^f \\ &\qquad + \sum_i \nabla . \left[\langle \rho_f \rangle^f D_{eff,f} \nabla \langle Y_{i,f} \rangle^f \left(c_{p,i} \langle T_f \rangle^f + h_{fg,i} \right) \right] \\ &\qquad + h_{fs} A_{fs} \left(\langle T_s \rangle^s - \langle T_f \rangle^f \right) + \dot{H}_{fs}^{mass} \end{aligned} \tag{2.14}$$

$$\sum_i (1-\varepsilon) c_{ps,i} \frac{\partial\left(\langle\rho_s\rangle^s \langle Y_{i,s}\rangle^s \langle T_s\rangle^s\right)}{\partial t} = k_{eff,s}\nabla^2\langle T_s\rangle^s + \sum_i \nabla.\left[\langle\rho_s\rangle^s D_{eff,s}\nabla\langle Y_{i,s}\rangle^s \left(c_{ps,i}\langle T_s\rangle^s\right)\right] - h_{fs}A_{fs}\left(\langle T_s\rangle^s - \langle T_f\rangle^f\right) - \dot{H}_{fs}^{mass} \quad (2.15)$$

The additional terms in the volume-averaged equations result from the closure of the volume-averaging process. The last two terms of the momentum equation (Eq. 2.11) are the heuristic skin and form drag terms, respectively, resulting from the frictional effects on the flow in the void constituent that are filtered through the volume-averaging. The non-equilibrium approach to treating heat and mass transfer is achieved through the solution of two coupled phase equations for energy transfer, (Eqs. 2.14-2.15), and mass transfer, (i.e. vapor mass fraction equation for the fluid constituent and liquid mass fraction equation for the solid constituent; Eqs. 2.12-2.13). The terms $h_{fs}A_{fs}\left(\langle T_s\rangle^s - \langle T_f\rangle^f\right)$, $\langle\dot{m}_{fs}\rangle$ and $\dot{H}_{fs}^{mass}$ are the heat and mass transfer closure terms that require careful consideration for dynamic coupling. The first term represents the convective interfacial heat transfer term between the fluid and solid phase of the porous region. This convective coefficient h_{fs} is evaluated using a local empirical heat transfer correlation as it is only a function of the fluid mixture properties, the fluid flow, and the internal geometry of the porous material. This term is not dynamic in nature and is present with the same form as in non-mass-transfer problems [36]. $\langle\dot{m}_{fs}\rangle$ is the local interfacial mass exchange term representing the mass flux exchanged between the moist solid and fluid mixture phases (see Fig. 2.2). This term is dynamically varying and will be discussed extensively in subsequent sections. $\dot{H}_{fs}^{mass}$ is the interfacial closure term that is analogous to the species energy diffusion term. It represents the heat exchanged between the phases accompanying mass exchange. It is also dynamically varying and is related to the source of the vaporization energy and the apportioning of this energy on the different phases. This term will also be discussed in subsequent sections. It is also worth mentioning that the effective conductivities and mass diffusivities in the heat and mass transfer transport equations are considered porous material properties that are functions of the nature of the heat and mass transfer processes.

They represent effects of the transport phenomena (i.e. whether diffusive, capillary or surface tension effects) microscopically and are scaled-up through the volume-averaging process. They also represent dispersion and tortuosity effects and are often functions of moisture content and temperature. It is noted here however, that existing studies contain a great deal of empiricism when they handle these coefficients. It is noted that experiments are required to accurately estimate these properties at the microscopic level at different conditions, so that pore level simulations may be effectively used to arrive at the correct volume-averaged values for these effective properties.

Another aspect to highlight is the fact that the closure mass exchange source term is absent from the continuity equation. The present formulation utilizes a unique discretization approach that allows for the update of the mixture density within each time step for the continuity, momentum and energy equations, while it explicitly includes a source term in the mass transfer equations. This technique was described in the work of Khan et al. [25] and also resulted in the absence of the $\dot{H}_{fs}^{mass}$ source term from their formulation, as the total vaporization energy was apportioned to the void constitiuent of the porous material. While this assumption is not an issue for evaporative cooling cases, it is relatively inaccurate for cases with high temperature gradients. A solution for this issue will be presented in subsequent sections. Another difference from Khan et al. [25] is in regards to the liquid mass fraction $\langle Y_{w,s} \rangle^s$. Herein, we define the liquid mass fraction on a dry basis, as opposed to a wet basis, so that $\langle Y_{s,s} \rangle^s = 1$, and the solid density $\langle \rho_s \rangle^s$ is a constant value, which removes a non-linearity in the computational solution that is no longer required. By this approach, the level of water saturation of the porous material is not required to be specified in the formulation, unlike the work of Khan and Straatman [9], as they specified their solid matrix to be volume-saturated with water at the start of drying, which is not necessarily true.

2.2.3 Macroscopic Coupling Conditions

Interface conditions are required to robustly and accurately couple the transport equations in the pure fluid and porous regions. They also ensure the smoothness and continuity of solved quantities across interfaces. The interface conditions take into account the different

nature of the point equation on the fluid side compared to the volume-averaged equation on the porous side. The conditions for the fluid flow and pressure are cast as:

$$\mathbf{v}_{fl} = \langle \mathbf{v} \rangle_{por} \tag{2.16}$$

$$P_{fl} = \langle P \rangle^{f}_{por} \tag{2.17}$$

in which the extrinsic velocity and intrinsic pressure are continuous (see reference [37] for specifics). The fluxes of mass transfer have to match as well, i.e. the sum of the (liquid and vapor) diffusive mass fluxes leaving/entering on the porous side has to be continuous with the entering/leaving vapor flux on the fluid side. This is expressed mathematically as,

$$\left(-\rho_f D_f \frac{\partial Y_v}{\partial \boldsymbol{n}}\right)_{fl} = \left(-\langle \rho_f \rangle^f D_{eff,f} \frac{\partial \langle Y_{v,f} \rangle^f}{\partial \boldsymbol{n}} - \langle \rho_s \rangle^s D_{eff,s} \frac{\partial \langle Y_{w,s} \rangle^s}{\partial \boldsymbol{n}}\right)_{por} \tag{2.18}$$

For a combined heat and mass transfer problem, the macroscopic interface condition is different from that described by Betchen et al. [37]. In this case, the sum of both sensible and latent fluxes must be in balance, and this is expressed as,

$$\begin{aligned}\left(-k_f\left(\frac{\partial T}{\partial \boldsymbol{n}}\right) - \sum_i \left[\rho_f D_f \left(\frac{\partial Y_i}{\partial \boldsymbol{n}}\right)(c_{p,i}T + h_{fg,i})\right]\right)_{fl} \\ = \left(-k_{eff,f}\frac{\partial \langle T_f \rangle^f}{\partial \boldsymbol{n}}\right. \\ - \sum_i \left[\langle \rho_f \rangle^f D_{eff,f}\left(\frac{\partial \langle Y_{i,f} \rangle^f}{\partial \boldsymbol{n}}\right)\left(c_{p,i}\langle T_f \rangle^f\right.\right. \\ \left.\left. + h_{fg,i}\right)\right] - k_{eff,s}\frac{\partial \langle T_s \rangle^s}{\partial \boldsymbol{n}} \\ \left. - \sum_i \left[\langle \rho_s \rangle^s D_{eff,s}\left(\frac{\partial \langle Y_{i,s} \rangle^s}{\partial \boldsymbol{n}}\right)\left(c_{ps,i}\langle T_s \rangle^s\right)\right]\right)_{por}\end{aligned} \tag{2.19}$$

Equations (2.16-2.19) represent the mathematical conditions of the conjugate coupling across macroscopic interfaces. The actual implementation and discretization selected to

achieve these conditions is presented in detail for the hydrodynamics by Betchen et al. [37]. In regards to heat and mass transfer, a discussion will follow in a subsequent section.

2.3 Dynamic Coupling models

Now that the formulation of the conjugate problem is presented along with a means for coupling regions across interfaces, the task turns to formulating physics-based dynamic models that account for mass and energy transfers at microscopic (interstitial) and macroscopic interfaces. As noted in section 2.2, the terms that require specific attention are the mass exchange terms and their associated vaporization energy terms. In the subsections to follow, models are formed for these terms at microscopic and macroscopic interfaces that, when combined with the formulation of section 2.2, yield a complete non-equilibrium heat and mass transfer model that can be used for a variety of drying processes.

2.3.1 Coupling of phase heat and mass transfer at microscopic interfaces

When one considers the mass exchange term, a first choice and a seemingly reasonable form for this term would be a mass transfer analogue for Newton's law of cooling, as given by Khan et al. [25],

$$\langle \dot{m}_{fs} \rangle = \langle \rho_f \rangle^f h_{fsm} A_{fs} \left(\langle Y_v \rangle^{fs} - \langle Y_{v,f} \rangle^f \right) \tag{2.20}$$

where h_{fsm} is a convective mass transfer coefficient that is obtained from an empirical correlation of mass transfer based on the characteristics of the flow and the geometry of the porous material and $\langle Y_v \rangle^{fs}$ is the surface fluid mass fraction (assumed at 100 % relative humidity in the work of Khan et al. [25]). The above expression is suitable whenever the moist solid has sufficient liquid water present, however if drying out is imminent, either the expression is not suitable or it has to be empirically adjusted [25]. Equation 2.20 is also based on pure diffusion through the mass transfer boundary layer and does not consider an advective flux near the solid surface which, in cases where advective effects are considerable, will compromise the accuracy. The physics of the mass transfer process indicates the existence of two main resistances. The first is an internal resistance from the core of the solid to the microscopic interface. This resistance becomes important when the

moist material gets relatively dry, meaning the solid constituent supply of moisture becomes less than the air side capacity for moisture withdrawal. The second resistance is on the air side as the surface vapor diffuses and is advected to the air stream. Phase change is considered to occur at the microscopic interface and is assumed not to interplay with these resistances. Furthermore, the higher of these two described resistances is considered rate-determining. To develop an air side resistance expression, we assume the solid portion of the porous medium to consist of uniform sized spherical particles (See Fig. 2.2). These particles are analogous to spray droplets in an air stream [38] when we consider mass transfer.

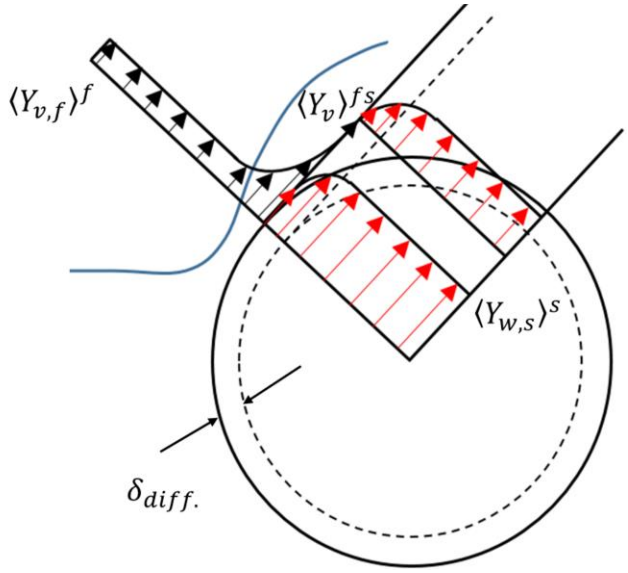

Figure 2.3: Schematic showing a spherical solid holding liquid water within its micro-pores subjected to a stream of moist air.

Figure 2.3 shows a schematic of a spherical solid showing the profiles of liquid and vapor mass fraction in the solid and moist air. If we consider the thin vapor mass fraction diffusion layer using a quasi-steady, one dimensional (i.e. radial) diffusion *point* equation, then taking both advection and diffusion into consideration [38], we obtain,

$$\langle \dot{m}_{fs} \rangle = \langle \rho_f \rangle^f h_{fsm} A_{fs} \, ln\left(\frac{1 - \langle Y_{v,f}\rangle^f}{1 - \langle Y_v\rangle^{fs}}\right) \tag{2.21}$$

Or, in the interest of implicit implementation and convergence control, we cast Eq. 2.21 as,

$$\langle \dot{m}_{fs} \rangle = \langle \rho_f \rangle^f h_{fsm} A_{fs} \frac{\ln(1+B)}{B} \left(\frac{\langle Y_v \rangle^{fs} - \langle Y_{v,f} \rangle^f}{1 - \langle Y_v \rangle^{fs}} \right) \tag{2.22}$$

where B is the local Spalding mass transfer number, defined by $(\langle Y_v \rangle^{fs} - \langle Y_{v,f} \rangle^f)/(1 - \langle Y_v \rangle^{fs})$. Another change we introduce is in regards to the surface vapor mass fraction. To prolong the validity of Eq. 2.22 as the material loses moisture with time, we introduce the deviation from surface vapor saturation using the water activity concept. It has been mentioned earlier that the water activity is an application of the thermodynamic equilibrium for the moist material; it introduces a relation between the liquid water mass fraction $\langle Y_{w,s} \rangle^s$ and the solid surface vapor relative humidity (i.e. water activity) that is based on an equal chemical potential for both phases [6]. This relation is often referred to as the sorption isotherm, as it is different for different surface temperatures. Based on this approximation, the surface vapor mass fraction is defined as,

$$\langle Y_v \rangle^{fs} = \frac{a_w P_{sat.}}{\langle \rho_f \rangle^f R_v \langle T_s \rangle^s} \tag{2.23}$$

with a_w representing the water activity and P_{sat} calculated at the particle surface temperature. Equation 2.22 is valid as long as the thermodynamic equilibrium assumption is valid. If the solid side resistance is rate-determining, the expression will not be accurate. In this case, as drying out becomes imminent, the surface of the solid becomes almost dry and the moisture is mostly embedded in the core of the solid constituent, which violates the thermodynamic equilibrium assumption, since the present formulation does not include the effect of shrinkage. Given that the process of liquid diffusion in the solid constituent is assigned an effective diffusivity $D_{eff,s}$, it is physically reasonable to assume a significant diffusion thickness within the solid particle, in which the significant part of the liquid concentration difference occurs based on this effective diffusivity; a concept that is analogous to the one widely used in the lumped conduction models [39]. Usually lumped conduction models have a strong dependence on the order of the transient. In the present model however this dependence on the transient can impose time step restrictions. Thus,

instead of the lumped diffusion approach, we estimate a significant diffusion thickness using the concept of the volume-averaging. Since the boundary layer thickness on the vapor side is considered of a length scale that is small enough not to violate a fixed volume averaged quantity throughout the fluid volume in a CFD cell, the significant diffusion thickness $\delta_{diff.}$ is reasonable to be of the same order of magnitude, but with respect to the solid volume. If we assume that the ratio of length scales associated with both resistances is proportional to the phase volume ratio then,

$$\delta_{diff.} = \frac{d_p}{Sh}\left(\frac{1-\varepsilon}{\varepsilon}\right)^{1/3} \tag{2.24}$$

with (d_p/Sh) representing that ratio of the average particle diameter over the local Sherwood mass transfer number; i.e. the vapor mass transfer boundary layer thickness. Then, based on Eq. 2.24, the solid side mass exchange expression can be cast as,

$$\langle \dot{m}_{fs} \rangle = \langle \rho_s \rangle^s \frac{D_{eff,s}}{\delta_{diff.}} A_{fs} \left(\langle Y_{w,s} \rangle^s - \langle Y_{w,s} \rangle^{fs} \right) \tag{2.25}$$

For the solid side resistance to be dominant, the surface liquid fraction $\langle Y_{w,s} \rangle^{fs}$ must be negligible. A check is performed locally within the non-linear CFD loop on whether the mass transfer by Eq. 2.22 or Eq. 2.25 is lower in value and the lower value is implemented implicitly. When Eq. 2.25 is utilized, we equate the expression given by Eq. 2.20 to Eq. 2.25, and obtain a mass transfer coefficient that is smoothly declining as a function of $\langle Y_{w,s} \rangle^s$. The implicit technique of implementation ensures smooth convergence.

Now we turn our attention to the energy exchange closure term $\dot{H}_{fs}^{mass}$. This term basically accounts for the addition/subtraction of enthalpy due to the mass flux entering/exiting each of the phase volumes. In this respect, the moisture mass either leaves the solid phase as a liquid – i.e. indicating it takes its vaporization energy from the fluid constituent – or it leaves as a vapor, withdrawing its vaporization energy from the solid constituent. In evaporative cooling applications [25], the former approximation could be selected, while for materials that are highly resistive to liquid diffusion and involve a significant difference

between solid and fluid constituents' temperature – i.e. significant thermal non-equilibrium – the latter approximation is usually selected (an observation that is made for most of the particle and grain drying studies [27],[30],[32]). Both approximations, however, introduce a loss of generality as both phases participate in the evaporation process [34]. To obtain a general expression for the energy of mass exchange, we assume that the shares of the vaporization energy are closely correlated to the heat transfer, i.e. conductive/advective resistances for both phases. We consider the local Biot number defined as,

$$Bi = \frac{h_{fs}(\frac{d_p}{Nu}\left(\frac{1-\varepsilon}{\varepsilon}\right)^{\frac{1}{3}})}{k_{eff,s}} \tag{2.26}$$

noting that we estimate the length scale of solid conduction by a local nusselt number (Nu) in a manner similar to Eq. 2.24. Since this local Biot number represents the ratio between the resistances of solid conduction to the outside fluid convection, we use it to define a proportioning factor α, where this factor represents the fraction of the vaporization energy that the solid constituent contributes. Assuming that solid-to-fluid ratio of the share of mass transfer energy is proportional to the inverse ratio of heat resistances, we define the proportioning factor as,

$$\alpha = \frac{1}{Bi+1} \tag{2.27}$$

Based on this proportioning factor α, the heat transfer exchange term is defined as,

$$\dot{H}_{fs}^{mass} = \langle \dot{m}_{fs} \rangle [\alpha h_v(\langle T_s \rangle^s) + (1-\alpha) h_l(\langle T_s \rangle^s)] \tag{2.28}$$

where h_v and h_l are the vapor and liquid specific enthalpies evaluated at the surface particle temperature. This apportioning process is valid when the surface of the solid constituent is relatively wet. For cases when Eq. 2.25 is used, the surface of the solid is assumed dry and hence the outer fluid region is assumed not to be in contact with the liquid embedded in the core of the solid constituent. In this case α = 1, indicating that all of the vaporization energy is obtained from the solid constituent. In Eq. 2.28, h_v and h_l are absolute enthalpies referenced at absolute zero temperature. Specific heats of liquid and vapor moistures,

referenced at 0 K are used for this purpose as adopted from Pakowski et al. [40]. To perform the proportioning described here within the context of the unique discretization approach used in Khan et al. [25], the term $\langle \dot{m}_{fs} \rangle h_v \left(\langle T_f \rangle^f \right)$ is added explicitly to the source term in the fluid temperature energy equation in the porous region.

2.3.2 Coupling of heat and mass transfer at macroscopic interfaces

The present subsection introduces an approach for practical implementation of the mathematical conditions that were presented in section 2.2.3. The main focus is directed at coupling the fluid side equation to the two non-equilibrium equations on the porous side for heat and mass transfer. If we idealize the interface condition to be one dimensional, following on the work of Betchen et al. [37] and Khan et al. [25], we are able to produce moisture and temperature circuit analogues for mass and heat transfer exchange processes, respectively. First, we consider the moisture exchange circuit illustrated in Fig. 2.4, which shows a clear fluid cell (P) with a porous cell (E) adjacent to its east face, separated by face 'e'. The diffusion mass fluxes obtained from the defined resistances are implemented implicitly, as the in-house code solves both regions and both equations simultaneously. Five resistances are introduced: R_{v1_f} and R_{v_f} represent the fluid leg resistances that link the nodal fluid vapor mass fractions. R_{v2_s}, R_{f-s} and R_{W_s} are the solid leg resistances that link the porous node's solid phase liquid fraction to the fluid node's vapor fraction. The fluid leg of the resistance is straightforward and is treated using a technique similar to Khan et al [25], where the relevant resistances are defined as,

$$R_{v1_f} = \frac{\Delta x_{Pe}}{\rho_{f_P} \varepsilon A_e D_f} \quad , \quad R_{v_f} = \frac{\Delta x_{eE}}{\langle \rho_f \rangle^f{}_E A_e D_{eff,f}} \tag{2.29}$$

Using the harmonic mean formulation [37] to couple the two cells, we obtain,

$$\dot{m}_{v_f} = \frac{\langle Y_{v,f} \rangle^f{}_E - Y_{v\ P}}{R_{v1_f} + R_{v_f}} \tag{2.30}$$

Now, we shift attention to the solid leg of the resistance, which requires consideration of two factors: the dynamic nature of the variation in its resistances which vary strongly in

space and time and necessitate a strong and implicit form of coupling; and, the fact that the two nodal values are for different quantities, i.e. liquid and vapor fractions. The driving potential difference for mass exchange in this case has to be consistent with both sides and representative of the physical transport occurring. A technique for achieving these requirements is presented here. Two modes of mass transfer are considered. In the first mode, the surface of the solid constituent at the macroscopic interface is considered wet, meaning that the liquid availability is high enough so that the clear fluid side capacity to entrain vapor is the controlling factor for mass transfer. Usually as the convective flow moves across and through the moist material, this capacity remains relatively unchanged on the fluid side as the fluid is renewable and hence, in the literature this mode of mass transfer is referred to as the *Constant drying rate period* [5],[7],[8].

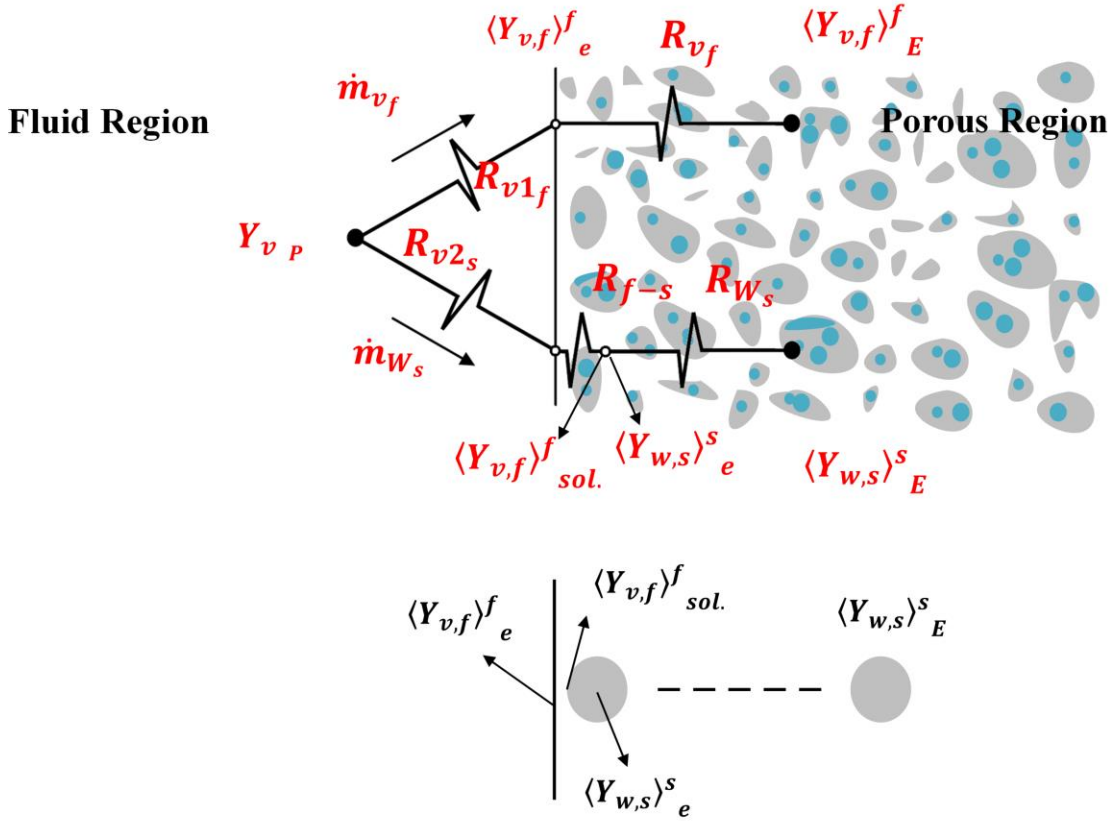

Figure 2.4: Moisture circuit analogue at the macroscopic interface.

In the present paper, without loss of generality, we introduce the term *Convectively dominant* for this mode. Referring to Fig. 2.4, consider a spherical solid that is the closest

to the fluid/porous interface between cells P and E. The liquid moisture mass fraction inside of this spherical solid is $\langle Y_{w,s}\rangle^{s}{}_{e}$ and has the value of the liquid moisture presence based on the diffusion resistance within half the control-volume at E. The surface vapor fraction of this spherical solid $\langle Y_{v,f}\rangle^{f}{}_{sol.}$, is then obtained using Eq. 2.23 since the surface is considered wet in this mode of mass transfer. Utilizing the same vapor moisture boundary layer concept developed in section 2.3.1, Eq. 2.22 may be used with a driving potential difference ($\langle Y_{v,f}\rangle^{f}{}_{sol.} - \langle Y_{v,f}\rangle^{f}{}_{e}$) and an area $A_e(1-\varepsilon)$ to characterize the mass transport between this spherical solid and the clear fluid side. An interface Spalding mass transfer number $B_{interf.}$ is defined based on the same potential difference, and an interface Sherwood number $Sh_{interf.}$ is utilized to obtain the mass transfer coefficient. The same empirical correlation that is used interstitially is used for $Sh_{interf.}$, however the magnitude of the velocity calculated to arrive at the interface Reynolds number is estimated at the interface based on cell (E)'s two transverse extrinsic velocities and the axial interface intrinsic velocity. Using the above approximations, the solid leg resistances are,

$$R_{v2_s} = \frac{\Delta x_{Pe}}{\rho_{f_P}(1-\varepsilon)A_e D_f} \tag{2.31a}$$

$$R_{f-s} = \frac{d_P B_{interf.}\left(1-\langle Y_{v,f}\rangle^{f}{}_{sol.}\right)}{\rho_{f_P}(1-\varepsilon)A_e D_f Sh_{interf.}\ \ln\left(1+B_{interf.}\right)} \tag{2.31b}$$

$$R_{W_s} = \frac{\Delta x_{eE}}{\langle \rho_s\rangle^{s}{}_{E} A_e D_{eff,s}} \tag{2.31c}$$

One can then obtain the following expression for the mass flux $\dot{m}_{w_s}$ which is equal to:

$$\frac{\rho_{f_P}(1-\varepsilon)D_f A_e(\langle Y_{v,f}\rangle^{f}{}_{sol.} - Y_{v\ P})}{\Delta x_{Pe} + \dfrac{d_P B_{interf.}(1-\langle Y_{v,f}\rangle^{f}{}_{sol.})}{Sh_{interf.}\ln(1+B_{interf.})}} = \frac{\langle \rho_S\rangle^{S}{}_{E}\ D_{eff_s} A_e(\langle Y_{w,S}\rangle^{S}{}_{E} - \langle Y_{w,S}\rangle^{S}{}_{e})}{\Delta x_{eE}} \tag{2.32}$$

Equation 2.32 achieves the required physical transport, but is not useful for coupling. In order to achieve the implicit coupling, we have to define a single value for the moisture driving potential at the interface that is compatible with both sides so that it is possible to

ensure the continuity of the flux across the interface by utilizing the harmonic mean formulation. The concept of the equilibrium ratio, developed by Whitman [41], was useful in that sense. However, unlike the equilibrium ratio between the two phases' concentrations in his two liquid films, the phase ratio we define here is not of fixed value. It is non-linearly varying in space and time. Instead of developing a ratio between both liquid and vapor mass fractions, the phase ratio (K) is defined herein as,

$$\mathrm{K} = \frac{\langle \rho_s \rangle^s{}_E D_{eff,s} \langle Y_{w,s} \rangle^s{}_e}{\rho_{f_P}(1-\varepsilon) D_f \langle Y_{v,f} \rangle^f{}_{sol.}} \tag{2.33}$$

The ratio is dimensionless and is selected to include densities and diffusivities as a means for controlling its order of magnitude and variation. Using the harmonic mean formulation [37], Eq. 2.32 can now be recast as,

$$\dot{m}_{W_s} = \frac{A_e(\langle \rho_s \rangle^s{}_E D_{eff,s} \langle Y_{w,S} \rangle^S{}_E - \mathrm{K}\, \rho_{f_P}(1-\varepsilon) D_f Y_{v\ P})}{\mathrm{K}\left(\Delta x_{Pe} + \dfrac{d_P B_{interf.}\left(1 - \langle Y_{v,f} \rangle^f{}_{sol.}\right)}{Sh_{interf.} \ln\left(1 + B_{interf.}\right)}\right) + \Delta x_{eE}} \tag{2.34}$$

which is implemented implicitly. The ratio K is locally available for convectively dominant cases, since Eqs. 2.23 and 2.32 make the calculation of $\langle Y_{v,f} \rangle^f{}_{sol.}$ and $\langle Y_{w,S} \rangle^S{}_e$ straightforward.

In the second mode of mass transfer, the surface of the solid constituent at the fluid/porous interface is considered dry; i.e. the delivered mass flux from the solid side is lower than the air side capacity to withdraw vapor moisture so that the solid side transport of liquid is the controlling factor. Since the ability to transport moisture depends on the amount of moisture present, this case is referred to in the literature as the *Falling drying rate period* [5],[7],[8], which we refer to as *Diffusively dominant*. A dry interface leads to the presence of a traveling liquid moisture front that shrinks inside the porous material and develops a dry layer of porous material at the interface rendering the mechanism of mass transport as mainly vapor diffusion [8]. In a non-volume-averaged porous domain, the dry layer thickness will increase significantly with time as the substance dries up. However, in the

present formulation we use a single value for liquid mass fraction to characterise the whole control volume and hence, to satisfy the concept of volume-averaging, this thickness has to be small enough and compatible with the microscopic scales of the volume-averaging process such that the values of the volume-averaged liquid mass fraction for the porous cells adjacent to the macroscopic interface are representative of the moisture present. Thus, we assume the dry layer thickness to be of the same order of magnitude as the drying boundary layer thickness. The interface resistance network shown in Fig. 2.4 is also used to represent diffusively dominant cases. For this case, the dry layer resistance is R_{f-s}. The main solid leg circuit resistances R_{v2_s} and R_{W_s} have the same definition as in Eq. 2.31, while the dry layer resistance is modified to,

$$R_{f-s} = \frac{d_p / Sh_{interf.}}{\rho_{f_P}(1-\varepsilon) A_e D_f} \tag{2.35}$$

Based on Eq. 2.35, the solid leg mass flux for diffusively dominant cases is then given by,

$$\dot{m}_{W_s} = \frac{A_e(\langle \rho_S \rangle^S{}_E D_{eff,s} \langle Y_{w,S} \rangle^S{}_E - \mathrm{K}\, \rho_{f_P}(1-\varepsilon) D_f Y_{v\ P})}{\mathrm{K}\ \left(\Delta x_{Pe} + \frac{d_P}{Sh_{interf.}}\right) + \Delta x_{eE}} \tag{2.36}$$

Thus, while Eq. 2.33 still represents the phase ratio in the diffusively dominant mode, as the surface of the solid constituent becomes dry, the $\langle Y_{v,f} \rangle^f{}_{sol.}$ is no longer valid as estimated by Eq. 2.23. Moreover, $\langle Y_{w,S} \rangle^S{}_e$ is no longer available. Since we assume the liquid mass fraction to be negligible at the interface, the following equation representing an estimate of the mass transfer at the dry layer can be cast as,

$$\rho_{f_P}(1-\varepsilon) D_f \left(\langle Y_{v,f} \rangle^f{}_{sol.} - \langle Y_{v,f} \rangle^f{}_e \right) = \langle \rho_S \rangle^S{}_E D_{eff,s} \langle Y_{w,s} \rangle^s{}_e \tag{2.37}$$

After inserting Eq. 2.33 into Eq. 2.37, we arrive at,

$$\mathrm{K} = 1 - \frac{1}{1 + \frac{\langle \rho_s \rangle^s{}_E D_{eff,s} \langle Y_{w,s} \rangle^s{}_e}{\rho_{f_P}(1-\varepsilon) D_f \langle Y_{v,f} \rangle^f{}_e}} \tag{2.38}$$

In the solution procedure, the ratio $\langle Y_{w,s}\rangle^{s}{}_{e}/\langle Y_{v,f}\rangle^{f}{}_{e}$ is estimated explicitly from the solution of the previous time step, since extrapolation of either of the mass fraction values independently could artificially increase the importance of one side's resistance over the other side.

To determine the mode of mass transfer of the problem, a check based on Eq. 2.32 is performed locally at every time step before calculating the values of any of the solid leg resistances. The check sets $\langle Y_{w,s}\rangle^{s}{}_{e}$ to zero and considers the interface convectively dominant if the left hand side is lower than the right, and diffusively dominant otherwise.

We now turn our attention to the energy exchange closure term, $\dot{H}_{fs}^{mass}$, at the macroscopic interface. Recall that Eq. 2.19 represents the mathematical condition of heat transfer at the interface. In a manner similar to the notion that the pressure and normal stresses at the interface balance separately on each side instead of their sum (Betchen et al. [37]), we assume that the conduction and the species diffusive energy terms also balance separately. The conduction terms are set in balance using the approach presented in Betchen et al. [37] and is implemented implicitly. The fluid species diffusion energy balance between the clear fluid and the fluid portion of the porous cell is implemented explicitly as source terms in the discrete transport equations and is represented through the species diffusion energy term in Eqs. 2.6 and 2.14. The solid portion of the porous cell to the clear fluid cell's species diffusion energy balance is expressed as,

$$\dot{H}_{fs_{macro.}}^{mass} = \| \dot{m}_{W_s}.h_{fs_{macro.}}^{S} \|.\boldsymbol{n} = \left\| \dot{m}_{W_s}.h_{fs_{macro.}}^{f} \right\|.\boldsymbol{n} \tag{2.39}$$

where $\dot{H}_{fs_{macro.}}^{mass}$ represents the energy source/sink that is explicitly added/subtracted from the solid portion of the porous cell and subtracted/added to the clear fluid cell. $h_{fs_{macro.}}^{S}$ and $h_{fs_{macro.}}^{f}$ are the interface values for the specific enthalpy at the solid and fluid sides, respectively. To determine the value for these enthalpies, we follow an approach that is analogous to Eqs. 2.26-2.28 for the apportioning of vaporization energy between the phases on the solid side leg of the species energy exchange. Defining an interface Biot number and an interface proportioning factor as,

$$Bi_{interf.} = \frac{(1-\varepsilon)k_f}{k_{eff,s}} \quad , \quad \alpha_{interf.} = \frac{1}{Bi_{interf.}+1} \tag{2.40}$$

and following on with the same reasoning as for the microscopic interface, we obtain,

$$\dot{H}^{mass}_{fs_{macro.}} = \dot{m}_{W_s}\left[\alpha_{interf.}h_v\left(\langle T_s\rangle^s{}_e\right) + (1-\alpha_{interf.})h_l\left(\langle T_s\rangle^s{}_e\right)\right] \tag{2.41}$$

which is utilised for convectively dominated transport. For diffusively dominated transport $\alpha_{interf.} = 1$. The interface solid temperature value is evaluated using the harmonic mean formulation. We also add the term $\dot{m}_{W_s}h_v(T_P)$ explicitly in the energy equation in the fluid cell adjacent to the interface to be consistent with the unique discretization approach used in Khan et al. [25].

2.4 Verification of heat/mass transfer formulation

The models described in section 2.3 are implemented into the in-house conjugate CFD code described in [25]. Cases have been chosen to demonstrate the viability of the dynamic coupling formulation across a wide range of drying applications. Note once again that the key feature of the present approach is that the microscopic and macroscopic interface treatments are self-adjusting in response to physical changes that occur during the process such that no ad-hoc coefficients require adjustment from case to case. It is shown in the following cases that an expression is required to characterize the dependence of $D_{eff,s}$ with respect to moisture and temperature; a relationship that could be provided experimentally. The verification considers drying of a bed of coal particles, which focuses on heat and mass exchanges inside the porous bed without the presence of a macroscopic interface. Cases are then presented to demonstrate the efficacy of the formulation in diffusively-dominant and convectively-dominant drying modes by considering conjugate domain cases with microscopic and macroscopic interfaces. All simulations were run serially using a single 2.4 GHz Intel ® Core ™ i7 processor with 6 GB of RAM.

2.4.1 Hot air drying of a packed bed of coal particles

The microscopic interface treatment inside the porous region is validated using a study of coal packed-bed particle drying (Stakić and Tsotsas [33]), which is depicted in Fig. 2.5.

For this case, air flowing at 1 m/s, with 0.008 specific humidity and 100°C enters the bottom of a vertical cylindrical bed containing coal particles at 20°C and $\langle Y_{w,S} \rangle^{S}_{init.} =$ 0.423 kg/kg dry solid. A distributor is mounted at the bed inlet so that the inlet velocity profile can be assumed uniform. The distributor also prevents back conduction and diffusion making possible the exclusion of macroscopic interfaces in the problem. The bed is cylindrical and the walls are considered insulated. Making use of axisymmetry, the two dimensional half of the bed is simulated with one side as a symmetry boundary condition and the other side as a heat and mass insulated wall. The domain consists of structured Cartesian elements with mesh refinement at the cylinder wall (y=D/2). After grid and temporal convergence testing, a mesh of 25×25×1 and a time step of 5 seconds were utilised. This yielded overall heat and mass transfer results that were grid-independent to better than 0.1%, and smoothly varying profiles within the domain. A typical simulation of this case required approximately 8 minutes of wall-clock time. Table 1 shows the relevant information for the simulations, where most properties are obtained from Stakić and Tsotsas [33]. The permeability is evaluated using the Ergun equation [42] and the specific interfacial surface area is evaluated as $6(1-\varepsilon)/d_P$. The Forchheimer coefficient c_E and fluid effective diffusivity $D_{eff,f}$ were obtained from Khan et al. [25]. $D_{eff,f}$ was not assumed to vary because the porosity is relatively high and hence, capillary and other effects that contribute to the change in the fluid diffusivity can be neglected.

Boundary conditions are imposed as follows: on the inlet (x=0) plane, the velocity was set to (u,v,w) = (1,0,0) m/s, pressure extrapolated from inside the domain, and temperature and specific humidity at 100°C and 0.008, respectively; at the outlet (x=h) plane, a zero-gradient boundary condition is specified for all quantities except for pressure, which is set to an atmospheric value; on the symmetry (y=0) plane, normal gradients are set to zero for all quantities with the exception of the normal (v) velocity component, which is set to zero; on the wall (y=D/2), no-slip/impermeable conditions are set for velocity combined with a zero flux (i.e. insulated) condition for heat and mass transfer, while pressure was extrapolated.

Table 2.1: Coal Particles Properties [33], [25].

h (m)	0.2	Dry Solid specific heat, c_{ps} (kJ/kg.K)	1.55
D (m)	0.15	Specific interfacial area, A_{fs} (m^{-1})	125.2
Porosity, ε	0.52	Average Particle diameter, d_p (m)	0.023
Permeability, K (m^2)	2.152×10^{-6}	Solid effective thermal conductivity, $k_{eff,s}$ (W/m.K.)	0.058
Forchheimer Coefficient, c_E	0.244	Fluid effective thermal conductivity, $k_{eff,f}$ (W/m.K.)	0.0237
Dry Solid density, $\langle \rho_s \rangle^s$ (kg/m^3)	1250	Fluid effective diffusivity, $D_{eff,f}$ (m^2/s)	1.522×10^{-6}

The coal particles water activity is defined as [33],

$$a_W = 1 - \exp\ (-14.027\ \langle T_s \rangle^{s\,0.62} \langle Y_{W_s} \rangle^{s\,2.7}) \tag{2.42}$$

We also introduce an expression to characterize the effective liquid-in-solid diffusivity as,

$$D_{eff,s} = (2.0 \times 10^{-10}) \times \frac{(\langle Y_{W_s} \rangle^s)^n}{Sh} (\langle T_s \rangle^s - 273.15)^{3.3} \tag{2.43}$$

where n is a calibration exponent, having a range between 3.5 and 6.5 for different particle liquid moisture fractions. It is worth mentioning that $D_{eff,s}$ is the only element of calibration required in the present formulation, and this is simply required to give the correct dependence of $D_{eff,s}$ with moisture and temperature, a relationship that can be provided experimentally

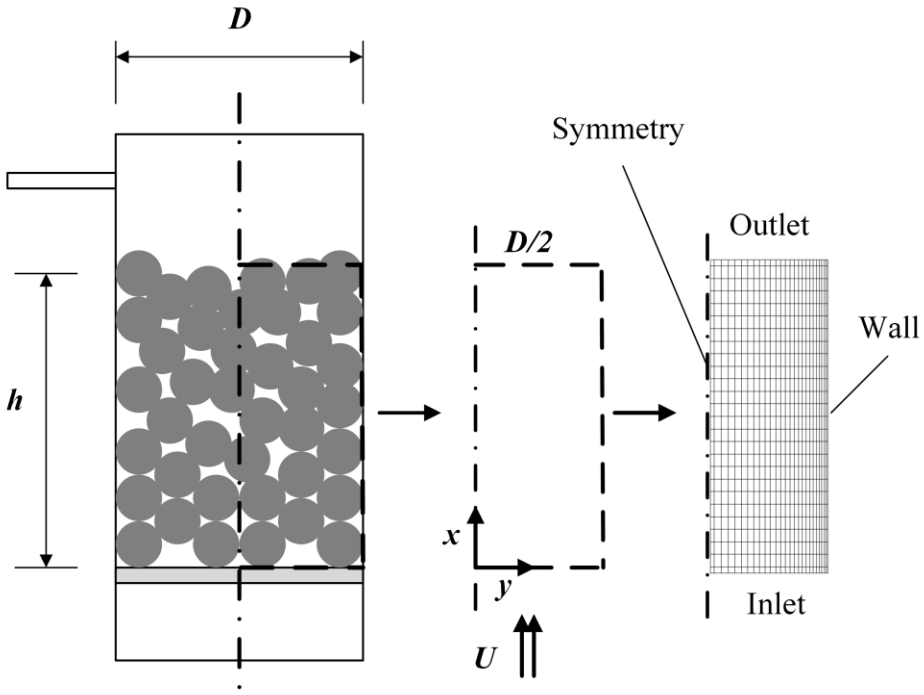

Figure 2.5: A schematic of the Coal packed bed and simulation setup.

To this end, the temperature dependence in Eq. 2.43 is directly adopted from Stakić and Tsotsas [33]. The liquid moisture dependence requires calibration however, since the model they used for the drying kinetics had some dependence on the shrinking particle diameter [33], [43] while our model neglects shrinkage. The average values of the solid diffusion coefficient fall between 2.0 x10^{-8} and 2.4 x10^{-10}, which match relatively well with reported literature on the overall drying effective diffusivity [44]. Local Nusselt and Sherwood numbers are based on correlations reported by Ginzburg and Savina [45], which are preferred in cases of relatively large particles [33]. The correlations take the forms,

$$Nu = \frac{h_{fs} d_P}{k_f} = C_T . Re_{d_P}^{m_T} . Pr_{d_P}^{n_T} \tag{2.44}$$

$$Sh = \frac{h_{fsm} d_P}{D_f} = C_m . Re_{d_P}^{m_m} . Sc_{d_P}^{n_m} \tag{2.45}$$

where, $n_T = n_m = 0.33$ and for $Re_{d_P} > 300$, $C_T = C_m = 0.977$ and $m_T = m_m = 0.595$ while for, $Re_{d_P} \leq 300$, $C_T = C_m = 1.83$ and $m_T = m_m = 0.485$.

Figures 2.6 and 2.7, show the average solid constituent's moisture content and temporal temperature variation for the coal packed bed on the symmetry line of the bed. The

comparison between the present model and the experiment reported by Stakić and Tsotsas [33] shows excellent agreement in terms of the physical trends suggesting that the dynamic coupling model correctly represents the physics of the drying problem. The rate of drying is observed to change as a function of different factors that interplay together to cause the observed drying regimes. These factors include the temperature variation, water activity, effective diffusivity variation and mode of interstitial mass transfer (i.e. whether the convective expression is active or the diffusive one). One may conclude however that the rate of drying becomes very low at an average moisture content of about 0.17 kg/kg dry solid which may be called 'the equilibrium moisture content' of the present case of drying. The temperature variation shown in Fig. 2.7 indicates that heating of the cold bed solid particles is non-linear in time, depending on whether the drying rate is high enough so that the energy supplied with incoming air is utilized directly in evaporation (i.e. supplies an amount of heat that is almost equal to the amount that the solid constituent contributes with in the evaporation) or is utilized sensibly to heat the bed (i.e. the drying rate is small so that heat is mostly raising the enthalpy of the solid constituent). Arriving at the correct trend for heat transfer in Fig. 2.7 was possible using the $\dot{H}_{fs}^{mass}$ term as defined in Eq. 2.28.

Figure 2.8 illustrates the variation of the liquid moisture fraction, fluid temperature and particle temperature along the height of the bed at different instants in time. A typical drying scenario is observed for the liquid moisture, wherein a drying front propagates from inlet to outlet with increasing time. The drying front moves as the air capacity becomes exhausted. The drying capacity is different in the coal-drying case as compared to other more highly saturated materials (i.e. particles with saturated surfaces), since lower water activities tend to decrease this capacity, resulting in a final moisture content that is still relatively high. To elaborate further on this point, the rate of local mass transfer is much lower in the present case as the local difference between the coal temperature-dependent water activity and air relative humidity decreases. This is consistent with information present in the literature about coal drying. If we compare this to the case of drying of wet wood wool that was reported by Khan et al. [25], the absence of water activity and its temperature-dependence in their interface model results in predictions of dry-out of the wood wool.

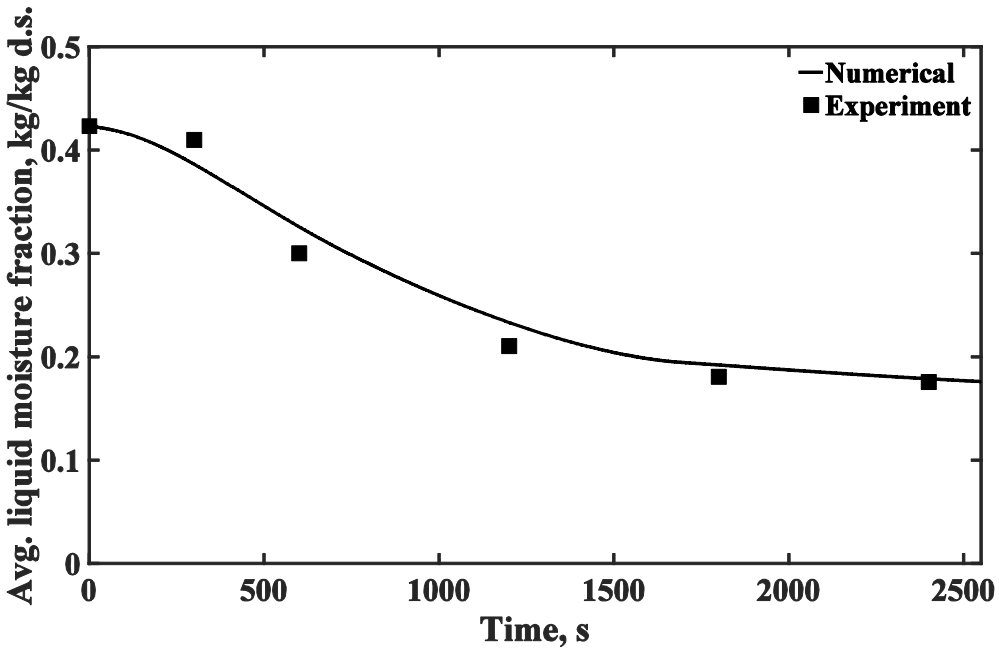

Figure 2.6: Temporal variation of the coal bed averaged liquid mass fraction compared to the experimental results reported in Stakić and Tsotsas [33].

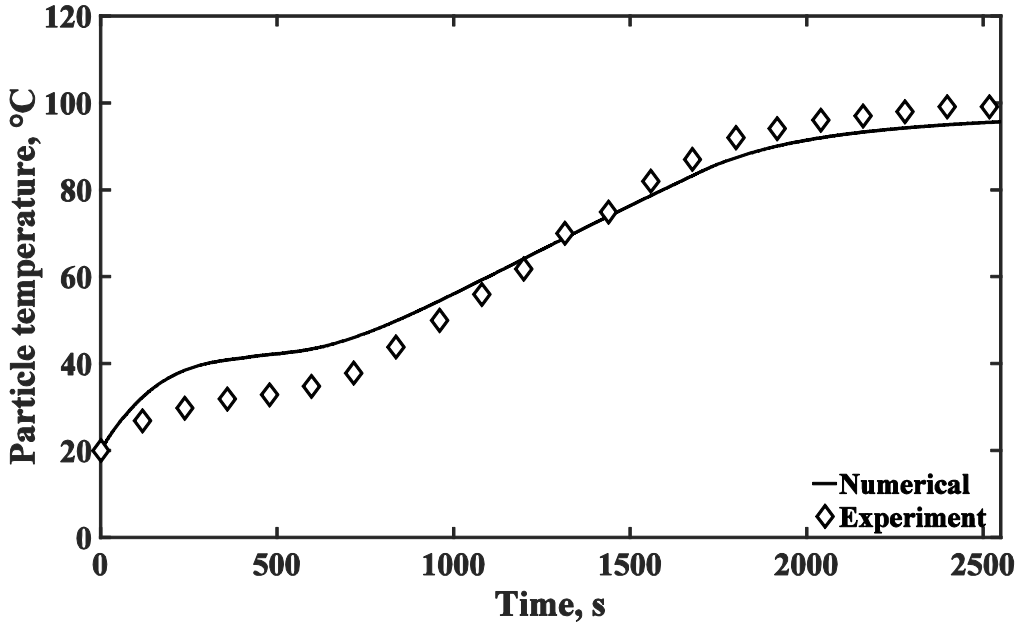

Figure 2.7: Temporal variation of the coal bed averaged solid particle temperature compared to the experimental results reported in Stakić and Tsotsas [33].

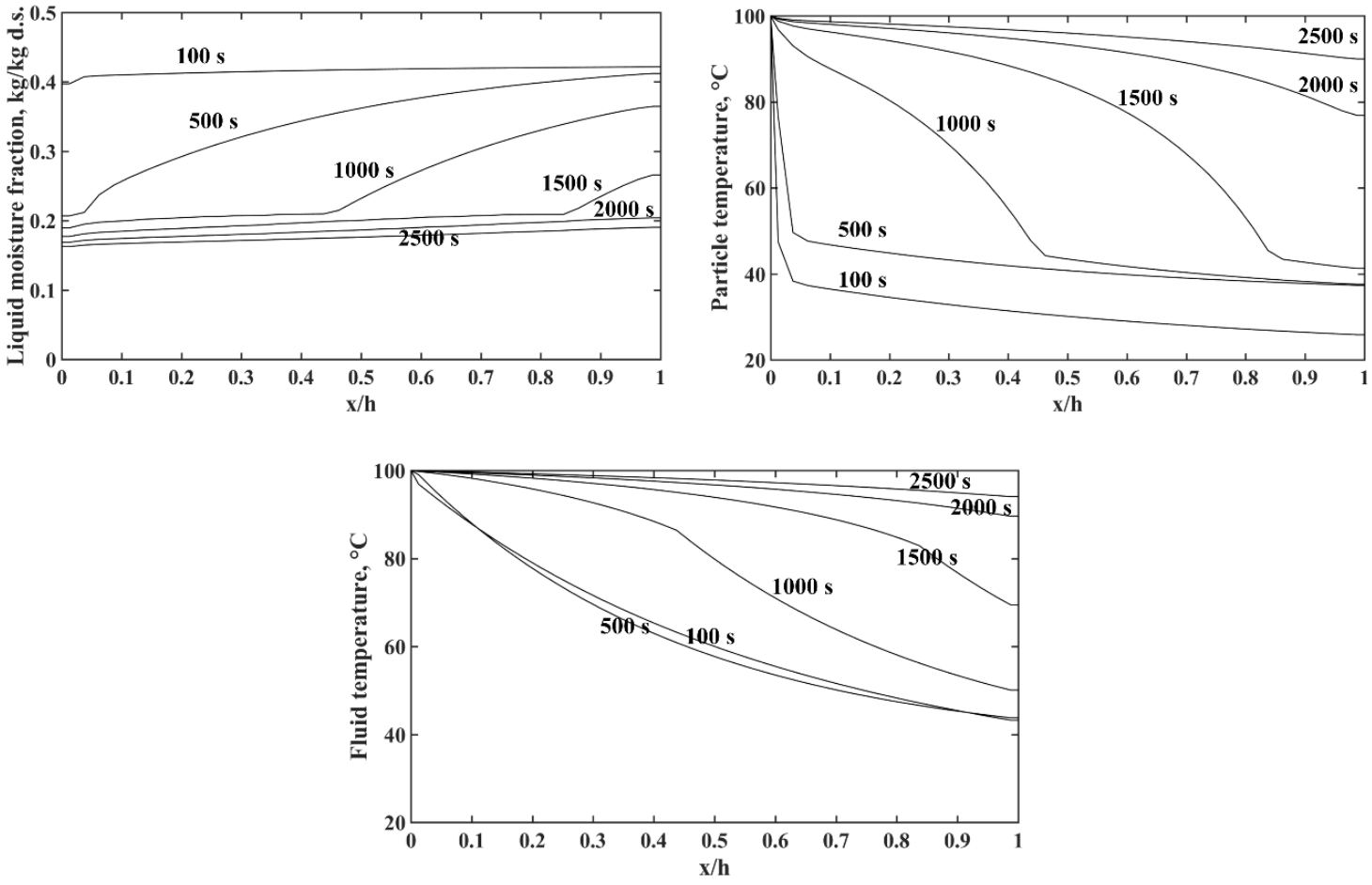

Figure 2.8: Axial variation of the centerline value for liquid moisture fraction, particle and void temperatures at different simulation times.

A gradual increase of fluid and particle temperature is also illustrated in Fig. 2.8, in which a heating front propagates in an analogous manner to the drying front. The rate at which fluid is being heated is significantly faster than the rate of particle heating which indicates the strong thermal non-equilibrium and the fact that the thermal resistance inside the solid is low as compared to the fluid-side resistance. This also indicates that most of the mass transfer energy is withdrawn from the solid constituent.

2.4.2 Drying of an apple slice

The present section builds on the coal particle drying simulation, which focused on dynamic coupling at microscopic interfaces inside a porous region, and presents a

conjugate case that contains both microscopic and macroscopic interfaces, where the macroscopic interface is subject to diffusively dominant mass transfer. The problem considered is the convective drying of an apple slice. The domain that we adopt here is the same as that utilized by Khan and Straatman [9] to mimic experiments conducted by Velić et al. [35]. In their study, a $20\times 20 \times 5$ mm^3 rectangular (peeled) apple slice was placed in an air stream with an inlet condition of 60°C and 9% relative humidity, with inlet air velocities in the range 0.64 - 2.75 m/s. Herein, our base case is selected to have an inlet air velocity of 1.5 m/s. The domain of study utilizes symmetry to reduce the domain of the problem to a quarter of the apple slice with part of the surrounding air stream simulated [9]. The simulation setup is directly adopted from Khan and Straatman [9], including the mesh (30×20×20 control-volumes with refinement in proximity of all fluid/porous interfaces) and the time-step specification (50 seconds with gradual increase from the beginning of the simulation for purposes of numerical stability). A typical simulation of this case required approximately 29 minutes of wall-clock time. Figure 2.9 shows the simulation setup. Boundary conditions were imposed as follows: at the inlet (x=0) plane, velocity was specified as (u,v,w)=(1.5,0,0) m/s with a temperature of 60°C and 9% relative humidity, with pressure extrapolated from inside the domain; at the outlet (x=L) plane, zero-gradients were specified for all quantities except for pressure, which was set to atmospheric; on the symmetry planes (y=0 and z=0), zero-gradients for all quantities except for the normal velocity component, which was set to zero; on the top and right-side faces of the domain, a zero-gradient is specified for all quantities except for pressure, which is extrapolated from inside the domain. The apple slice is specified to have an initial moisture content of 7.45 kg/kg dry solid [9]. Table 2 summarizes the values of the properties required for the present simulations, as cited from [9]. To evaluate the two apple diffusivities, $D_{eff,f}$ and $D_{eff,s}$, a simulation was carried out setting $D_f = D_{eff,f} = D_{eff,s} = D_{eff}$, where D_{eff} is the drying process effective diffusivity obtained directly from Velić et al. [35], and resulting trend have been matched to their experiment.

This approach is identical to the one used by Khan and Straatman [9], given the absence of reliable diffusivity information from the literature. Herein, $D_{eff,f}$ is evaluated by carrying out the fluid leg mass flux balance given by Eq. 2.30 using this simulation result and setting

D_f to its true value. The same procedure was used to obtain an initial estimate for $D_{eff,s}$, which was calibrated later to obtain a better match with the experiment at different inlet velocities. Figure 2.10 shows the variation of the diffusivities with liquid moisture ratio (ratio of moisture content to initial moisture content).

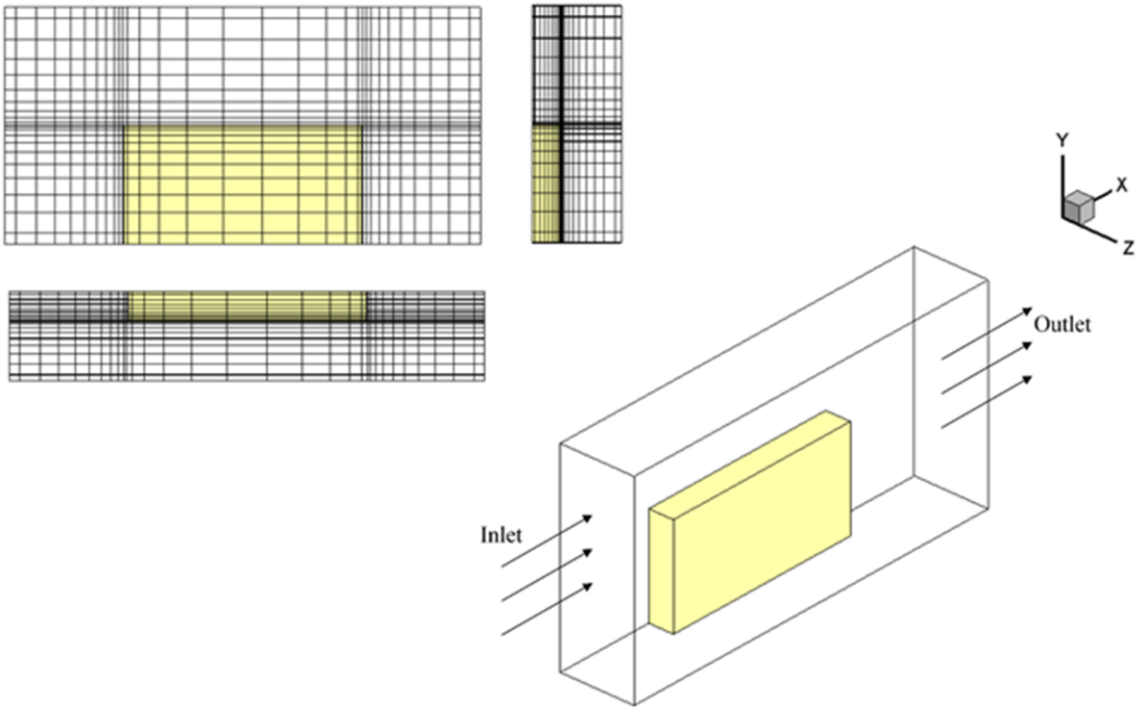

Figure 2.9: Schematic and grid used for simulation of drying of an apple slice.

The trend for the variation of the fluid diffusivity is similar to the variations reported for vapor diffusion in the literature [46]. The trend of the liquid-in-solid effective diffusivity varies within the same orders of magnitude as given by Khan and Straatman [9] and is reasonable in terms of the order of magnitude comparison to the overall drying effective diffusivity obtained from Velić et al [35]. Local heat and mass transfer correlations are different from calibrated correlations utilized in the work of Khan and Straatman [9], which are taken from Geankoplis [47] for spherical particles. The correlations involve a fixed term that is independent of the flow and a variable term, given as,

$$Nu = \frac{h_{fs} d_P}{k_f} = C_{T1} + C_T . Re_{d_P}^{m_T} . Pr_{d_P}^{n_T} \tag{2.46}$$

$$Sh = \frac{h_{fsm} d_P}{D_f} = C_{m1} + C_m . Re_{d_P}^{m_m} . Sc_{d_P}^{n_m} \quad (2.47)$$

where $C_{T1} = C_{m1} = 2$, $C_T = C_m = 0.552$, $m_T = m_m$ =0.53 and $n_T = n_m$ =0.33 for $1 < Re_{d_P} < 48000$.

Table 2.2 : Apple slice drying properties [9].

Porosity, ε	0.206	Specific interfacial area, A_{fs} (m^{-1})	11650
Permeability, K (m^2)	8.89×10^{-13}	Average Particle diameter, d_p (μm)	103
Forchheimer Coefficient, c_E	0.244	Solid effective thermal conductivity, $k_{eff,s}$ (W/m.K.)	0.3335
Dry Solid density, $\langle \rho_s \rangle^s$ (kg/m^3)(1)	124.85	Fluid effective thermal conductivity, $k_{eff,f}$ (W/m.K.)	0.0865
Dry Solid specific heat, c_{ps} (J/kg.K)	252		

(1) The dry solid density is the solid matrix density multiplied by the solid volume fraction, provided by Khan and Straatman [9].

In regards to the local water activity, Toujani et al. [48] obtained the water activity of apple slices at temperatures up to 70°C. Water activities below 70 % occur for moisture contents below 0.3 kg/kg dry. Given that the present apple slice starts at 7.45 kg/kg dry solid, it was deemed suitable to assume particle surface saturation for the convective interstitial mode of mass transfer.

The present case starts with a diffusively-dominant mode for mass transfer, since the liquid-in-solid diffusivity is small enough that the macroscopic diffusive resistance at the fluid/porous interface is the rate determining resistance.

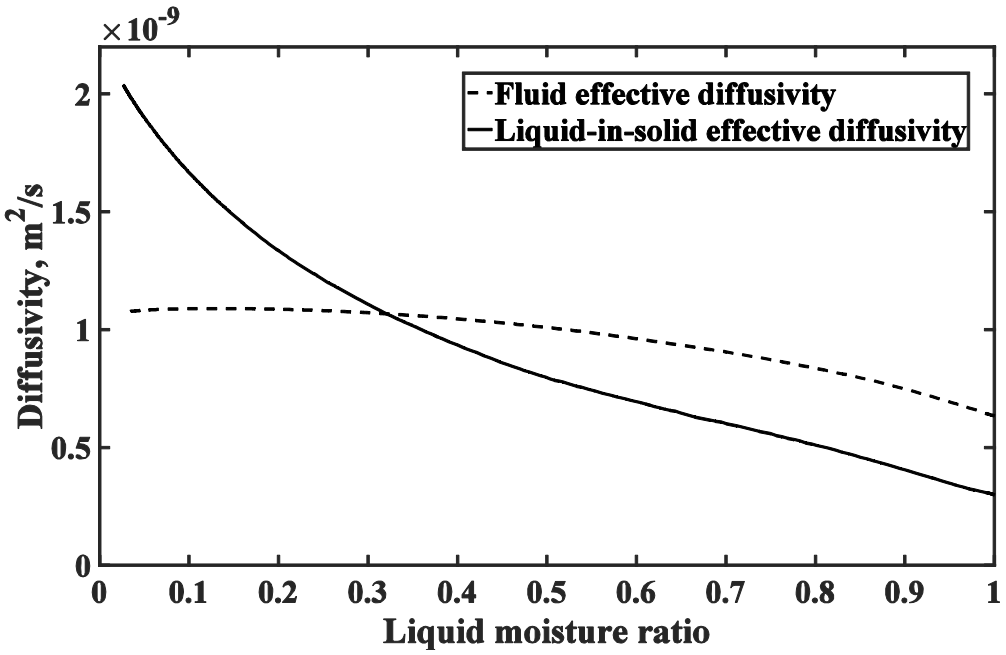

Figure 2.10: Apple diffusivities as a function of the liquid moisture ratio.

This is consistent with the reports in the literature about absence of a constant drying rate period for some fruits and vegetables drying experiments [35],[49],[50]. The ratio $\langle Y_{W,s}\rangle^{s}{}_{e}/\langle Y_{v,f}\rangle^{f}{}_{e}$ in Eq. 2.38 for the present case is determined based on the instantaneous average moisture content of the whole apple slice for all the macroscopic interfaces as a means for simplification and better convergence characteristics. Figure 2.11 shows the variation of the average moisture ratio with time for inlet velocities of 0.64, 1.5 and 2.75 m/s, and shows that the physical effect of changing flow velocities is achieved with the current coupling technique; i.e., the higher the velocity, the faster the drying rate. The agreement between the model and experiment is generally good and is best for the middle flow velocity in terms of the trend and margin. While the low and high speeds show qualitative agreement, larger discrepancies between model and experiment are evident. One reason for the larger discrepancies could be the velocity effect on enhancing vapor diffusion through the interface dry solid layer. It is observed that the present model accounts for advective effects on the drying boundary layer for convectively-dominant modes of mass transfer. However, for the diffusively-dominant mode, the expression used for the vapor transport inside the dry solid layer given by Eq. 2.37 is purely diffusive. It is physically reasonable however that the higher the velocity passing across the macroscopic

interface, the higher the rate of vapor transport that can happen through the dry layer into the air stream [51]. This effect can be accounted for by modifying the expression used for the phase ratio as,

$$\mathrm{K} = \frac{1}{\beta}\left(1 - \frac{1}{1 + \dfrac{\langle \rho_s \rangle^s{}_E D_{eff,s} \langle Y_{w,s} \rangle^s{}_e}{\rho_{f_P}(1-\varepsilon) D_f \langle Y_{v,f} \rangle^f{}_e}}\right) \tag{2.48}$$

where β is a coefficient that we introduce as a vapor diffusion enhancement factor [52]. Figure 2.12 reproduces the drying rate plots given in Fig. 2.11, with the inclusion of Eq. 2.48 using β values of 0.87, 1 and 1.11 for 0.64, 1.5 and 2.75 m/s, respectively. While this approach introduces a calibration factor, it is shown to reduce the discrepancies to within a maximum of 4 % of the experiments.

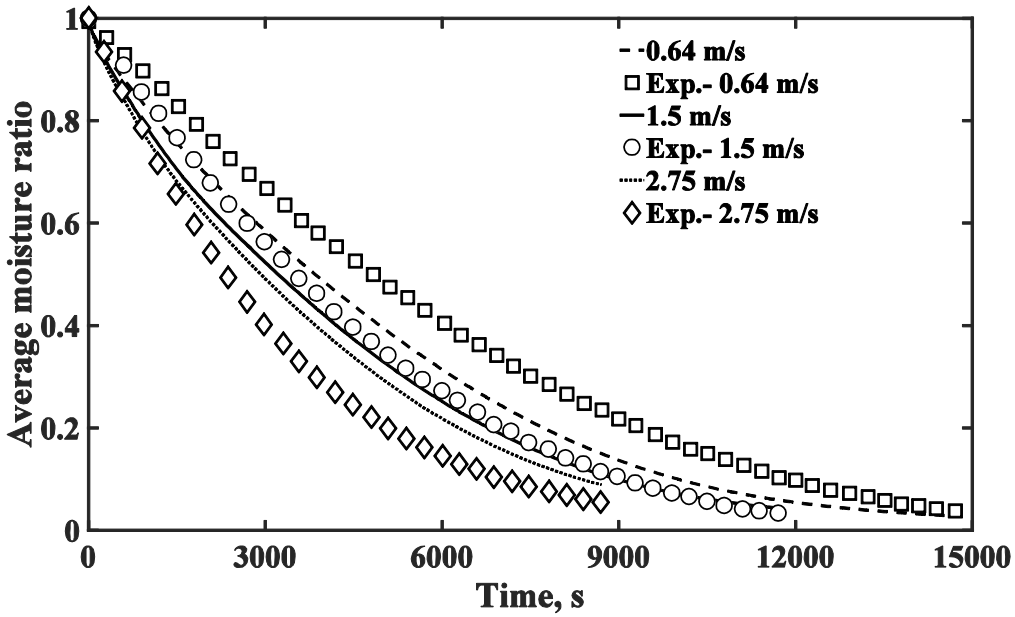

Figure 2.11: Temporal variation of the averaged apple moisture ratio for different inlet velocities compared to the experimental results of Velić et al. [35].

It is of particular interest to show how the present model approaches the physical threshold of moisture capacity. In Khan and Straatman [9], the moisture threshold was achieved, but an adhoc exponentially-varying coefficient was required to properly approach the

threshold. Considering first the influence of inlet relative humidity, Fig. 2.13 shows the temporal variation of the average moisture ratio for 1.5 m/s with inlet relative humidities of 9, 40, 70 and 90%. The drying rate is shown to decline smoothly as the relative humidity increases until it becomes very weak at the 90% case, adhering to the expected physical behavior as the capacity of the air to entrain vapor moisture decreases. Considering the influence of increasing inlet temperature, Fig. 2.14 shows the different drying rates achieved at a fixed inlet specific humidity. A decrease of the drying rate is observed with increasing incoming air stream temperature, which is also consistent with the physics of the problem. In this manner, the present formulation inherently incorporates the changing physics associated with approaching moisture thresholds without the need for additional tuning or calibration.

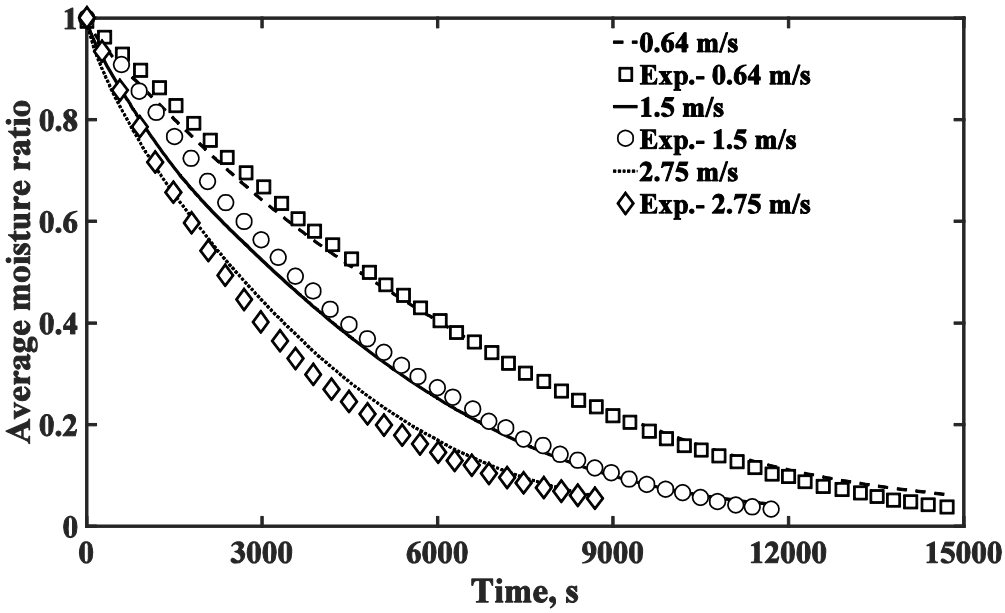

Figure 2.12: Temporal variation of the averaged apple moisture ratio for different inlet velocities accounting for the advective effects; comparison to the experimental results of Velić et al. [35].

Spatial and temporal variation of the solved moisture and temperature fields are shown in Figs. 2.15-2.17. Temporal variation of the liquid moisture distribution is shown in Fig. 2.15, where it is observed that the liquid moisture decreases inside the apple slice gradually

as the material dries up with faster rate closer to the leading edge of the apple slice. The relative humidity is highest inside the apple flesh. In this case the void space becomes quickly saturated with vapor indicating that most of the mass transfer occurs at the fluid/porous interfaces, which is attributed to the low porosity of the apple slice. The relative humidity of the surroundings is highest when the drying rate is high and it declines as the rate that air picks up moisture from the apple slice decreases. The contours of fluid and solid temperature inside the apple slice, shown in Figs. 2.16-2.17, show similar variation with a small degree of thermal non-equilibrium. The core of the apple is cool when the mass transfer rate (drying rate) is high, as seen at 500 seconds, because the inner part of the apple slice supplies most of the vaporization energy. As the apple slice dries, the rate of mass transfer decreases and the core starts to warm up, taking sensible heat from the surrounding. The behavior is physically reasonable and it is consistent with the fear of frost injuries that is of concern to the drying industry of fruits and vegetables.

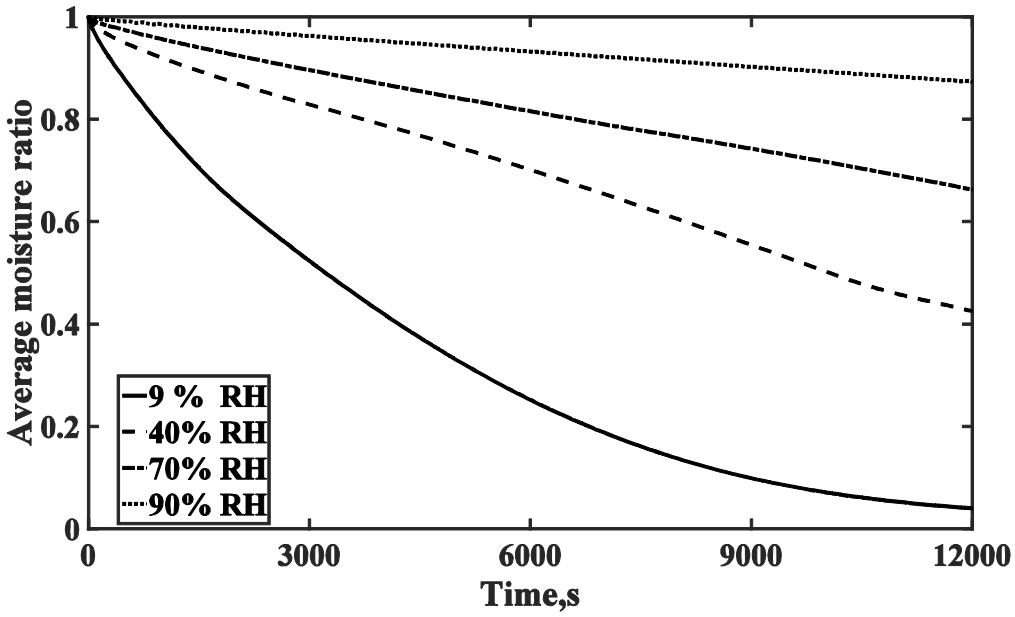

Figure 2.13: Temporal variation of the averaged apple moisture ratio as a function of inlet airflow relative humidity for 1.5 m/s inlet velocity.

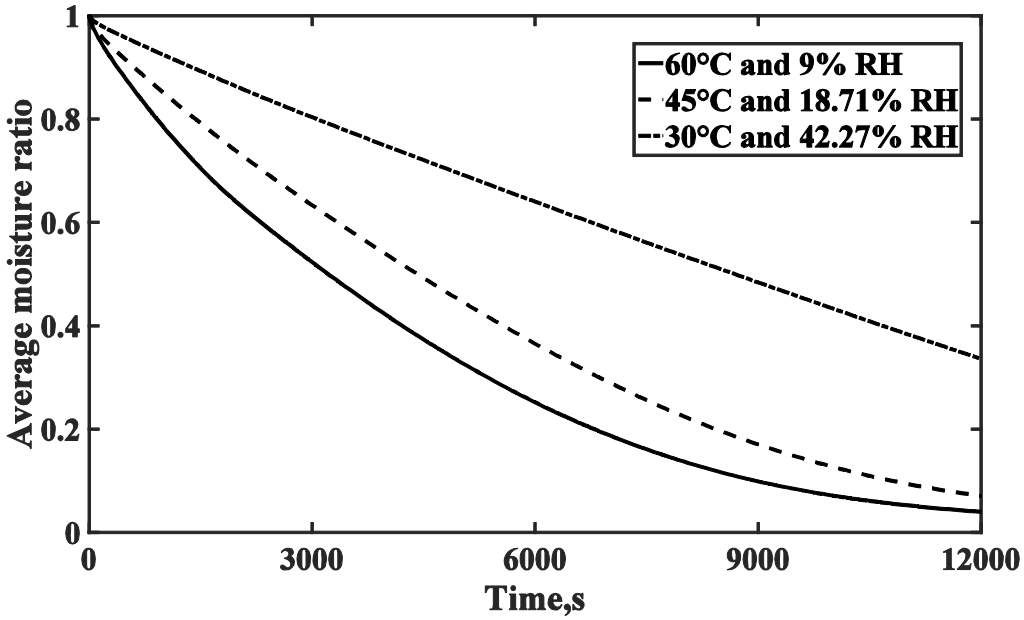

Figure 2.14: Temporal variation of the averaged apple moisture content as a function of the inlet temperature at a fixed inlet specific humidity for 1.5 m/s inlet velocity.

2.4.3 Dehydration of mineral plaster

Convectively-dominant mass transfer is verified herein by simulating a case of dehydration of mineral plaster, as adopted from the work of Defraeye et al. [8]. This case was selected because it provides the necessary information and relevant properties, especially the diffusivities, which are not easily found in the literature, and because the constant drying-rate period is long and clearly visible [8]. This particular case has not been experimentally tested but different modeling approaches have been utilized to simulate and analyze it [8]. While the total simulation time of the case is 15 days, which is the time it takes to fully dehydrate the mineral plaster under consideration, we are mainly interested in the first two hours of the simulation since this is a period of convectively-dominant drying and is well within the constant drying rate period as reported by Defraeye et al [8]. The simulation setup is based on a small-scale wind tunnel test section reported in the work of James et al. [53] shown in Fig. 2.18. A long inlet section (not included in the simulation) provides fully-developed laminar flow to the surface of a plaster substrate, which is comprised of

mineral plaster placed inside a heat and mass insulated enclosure. The test section is 500 mm long with heights of the porous and air regions of 37.5 mm and 20.5 mm, respectively.

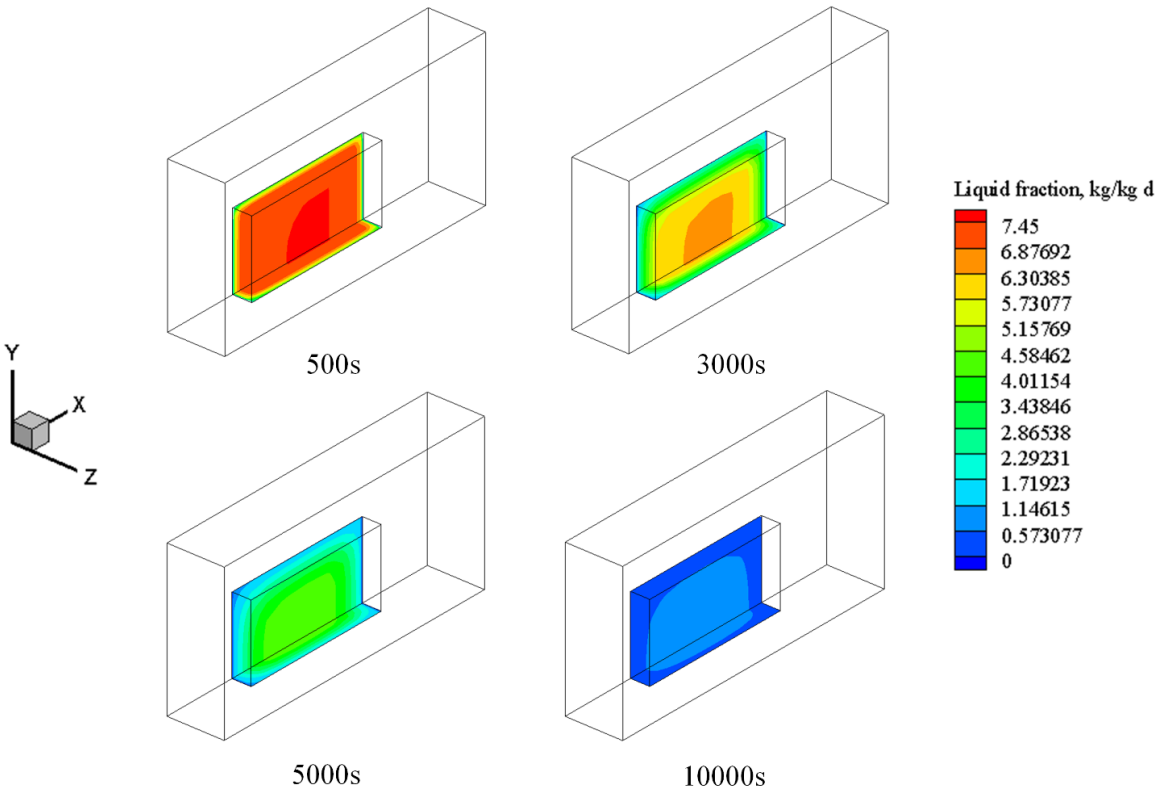

Figure 2.15: Contour plots for liquid apple moisture spatial variation along the domain-cutting symmetry planes at different time instances.

Boundary conditions were imposed as follows: at the inlet, air enters the channel at 23.8 °C and 71.9 % relative humidity with a mass flow rate based on a bulk air velocity of 0.8 m/s with pressure extrapolated from inside the domain; all walls were assigned no-slip, no-penetration boundary conditions with pressure extrapolated from inside the domain. In addition, the walls did not admit heat or mass transfer. At the channel outlet, a zero-gradient condition was used for all variables, with the exception of pressure, which was set to atmospheric. The plaster was given an initial temperature of 20°C. A mesh of 172 x 74 x 1 control volumes was used based on the same spatial resolution as the work of Defraeye et al [8]. The simulation was carried out based on an adaptive time stepping approach that was necessary to achieve convergence given the high time and space non-linearity of the

problem. A typical simulation requires several hours in this problem given the above reasons, which is expected based on information from Defraeye et al. [8].

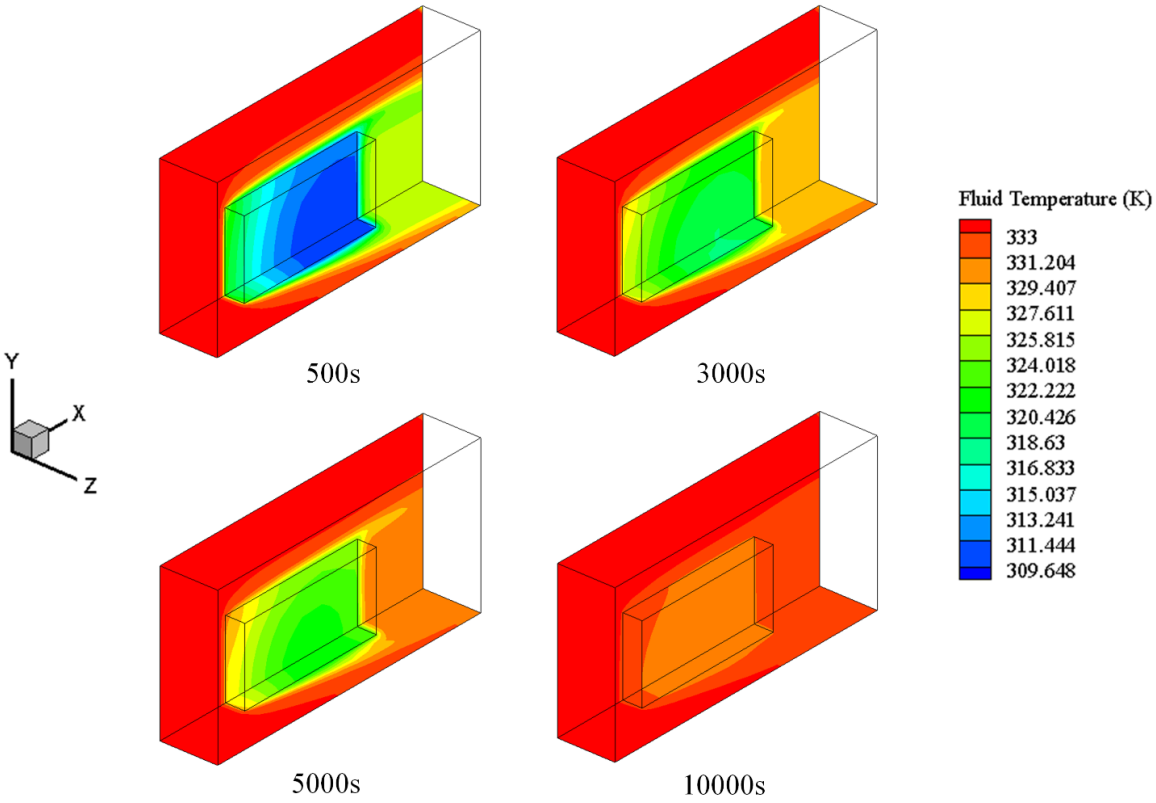

Figure 2.16: Contour plots for fluid temperature spatial variation along the domain-cutting symmetry planes at different time instances.

Mineral plaster is a form of plaster that have a low chemical content of water, given by the formula ($CaSO_4 \cdot \frac{1}{2} H_2O$). Table 3 summarizes the relevant mineral plaster properties. Since Defraeye et al [8], treated the material as non-porous, they did not specify the values of the pore diameter and the porosity, which were selected herein from Bochen [54]. The permeability was calculated using the Ergun equation [42] and the specific surface area using the porosity and the particle diameter. The solid specific heat was based on Defraeye et al [8] while the fluid and solid conductivity were apportioned based on the porosity and their overall porous material conductivity.

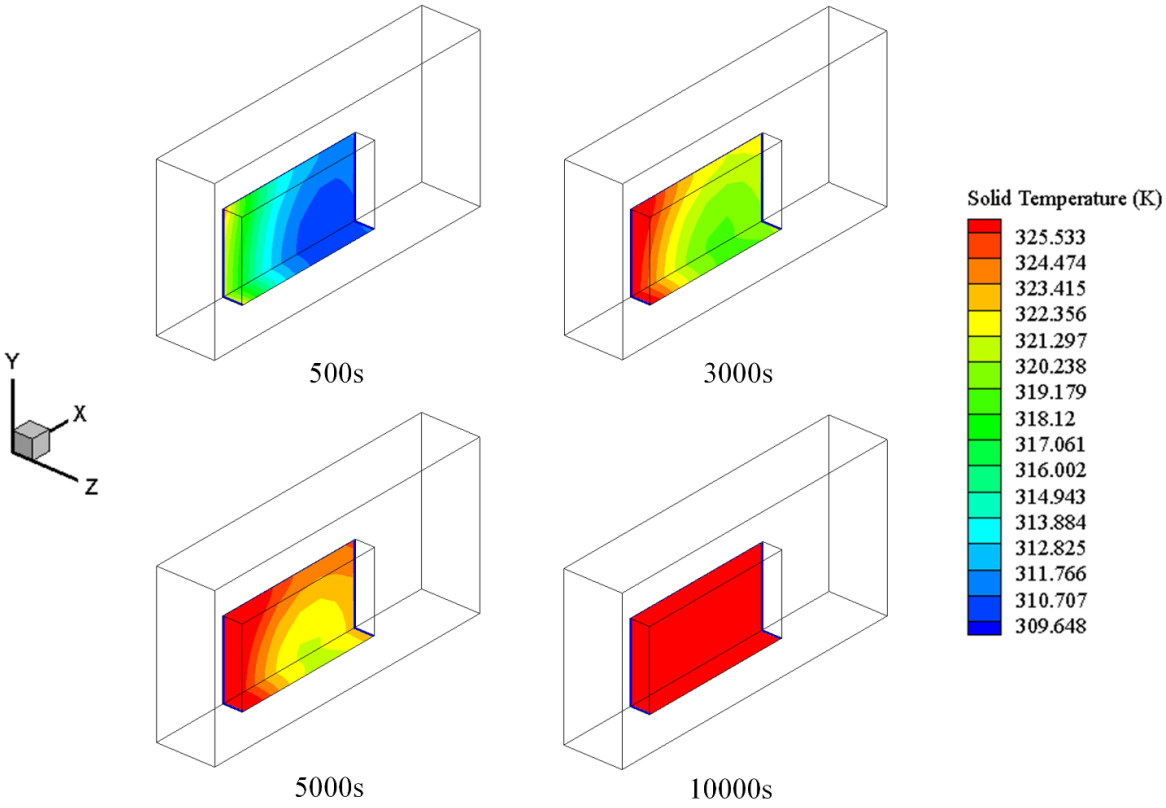

Figure 2.17: Contour plots for solid temperature spatial variation along the domain-cutting symmetry planes at different time instances.

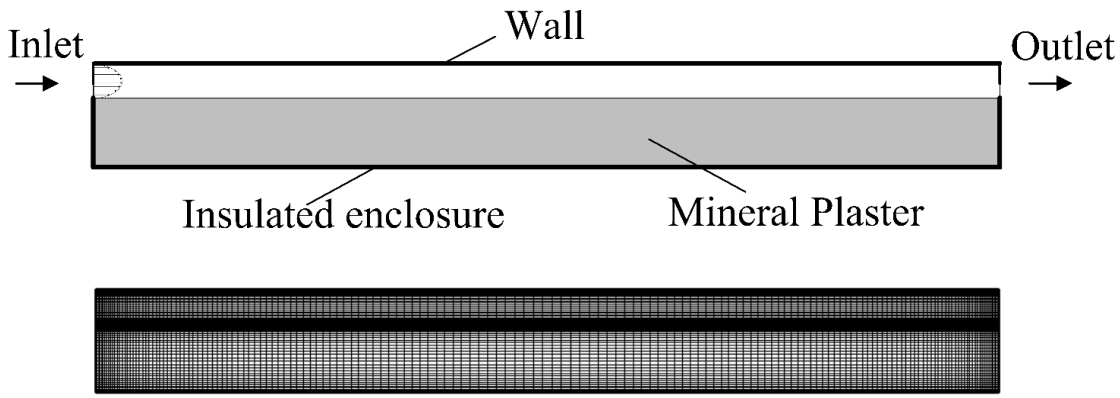

Figure 2.18: Simulation setup for the mineral plaster dehydration process.

Table 2.3: Mineral Plaster properties.

Porosity, ε	0.15	Specific interfacial area, A_{fs} (m^{-1})	112500
Permeability, K (m^2)	$2x10^{-15}$	Average Particle diameter, d_p (μm)	8
Forchheimer Coefficient, c_E	0.244	Solid effective thermal conductivity, $k_{eff,s}$ (W/m.K.)	1.02
Dry Solid density, $\langle\rho_s\rangle^s$ (kg/m^3)(1)	1900	Fluid effective thermal conductivity, $k_{eff,f}$ (W/m.K.)	0.18
Dry Solid specific heat, c_{ps} (J/kg.K)	1050		

The dry solid density and the initial moisture content was calculated based on an initial water content and a total solid mass of 126 kg/m^3 and 1615 kg/m^3 of the whole porous material, respectively [8]. The initial liquid moisture mass fraction is 0.078021 kg/kg dry solid. Figure 2.19 shows the trends of variation for the fluid and solid diffusivities. The fluid diffusivity was calculated based on the provided expression of vapor permeability by Defraeye et al. [8]. The primary liquid transport mechanism considered in their work is the capillary forces as they solved for capillary pressure as a transport variable. In our formulation we consider the capillary effect through a gradient-type diffusion expression and hence, it was necessary to link both approaches by equating the two expressions for the liquid transport flux. Utilizing their correlation for relating the capillary pressure and the liquid mass fraction, we were able to arrive at a suitable correlation after smoothing and curve fitting. The liquid diffusivity endures a sharp drop that is consistent with the fact that mineral plaster is a non-hygroscopic material. This sharp drop and the relatively high initial value of the diffusion coefficient are the main reason why the convective domination

is observed clearly in this simulation. With respect to the water activity, the surface of the solid constituent is assumed saturated as the case should be for a non-hygroscopic material [6]. Eqs. 2.46-2.47 are used for the local heat and mass transfer correlations and the mass transfer correlation is also utilised at the macroscopic interface.

Figure 2.20 displays the average moisture ratio change with time. The material only loses 1.75% of its moisture content in this time, since the total drying time is on the order of 15 days. The profile shows a consistent decrease of moisture with time without any abrupt changes in the drying rate, which is compatible with the notion of a constant drying rate period. The contour plots for the liquid moisture content displayed in Fig. 2.21 are very similar to those displayed in Defraeye et al. [8]. The plots show a gradual moisture decrease, which starts at the leading edge of the plaster and moves into the core slowly until it reaches the downstream bottom corner. The contours for relative humidity and temperature are shown in Figs. 2.22-2.23. Typical boundary layer growth is observed for both relative humidity and fluid temperature, as relative humidity increases along the channel and temperature decreases indicating that the air stream is the main source of vaporization energy. Within the porous region itself, the temperature is nearly constant at a value that is very close to the wet bulb temperature (approximately 20°C [8]), indicating that vaporization heat removed from the porous region is restored sensibly by energy provided from the air. Very small temperature deviations (less than 0.3°C) are computed inside the porous material, but not resolved in the figures. These temperatures are higher for locations that have lower moisture contents forming fronts that are analogous to the ones shown in Fig. 2.21.

As a final means of comparison, the average surface heat and mass transfer coefficients over the length of the macroscopic interface are evaluated based on the definitions used by Defraeye et al. [8]. The present simulation yields a mass transfer coefficient of 5.73×10^{-8} s/m (based on vapor pressure) as compared to 3.77×10^{-8} s/m, while for heat transfer, an average coefficient of 2 W/m^2K was computed compared to 5.34 W/ m^2K. Given the different modelling approaches, and in particular, our porous verses their non-porous formulation, the computed values compare very well for both heat and mass transfer.

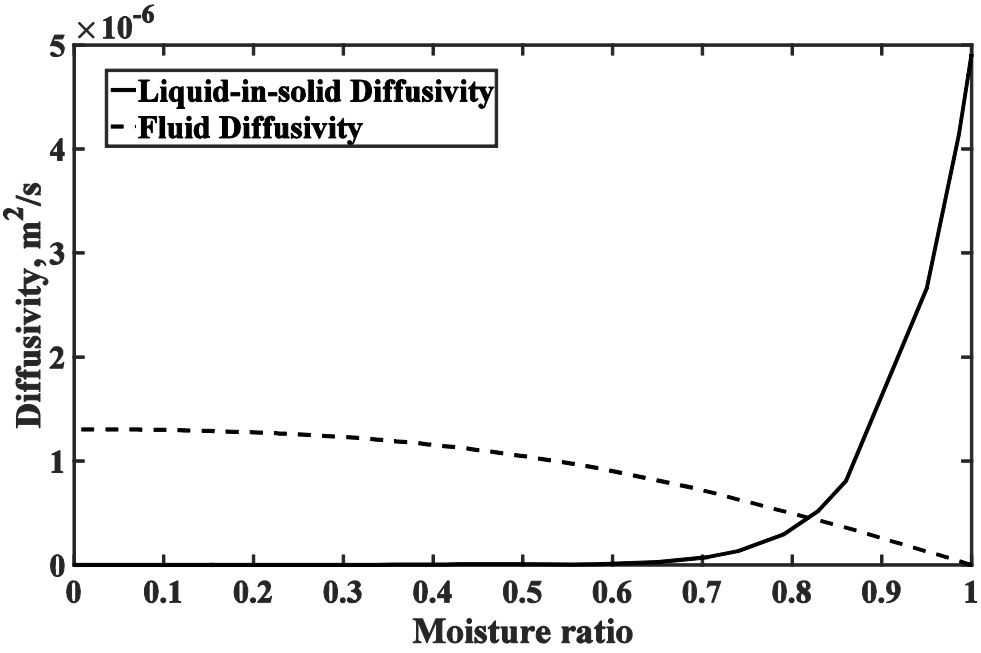

Figure 2.19: Mineral plaster diffusivities as a function of the moisture ratio.

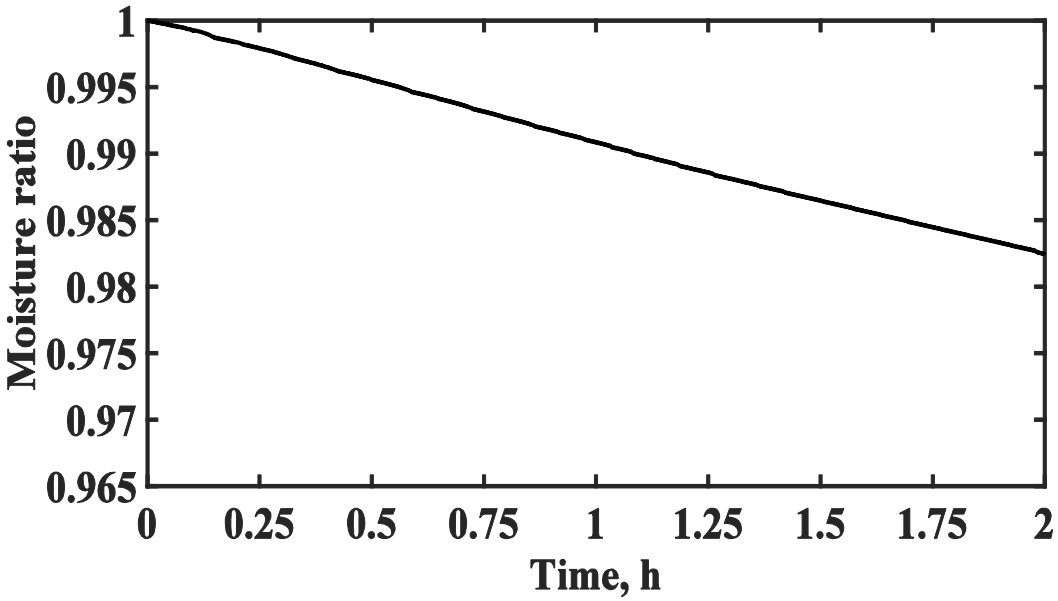

Figure 2.20: Variation of the average moisture ratio as a function of the drying time for mineral plaster.

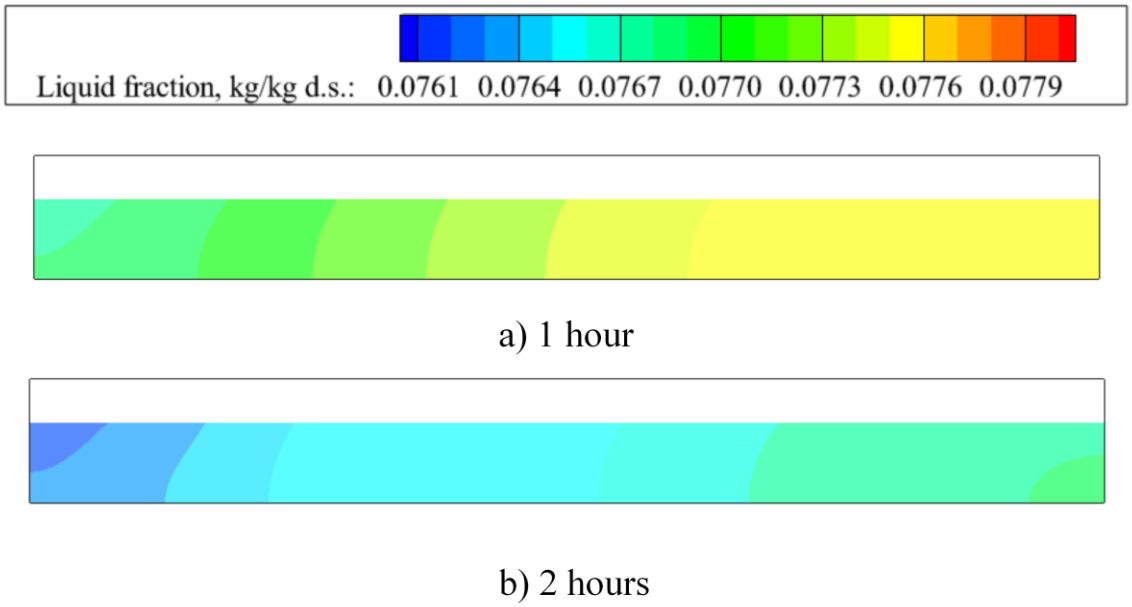

Figure 2.21: Temporal variation for the distribution of liquid moisture content of mineral plaster (a scale with four decimal places was necessary to observe the moisture fronts).

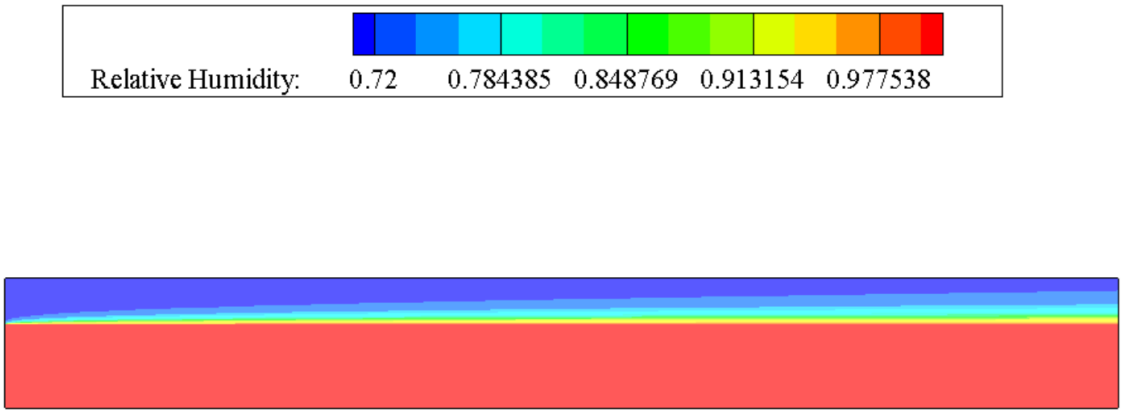

Figure 2.22: Relative humidity distribution at 1 hour of simulation time for mineral plaster.

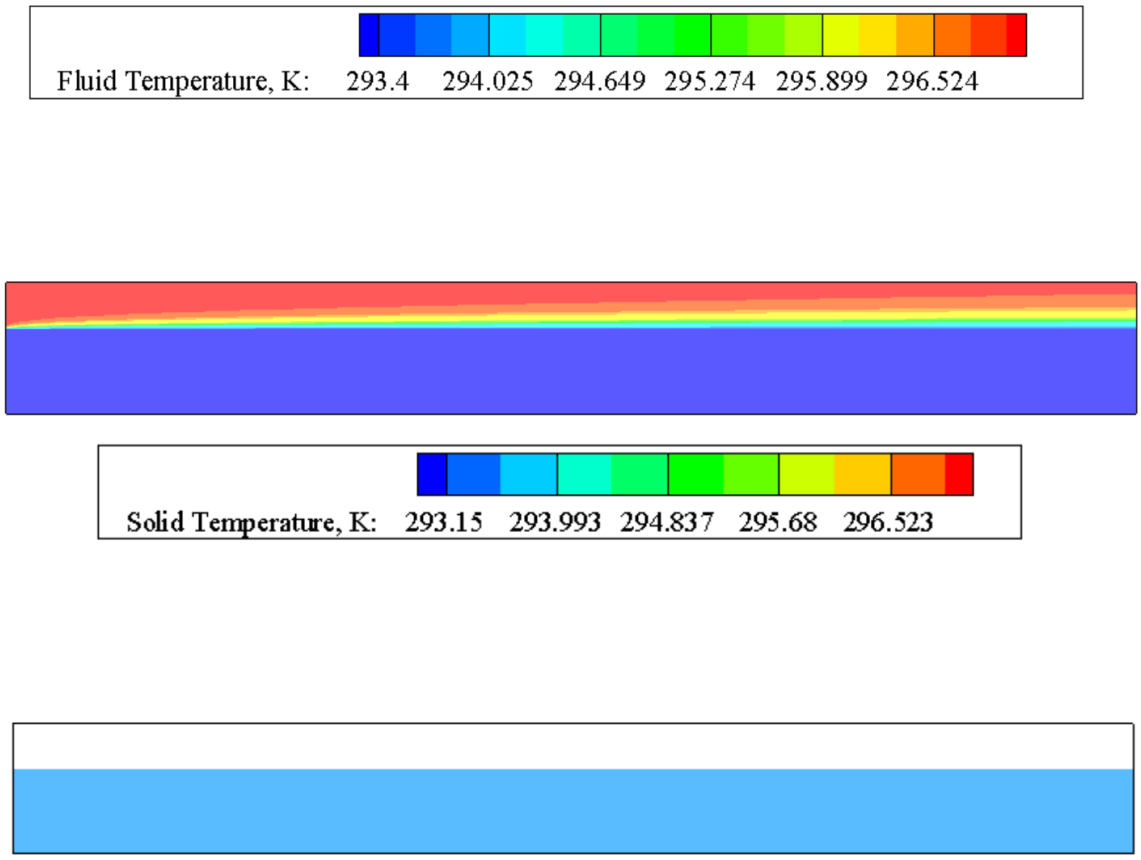

Figure 2.23: Distributions of temperatures at 1 hour of simulation time for mineral plaster.

2.5 Summary

In the present study, a dynamically-coupled approach has been introduced for modelling heat and mass transfer in conjugate fluid/porous domains. The dynamic-coupling means that heat and mass exchanges between constituents inside the porous media (microscopic level) and across fluid/porous interfaces (macroscopic level), vary dynamically in response to the local spatial and temporal condition of the interface. The key novelties are summarized as:

- Models are presented that track the variations of heat and mass transfer resistances inside the fluid and solid phases and allow for switching between expressions developed for these heat and mass exchanges on both scales without the sacrifice of numerical stability.

- A technique for apportioning of the vaporization energy on different phases is incorporated.
- A concept is introduced for the phase ratio, which is implemented to achieve implicit conjugate coupling at the macroscopic interfaces.

The model involves details that allow the application to very different interface heat and mass transfer problems. Three cases were introduced to validate and illustrate the capability of the model. A coal packed bed of particles is simulated to verify the interstitial coupling approach of the formulation. Results of the moisture and temperature profiles showed excellent agreement in terms of trends and thresholds. The case of drying of an apple slice was tested to verify the efficacy of the dynamic macroscopic coupling for diffusively-dominant mass transfer. Comparison to experiments indicated an agreement to within 4% in terms of drying rates and time. In addition, the physical thresholds of relative humidity and temperature were approached smoothly without the need for additional tuning, a feature that makes the present formulation particularly attractive. Finally, a convectively-dominant case of mineral plaster dehydration was simulated. The predicted boundary layer growth, nearly constant material temperature and the gradual propagation of the drying fronts inside the porous materials showed that the physics of the problem are accurately represented, and heat and mass transfer rates compare well to previous work on the same problem. Thus, it is concluded that the present dynamic-coupling approach is capable of representing the physics of heat and mass transfer across interfaces between different phases in a generic way without case specificity and with a lesser level of empiricism than any existing modelling approach. This means that the present model, with little calibration or tuning, is capable of modelling non-equilibrium heat and mass transfer for both diffusively and convectively-dominated interfaces.

References

[1] Luikov, A. V. (1966). Heat and Mass Transfer in Capillary Bodies, Pergamon Press, Oxford. England.

[2] Whitaker, S. (1977). A Theory of drying. *Advances in heat transfer*, *13*, 119-203.

[3] Stanish, M. A., Schajer, G. S., & Kayihan, F. (1986). A mathematical model of drying for hygroscopic porous media. *AIChE Journal*, *32*(8), 1301-1311.

[4] Younsi, R., Kocaefe, D., Poncsak, S., & Kocaefe, Y. (2007). Computational modelling of heat and mass transfer during the high-temperature heat treatment of wood. *Applied thermal engineering*, *27*(8), 1424-1431.

[5] Perré, P., & Turner, I. W. (1999). A 3-D version of TransPore: a comprehensive heat and mass transfer computational model for simulating the drying of porous media. *International Journal of heat and mass transfer*,*42*(24), 4501-4521.

[6] Keey, R. B. (1972). Drying: Principles and Practice, International Series of Monographs in Chemical Engineering, vol. 13.

[7] Nasrallah, S. B., & Perre, P. (1988). Detailed study of a model of heat and mass transfer during convective drying of porous media. *International journal of heat and mass transfer*, *31*(5), 957-967.

[8] Defraeye, T., Blocken, B., & Carmeliet, J. (2012). Analysis of convective heat and mass transfer coefficients for convective drying of a porous flat plate by conjugate modelling. *International Journal of Heat and Mass Transfer*, *55*(1), 112-124.

[9] Khan, F. A., & Straatman, A. G. (2016). A conjugate fluid-porous approach to convective heat and mass transfer with application to produce drying.*Journal of Food Engineering*, *179*, 55-67.

[10] Sarsavadia, P. N., Sawhney, R. L., Pangavhane, D. R., & Singh, S. P. (1999). Drying behaviour of brined onion slices. *Journal of Food Engineering*,*40*(3), 219-226.

[11] Menges, H. O., & Ertekin, C. (2006). Mathematical modeling of thin layer drying of Golden apples. *Journal of Food Engineering*, *77*(1), 119-125.

[12] Karoglou, M., Moropoulou, A., Maroulis, Z. B., & Krokida, M. K. (2005). Drying kinetics of some building materials. *Drying technology*, *23*(1-2), 305-315.

[13] Zhang, M., Jiang, H., & Lim, R. X. (2010). Recent developments in microwave-assisted drying of vegetables, fruits, and aquatic products—Drying kinetics and quality considerations. *Drying Technology*, *28*(11), 1307-1316.

[14] Perazzini, H., Freire, F. B., & Freire, J. T. (2013). Drying kinetics prediction of solid waste using semi-empirical and artificial neural network models.*Chemical Engineering & Technology*, *36*(7), 1193-1201.

[15] Islam, M. R., Ho, J. C., & Mujumdar, A. S. (2003). Convective drying with time-varying heat input: Simulation results. *Drying technology*, *21*(7), 1333-1356.

[16] Hussain, M. M., & Dincer, I. (2003). Two-dimensional heat and moisture transfer analysis of a cylindrical moist object subjected to drying: a finite-difference approach. *International Journal of Heat and Mass Transfer*, *46*(21), 4033-4039.

[17] Younsi, R., Kocaefe, D., Poncsak, S., & Kocaefe, Y. (2006). Thermal modelling of the high temperature treatment of wood based on Luikov's approach. *International Journal of Energy Research*, *30*(9), 699-711.

[18] Chourasia, M. K., & Goswami, T. K. (2007). CFD simulation of effects of operating parameters and product on heat transfer and moisture loss in the stack of bagged potatoes. *Journal of Food Engineering*, *80*(3), 947-960.

[19] Kaya, A., Aydın, O., & Dincer, I. (2006). Numerical modeling of heat and mass transfer during forced convection drying of rectangular moist objects.*International journal of heat and mass transfer*, *49*(17), 3094-3103.

[20] Mohan, V. C., & Talukdar, P. (2010). Three dimensional numerical modeling of simultaneous heat and moisture transfer in a moist object subjected to convective drying. *International Journal of Heat and Mass Transfer*, *53*(21), 4638-4650.

[21] Esfahani, J. A., Majdi, H., & Barati, E. (2014). Analytical two-dimensional analysis of the transport phenomena occurring during convective drying: Apple slices. *Journal of Food Engineering*, *123*, 87-93.

[22] Erriguible, A., Bernada, P., Couture, F., & Roques, M. (2006). Simulation of convective drying of a porous medium with boundary conditions provided by CFD. *Chemical Engineering Research and Design*, *84*(2), 113-123.

[23] Lamnatou, C., Papanicolaou, E., Belessiotis, V., & Kyriakis, N. (2010). Finite-volume modelling of heat and mass transfer during convective drying of porous bodies–Non-conjugate and conjugate formulations involving the aerodynamic effects. *Renewable Energy*, *35*(7), 1391-1402.

[24] De Bonis, M. V., & Ruocco, G. (2008). A generalized conjugate model for forced convection drying based on an evaporative kinetics. *Journal of Food Engineering*, *89*(2), 232-240.

[25] Khan, F. A., Fischer, C., & Straatman, A. G. (2015). Numerical model for non-equilibrium heat and mass exchange in conjugate fluid/solid/porous domains with application to evaporative cooling and drying. *International Journal of Heat and Mass Transfer*, *80*, 513-528.

[26] Ilic, M., & Turner, I. W. (1986). Drying of a wet porous material. *Applied mathematical modelling*, *10*(1), 16-24.

[27] Sitompul, J. P., Istadi, & Sumardiono, S. (2003). Modelling and simulation of momentum, heat, and mass transfer in a deep-bed grain dryer. *Drying Technology*, *21*(2), 217-229.

[28] Saastamoinen, J. J. (2005). Comparison of moving bed dryers of solids operating in parallel and counterflow modes. *Drying technology*, *23*(5), 1003-1025.

[29] Zhonghua, W., & Mujumdar, A. S. (2007). Simulation of the hydrodynamics and drying in a spouted bed dryer. *Drying Technology*, *25*(1), 59-74.

[30] Stakić, M., Stefanović, P., Cvetinović, D., & Škobalj, P. (2013). Convective drying of particulate solids–Packed vs. fluid bed operation. *International Journal of Heat and Mass Transfer*, *59*, 66-74.

[31] Zhang, K., & You, C. (2011). Experimental and numerical investigation of lignite particle drying in a fixed bed. *Energy & Fuels*, *25*(9), 4014-4023.

[32] Messai, S., El Ganaoui, M., Sghaier, J., Chrusciel, L., & Slimane, G. (2014). Comparison of 1D and 2D models predicting a packed bed drying.*International Journal for Simulation and Multidisciplinary Design Optimization*, *5*, A14.

[33] Stakić, M., & Tsotsas, E. (2004). Modeling and numerical analysis of an atypical convective coal drying process. *Drying technology*, *22*(10), 2351-2373.

[34] Y.A. Cengel and M.A. Boles. Thermodynamics an Engineering Approach: Sixth edition. New York, McGraw Hill Company, 738-747, 2008.

[35] Velić, D., Planinić, M., Tomas, S., & Bilić, M. (2004). Influence of airflow velocity on kinetics of convection apple drying. *Journal of Food Engineering*,*64*(1), 97-102.

[36] M. Kaviany, Principles of Heat Transfer in Porous Media, second ed., Springer-Verlag, New York, NY, 1995.

[37] Betchen, L., Straatman, A. G., & Thompson, B. E. (2006). A nonequilibrium finite-volume model for conjugate fluid/porous/solid domains. *Numerical Heat Transfer, Part A: Applications*, *49*(6), 543-565.

[38] Spalding, D. B. (1953, December). The combustion of liquid fuels. In *Symposium (international) on combustion* (Vol. 4, No. 1, pp. 847-864). Elsevier.

[39] Incropera, F., Dewitt, D., Bergman, T., & Lavine, A. (2006). Fundamentals of Heat and Mass Transfer, 5th edition. Wiley, Hoboken, NJ, 927.

[40] Pakowski, Z., Bartczak, Z., Strumillo, C., & Stenström, S. (1991). Evaluation of equations approximating thermodynamic and transport properties of water, steam and air for use in CAD of drying. *Drying Technology*, *9*(3), 753-773.

[41] Whitman, W. G. (1923). Preliminary experimental confirmation of the two-film theory of gas absorption. *Chem. Met. Engng* 29, 146-148.

[42] Yu, Q., Thompson, B. E., & Straatman, A. G. (2006). A unit cube-based model for heat transfer and fluid flow in porous carbon foam. *Journal of heat transfer*, *128*(4), 352-360.

[43] Stakić, M., Banjac, M., & Urošević, T. (2011). Numerical study on hygroscopic material drying in packed bed. *Brazilian Journal of Chemical Engineering*, *28*(2), 273-384.

[44] Fu, B. A., & Chen, M. Q. (2015). Thin-layer drying kinetics of lignite during hot air forced convection. *Chemical Engineering Research and Design*, *102*, 416-428.

[45] Ginzburg, A.S., & Savina, I.M. (1982). Moist Transport Characteristics of Food Products Handbook, *Light and Food Industry*, Moscow.

[46] Defraeye, T., Blocken, B., & Carmeliet, J. (2013). Influence of uncertainty in heat–moisture transport properties on convective drying of porous materials by numerical modelling. *Chemical Engineering Research and Design*, *91*(1), 36-42.

[47] Geankoplis, C. J. (1978). *Mass Transport Phenomena*.

[48] Toujani, M., Hassini, L., Azzouz, S., & Belghith, A. (2012). Experimental and mathematical investigations of apple slices convective drying. *Journal of Food Science and Engineering*, *2*(6), 314.

[49] Bimbenet, J. J., Daudin, J. D., & Wolff, E. (1985). Air drying kinetics of biological particles. In *Drying'85* (pp. 178-185). Springer Berlin Heidelberg.

[50] Magee, T. R. A., & Wilkinson, C. P. (1992). Influence of process variables on the drying of potato slices. *International journal of food science & technology*, *27*(5), 541-549.

[51] Yiotis, A. G., Tsimpanogiannis, I. N., Stubos, A. K., & Yortsos, Y. C. (2006). Pore-network study of the characteristic periods in the drying of porous materials. *Journal of Colloid and Interface Science*, *297*(2), 738-748.

[52] Webb, S. W., & Ho, C. K. (1998). *Review of enhanced vapor diffusion in porous media* (No. SAND--98-1819C; CONF-980559). Sandia National Labs, Albuquerque, NM (United States).

[53] James, C., Simonson, C. J., Talukdar, P., & Roels, S. (2010). Numerical and experimental data set for benchmarking hygroscopic buffering models. *International Journal of Heat and Mass Transfer*, *53*(19), 3638-3654.

[54] Bochen, J. (2009). Study on the microstructure of thin-layer facade plasters of thermal insulating system during artificial weathering. *Construction and Building Materials*, *23*(7), 2559-2566.

Chapter 3

3 Heat and mass transfer in Conjugate Fluid/Porous domains under turbulent flow conditions

3.1 Introduction

Study of processes involving Porous media and Conjugate Fluid/Porous/Solid domains [1-2] has attracted significant attention in the past two decades. The applications are numerous including flow, heat and mass transfer processes in packed beds, metal foams, dryers, food processing and storage facilities and different other chemical and catalytic multi-phase applications. It is becoming crucial to characterise the heat and mass transfer processes between the different phases inside a porous material as well as between a porous continuum and its surrounding air regions. Most of the above mentioned applications are turbulent in nature and hence, the challenges of characterizing turbulence also need to be addressed. Due to the fact that all of these applications involve multiple spatial and temporal scales with the presence of turbulence, porous media and macroscopic transport, measurement techniques that characterise these processes locally are either nonexistent or limited, leaving only three options for physical model development. The first option is to depend on empiricism as a tool to establish physical thresholds for flow, heat and mass transfer [3-5]. The second option is to undertake detailed physical modelling for these multiple spatial and time scales [6-7]. The third option is to compromise between computational time, empiricism and detailed scale modeling in order to have a successful, general and economic modeling process (i.e. a dynamic Coupling approach) [8] (the interested reader is encouraged to look into the work of Elhalwagy and Straatman [8] for details).

Turbulent heat and mass transfer modeling is of special importance to drying and food processing applications and numerous studies have been reported in the literature. The first category of applications is concerned with drying. Curcio et al. [9] modeled the coupled turbulent air flow around a cylindrical food sample and the heat and mass transfer as the

sample dries. A continuity condition for the heat and mass transfer fluxes is utilised as a boundary condition and a thermodynamic equilibrium assumption at the interface is invoked for linking the liquid and vapor moisture concentrations. It was not mentioned whether the model used to obtain sample solutions was conjugate or non-conjugate with respect to the surrounding air. The two-equation k-ε turbulence model was utilised with standard wall function to account for the boundary layer effects. The vapor diffusion within the sample was neglected and hence the approach is not capable of treating problems like porous foods, where non equilibrium heat and mass transfer is present. Another study by De Bonis and Ruocco [10] investigated the jet-impingement of air into a wet protrusion to enhance moisture removal. They also utilised a non-porous approach but with considering conjugate local thermal non-equilibrium. Standard k-ε turbulence model and wall function were used. While considering the vapor inside the protrusion, they lumped the diffusion of liquid and vapor into a single diffusivity. An Arrhenius expression was utilised for surface evaporation, i.e. the interface mass exchange, rendering the technique to be non-generic [8]. The same modeling approach was used for parallel convective flow over the wet protrusion by Caccavale et al. [11]. Ateeque et al. [12] reported on a study that considered turbulent airflow around a potato slice. They utilised a k-ω SST model based on an investigation of flow separation for a backward facing step with different turbulence models. A non-conjugate/non-porous heat and mass transfer model was used to couple the slice and the surrounding air via surface transfer coefficients. Spatial dependence of heat and mass transfer coefficients was observed to develop based on the turbulent flow field solution with higher values at the upstream face and lowest values at the back face. A saturated ceramic brick drying process has been investigated by Van Belleghem et al. [13]. They utilised a realizable k-ε model with low Reynolds number modeling near the Air/brick interface to resolve turbulent effects. The liquid and vapor transport processes have been lumped into one equation for moisture in which the liquid flux is modeled by the Darcy law using capillary pressure as a transport variable in their discretization. They had empirical specification for the transfer fluxes at the Air/brick interface. They also neglected the transport of any turbulence to the inside of the drying specimen. Turbulent flow around an apple slice has been investigated in terms of drag coefficient, Nusselt number, Separation angle and back reciriculation length by Defraeye et al. [14]. A wide range of

models were tested including different versions of *k*-*ε,* *k*-ω and Reynolds stress models (RSM). A low Reynolds number model was utilised in the wall-adjacent region, as well as a standard wall-function. The *k*-ω SST was selected with low Reynolds number modeling for its accurate wake size, effect on heat transfer and sepration. It is noted however that a significant refinement was utilised in that case. A switch to standard wall-functions deteriorated the performance of the *k*-ω SST model significantly in comparison to the *k*-*ε* model solution for the same conditions.

The second category of applications concerns produce stacking and storage that depend upon a porous media modeling approach within boxes or stacks of produce. This approach relies on obtaining information from a void-level simulation to provide closure of resistance and heat and mass exchange terms for a macroscopic porous media model. The closure process is either empirical so that it depends on empirical equations [15], final experimental verification [16] or sensitivity analysis [17] for closure parameters; or is physically based, i.e. depends on choosing a representative elementary volume (REV) of the porous media [18-19]. Turbulence has been modelled with the RNG *k*-*ε* [15, 20], *k*-ω SST [16-19] and RSM [21] models. Comparisons between turbulence models were carried out to arrive at the choice of these models based on the average relative error between simulations and experiments with respect to velocities [18] and temperatures [16] however local differences in regions near the interfaces were not considered. Tutar et al. [20] concluded that inlet turbulence intensity has only a small effect on heat and mass transfer. They also concluded that increase of flow rate has a more pronounced effect on heat and mass transfer as compared to turbulent and three dimensional effects. Most of the produce stacking studies did not involve any details on the porous media closure terms for the turbulence equations or the special turbulence mathematical conditions for fluxes at the air/porous interface [15-20], relying only on the techniques available in the utilised commercial software ANSYS FLUENT^{TM} [22]. Some of the studies resorted to a switch to force the tubulence model to be off within porous media [15].

Another group of studies focuses on detailed modeling for turbulence inside porous materials. Simplified modeling approaches were developed by Alvarez et al. [23] and Alvarez and Flick [24]. The models depended only on Darcy–Forchheimer equation,

neglecting convective and Brinkman effects. They were one-equation models in which the k equation is solved while the dissipation is estimated with an algebraic expression involving four empirical constants [23] and enhanced later to include only two constants [24]. The turbulence effect has been carried into the heat transfer utilising only a heat transfer Nusselt number correlation that includes turbulence intensity. The main work for modeling took the direction for development of a Porous media k-ε model using volume and time averaging, known as Double decomposition [25]. Early attempts were made by Lee and Howell [26], Wang and Takle [27], Antohe and Lage [28] and Getachew et al. [29]. The turbulent kinetic energy was defined based on a time average of the square of the volume-averaged velocity fluctuation. Later, Nakayama and Kuwahara (NK) [30] and Pedras and De Lemos (PDL) [31] adopted another definition based on squaring the local velocity fluctuation first and then carrying out the Double decomposition. A third definition of k was developed by Teruel and Rizwan-uddin (TR) [32-33]. Their definition added to the former a term characterising dispersive kinetic energy based on spatial deviations of the volume averaged process for velocity. The three forms for the macroscopic k-ε model by PDL, NK and TR are the most widely used forms through the literature. They utilised different pore-level simulations to close these models and include the additional drag terms. They arrived at three different estimates for the drag terms. Pore level simulations may be used to close all these three forms successfully [34]. There is no conclusive judgement as yet, however, as to which one of them is better. Another group of models have been created that did not use the k-ε modeling approach. RSM has been used by Moureh et al. [35], however the model was used without additional porous media terms. It has also been used and mathematically analyzed inside porous media by Mößner and Radespiel [36]. Drouin et al. [37] added two more equations to treat dispersive k and ε separately in addition to the standard macroscopic ones. Kuwata et al. [38] and Kuwata and Suga [39] used a multiscale modeling approach that separated the dispersive, macro and microscopic k and ε treatments within a k and ε approach [38] and a second-moment closure approach [39]. Low Reynolds number approaches were also utilised including the work of Kundu et al. [40] that developed a Lam-Bremhorst version and compared it to DNS data for a pore level study. While these modeling approaches are all successful they are time-consuming due to the additional equations (e.g. RSM and Multiscale models) and/or additional non linearity or

stability effects (e.g. Low-Re-LB) rendering the usual two equation *k*-ε model to be the most versatile in most applications.

A special treatment for coupling turbulence through transition regions between porous and clear fluids is deemed necessary and hence significant research has been carried out to understand the physics of the process and formulation of the necessary transport equations to model it. One approach depends on utilizing different turbulence models for the interface-adjacent air region and the free-stream air region. Kuznetsov [41] utilized dimensionless fully-developed pipe flow equations to represent turbulence for flow around and through a porous layer. A *k*-*l* model was used for the adjacent layer while a *k*-ε model was used in the outer air stream with a suitable compatibility condition in between. The porous region was modeled using the Brinkman-Forchheimer-extended Darcy equation. The same group has also utilised a Cebecci-Smith two-layer model for the two regions [42-43] with dedicating more interest to thermal dispersion effects inside the porous region [43]. One disadvantage was the dependence on dimensionless analytical expressions that made their modeling case-specific and hence not suitable in other CFD studies. Suga and Nichiguchi [44] had a similar approach utilising what is known as an analytical wall-function that carries the effect of roughness and matches the profile on the outside of the porous material to an analytical approximation to the Darcy equation solution inside the porous region. Fetzer et al. [45] resolved the viscous layer around the porous region with sufficient refinement and utilised an algebraic turbulence model (Prandtl mixing length, Han-Van Driest and Baldwin-Lomax) on the outer region. A capillary pressure technique has been used for mass transfer modeling in this work. Another study by Beyhaghi et al. [46] used a three-way coupling approach between a pore-network model inside the porous region, a mass transfer code for the outside of the porous region and an outside solution of flow and turbulence by FLUENT^{TM} [22] with a no-slip condition at the interface. The main disadvantage in all the papers that utilised this approach is a laminar treatment inside the porous region which makes it not suitable when turbulence penetrates a macroscopic interface.

Another group of studies have focused entirely on pore level simulations like bundles of rods [47] or cubic blocks [48] and their interaction with an adjacent fluid region to better

understand the physics of the process without including any interface treatments. The third approach resorted to using both Direct numerical simulations (DNS) through a layer modeled as an inline or staggered cubic blocks/spheres and an adjacent clear fluid region, as well as a continuum modeling approach for the same geometry but with considering a porous media region. Jin and Kuznetsov [49] utilised this approach and then volume- and time-averaged the DNS data to obtain macroscopic results from which they concluded that turbulence scaling is restricted by the pore size and hence, a zero equation model was enough to model turbulence inside the porous region. Breugem and Boersma [50] used the same equations for both porous and fluid regions however they introduced a transition region with a gradient of porosity to induce a gradual change between the two regions and hence, a k-ε interface condition was not necessary in this case. Suga [51] used the same gradual change in porosity with PIV experiments outside the porous region and LES inside of it to develop a four-equation k-ε model [38] and to study the physics of turbulence at the interface. While all of these sophosticated modeling approaches are promising, they are very complex, often case-specific, or require prohibitive refinement for general-purpose CFD. The final approach to be discussed herein was developed by Silva and DeLemos [52]. The model followed on the work of Ochoa-Tapia and Whitaker [53] for velocity at Fluid/Porous interfaces and introduced a continuous flux condition for k and ε to be utilised with a jump coefficient for the momentum transfer [53] and later, DeLemos [54] introduced a jump coefficient for the k and ε as well. The model is absolutely suitable for general purpose CFD and has been used with multiple values of the jump coefficent [54]. However, it has two drawbacks. The first issue is that the modification of turbulence at the interface depends on a jump coefficient that is adjustable and there is no specific guideline on how to estimate it. The second issue is that it is based on an assumption of a highly-permeable porous media. Generally, turbulence inside porous media is important for larger microscales e.g. particle sizes and relatively higher porosities i.e. $\phi > 0.3$. While there is a tendency to neglect turbulence in cases of lower permeabilities and porosities, resolving the decay of turbulence at Fluid/Porous interfaces in these cases is of importance as it affects other physical processes like heat and mass transfer. For low-permeability materials like fruits and vegetables (in drying processes), the interface condition of DeLemos is not necessarily valid since the porosity is of the order of 0.2 and lower [8], resulting in very

low fluid permeability and hence turbulence is expected to decay at the interface which is not considered in the interface model by De Lemos [54].

The present paper aims at extending the Dynamic Coupling technique developed by Elhalwagy and Straatman [8] to handle turbulent flow in addition to the heat and mass transfer capability. This extension is introduced to treat turbulence at the interface and inside Porous materials for cases of high and low permeabilities with implementing a capability to allow turbulence decay at the interface for low permeability media to evolve naturally without an ad-hoc switch off that is not accurate for heat and mass transfer predictions at the interface. The merits of a dynamic coupling approach are: that it is developed to allow the micro- and macroscopic interfaces to react in a physically correct manner to local and temporal changes that happen during different transport phenomena with minimal case-specificity or empiricism; and it lends itself to numerical solution in a reasonable computational time. A full mathematical treatment of the flow, turbulence, heat and mass transfer is described in the next section, and their respective dynamic coupling processes at the microscopic level, i.e. interstitially within the porous media or at the macroscopic level at the Fluid/Porous interface are presented in the following section. This section also includes a new interface turbulence coupling technique that works on high or low permeability porous media (See Fig. 3.1). This is followed by CFD studies for two dimensional channel flow cases with a porous obstruction; testing the different turbulence coupling approaches; followed by the drying of produce slices. An apple slice with a porosity of 0.206 and a potato slice with a porosity of 0.04 are considered.

3.2 Model formulation

The present work utilizes a conjugate flow, heat and mass transfer technique formulated to work simultaneously in fluid/porous/solid regions. The technique solves the conservation of mass, momentum, energy and moisture equations, along with a turbulence model, in the clear fluid and porous regions while considering the local non-equilibrium heat and mass transport inside the porous material as well as conjugate coupling at the macroscopic fluid/porous interface. Turbulence is approximated in the momentum, mass and energy balances using the Boussinesq approach with the use of an eddy viscosity, turbulence

conductivity and turbulence diffusivity, and is modeled using the standard k-ε model. A mixture approach is utilised herein with the fluid considered as moist air (dry air and water vapor). While the system of equations is treated as incompressible, due to the transport of vapor, the technique considers a subtle variation for density ρ_f which does not affect the

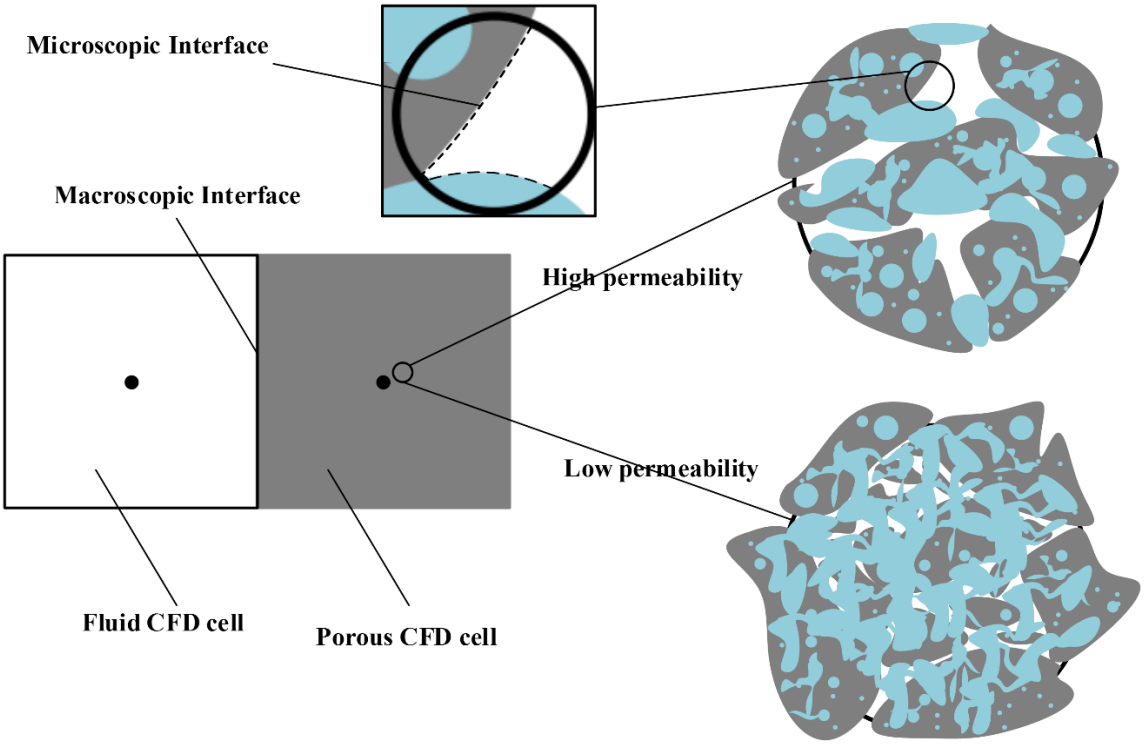

Figure 3.1: Schematic of a Fluid/porous transition showing the differences between a micro- and macroscopic interface and low and high permeability porous regions (moist air is white, liquid is blue and solid is grey).

incompressibility, but is necessary for a moisture transport solution. The vapor moisture is characterised in the mass transfer equations with the local vapor mass fraction Y_v. Thermodynamic relations are used to relate the local pressure P, temperature T, density ρ_f, mass fraction Y_v and relative humidity RH to achieve the necessary coupling [8].

3.2.1 Fluid Region

In a time-averaged framework in the absence of external forces, external heat and mass sources, the clear fluid *point* forms of the mass, momentum, turbulent kinetic energy,

turbulence energy dissipation, moisture and heat transfer equations may be cast, respectively, as:

$$\frac{\partial \overline{\rho_f}}{\partial t} + \nabla \left(\overline{\rho_f}\, \bar{\mathbf{v}} \right) = 0 \tag{3.1}$$

$$\frac{\partial (\overline{\rho_f}\, \bar{\mathbf{v}})}{\partial t} + \nabla \left(\overline{\rho_f}\, \bar{\mathbf{v}}\, \bar{\mathbf{v}} \right) = -\nabla \left(\bar{P} + \frac{2}{3} \overline{\rho_f}\, k \right) + \nabla \left[\left(\mu_f + \mu_t \right) . \left(\nabla\, \bar{\mathbf{v}} + (\nabla\, \bar{\mathbf{v}})^T \right) \right] \tag{3.2}$$

$$\frac{\partial (\overline{\rho_f} k)}{\partial t} + \nabla \left(\overline{\rho_f}\, k\, \bar{\mathbf{v}} \right) = \nabla \left[\left(\mu_f + \frac{\mu_t}{\sigma_k} \right) \nabla\, k \right] + P_k - \overline{\rho_f}\, \varepsilon \tag{3.3}$$

$$\frac{\partial (\overline{\rho_f}\, \varepsilon)}{\partial t} + \nabla \left(\overline{\rho_f}\, \varepsilon\, \bar{\mathbf{v}} \right) = \nabla \left[\left(\mu_f + \frac{\mu_t}{\sigma_\varepsilon} \right) \nabla\, \varepsilon \right] + C_{1\varepsilon}\, P_k \frac{\varepsilon}{k} - C_{2\varepsilon}\, \overline{\rho_f}\, \frac{\varepsilon^2}{k} \tag{3.4}$$

$$\frac{\partial (\overline{\rho_f}\, \overline{Y_v})}{\partial t} + \nabla \left(\overline{\rho_f}\, \overline{Y_v}\, \bar{\mathbf{v}} \right) = \nabla \left[\overline{\rho_f} \left(D_f + \frac{\mu_t}{\overline{\rho_f} Sc_t} \right) \nabla\, \overline{Y_v} \right] \tag{3.5}$$

$$\begin{aligned} &\sum_i c_{p,i} \frac{\partial (\overline{\rho_f}\, \overline{Y_\iota}\, \bar{T})}{\partial t} + \sum_i h_{fg,i} \frac{\partial (\overline{\rho_f}\, \overline{Y_\iota})}{\partial t} \\ &\qquad + \sum_i c_{p,i} \nabla . \left(\overline{\rho_f}\, \overline{Y_\iota}\, \bar{T}\, \bar{\mathbf{v}} \right) + \sum_i h_{fg,i} \nabla . \left(\overline{\rho_f}\, \overline{Y_\iota} \bar{\mathbf{v}} \right) \\ &\qquad = \nabla \left[\left(\lambda_f + \frac{\mu_t c_{p,a}}{Pr_t} \right) \nabla\, \bar{T} \right] \\ &\qquad + \sum_i \nabla . \left[\overline{\rho_f} \left(D_f + \frac{\mu_t}{\overline{\rho_f} Sc_t} \right) (\nabla\, \overline{Y_\iota}) . \left(c_{p,i} \bar{T} + h_{fg,i} \right) \right] + \overline{\rho_f}\, \varepsilon \end{aligned} \tag{3.6}$$

where,

$$\mu_t = C_\mu \overline{\rho_f}\, \frac{k^2}{\varepsilon} \tag{3.7}$$

and,

$$P_k = -\overline{\rho_f}\, \overline{\mathbf{v}' \mathbf{v}'} : \nabla\, \bar{\mathbf{v}} = \mu_t (\nabla\, \bar{\mathbf{v}} + (\nabla\, \bar{\mathbf{v}})^T) : \nabla\, \bar{\mathbf{v}} \tag{3.8}$$

Herein, the 'overbar' signifies time averaging, μ_t is the eddy viscosity and P_k is the turbulence energy production. The use of i represents a species counter, $c_{p,i}$ is the specific heat of species i and is calculated with a reference at 0 °C for water vapor, and $h_{fg,i}$

accounts for the latent heat of vaporization at a reference temperature of 0 °C, which vanishes for dry air. The model constants: σ_k, σ_ε, C_μ, $C_{1\varepsilon}$ and $C_{2\varepsilon}$ take the values of 1, 1.3, 0.09, 1.44, and 1.92, respectively [55], while the turbulent Prandtl Pr_t and Schmidt Sc_t numbers take the values of 0.85 and 0.7 [22], respectively. The model adopts a discretization technique that separates the sensible and latent energies in transient, advective and diffusive terms for the reasons described in detail by Elhalwagy and Straatman [8] and Khan et al [2].

3.2.2 Porous Region

The porous media modelling utilises the theory of volume-averaging by Whitaker [56]. The moist porous material is comprised of a void portion that contains the moist air and a solid portion. Herein, we lump the solid matrix, the free water (i.e. liquid exposed to air) and the bound water (i.e. liquid within the solid's micropores) into the solid portion assuming only one microscopic interface separating the moist air from the solid/water portion [8]. Fig. 3.1 depicts the structure of porous regions and the microscopic interfaces. This approach greatly simplifies the complex equations of the problem. Turbulence modeling of the porous material requires both time- and volume-averaging (i.e. double decomposition) [25] in this case. For a time-averaging process of any instantaneous entity φ, the time-averaged value of this entity over a period of time Δt is given by:

$$\bar{\varphi} = \frac{1}{\Delta t}\int_{t}^{t+\Delta t} \varphi \, dt \tag{3.9}$$

Then one can estimate the time-fluctuation φ' by:

$$\varphi' = \varphi - \bar{\varphi} \tag{3.10}$$

From the volume averaging theory, an average of the entity φ over the volume of an REV (i.e. an extrinsic average) may similarly be defined as:

$$\langle \varphi_x \rangle = \frac{1}{V}\int_{V_x} \varphi_x \, d\, V \tag{3.11}$$

where x is a phase index (here we consider an entity that is relevant only to phase x), V_x is the volume of phase x within the REV and V is the total volume of the REV. Alternatively, by averaging only over the volume of phase x (i.e. an intrinsic average), one arrives at:

$$\langle \varphi_x \rangle^x = \frac{1}{V_x} \int_{V_x} \varphi_x \, d\, V \tag{3.12}$$

It may be noticed from the definition of these averages that the ratio $\langle \varphi_f \rangle / \langle \varphi_f \rangle^f$ defines the porosity ϕ. Similar to time averaging, a spatial-deviation for φ_x may be cast as,

$$\widetilde{\varphi_x} = \varphi_x - \langle \varphi_x \rangle^x \tag{3.13}$$

In order to model the turbulence for porous media, one applies time-averaging followed by volume-averaging, or vise-versa, on the *point instantaneous* form of the relevant transport equations. This process (i.e., the double decomposition) is well-studied by PDL [31], who showed that the order of the averaging processes does not affect the final result. The interest in porous media herein is on intrinsic volume-averages except for the velocity field where an extrinsic average is useful for flow characterisation. In the absence of external forces, external heat and mass sources, the *double-decomposed* forms of the mass, momentum, turbulent kinetic energy, turbulence energy dissipation, moisture mass fractions and energy for the relevant phases are cast, respectively, as:

$$\phi \frac{\partial \langle \overline{\rho_f} \rangle^f}{\partial t} + \nabla \left(\langle \overline{\rho_f} \rangle^f \langle \bar{\mathbf{v}} \rangle \right) = 0 \tag{3.14}$$

$$\begin{aligned} \frac{\partial (\langle \overline{\rho_f} \rangle^f \, \langle \bar{\mathbf{v}} \rangle)}{\partial t} + \frac{1}{\phi} \nabla \left(\langle \overline{\rho_f} \rangle^f \, \langle \bar{\mathbf{v}} \rangle \, \langle \bar{\mathbf{v}} \rangle \right) \\ = -\phi \, \nabla \left(\langle \bar{P} \rangle^f + \frac{2}{3} \langle \overline{\rho_f} \rangle^f \, \langle k \rangle^f \right) \\ + \nabla \left[\left(\mu_f + \mu_t \right) . \left(\nabla \langle \bar{\mathbf{v}} \rangle + (\nabla \langle \bar{\mathbf{v}} \rangle)^T \right) \right] - \frac{\phi \, \mu_f}{K} \langle \bar{\mathbf{v}} \rangle \\ - \frac{\phi \, \langle \overline{\rho_f} \rangle^f c_E}{\sqrt{K}} |\langle \bar{\mathbf{v}} \rangle| \langle \bar{\mathbf{v}} \rangle \end{aligned} \tag{3.15}$$

$$\phi \frac{\partial\left(\langle\overline{\rho_f}\rangle^f \langle k\rangle^f\right)}{\partial t} + \nabla\left(\langle\overline{\rho_f}\rangle^f \langle k\rangle^f \langle\bar{\mathbf{v}}\rangle\right) = \phi\,\nabla\left[\left(\mu_f + \frac{\mu_t}{\sigma_k}\right)\nabla\langle k\rangle^f\right] + \langle\overline{P_k}\rangle - \phi\,\langle\overline{\rho_f}\rangle^f\,\langle\varepsilon\rangle^f + \frac{\phi\, c_k\,\langle\overline{\rho_f}\rangle^f\,\langle k\rangle^f}{\sqrt{K}}|\langle\bar{\mathbf{v}}\rangle| \tag{3.16}$$

$$\phi \frac{\partial(\langle\overline{\rho_f}\rangle^f \langle\varepsilon\rangle^f)}{\partial t} + \nabla\left(\langle\overline{\rho_f}\rangle^f \langle\varepsilon\rangle^f \langle\bar{\mathbf{v}}\rangle\right) = \phi\,\nabla\left[\left(\mu_f + \frac{\mu_t}{\sigma_\varepsilon}\right)\nabla\langle\varepsilon\rangle^f\right] + C_{1\varepsilon}\,\langle\overline{P_k}\rangle\frac{\langle\varepsilon\rangle^f}{\langle k\rangle^f} - \phi C_{2\varepsilon}\,\langle\overline{\rho_f}\rangle^f\,\frac{\langle\varepsilon\rangle^{f\,\mathbf{2}}}{\langle k\rangle^f} + \frac{\phi\, C_{2\varepsilon}\, c_k\,\langle\overline{\rho_f}\rangle^f\,\langle\varepsilon\rangle^f}{\sqrt{K}}|\langle\bar{\mathbf{v}}\rangle| \tag{3.17}$$

$$\phi \frac{\partial\left(\langle\overline{\rho_f}\rangle^f \overline{\langle Y_{v,f}\rangle^f}\right)}{\partial t} + \nabla.\left(\langle\overline{\rho_f}\rangle^f \overline{\langle Y_{v,f}\rangle^f}\langle\bar{\mathbf{v}}\rangle\right) = \nabla.\left(\langle\overline{\rho_f}\rangle^f D_{eff,f}\nabla\overline{\langle Y_{v,f}\rangle^f}\right) + \overline{\langle\dot{m}_{fs}\rangle} \tag{3.18}$$

$$(1-\phi)\frac{\partial\left(\overline{\langle\rho_s\rangle^s}\,\overline{\langle Y_{w,s}\rangle^s}\right)}{\partial t} = \nabla.\left(\overline{\langle\rho_s\rangle^s}\, D_{eff,s}\,\nabla\,\overline{\langle Y_{w,s}\rangle^s}\right) - \overline{\langle\dot{m}_{fs}\rangle} \tag{3.19}$$

$$\sum_i \phi c_{p,i} \frac{\partial\left(\langle\overline{\rho_f}\rangle^f \overline{\langle Y_{\iota,f}\rangle^f}\ \overline{\langle T_f\rangle^f}\right)}{\partial t} + \sum_i \phi h_{fg,i} \frac{\partial\left(\langle\overline{\rho_f}\rangle^f \overline{\langle Y_{\iota,f}\rangle^f}\right)}{\partial t}$$
$$+ \sum_i c_{p,i} \nabla.\left(\langle\overline{\rho_f}\rangle^f \overline{\langle Y_{\iota,f}\rangle^f}\ \overline{\langle T_f\rangle^f} \langle\bar{\mathbf{v}}\rangle\right) + \sum_i h_{fg,i} \nabla.\left(\langle\overline{\rho_f}\rangle^f \overline{\langle Y_{\iota,f}\rangle^f} \langle\bar{\mathbf{v}}\rangle\right)$$
$$= \nabla\left(\lambda_{eff,f}\left(\nabla\ \overline{\langle T_f\rangle^f}\right)\right)$$
$$+ \sum_i \nabla.\left[\langle\overline{\rho_f}\rangle^f D_{eff,f}\left(\nabla\overline{\langle Y_{\iota,f}\rangle^f}\right)\left(c_{p,i}\overline{\langle T_f\rangle^f} + h_{fg,i}\right)\right] \tag{3.20}$$
$$+ \phi\ \langle\overline{\rho_f}\rangle^f\ \langle\varepsilon\rangle^f + h_{fs} A_{fs}\left(\overline{\langle T_s\rangle^s} - \overline{\langle T_f\rangle^f}\right) + \overline{\dot{H}_{fs}^{mass}}$$

$$\sum_i (1-\phi) c_{ps,i} \frac{\partial\left(\langle\overline{\rho_s}\rangle^s \overline{\langle Y_{\iota,s}\rangle^s}\ \overline{\langle T_s\rangle^s}\right)}{\partial t}$$
$$= \nabla\left(\lambda_{eff,s}\left(\nabla\ \overline{\langle T_s\rangle^s}\right)\right)$$
$$+ \sum_i \nabla.\left[\langle\overline{\rho_s}\rangle^s D_{eff,s}\left(\nabla\ \overline{\langle\overline{\rho_s}\rangle^s}\right)\left(c_{ps,i}\overline{\langle T_s\rangle^s}\right)\right] \tag{3.21}$$
$$- h_{fs} A_{fs}\left(\overline{\langle T_s\rangle^s} - \overline{\langle T_f\rangle^f}\right) - \overline{\dot{H}_{fs}^{mass}}$$

where,

$$\mu_t = C_\mu \langle\overline{\rho_f}\rangle^f\ \frac{\langle k\rangle^{f\,\mathbf{2}}}{\langle\varepsilon\rangle^f} \tag{3.22}$$

and,

$$\langle\overline{P_k}\rangle = -\langle\overline{\rho_f}\rangle^f\ \overline{\langle\mathbf{v}'\mathbf{v}'\rangle} :\ \nabla\langle\bar{\mathbf{v}}\rangle = \mu_t(\nabla\langle\bar{\mathbf{v}}\rangle + (\nabla\langle\bar{\mathbf{v}}\rangle)^T) :\ \nabla\langle\bar{\mathbf{v}}\rangle \tag{3.23}$$

where $\langle\ \rangle$ signifies volume averaging. Several additional terms are present in the double-decomposed equations. The last two terms in the momentum equation (Eq. 3.15) are drag terms that carry the effects of the additional porous media resistance to the flow. PDL [31] added a reflection term for this effect in the k and ε equations (last term in Eq. 3.16 and last term in Eq. 3.17). All of the k-ε model constants take the usual values as above [55]. The closure term constant c_k takes a value of 0.28 [31]. Four coupled phase equations for moisture (Eq. 3.18 and 3.19) and heat (Eq. 3.20 and 3.21) are present in the formulation to

carry the effect of local phase non-equilibrium. The vapor fluid mass fraction is defined for a gas mixture approach to be per unit mass of the whole fluid mixture while the water liquid fraction is defined on a dry basis due to the better numerical discretization and stability for this definition [8]. The turbulence energy dissipation term is added to the fluid phase energy equation to reflect the turbulence effect on the temperature field. As the water mechanism of transport inside the porous material is a combination between diffusion, capillary and surface tension phenomena, turbulence inside the solid phase is not considered. To couple these different phase equations, a mass exchange term $\overline{\langle \dot{m}_{fs} \rangle}$ is present in the moisture equations. Also, a sensible energy exchange (i.e. convective) term $h_{fs} A_{fs} \left(\overline{\langle T_s \rangle^s} - \overline{\langle T_f \rangle^f} \right)$, where h_{fs} is a local convective (interstitial) heat transfer coefficient that is evaluated based on a local heat transfer Nusselt number correlation, is added to the energy equations. Another energy coupling term is the latent energy term, $\overline{\dot{H}_{fs}^{mass}}$, which characterizes the enthalpy exchange accompanying mass exchange. These terms are the core of the dynamic coupling process for local microscopic interfaces [8] and will be described in the next section. The effective conductivities and diffusivities represent all the elliptic transport effects that may be lumped inside a diffusion term for the different phases. They contain the effects of diffusion, capillary, surface tension, tortuosity, thermal/mass dispersion, turbulence fluxes (if applicable) and turbulent dispersion effects (if applicable) [8, 34]. They are often functions of both the moisture content and the local temperature. Most of the literature evaluates them as a single quantity based on average measurements or empirical formulae [8] because of the very expensive process to perform non-invasive experiments to predict local and phase specific quantities. Numerical simulations are used to obtain an approximate expression for the individual phases that may be calibrated later to match an experimental trend for the moisture loss process during drying [4, 8].

3.2.3 Fluid/Porous Interface Conditions

In order to reconcile the two different natures of the *point* equation in a clear fluid region with a *Volume-averaged* equation in a porous media region, creative mathematical techniques are devised to satisfy a smooth continuity of the mathematical quantities as well

as achieve a strong and implicit form of numerical coupling across the macroscopic interface i.e. (Fluid/Porous interface) (See Fig. 3.1). The present work builds on the previous works of Betchen et al. [1], Khan et al. [2] and Elhalwagy and Straatman [8] to achieve this purpose for turbulent flow, heat and mass transfer. For velocity, we adopt the extrinsic continuity condition [1] given by,

$$\bar{\mathbf{v}}_{fl} = \langle \bar{\mathbf{v}} \rangle_{por} \tag{3.24}$$

We also adopt the continuity of the intrinsic shear and normal stresses across the interface [1] which are given, respectively, by,

$$(\boldsymbol{n} \,.\, \boldsymbol{t} \,.\, \bar{\tau}\,)_{fl} = (\boldsymbol{n} \,.\, \boldsymbol{t} \,.\, \langle \bar{\tau} \rangle^{f}\,)_{por} \tag{3.25}$$

$$(\boldsymbol{n} \,.\, \boldsymbol{n} \,.\, \bar{\tau}\,)_{fl} = (\boldsymbol{n} \,.\, \boldsymbol{n} \,.\, \langle \bar{\tau} \rangle^{f}\,)_{por} \tag{3.26}$$

While the condition was presented in Betchen et al. [1] for laminar flow, herein, we extend it to turbulent flow as well; i.e., τ here is the total fluid stress tensor including molecular and turbulent diffusive effects. Applying Eqs. 3.25 and 3.26 to Eqs. 3.2 and 3.15 is possible by allowing a fraction ϕ of the total fluid stress from the fluid side to be carried into the fluid portion of the porous side implying that the rest is carried by the solid portion [1]. For low permeability porous media (illustrated in Fig. 3.1), i.e. low porosity foods, the authors could not simplify (Eq. 3.25) further unless by considering a Wall-function-like approach for treating the macroscopic interface (more details will follow in the next section). Following the same approach by Betchen et al. [1], for a highly permeable porous media, (Eq. 3.25) may be simplified as,

$$[\left(\mu_f + \mu_t\right)\left(\frac{\partial \bar{\mathbf{v}}}{\partial \boldsymbol{n}}\right)]_{fl} = [\frac{\left(\mu_f + \mu_t\right)}{\phi}\left(\frac{\partial \langle \bar{\mathbf{v}} \rangle}{\partial \boldsymbol{n}}\right)]_{por} \tag{3.27}$$

(Eqs. 3.24-3.27) are the momentum coupling conditions at the interface. As a result of generalising the form of (Eq. 3.26) to include turbulent flows, following the same approach by Betchen et al. [1], the continuity of the kinematic pressure is intrinsically forced as,

$$(\bar{P} + \frac{2}{3}\overline{\rho_f}\, k)_{fl} = (\langle \bar{P} \rangle^{f} + \frac{2}{3}\langle \overline{\rho_f} \rangle^{f}\, \langle k \rangle^{f})_{por} \tag{3.28}$$

(Eq. 3.28) is utilised as a pressure condition at the interface and is important for pressure-velocity coupling as well. In order to develop a *k*-ε model interface condition that is compatible with the above conditions for velocity and pressure, a similar derivation to De Lemos [54] is carried out starting with (Eq. 3.27) instead of the jump coefficient version for the same equation. For brevity, the final result only is shown here as,

$$[\left(\mu_f + \frac{\mu_t}{\sigma_k}\right)(\frac{\partial k}{\partial \boldsymbol{n}})]_{fl} = [\phi\left(\mu_f + \frac{\mu_t}{\sigma_k}\right)(\frac{\partial \langle k\rangle^f}{\partial \boldsymbol{n}})]_{por} \tag{3.29}$$

$$[\left(\mu_f + \frac{\mu_t}{\sigma_\varepsilon}\right)(\frac{\partial \varepsilon}{\partial \boldsymbol{n}})]_{fl} = [\phi\left(\mu_f + \frac{\mu_t}{\sigma_\varepsilon}\right)(\frac{\partial \langle \varepsilon\rangle^f}{\partial \boldsymbol{n}})]_{por} \tag{3.30}$$

Eqs. (3.29-3.30) represent the turbulence coupling at the fluid/porous interface. For the turbulent mass transfer coupling, we directly adopt the continuity of the diffusion fluxes condition [2, 8] in the time-averaged form which is cast as,

$$\begin{aligned}\left(-\overline{\rho_f}\ \left(D_f + \frac{\mu_t}{\overline{\rho_f} Sc_t}\right)\frac{\partial \overline{Y_v}}{\partial \boldsymbol{n}}\right)_{fl} \\ = \left(-\langle\overline{\rho_f}\rangle^f D_{eff,f}\frac{\partial\overline{\langle Y_{v,f}\rangle^f}}{\partial \boldsymbol{n}} - \langle\overline{\rho_s}\rangle^s D_{eff,s}\frac{\partial\ \overline{\langle Y_{w,s}\rangle^s}}{\partial \boldsymbol{n}}\right)_{por}\end{aligned} \tag{3.31}$$

For heat transfer, we adopt the continuity of the sum of the sensible and latent energy fluxes [8] given in the time averaged frame by,

$$\left(-\left(\lambda_f+\frac{\mu_t c_{p,a}}{Pr_t}\right)\left(\frac{\partial\,\bar{T}}{\partial \boldsymbol{n}}\right)-\sum_i\left[\overline{\rho_f}\left(D_f+\frac{\mu_t}{\overline{\rho_f}Sc_t}\right)\left(\frac{\partial \bar{Y}_i}{\partial \boldsymbol{n}}\right)\left(c_{p,i}\,\bar{T}+h_{fg,i}\right)\right]\right)_{fl}$$
$$=\left(-\lambda_{eff,f}\frac{\partial\overline{\langle T_f\rangle^f}}{\partial \boldsymbol{n}}\right.$$
$$-\sum_i\left[\langle\overline{\rho_f}\rangle^f D_{eff,f}\left(\frac{\partial\overline{\langle Y_{i,f}\rangle^f}}{\partial \boldsymbol{n}}\right)\left(c_{p,i}\,\overline{\langle T_f\rangle^f}\right.\right. \tag{3.32}$$
$$\left.\left.+h_{fg,i}\right)\right]-\lambda_{eff,s}\frac{\partial\overline{\langle T_s\rangle^s}}{\partial \boldsymbol{n}}$$
$$\left.-\sum_i\left[\langle\overline{\rho_s}\rangle^s D_{eff,s}\left(\frac{\partial\overline{\langle Y_{i,s}\rangle^s}}{\partial \boldsymbol{n}}\right)\left(c_{ps,i}\overline{\langle T_s\rangle^s}\right)\right]\right)_{por}$$

Eqs. (3.31-3.32) close the macroscopic interface conjugate coupling process with the mass and heat transfer conditions, respectively. Implementation and discretization to achieve the above conditions will be discussed in a subsequent section.

3.3 Extended dynamic coupling models

After presenting the conjugate modeling framework and the mathematical conditions for the macroscopic coupling of the different regions, this section focuses on the dynamic treatment for different closure and exchange terms interstitially and macroscopically involving turbulence, heat and mass transfer. The interest herein is directed to the interstitial closure for heat and mass transfer, the macroscopic *k*-ε model coupling across macroscopic interfaces for high and low permeability porous interfaces and the turbulent heat and mass transfer circuit analogues for macroscopic coupling. When combining these dynamic models with the formulation in section 3.2, a full model for non-equilibrium turbulent flow, heat and mass transfer is achieved, which is suitable for use with different drying problems.

3.3.1 Interstitial closure for heat and mass transfer

Herein, due to the similarity between the laminar and turbulent description of the interstitial closure terms and their implementation, a concise treatment will be presented. The

interested reader is encouraged to look up all the details of the derivation and implementation in the work of Elhalwagy and Straatman [8].

Considering mass transfer, there are two main modes describing the process. Either, the mass transfer is *convectively dominant* [8] in which enough liquid water is present inside the solid constituent of the porous region and, hence, the moisture capacity of the fluid constituent and its capability to withdraw vapor moisture is the controlling factor. Or, drying out is imminent and the solid constituent is starting to run out of water, and hence the controlling factor is the availability of liquid water and the ability of the solid constituent to supply it to the interstitial interface to be convected as vapor to the fluid constituent. This second mode is termed as *diffusively dominant* [8]. We will state the equations for the mass exchange closure term $\overline{\langle \dot{m}_{fs} \rangle}$ for each case. In our in-house code, a check is performed within the non-linear loop to determine the lower amount of mass exchange from both expressions (i.e. the rate determining value) and the result is implemented implicitly to control convergence [8]. This technique eliminates the need for specification of an empirical threshold in which a predetermined amount of moisture inside CFD cells is chosen to separate convective from diffusive dominance transport.

Convective dominance

$$\overline{\langle \dot{m}_{fs} \rangle} = \langle \overline{\rho_f} \rangle^f h_{fsm} A_{fs} \frac{\ln(1+B)}{B} \left(\frac{\overline{\langle Y_v \rangle^{fs}} - \overline{\langle Y_{v,f} \rangle^f}}{1 - \overline{\langle Y_v \rangle^{fs}}} \right) \tag{3.33}$$

where h_{fsm} is an interstitial mass transfer coefficient estimated with a local mass transfer Sherwood number correlation, B is the Spalding mass transfer number which is equal to the last bracket on the RHS of Eq. 3.33 and $\overline{\langle Y_v \rangle^{fs}}$ is the vapor mass fraction at the interstitial interface and is evaluated based on the relative humidity of the air adjacent to the interface (i.e. Water activity [8]) and the temperature of the interface $\overline{\langle T_s \rangle^s}$.

Diffusive dominance

$$\overline{\langle \dot{m}_{fs} \rangle} = \langle \bar{\rho}_s \rangle^s \frac{D_{eff,s}}{\delta_{diff.}} A_{fs} \overline{\langle Y_{w,s} \rangle^s} \quad , \quad \delta_{diff.} = \frac{d_p}{Sh} \left(\frac{1-\phi}{\phi} \right)^{1/3} \tag{3.34}$$

where $\delta_{diff.}$ is a significant liquid-in-solid diffusion thickness [8] and $\frac{d_p}{Sh}$ is the drying boundary layer thickness (i.e. the porous media particle diameter over the Sherwood number).

Now we shift our attention to the heat transfer closure term $\overline{\dot{H}_{fs}^{mass}}$. This term is an enthalpy exchange term that accounts for the energy accompanying the mass flux $\overline{\langle \dot{m}_{fs} \rangle}$ as it leaves the solid phase to the fluid phase. For convectively dominant mass transfer, liquid is available at the surface of the solid constituent and hence, the vaporization energy is withdrawn from both phases in different proportions [8]. An apportioning factor α is evaluated based on a local Biot number Bi to determine, based on the capability of the fluid flow to convect heat in comparison to the capability of the solid phase to conduct heat, the fraction of transported vapor that absorbed its latent energy from the solid portion. The rest of the transported vapor absorbs its latent energy from the fluid constituent. As for diffusively dominant mass transfer, the surface of the solid constituent is deemed dry. Thus, the latent energy is totally apportioned to the solid constituent, i.e., α = 1. Based on the above description, $\overline{\dot{H}_{fs}^{mass}}$ is given by [8],

$$\overline{\dot{H}_{fs}^{mass}} = \overline{\langle \dot{m}_{fs} \rangle}\left[\alpha \overline{h_v}\left(\overline{\langle T_s \rangle^s}\right) + (1-\alpha)\overline{h_l}\left(\overline{\langle T_s \rangle^s}\right)\right] \tag{3.35}$$

where h_v is the absolute enthalpy of water vapor and h_l is absolute liquid water enthalpy. The model for the mass enthalpy exchange is capable to treat evaporative cooling as well as drying due to the generic form of Eq. 3.35 that allows a dynamic applicability [8].

3.3.2 Turbulence coupling across macroscopic interfaces

This subsection is dedicated to the interface *k*-ε model treatment. It is well reported in the literature that *k*-ε models are not suitable on their own to characterize turbulence transport very close to walls [55]. Due to the steep gradients of turbulent quantities very near to the viscous sublayer and the presence of the viscous sublayer itself which cannot be resolved by Reynolds-averaged turbulence modeling. At a Fluid/Porous interface while the conditions of the turbulent coupling were carefully selected to ensure a stable and reasonable treatment of the *k* and ε, they apply the usual form of the *k*-ε model on both sides of the interface and hence, they cannot resolve the blockage and shear wall-like effects. For low porosity materials (i.e. $\phi = 0.2$ or lower) the interface should behave from the clear fluid side, in turbulence modeling, similar to a wall. As for the porous side, while

it is common to neglect the void space in this porosity range and treat the material as totally solid, we choose to treat this side as porous for the following reasons. The first one is the fact that vapor diffusion plays a significant role for some low porosity materials, e.g. De Bonis and Ruocco [10] and Van Belleghem et al. [13]. Instead of lumping the liquid and vapor in one equation to represent total moisture, separation in two equations is more physically correct in this case. So while the inside convection may not be important, the diffusion for vapor is important and hence the formulation should allow a continuum of fluid to be present across both clear fluid and porous regions. The second reason is the fact that porosity changes occur during drying in a lot of cases. So as a first step to include a spatial and temporal porosity gradient into a model, one should be able to treat low and high porosity materials with porous media modeling so that later a model that includes shrinkage and porosity gradients may switch between low and high porosity numerical treatments dynamically during solution. The third reason actually relates to developing a more generic coupling approach for turbulence. It is expected that Eqs. 3.29-3.30 may behave very well in high porosities, i.e. $\phi > 0.3$, as it is a very close approach to the work of De Lemos [52, 54] that has been widely used in the literature. At very low porosities $\phi < 0.1$, a wall function approach is expected to be more accurate. Between both regimes neither of the approaches alone is expected to be accurate and a hybrid approach should be the best in that case. The present approach is a first step towards achieving that. Now we consider a wall-function-like approach to treat the first row of CFD cells in the clear fluid region that is adjacent to the macroscopic interface. Since the pressure-velocity coupling technique [1] requires sufficient grid refinement at the macroscopic interface, a standard wall function approach was deemed not suitable due to its restriction on refinement. An enhanced wall-like treatment is developed in the present work. The treatment has multiple features taken from different sources and is modified to be compatible with a low-permeability porous media rather than a wall. To be able to discuss the enhanced wall-like treatment approach, we revert back to some basic definitions for wall functions. In order to generally describe the profiles of turbulence and velocity in the interface-adjacent region, dimensionless definitions have to be stated. The dimensionless interface-distance y^+ and dimensionless shear velocity u^+ are given, respectively, by [55, 22],

$$y^+ = \frac{\overline{\rho_f}\, {C_\mu}^{1/4} k^{1/2} y}{\mu_f} \quad , \quad u^+ = \frac{u - u_{int.}}{u^*} \tag{3.36}$$

where y is the distance between the geometric center of the first clear fluid CFD cell that is adjacent to the macroscopic interface and the interface itself, u is the shear-component velocity value at the same CFD cell (i.e. parallel to the interface), $u_{int.}$ is the slip-shear-component velocity at the interface (i.e. at the integration point for the same CFD cell). u^* is the friction velocity [55, 22] which also takes these definitions with the widely known approximations of turbulent boundary layer flows,

$$u^* = -\overline{u'v'}^{1/2} = (\frac{\tau_{int.}}{\overline{\rho_f}})^{1/2} = {C_\mu}^{1/4} k^{1/2} \tag{3.37}$$

where $\tau_{int.}$ here is the interface shear stress. In order to establish a valid interface k-ε model treatment, a modification for the definition of turbulent viscosity μ_t near the interface needs to be described. One assessed approach was the introduction of a two-layer model (i.e. a viscosity affected layer and a fully turbulent layer) with introducing a blending function in-between [22]. Because of the complexity of velocity and turbulence transport near the interface (i.e. a two sided coupling rather than a usual one sided coupling for walls), the introduction of two expressions and their blending may cause stability problems and hence the approach was not utilised in the present work. Analytical wall function (AWF) [57, 44] was also assessed. Its eddy-viscosity expression was deemed suitable herein however, the use of integration was avoided as the form of the exact integrable equations affects stability as well [57, 44]. A ramp distribution of turbulent viscosity near the interface is adopted. The expression after being adapted to our definitions in Eqs. 3.36-3.37 may be wrote as,

$$\mu_t = \mu_f\, {C_\mu}^{\frac{3}{4}} C_l (y^+ - 5) \tag{3.38}$$

where $C_l = \frac{\kappa}{{C_\mu}^{3/4}} = 2.55$ [57,44]. The expression was originally developed for the turbulent region (i.e. $y^+ > 5$). We generalise the expression here with setting a suitable lower bound as will be shown shortly. To seek easy implementation, Eq. 3.38 is recast in the following form,

$$\mu_t = C_\mu \overline{\rho_f}\,\frac{k}{\boldsymbol{\tau}} \quad , \quad \boldsymbol{\tau} = \frac{\overline{\rho_f}\,k}{\mu_f\,\eta} \quad , \quad \eta = C_\mu^{\frac{-1}{4}}\,C_l(y^+ - 5) \tag{3.39}$$

where $\boldsymbol{\tau}$ is the reciprocal of the turbulent time scale and has a definition of, $\boldsymbol{\tau} = \frac{\varepsilon}{k}$ for interior CFD cells to be equivalent to Eqs. 3.7 and 3.22. The parameter η is another dimensionless length scale. A lower bound is selected for μ_t for prevention of negative values based on Eq. 3.38, ($\mu_t \geq 0.1\mu_f$) and this condition is achieved for $\eta \geq 1$. This length scale condition extends the validity of Eq. 3.39 for the different wall function regions. For the turbulent layer (i.e. $y^+ > 5$), the turbulence energy dissipation of the clear fluid interface CFD cell is forced explicitly as [22],

$$\varepsilon = \frac{k^{3/2}}{C_l\,y} \tag{3.40}$$

At this point, a definition for the dimensionless velocity profile needs to be introduced. Instead of breaking the profile into a viscous layer ($u^+ = y^+$), a buffer layer and a log law layer ($u^+ = \frac{1}{\kappa}\ln(y^+) + E$) [55], we introduce the single expression of Kader [58, 22] which represents a single function for all the regions as,

$$u^+ = e^{\Gamma}y^+ + e^{1/\Gamma}\left(\frac{1}{\kappa}\ln(y^+) + E\right) \quad , \quad \Gamma = \frac{-0.01{y^+}^4}{1 + 5y^+} \tag{3.41}$$

Equation 3.41 allows the turbulent energy production for a clear fluid interface CFD cell in the fully turbulent region to be cast as,

$$P_k = \overline{\rho_f}\,{u^*}^2\frac{\partial u}{\partial y} = \overline{\rho_f}^2\left(\frac{u - u_{int.}}{u^+}\right)^2\frac{{C_\mu}^{1/2}k}{\mu_f}\frac{\partial u^+}{\partial y^+} \tag{3.42}$$

Equation 3.42 provides a stable implementation for the explicit P_k term where u^+ and $\frac{\partial u^+}{\partial y^+}$ are evaluated based on (Eq. 3.41). For the viscous sublayer (i.e. $y^+ < 5$), the turbulence energy production $P_k$vanishes [57, 44]. As for the dissipation ε, the exact approximation for the famous low Reynolds number term [59] is forced explicitly as,

$$\varepsilon = \frac{\mu_f}{\overline{\rho_f}} \left(\frac{\partial k^{1/2}}{\partial y}\right)^2 \approx \frac{2\mu_f k}{\overline{\rho_f}\, y^2_{viscous\ edge}} \approx \frac{2}{25} C_\mu^{\frac{1}{2}} \frac{\overline{\rho_f}}{\mu_f}\, k^2 \tag{3.43}$$

Where the viscous edge is assumed at $y^+ = 5$. In our in-house code, switching between expressions for the two regions is decided based on a check of the dimensionless interface distance that occurs within the non-linear CFD loop. Now, we shift our attention to the interface shear stress $\tau_{int.}$ and the reflection of the enhanced wall-like treatment on the interface velocity condition. Based on Eq. 3.41, one may cast the interface shear stress as,

$$\tau_{int.} = \mu_t \frac{\partial u}{\partial y} = \overline{\rho_f} C_\mu^{\frac{1}{2}} \frac{\mu_t}{\mu_f} k \frac{\partial u^+}{\partial y^+} \tag{3.44}$$

Equation 3.44 does not offer the best numerical stability and may be cast for the interest of simplification and implicit implementation as,

$$\tau_{int.} = \overline{\rho_f} u^* u^* = \overline{\rho_f} \left(C_\mu^{\frac{1}{2}} \frac{\mu_t}{\mu_f} k \frac{\partial u^+}{\partial y^+}\right)^{1/2} \frac{(u - u_{nb})}{u^+} \tag{3.45}$$

where u_{nb} is the neighboring CFD cell shear velocity (i.e. porous cell on the other side of the macroscopic interface). Figure 3.2 illustrates the coupling process. The leading term in Eq. 3.45 may be thought of as a modified CFD diffusion influence coefficient. The standard way to implement the interface velocity condition in our in-house code is to use harmonic mean formulation [1] to implement Eq. 3.27. This is generalized whether the porous region is considered of high or low permeability. For low permeability, we keep this standard approach, however, we also implement Eq. 3.45 implicitly based on Eq. 3.25 using the necessary apportioning of the shear stress based on porosity as mentioned earlier. Then, we correct for the difference of the two expressions explicitly. In a high permeability porous media case, all of the above equations for wall-like treatment are switched off leaving the standard condition of Eq. 3.27 and the usual *k*-ε model discretization alone as they are enough to characterize the coupling process in this case. In regards to heat and mass transfer treatments for wall-like behavior, we defer the discussion to the next subsection.

3.3.3 Turbulent heat and mass transfer circuits for macroscopic coupling

The present subsection extends the macroscopic interface heat and mass transfer coupling approach that was developed in the work of Elhalwagy and Straatman [8] to include turbulence effects. The coupling approach depends on utilizing heat and mass transfer circuit analogues [8] to couple one equation in the fluid side to the two non- equilibrium equations in the porous side. Before introducing the circuit analogues, we will introduce the wall-like treatment for heat and mass transfer.

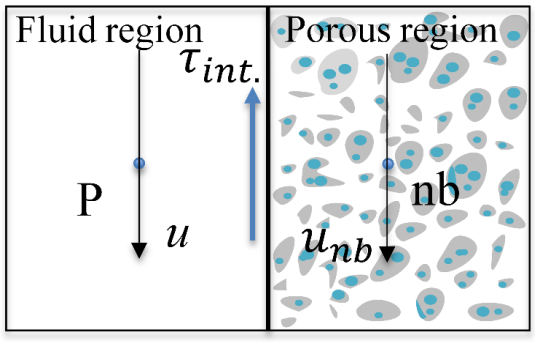

Figure 3.2: Shear stress at a macroscopic interface.

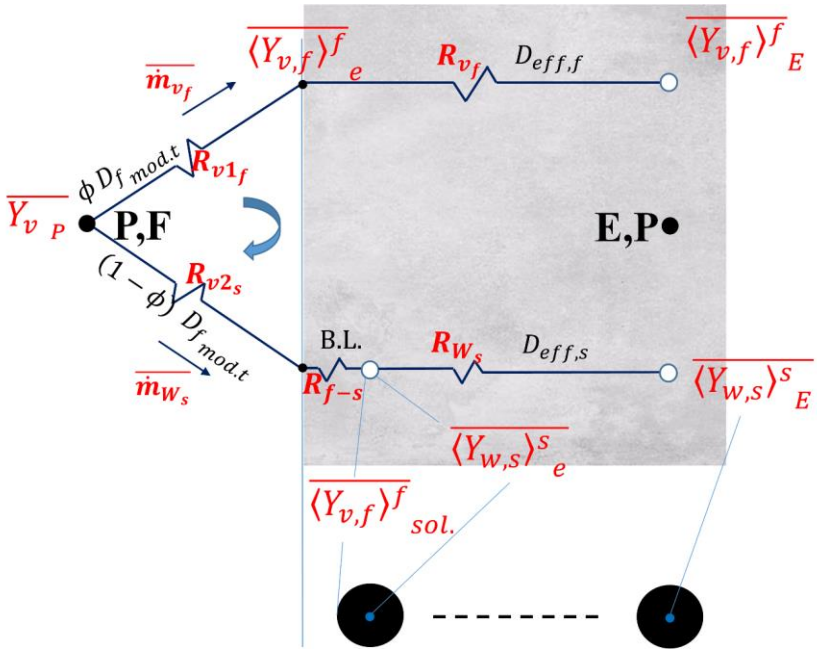

Figure 3.3: Moisture resistance analogue for the macroscopic interface.

We will consider the clear fluid CFD cell adjacent to the macroscopic interface as above. The dimensionless T^+ and dimensionless $Y_v{}^+$ are defined [22], respectively, by,

$$T^+ = \frac{(\bar{T} - \bar{T}_{int.})\overline{\rho_f} c_{pa} u^*}{q''_{int.}} \quad , \quad Y_v{}^+ = \frac{(\bar{Y}_v - \bar{Y}_{v_{int.}})\overline{\rho_f} u^*}{J''_{v_{int.}}} \tag{3.46}$$

where $\bar{T}_{int.}$ is the macroscopic interface temperature, $\bar{Y}_{v_{int.}}$ is the vapor mass fraction at the interface and $q''_{int.}$and $J''_{v_{int.}}$are the total interface heat and mass transfer fluxes, respectively, that represent the sum of the contributions from the two resistance legs as shown in Fig. 3.3. Unlike the explicit implementation for the velocity treatment, we will treat the heat and mass transfer wall-like treatment implicitly in order not to complicate the resistance circuit implementation. The diffusion terms over the entire heat and mass transfer discretization are treated using the harmonic mean formulation [1], therefore, we can use different conductivities and diffusivities between adjacent fluid CFD cells. Thereby, we decompose $q''_{int.}$and $J''_{v_{int.}}$ to define a modified conductivity $\lambda_{f_{mod.t}}$and diffusivity $D_{f_{mod.t}}$ for the interface-adjacent clear fluid CFD cell as,

$$q''_{int.} = -\lambda_{f_{mod.t}} \frac{\partial \bar{T}}{\partial y} \quad , \quad J''_{v_{int.}} = -\overline{\rho_f} D_{f_{mod.t}} \frac{\partial \bar{Y}_v}{\partial y} \tag{3.47}$$

Inserting Eq. 3.47 and Eq. 3.36 into Eq. .3.46, we arrive at these definitions for the modified conductivity and diffusivity,

$$\lambda_{f_{mod.t}} = \mu_f c_{pa} \frac{y^+}{T^+} \quad , \quad D_{f_{mod.t}} = \frac{\mu_f}{\overline{\rho_f}} \frac{y^+}{Y_v{}^+} \tag{3.48}$$

Now, we define two analogues for Eq. 3.41 to represent temperature and mass fraction wall-like profiles [58, 22] , respectively, as,

$$\begin{aligned} T^+ &= e^{\Gamma_{HT}}\, T^+{}_{lam.} + e^{1/\Gamma_{HT}}\, T^+{}_{turb.} \\ &= e^{\Gamma_{HT}}\, Pr\, y^+ + e^{1/\Gamma_{HT}}\, Pr_t \left(\frac{1}{\kappa} \ln(y^+) + E + \mathrm{P}_{HT} \right) \end{aligned} \tag{3.49}$$

$$Y_v{}^+ = e^{\Gamma_{MT}}\, Sc\, y^+ + e^{1/\Gamma_{MT}}\, Sc_t \left(\frac{1}{\kappa}\ln(y^+) + E + \mathrm{P}_{MT}\right) \tag{3.50}$$

where P_{HT} and P_{MT} are functions of the ratios Pr/Pr_t and Sc/Sc_t, respectively [22] and are evaluated here as -1.546 and -0.9494, respectively. The profile exponents are given by,

$$\Gamma_{HT} = \frac{-0.01\,(Pr\, y^+)^4}{1 + 5\, Pr^3 y^+} \quad , \quad \Gamma_{MT} = \frac{-0.01\,(Sc\, y^+)^4}{1 + 5\, Sc^3 y^+} \tag{3.51}$$

Using Eqs. 3.48-3.51, one can evaluate $\lambda_{f_{mod.t}}$ and $D_{f_{mod.t}}$ for low permeability interfaces. For high permeability materials they are defined as $(\lambda_f + \frac{\mu_t c_{p,a}}{Pr_t})$ and $(D_f + \frac{\mu_t}{\overline{\rho_f} Sc_t})$, respectively (i.e. equivalent to definitions for effective conductivity and diffusivity of interior fluid CFD cells).

Now we shift our attention to the circuit analog for moisture. Fig. 3.3 depicts the circuit for a Fluid cell (P) and a neighboring porous cell (E) at its east face, separated by integration face 'e'. The following description will be concise and, if interested, the reader may look up the full details in Elhalwagy and Straatman [8]. The fluid leg of the resistance is identical to the laminar version [8] with substituting the molecular diffusivity D_f with $D_{f_{mod.t}}$. For the solid leg we introduce some changes to the three resistances, R_{v2_s}, R_{f-s} and R_{W_s}. The main resistances $R_{v2_s}$and R_{W_s} may be given as,

$$R_{v2_s} = \frac{\Delta x_{Pe}}{\overline{\rho_f}_P (1-\phi) A_e D_{f_{mod.t}}} \quad , \quad R_{W_s} = \frac{\Delta x_{eE}}{\langle \overline{\rho_s} \rangle^s{}_E A_e D_{eff,s}} \tag{3.52}$$

Equation 3.52 retains its form for both modes of mass transfer. For the convectively dominant mode of mass transfer, the availability of liquid in the solid is high as it supplies vapor based on the capacity for clear fluid side. Thus, R_{f-s} is mainly based on a boundary layer expression similar to Eq. 3.33 in which the vapor-saturated surface of a wet particle at the interface supplies vapor to the clear fluid integration face. For low permeability porous media, as the solid side is filled with water, this vapor diffusion through the

boundary layer is assumed laminar since turbulent is highly unlikely to disperse inside such a densely packed region. Based on these assumptions, $R_{f-s_{conv.}}$ may be cast as,

$$R_{f-s_{conv.}} = \frac{d_P B_{interf.}(1 - \overline{\langle Y_{v,f}\rangle^f}_{sol.})}{\overline{\rho_f}_P(1-\phi)A_e D_f Sh_{interf.}\, ln(1+B_{interf.})} \tag{3.53}$$

Equation 3.53 may also be used for high permeability materials with substituting D_f with $D_{f_{mod.t}}$. Regarding the diffusively dominant mode of mass transfer, the interface particle surface is deemed dry as the liquid is scarce in this mode and the capability to diffuse it is rate-limiting. In this case, R_{f-s} represents a vapor diffusion layer within the solid constituent. The expression is similar to Eq. 3.53 since we assume a diffusivity for vapor that is based on the same length scale as the drying boundary layer [8]. As the liquid in the solid region is scarce, turbulence is considered to be a vapor diffusion enhancement factor [8]. $R_{f-s_{diffus.}}$ is cast as,

$$R_{f-s_{diffus.}} = \frac{d_p/Sh_{interf.}}{\overline{\rho_f}_P(1-\phi)A_e D_{f_{mod.t}}} \tag{3.54}$$

In order to implement Eqs. 3.52-3.54, we use the concept of the phase ratio [8] to ensure the continuity of the mass flux exchange across the macroscopic interface. Defining the phase ratio K as,

$$\mathrm{K} = \frac{\overline{\langle\rho_s\rangle^s}_E D_{eff,s}\overline{\langle Y_{w,s}\rangle^s}_e}{\overline{\rho_f}_P(1-\phi)D_{f_{mod.t}}\overline{\langle Y_{v,f}\rangle^f}_{sol.}} \tag{3.55}$$

one may utilise the harmonic mean formulation to express the mass flux through the solid leg for convectively dominant cases as,

$$\overline{\dot{m}_{W_s}} = \frac{A_e(\overline{\langle\rho_s\rangle^s}_E D_{eff,s}\overline{\langle Y_{w,s}\rangle^s}_E - \mathrm{K}\,\overline{\rho_f}_P(1-\phi)D_{f_{mod.t}}\overline{Y_v}_P)}{\mathrm{K}\left(\Delta x_{Pe} + \frac{d_P B_{interf.}\left(1-\overline{\langle Y_{v,f}\rangle^f}_{sol.}\right)}{\zeta\, Sh_{interf.}\,\ln(1+B_{interf.})}\right) + \Delta x_{eE}} \tag{3.56}$$

where $\zeta = 1$ for highly permeable material and $\zeta = D_f / D_{f_{mod.t}}$ for low permeability materials. While Eq. 3.55 is valid for both modes of mass transfer, the implemented form for diffusively dominant mass transfer may be given as [8],

$$\mathrm{K} = 1 - \frac{1}{1 + \dfrac{\langle \overline{\rho_s} \rangle^s{}_E D_{eff,s} \overline{\langle Y_{w,s} \rangle^s{}_e}}{\overline{\rho_f}_P (1-\phi) D_{f_{mod.t}} \overline{\langle Y_{v,f} \rangle^f}_e}} \tag{3.57}$$

The solid leg mass flux for diffusively dominant mass transfer is also given by,

$$\overline{\dot{m}_{W_s}} = \frac{A_e (\langle \overline{\rho_s} \rangle^s{}_E D_{eff,s} \overline{\langle Y_{w,s} \rangle^s}_E - \mathrm{K}\, \overline{\rho_f}_P (1-\phi) D_{f_{mod.t}} \overline{Y_v}_P)}{\mathrm{K} \left(\Delta x_{Pe} + \dfrac{d_P}{Sh_{interf.}} \right) + \Delta x_{eE}} \tag{3.58}$$

To determine the mode of mass transfer we depend on a check that is performed within the non-linear CFD loop [8] which is based on,

$$\begin{aligned} \overline{\dot{m}_{W_s}} &= \frac{\overline{\rho_f}_P (1-\phi) D_{f_{mod.t}} A_e (\overline{\langle Y_{v,f} \rangle^f}_{sol.} - \overline{Y_v}_P)}{\Delta x_{Pe} + \dfrac{d_P B_{interf.} \left(1 - \overline{\langle Y_{v,f} \rangle^f}_{sol.}\right)}{\zeta\, Sh_{interf.} \ln(1 + B_{interf.})}} \\ &= \frac{\langle \overline{\rho_s} \rangle^s{}_E D_{eff,s} A_e (\overline{\langle Y_{w,s} \rangle^s}_E - \overline{\langle Y_{w,s} \rangle^s}_e)}{\Delta x_{eE}} \end{aligned} \tag{3.59}$$

Equations 3.55-3.59 represent a complete implementation technique for the solid leg mass transfer coupling process. In regards to heat transfer, Eq. 3.32 is decomposed into two balances. The first balance is conductive and represents sensible energy and the second balance is diffusive based on latent energy fluxes [8]. A resistance analogue for conduction across the macroscopic interface is utilised to ensure the equality of conduction fluxes leaving/entering the clear fluid side with their counterparts that are entering/leaving the porous side. The implementation follows identically the description of Betchen et al. [1]. Herein, we substitute the molecular conductivity on the pure fluid side with the turbulent-affected conductivity $\lambda_{f_{mod.t}}$. As for the mass exchange enthalpy balance, it is given by [8],

$$\overline{\dot{H}^{mass}_{fs_{macro.}}} = \left\|\overline{\dot{m}_{W_s}}.\overline{h^{S}_{fs_{macro.}}}\right\|.\boldsymbol{n} = \left\|\overline{\dot{m}_{W_s}}.\overline{h^{f}_{fs_{macro.}}}\right\|.\boldsymbol{n} \tag{3.60}$$

and is implemented explicitly as,

$$\overline{\dot{H}^{mass}_{fs_{macro.}}} = \overline{\dot{m}_{W_s}}\left[\alpha_{interf.}\overline{h_v}\left(\overline{\langle T_s\rangle^s}_e\right) + (1-\alpha_{interf.})\overline{h_l}\left(\overline{\langle T_s\rangle^s}_e\right)\right] \tag{3.61}$$

where in a similar manner to Eq. 3.35, $\alpha_{interf.}$=1 for diffusively dominant interfaces and is evaluated based on an interface Biot number otherwise [8].

3.4 Verification

The complete formulation presented in sections 3.2 and 3.3 is implemented in our conjugate in-house code [1-2, 8]. The model is the first of its kind and is one of the very few models in the literature that treats conjugate flow, turbulence, heat and mass transfer simultaneously utilizing porous media modeling. This section is concerned with verification of the turbulence coupling approaches that were presented in subsection 3.3.2, followed by turbulent heat and mass transfer verification for the drying of apple and potato slices. Apple and potato are chosen as verification cases because they represent moderate (apple) and low (potato) porosity materials that facilitate verification of the turbulence model enhancements; and, they are both water-filled so convection involves both heat and mass transfer. In the first subsection we introduce the properties and relations necessary to characterize apple and potato flesh as porous media. This is followed in the remaining sections by verification of the turbulence and mass transfer models by studying the drying of the two produce slices.

3.4.1 Porous media properties for Apples and Potatoes

All the properties for apples are adopted from [8, 4] and presented in Table 1. We will mainly direct our attention towards potatoes as it is a lower-porosity flesh and, consequently, a low-permeability porous media. Thermophysical properties of individual phases, internal geometric parameters and closure coefficient estimates are of interest.

Srikiatden and Roberts [60] reported the densities of the solid matrix inside a potato ρ_{st} and the density of liquid moisture ρ_w as 1480 and 1020 kg/m^3, respectively where the densities here are defined based on phase specific volumes. Our density of interest $\langle\bar{\rho_s}\rangle^s$ is defined per unit volume of the solid/water mixture (i.e. the solid matrix density multiplied by the solid volume fraction inside the solid/water constituent). We assume the initial moisture concentration $\langle Y_{w,s}\rangle^s{}_{init.}$ inside the potato slice as 4.886 kg liquid per kg of dry solid [12]. In order to estimate the specific phase volume fractions within the solid/water constituent, we consider the following definitions [4, 60],

$$\langle Y_{w,s}\rangle^s{}_{init.} = \frac{\alpha_w \rho_w}{\alpha_{st}\rho_{st}} \quad , \quad \alpha_w\rho_w + \alpha_{st}\rho_{st} = \frac{1 + \langle Y_{w,s}\rangle^s{}_{init.}}{\frac{1}{\rho_{st}} + \frac{\langle Y_{w,s}\rangle^s{}_{init.}}{\rho_w}} \tag{3.62}$$

Solving Eq. 3.62, we estimate the phase specific volumes and $\langle\bar{\rho_s}\rangle^s$ as reported in Table 3.1. Krokida and Maroulis [61] recorded the porosity values for different produce during different types of drying processes as they vary for different moisture contents. Herein, we adopt their porosity recording for the corresponding moisture content as above in a convective drying process and we fix it through the drying process. As for the thermal conductivity we adopt a value of 0.551 W/m.K [12] for the whole potato slice and we use the porosity to apportion it on the different phases [8, 4]. We also adopt a potato specific heat value of 3778 J/kg.K [12] and use the solid matrix volume fraction to evaluate the solid portion specific heat [8, 4]. In order to estimate the particle diamater d_P, we use a suggestion by Feng et al. [62] to utilize the parenchyma cell size as a measure for the particle diameter where the parenchyma cell surface area is about 1/54.8 mm^2 for potatoes [63]. The permeability K is evaluated using the famous Ergun equation [64] and the interfacial surface area per unit volume A_{fs} is evaluated as $6(1-\phi)/d_P$ [8]. Table 3.1 summarizes all the properties of interest except for the phase diffusivities as we consider them to be functions of the moisture ratio as reported in section 3.4.3.

Table 3.1: Properties of Potatoes and Apples as Porous materials.

	Potato	Apple

Porosity, ϕ	0.04	0.206
Permeability, K (m^2)	$1.12x10^{-14}$	$8.89x10^{-13}$
Forchheimer Coefficient, c_E	0.244	0.244
Specific interfacial surface area, A_{fs} (m^{-1})	37775.6	11650
Average Particle diameter, d_p (μm)	152.4	103
Solid matrix volume fraction, α_{st}	0.1236	0.0689
Liquid volume fraction, α_w	0.8764	0.9311
Dry Solid density, $\langle\rho_s\rangle^s$ (kg/m^3)	182.96	124.85
Initial liquid moisture content, $\langle Y_{w,s}\rangle^s{}_{init.}$(kg Liq./kg dry solid)	4.886	7.45
Dry Solid specific heat, c_{ps} (J/kg.K)	467	252
Solid effective thermal conductivity, $\lambda_{eff,s}$ (W/m.K.)	0.5287	0.3335
Fluid effective thermal conductivity, $\lambda_{eff,f}$ (W/m.K.)	0.0223	0.0865

3.4.2 Two dimensional simulation of turbulent flow around a porous obstruction

This section considers the flow of air around and through a porous obstruction from the point of view of hydrodynamics. The high and low permeability macroscopic interface treatments are tested using the hydrodynamic representation of Apple and Potato slices, respectively. The numerical setup is comprised of a parallel-walled channel of 1 m in length (L) and 0.09 m in height (H) in which a 0.3 x 0.03 m^2 (i.e. l x h) porous obstruction is centered (see Fig. 3.4). The flow is two-dimensional in nature and hence a very small depth (1 mm) for this setup is utilized with symmetry boundary conditions to enable the use of the three dimensional in-house code. A uniform mesh of 90 x 40 x 1 was deemed sufficient based on a less than 2% grid independence with respect to the overall pressure drop for a base case of 2 m/s inlet velocity; i.e. corresponding to a Reynolds number of 4000. Figure 3.4 shows the numerical setup for the channel. At the inlet ($x = 0$) a uniform velocity U_{in} is imposed (with zero transverse components) and pressure is extrapolated from the domain interior. An inlet turbulence intensity of 2.5 % and a turbulence length scale of 0.0063 m (i.e. 0.07 H) were used to specify k and ε at the inlet [22]. At the outlet ($x = L$), outflow boundary conditions are used wherein zero-gradients are forced for all quantities except for the pressure which is set as atmospheric. A no slip condition was imposed at the lower and upper channel walls ($y = 0$, $y = H$) utilizing an enhanced wall treatment (EWT) technique, i.e. a refinement-free technique similar to the low-permeability macroscopic interface coupling presented earlier, but for walls utilizing a zero-gradient boundary condition for turbulent quantities, and pressure extrapolation. All steady state solutions were achieved using a non-iterative time advancement technique. Turbulence production was controlled using Menter's limiter [65, 22] only early in the transient whenever the velocity gradients evolution was numerically unstable.

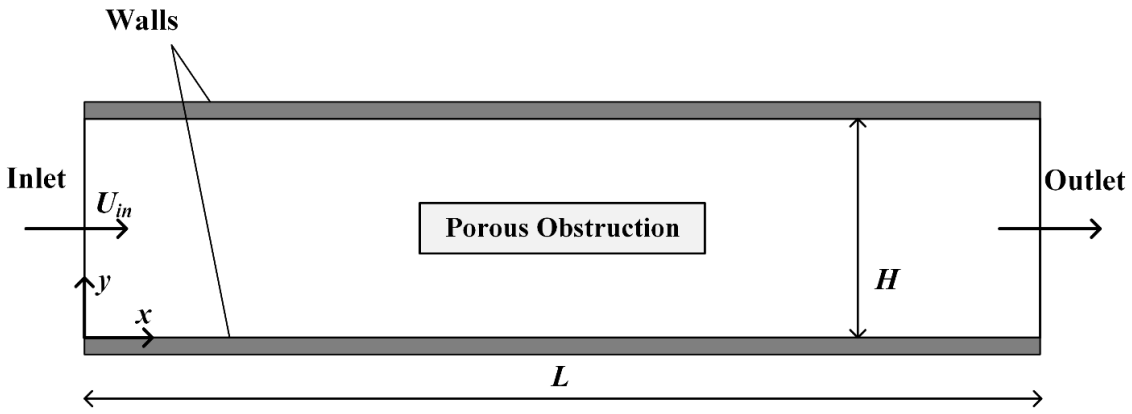

Figure 3.4: 2D flow numerical setup around and through a porous obstruction.

The purpose of this section is specifically to show how the enhanced wall-like treatment is necessary for low permeability fluid/porous interfaces by physically analyzing the turbulent flow behavior at the fluid/porous interface with and without it. The interface conditions for turbulent fluxes remain the same as given by Eqs. 3.29-3.30 for both cases. Figure 3.5 depicts the dimensionless pressure contours (normalized by $\rho_f U_{in}^2$) for a U_{in} = 2 m/s inlet velocity case using apple and potato properties. The results are very similar in terms of pressure for inclusion or lack of the use of EWT and hence we only report the case of an EWT. A gradual decline of pressure through the channel is shown with an impingement high pressure region at the porous upstream interface for both cases. One may notice two low-pressure leading edge regions as well indicating an acceleration of the flow around the upstream of the porous region that characterizes the separation/reattachment behavior. It is also observed that the impingement pressure is higher in the case of the potato properties due to the very low porosity/permeability. In general, the contours show physically reasonable behavior that is well established in the literature and very similar to flows around a solid obstruction because of the low permeabilities for both cases. This is the case regardless of whether an EWT was utilized or not, giving credence to the EWT approach and the fact that it does not cause any negative effect on the pressure behavior. It is also established in the present work that the pressure velocity coupling technique that was originally introduced by Betchen et al. [1], is numerically robust for high Reynolds numbers (herein it was tested for up to 20000), turbulent flows and very low permeability porous media.

Now, we turn our attention to the velocity contours and stream lines in Figs. 3.6-3.7. Figure 3.6 shows the axial velocity contours for a U_{in} = 2 m/s case. Both interface coupling techniques predict low velocity values inside the porous region that are on the orders of 10^{-7}-10^{-10} m/s, which is compatible with the low permeabilities considered. The two major features of such a flow in RANS modelling are the back recirculation zone and the separation/reattachment near the leading edge and both behaviors are captured herein. The EWT approach predicts longer and more developed back recirculation regions and more obvious negative velocity regions close to the leading edge, which characterizes the separation bubble. The sizing of the back recirculation is comparable to the work of Ateeque et al. [12]. The no-EWT approach under-predicts the size of both regions. The values for maximum velocities are generally higher in a no-EWT approach which suggests that the approach under-predicts the skin shear of the porous material and the overall drag on the flow. A case of higher porosity and permeability, 0.32 and 4.21 x 10^{-12}, respectively, were also considered herein to study the behavior for slightly more permeable materials. Such properties could be representing carrots for example [66]. While not given in figures, the contours show the same behavior as for apples with more pronounced acceleration around the porous slice and lesser size for the back recirculation zone. This case shows that the high permeability approach is suitable and numerically robust as well for relatively higher permeability materials.

A closer look may be taken by the stream lines for the hydrodynamic behavior of the problem in Fig. 3.7. The figure confirms the conclusions drawn from the contour plots. A well-developed back recirculation region may be observed for the EWT approach. The separation bubble interacts with the weak flow inside the porous region to form two back flow regions that are present across the macroscopic shear interfaces on the sides of the porous slice. Also, any weak penetration of the flow on the impingement face is drawn by the negative pressure points near the separation bubbles to exit the slice from the sides and join the accelerating flow. The separation bubble is very weak for the no-EWT approach and is not showing in the stream lines as it is very thin in this case and altered by the side exiting flow mentioned earlier. The back recirculation is weakly represented as well due to the faster acceleration of the flow around the slice that prevents forming a better development for the back wake. One may comment that a *k*-ω SST model may predict

better behavior for the separation/reattachment flow [12, 14], however it will require a different sophisticated technique for an EWT and will also require a different interface flux coupling for turbulence. We may also mention that no closed version for a porous media *k*-ω SST model is available in the literature to the best of the authors' knowledge. It is expected that the major features will remain the same with a *k*-ω SST model because of the lack of proper representation for a wall-like porous material in any interface flux coupling technique that is available.

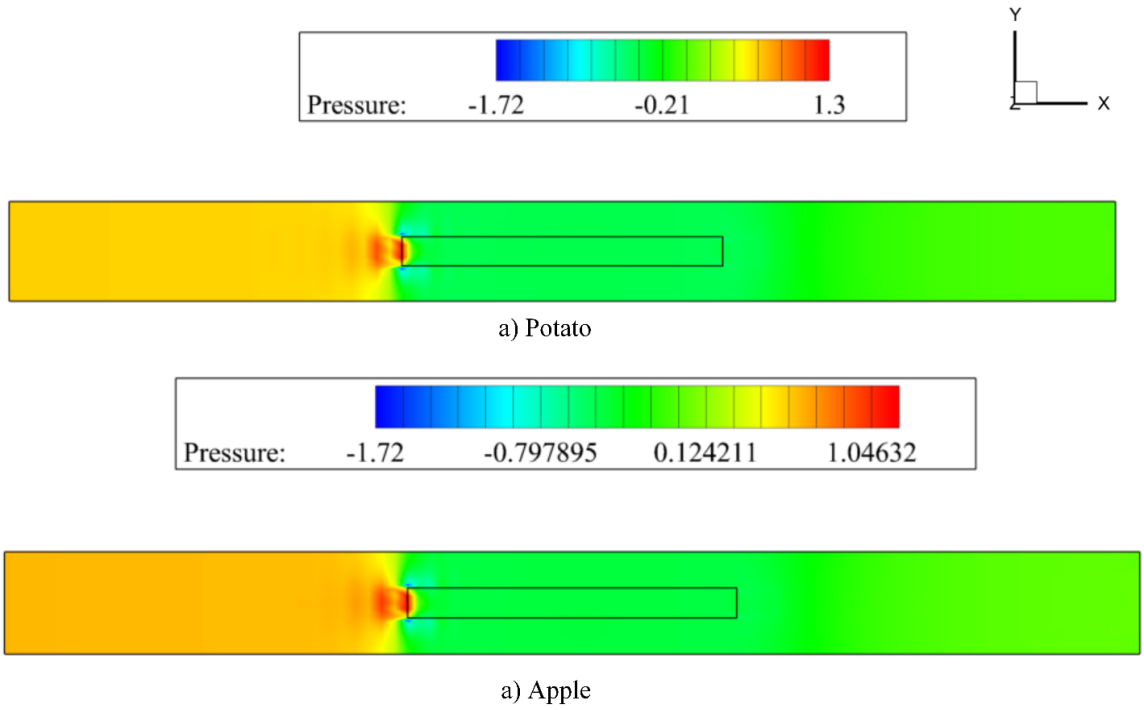

Figure 3.5: Normalized pressure contours for a 2 m/s flow over Potato and apple porous obstructions with the use of EWT.

The two back flow regions in the middle section of the slice are also absent herein as a slightly more permeable behavior of the porous media is noticed with a fraction of the penetrated flow traveling through the porous slice. Figures 3.8-3.9 depict the contours for normalized TKE and its dissipation for the 2 m/s case where TKE is normalized as $\langle k \rangle^f / U_{in}^2$ and the turbulence dissipation is normalized as $\langle \varepsilon \rangle^f h / U_{in}^3$. The major feature in the contours is the dissipation of turbulence at the EWT-interface and not allowing penetration inside the porous regions, which is physically correct, as the porous material

with as low a permeability behaves essentially for turbulence as a wall where any weak fraction of the flow that dissipates inside is laminar. Using a no-EWT treatment results in incorrect penetration for turbulence inside the porous region. The legends of the figures depicts a normalized value for turbulence and hence while the value is small for a no-EWT technique, it still represents considerable penetration of turbulence. The rest of the physical turbulence behavior shown in the contours is typical in which a growth of turbulence at the edge of the wall boundary layers starts developing along the channel, an impingement generation is observed at the upstream face and a shear and back recirculation turbulence for the porous region is generated that disperses and transports along the downstream section. The figures also show a higher generation of turbulence for relatively higher permeability; i.e., the apple case which is physically reasonable.

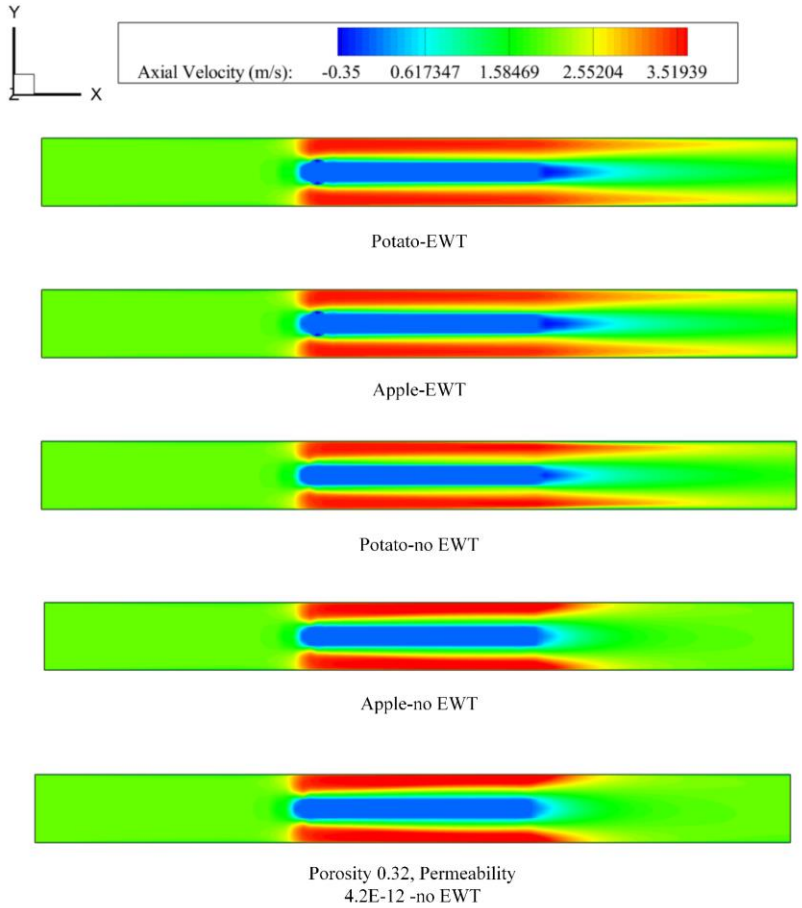

Figure 3.6: Axial velocity contours for a 2 m/s flow for cases of different porous properties and different interface treatments.

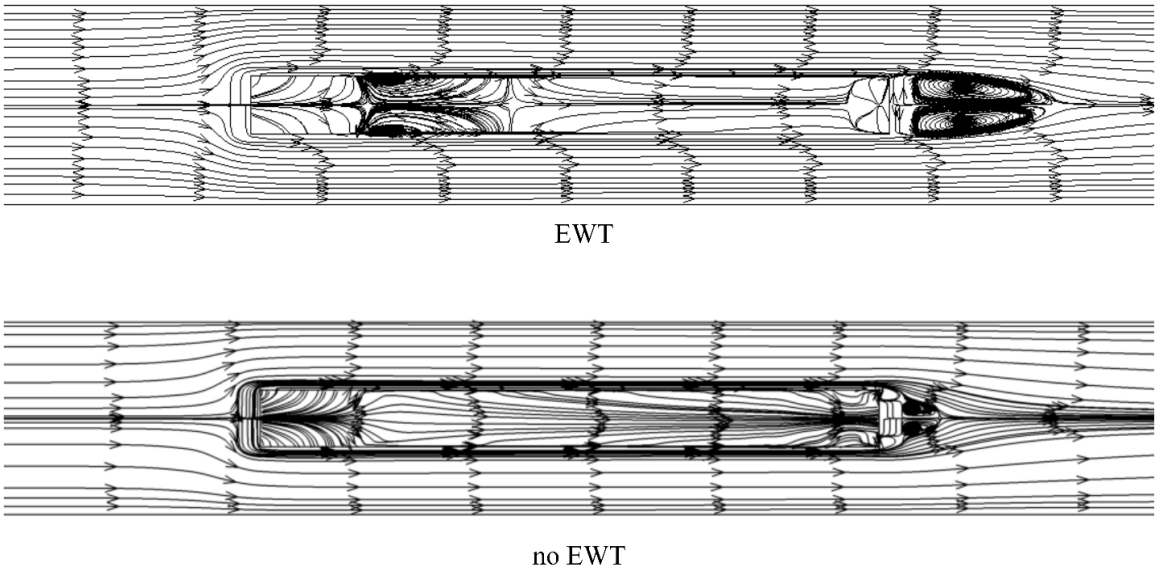

Figure 3.7: Streamlines for a flow of 2 m/s for Potato properties.

Figure 3.10 shows the flow and turbulence behavior for an EWT potato case of high velocity; i.e., U_{in}=10 m./s and Reynolds number of 20000. The physical features observed earlier are all preserved in this high velocity case indicating that the coupling holds well numerically and physically for higher Reynolds numbers and the unrealistic penetration of turbulence is not allowed to evolve.

It is also interesting to compare the two techniques of the interface coupling quantitatively. Following the same representation as De Lemos [54], the magnitude of the extrinsic velocity vector $|\langle\bar{\mathbf{v}}\rangle|$, normalized TKE and its dissipation are plotted transversely in Fig. 3.11 at an axial location of 0.75 l of the porous region where the flow shear at the interface is the main physical effect; i.e., away from recirculations and back flows, in order to produce results that are analogous to De Lemos's [54] for the interface coupling with different values of the turbulence jump coefficients.

The results for the case of no-EWT, in terms of the velocity, TKE and its dissipation, match the trends obtained by De Lemos [54] qualitatively for cases of zero or positive turbulence jump coefficients. Interestingly the case of EWT shows a behavior that is close to the negative jump coefficients coupling for De Lemos [54]. The sign of the jump coefficient

may be interpreted as the sign of the direction showing higher diffusion of the turbulence; i.e., for positive jumps, the diffusion is enhanced towards the porous region while for negative jumps, the diffusion is inhibited towards the porous region. In cases where an EWT is used, the turbulence diffusion is reduced to laminar as we consider flow near the interface; i.e. a boundary layer behavior and hence in terms of jump coefficients, it may be thought of as an explicit technique to include the physics of a negative jump coefficient.

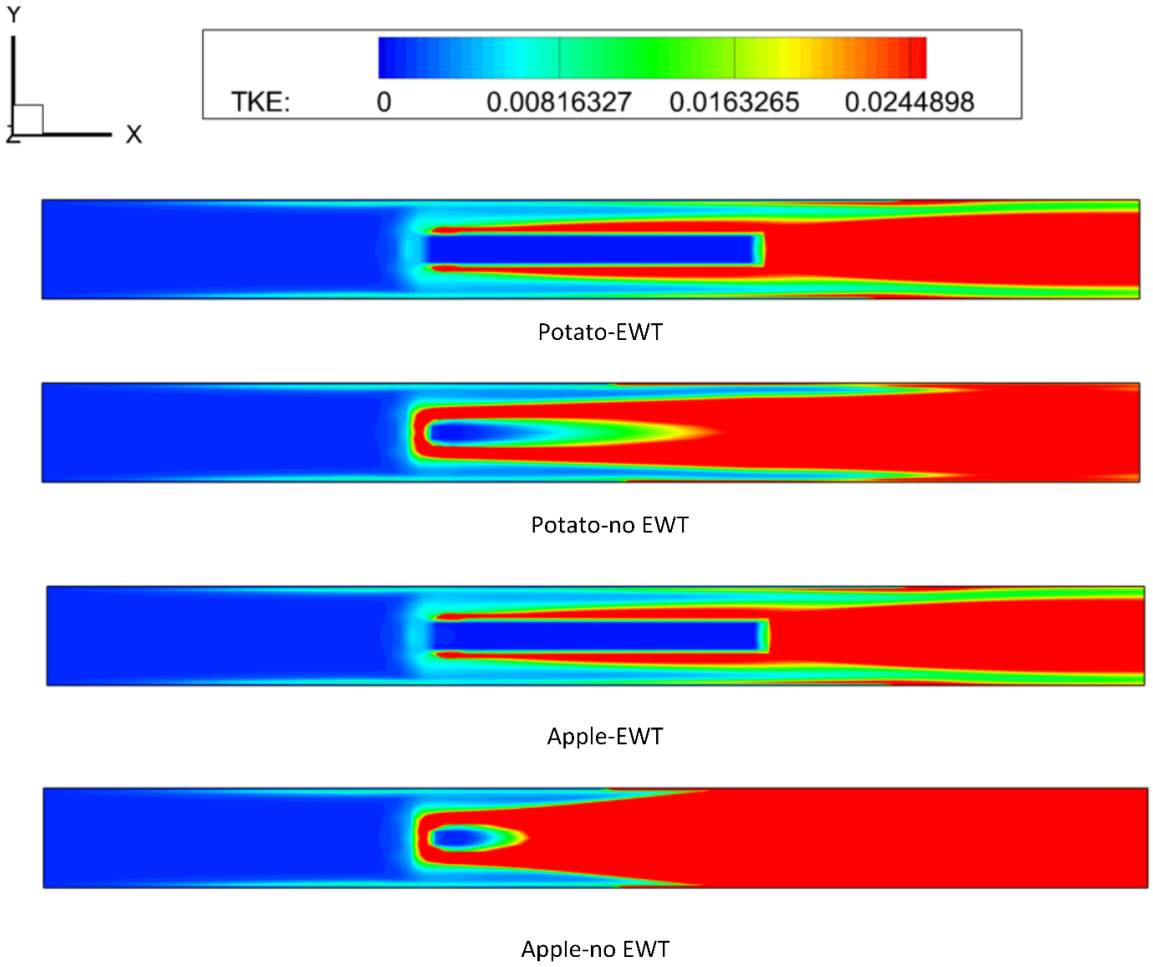

Figure 3.8: Normalized TKE contours for a flow of 2 m/s with different porosities and interface treatments (Scale is cut of above the reported maximum to show the penetration/dissipation of turbulence).

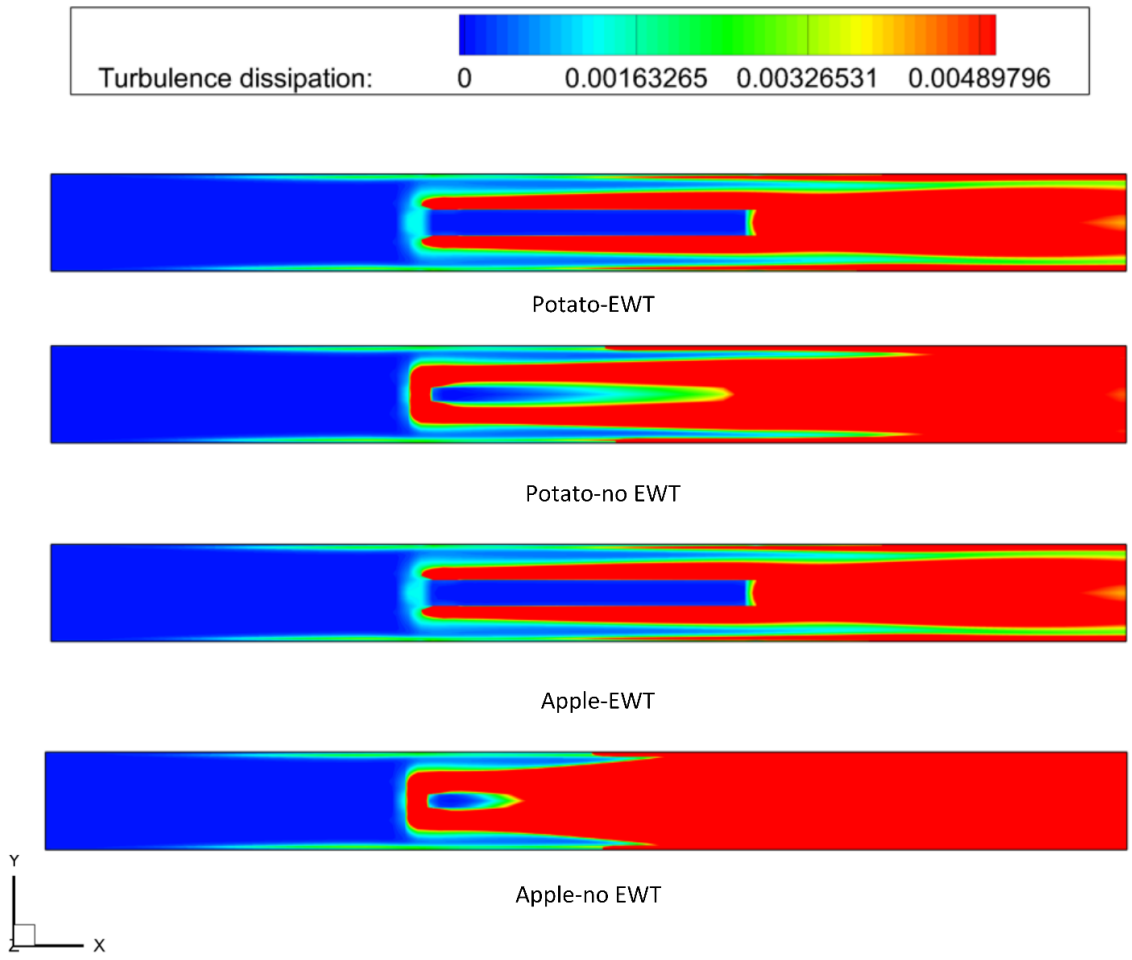

Figure 3.9: Normalized turbulence dissipation contours for a flow of 2 m/s with different porosities and interface treatments (Scale is cut of above the reported maximum to show the penetration/dissipation of turbulence).

The advantage here would be that it does not require an empirical specification. For the velocity, a turbulent boundary layer profile is observed as we consider clear fluid flow near the interface for an EWT technique. The shear is also higher in this case, which is compatible with a very low permeability; i.e., wall-like material. Consequently, further from the interface in the clear fluid side, the velocity profile for a no-EWT case shows over-predicted velocity values. In regards to turbulence profiles, a peak is observed close to the interface where the production and dissipation are at their highest. The values of both decay fast as we consider clear fluid flow further from the interface in an EWT, while they remain high and decay slowly for no EWT. The first behavior is dominated by wall-like

behavior for turbulent flows in the literature and is considered physically correct for a low permeability material, while the second behavior may be observed for a more permeable material. It is also pronounced in Fig. 3.11 that turbulence does not penetrate the interface for a low permeability material. One also observes that the profile of TKE does not follow exactly that of a negative jump coefficient profile in the work of De Lemos [54]. In a negative jump TKE profile, the decay of TKE as we consider clear fluid flows further from the interface maintain the same concaved shape while herein for an EWT, an inflection point may be observed at about y/h of 0.87. Consequently, one may conclude that the EWT may not be substituted by the use of a turbulence jump coefficient. One may conclude from the above discussion that the approach of macroscopic interface coupling using an EWT is numerically and physically robust and produces correct physical behavior. It is understood that an experimental validation of the technique is necessary and of great importance however herein the focus is directed to the different physical behaviors for different permeability values and interface treatments and resolving them numerically. It is also worth to mention that to date, to the best of the authors' knowledge, no general validation experiment for turbulent macroscopic interface coupling is available.

3.4.3 Turbulent convective drying of potato and apple slices

This section is concerned with verification of the turbulent heat and mass transfer capability of the dynamic coupling model. A conjugate fluid/porous case that involves both microscopic and macroscopic interface treatments is considered for different materials of low porosity and permeability, namely, potato and apple slices. The macroscopic interface is mainly subjected to diffusively dominant mass transfer. The numerical setup is directly adopted from the works of Elhalwagy and Straatman [8] and Khan and Straatman [4]. A 20 x 20 x 5 mm^3 rectangular produce slice is placed in an air stream for convective drying. A quarter of the slice is considered herein with two symmetry slice-cutting faces at $y = 0$ and $z = 0$. Figure 3.12 depicts the numerical setup. The domain is conjugate as it considers both the porous produce and the air surrounding the slice. A 30 × 20 × 20 computational mesh of Cartesian cells with refinement towards all fluid/porous interfaces is utilized [8, 4].

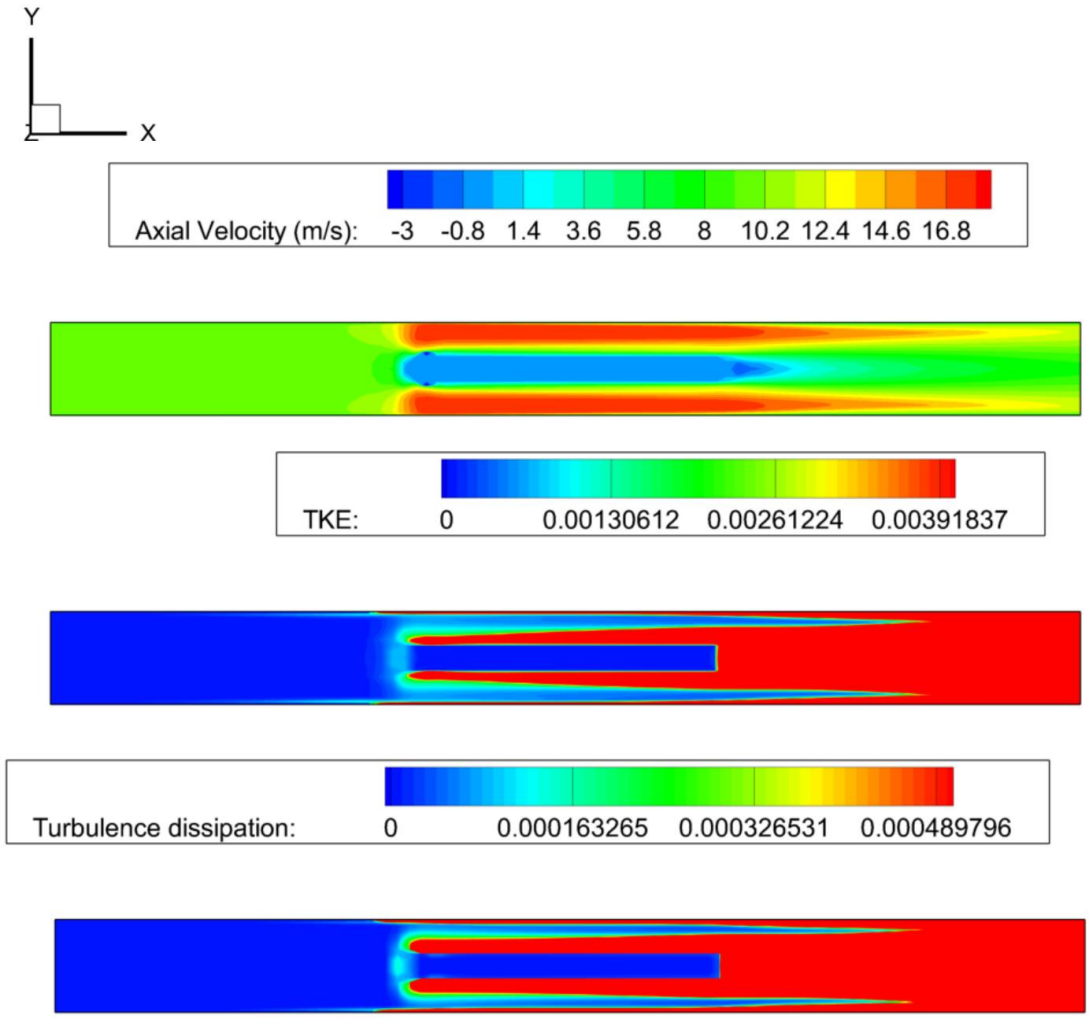

Figure 3.10: Velocity and turbulence contours of an EWT potato case of 10 m/s (Scale is cut of above the reported maximum to show the penetration/dissipation of turbulence).

An air stream with U_{in} = 4 m/s, 2.5% turbulence intensity, 70°C and 4% relative humidity is considered, where the slice is initially at 20°C with a uniform 4.886 kg/kg d.s. for Potato and 7.45 kg/kg d.s. for apple. A time step of 2 seconds is utilized that initially varies between 0.0005 and 2 s through the early transient for turbulence production control and heat and mass transfer stability purposes. A non-iterative time advancement was utilized to stabilize the hydrodynamics in the beginning, followed by switching on the heat and mass transfer solver. An iterative-implicit time marching technique for resolving all the equations for the drying transient is then utilized. At the inlet (x = 0), a uniform velocity,

temperature and relative humidity is set. Turbulence is set using the turbulence intensity and length scale technique [22] and pressure is extrapolated. At the outlet ($x = L$), a zero gradient condition is set for all quantities except for pressure, which is set as atmospheric. On the symmetry planes ($y = 0$ and $z = 0$), all quantities had a zero gradient specified except for normal velocity that is of zero value. For other boundary faces, a slip condition is utilized with zero gradients for all quantities except for an extrapolated pressure. All utilized porous media properties are adopted from Table 3.1.

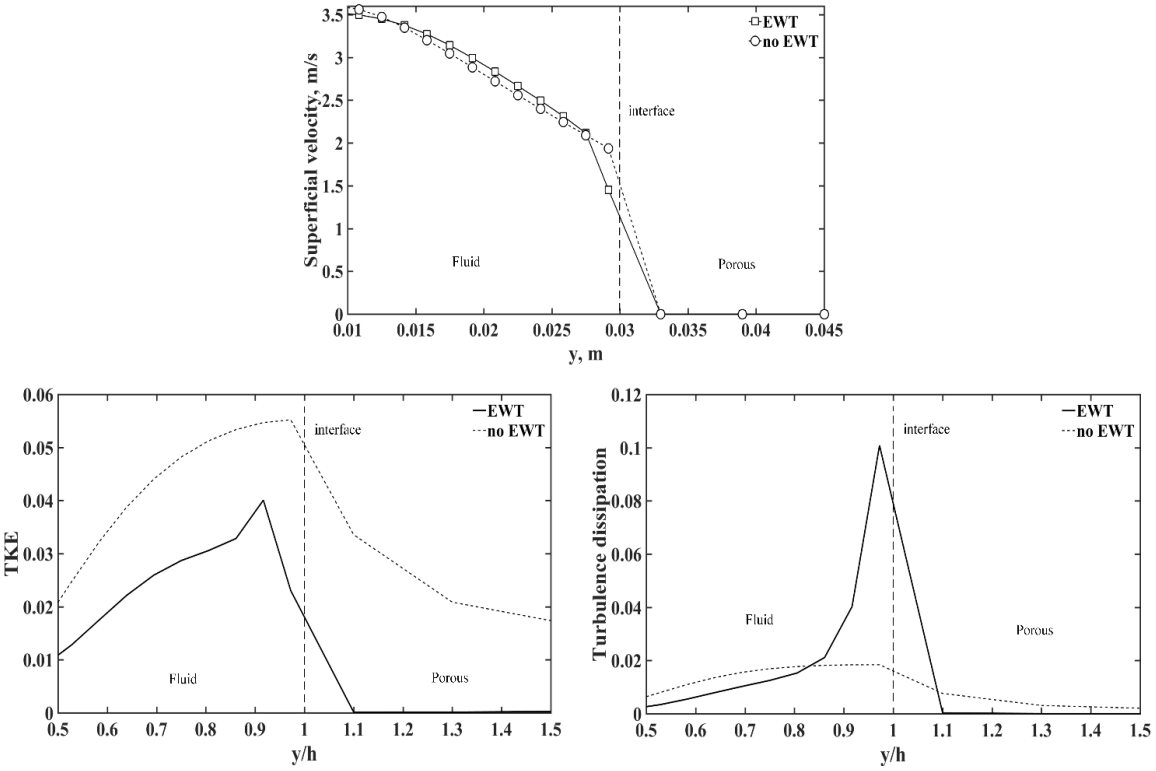

Figure 3.11: Transverse profiles for flow and turbulence across the shear macroscopic interface for x=0.75 l along the porous slice for a 2m/s potato case and different interface treatments.

The model has been tested for different velocities and has shown numerically stable and physically reasonable behavior. In terms of turbulence, the model also showed the same behavior as discussed in subsection 3.4.2, in which turbulence is not penetrating the slice for the enhanced treatment case for the potato slice, while the apple case with no EWT showed some penetration of turbulence to the inside of the flesh. The purpose of this

subsection is to establish the capability of the model for achieving reasonable prediction of the physics of heat and mass transfer for turbulent flows qualitatively, i.e. from a phenomenological point of view in which the physical behavior and trends are reasonably justified. In order to successfully predict the heat and mass transfer field, material diffusivities are needed as an input. Numerical simulations were carried out to provide an estimate of the variable diffusivities for the potato slice for laminar flow using the experiment by Srikiatden and Roberts [67] and utilizing the same technique for estimating the diffusivities described by Elhalwagy and Straatman [8] and Khan and Straatman [4]. Preliminary trends were obtained by accurately matching the drying simulation trend of the moisture ratio (i.e. instantaneous overall moisture content/ initial moisture content) versus time to the experimental data. The laminar diffusivities of the apple slice is directly adopted from Elhalwagy and Straatman [8].

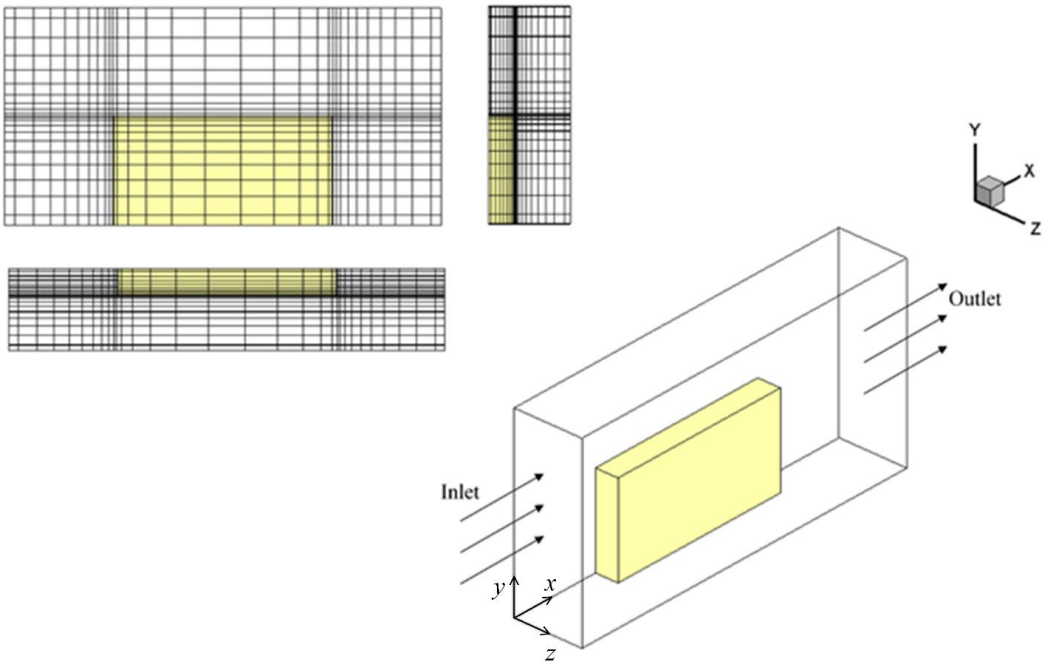

Figure 3.12: Numerical setup for turbulent convective drying of a slice of produce.

Herein, due to the effects of turbulence penetration in the case of the apple slice i.e. no EWT, and in the fluid side of the interface for the potato EWT case, these diffusivities were not utilized without modifications as in this case they should include the turbulence fluxes and dispersion effects. Following a sensitivity analysis approach for modifying the

diffusivities, we were able to arrive at a suitable estimate based on enhancing the diffusion by using a multiplier. It is common in the literature to perform these sensitivity studies and investigate the effect of different diffusivity trends on the final result [68-69]. It has also been concluded [68-69] that the qualitative physical trending and phenomena are not affected by the values of the diffusivities however quantitative differences occur in this case. It is stated herein that the utilized diffusivities are not to be considered material properties but are close estimates for the purpose of the present work. Figure 3.13 depicts the diffusivities variation with the moisture ratio for apple and potato simulations. Both trends are similar to the ones reported in the literature [8, 68-69] and they show higher values for the diffusivities which are introduced as a representation for turbulence effects. Figure 3.14 depicts the moisture ratio plotted against simulation time. While both trends show consistence with reports in the literature the potato case trend is highly diffusive as the process, as shown later, is more affected by diffusion inside the slice than is affected by the flow field due to the high fluid diffusivity, the low permeability and the EWT technique. One may also comment that the Potato slice does not fully dry out which is similar to the coal case reported by Elhalwagy and Straatman [8]. Now we turn our attention to the temporal and spatial variations observed during the drying process presented in Figs. 3.15-3.17.

Figure 3.15 shows the contour plots of liquid mass fraction variation with time for both cases. The results show a gradual decrease of the moisture content inside the produce slices with time that starts from the fluid/porous interface inward. The apple case show more pronounced drying effect towards the leading edge [8] because of the effect of the penetrating flow and the impingement of the flow on the upstream face, while the potato slice is showing highly diffusive profiles in the inside that are not affected by the outside flow field. This difference between both cases is attributed to the lower porosity of the potato slice i.e. 0.04 and the fact that with the EWT, the flow is purely laminar in the inside i.e. almost pure diffusion with neglected convection. Both cases show high relative humidity inside the flesh because of the small void space that becomes saturated almost instantly. Relative humidity on the surrounding starts with high values and as drying rate is reduced, it declines as the flesh dries. The profiles are physically correct and very similar to the work reported in the literature [4, 8, 69] for cases of both laminar and turbulent flows.

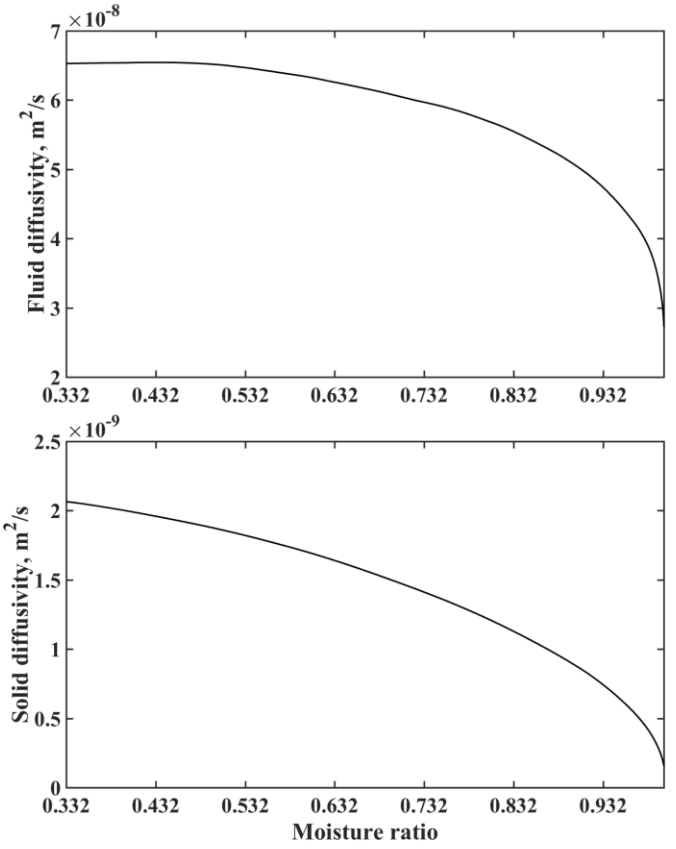

a) Potato

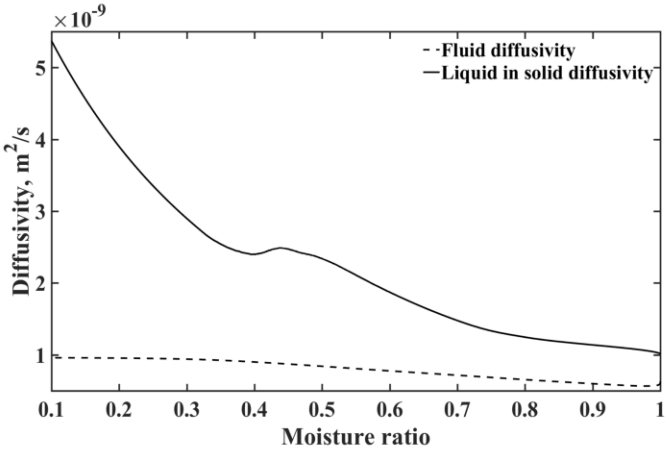

b) Apple

Figure 3.13: Diffusivities as a function of the moisture ratio.

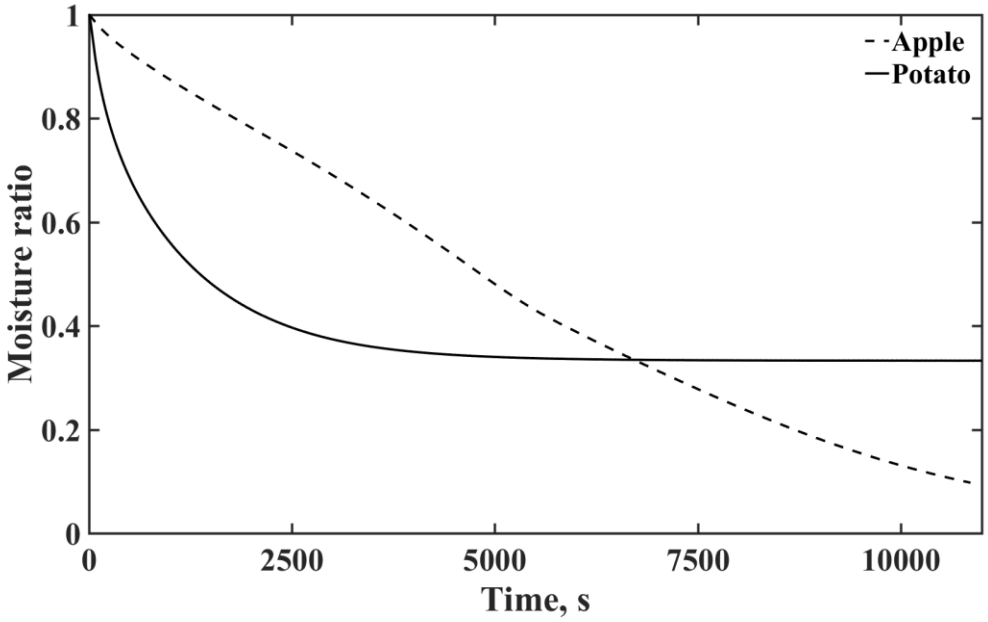

Figure 3.14: Moisture ratio versus time.

Figures 3.16 and 3.17, depict the contour plots for the phase temperatures as they vary with drying time. On the inside of the slices, both temperatures behave similarly with some degree of non-equilibrium present. The heat is conducted/dispersed from the upstream face and hence, this side has its lost heat restored sensibly in a faster rate as compared to the downstream section of the slice. This part shows some cooling due to the vaporization energy withdrawal. After the rate of drying becomes low, this effect gradually negates as sensible heat is supplied by conduction. The case of the potato shows a wider range for temperatures as compared to the apple case. This is attributed to the turbulence and convection penetrating inside the apples and enhancing mixing, which is not the case for the potato slice. One may also notice the downstream back wake effect on the fluid temperature for the potato slice while this is absent in the apple case. This is explained by the under-prediction of the wake effect for the apple case due to using a no-EWT approach as explained in subsection 3.4.2.

One may conclude from the above discussion that the turbulence enhancement to dynamic coupling for heat and mass transfer is correctly characterized. The physics of the convective drying is reasonably represented as can be seen from the results. It is understood that we depend on calibrated diffusivity values herein however the model has been tested

with different diffusivities and it showed the same phenomena observed here for all the different cases. The presented dynamic coupling technique hinges upon a correct specification of the diffusivities as an input to provide a quantitatively accurate solution, a specification that can be provided experimentally. The qualitative information however are very similar for different cases as found in the present work and in reports in the literature [68-69].

3.5 Summary

In the present work, a dynamic coupling approach for flow, heat and mass transfer within porous media and in conjugate fluid/porous domains is enhanced with the capability to treat turbulent flows. The approach utilised the Boussinesq's approach and the standard $k-\varepsilon$ model to treat the turbulence in the clear fluid region. A double-decomposed $k-\varepsilon$ porous media version is utilised inside the porous material [31]. An implicit interface coupling between fluid and porous regions is utilised with developing the necessary modifications to adapt to the dynamic coupling framework [8]; using turbulent enhanced diffusivities at the interface, apportioning of the turbulent-affected interface shear stress, introducing resistance networks to couple the two porous media phases to the clear fluid region for different modes of heat and mass transfer, and modifying turbulence behavior at the macroscopic interface to handle high- and low-permeability porous materials. The key modeling novelties may be summarized as:

- Development of a turbulence-extension to the flow, heat and mass transfer dynamic coupling model [8] in which the resistances of heat and mass transfer are explicitly tracked through conjugate fluid/porous domains, micro- and macroscopically, and physically based expressions are devised and selected to allow dynamic reactivity to them based on different physical modes of transport.

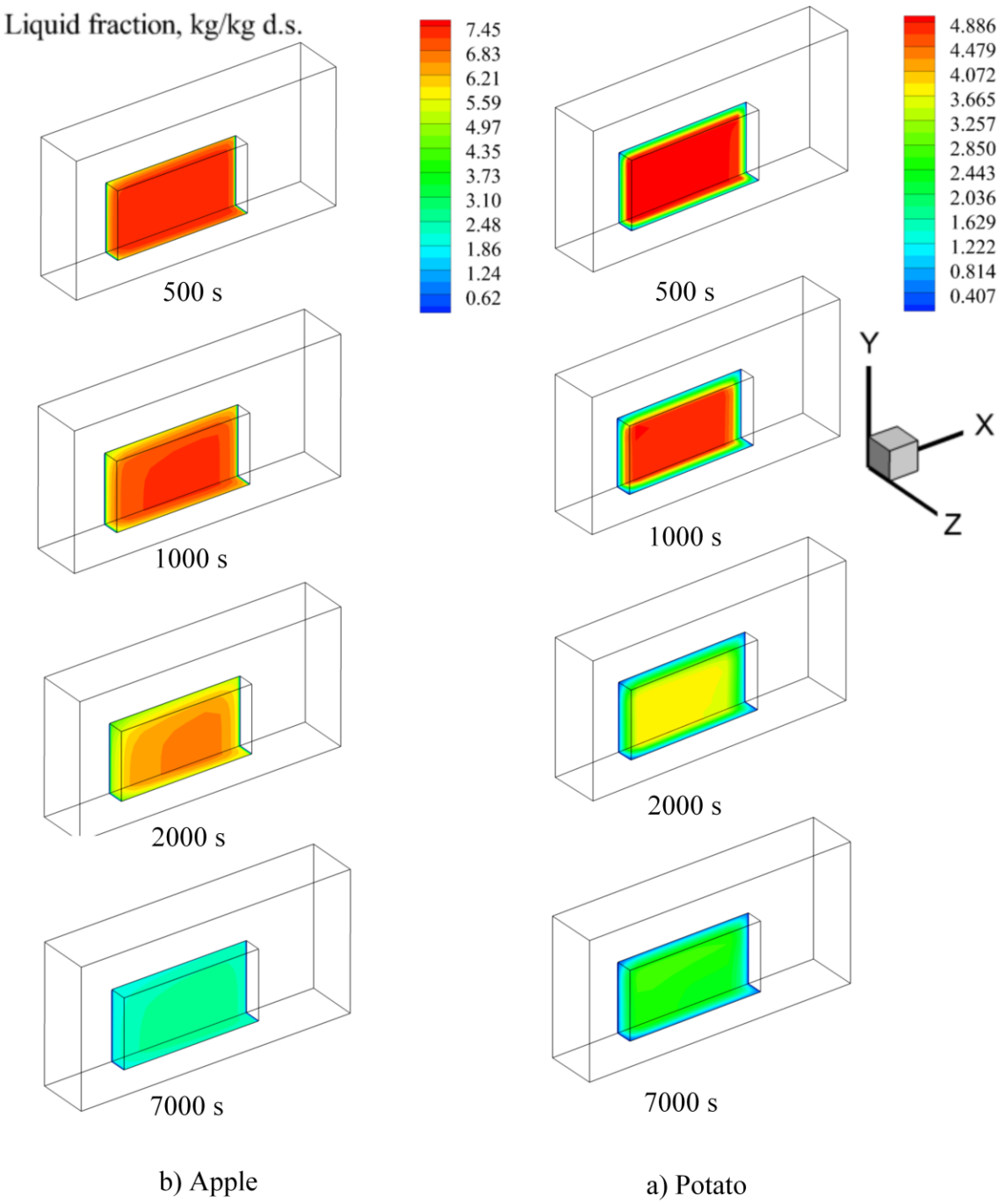

Figure 3.15: Contour plots for produce liquid moisture spatial variations at different time instances.

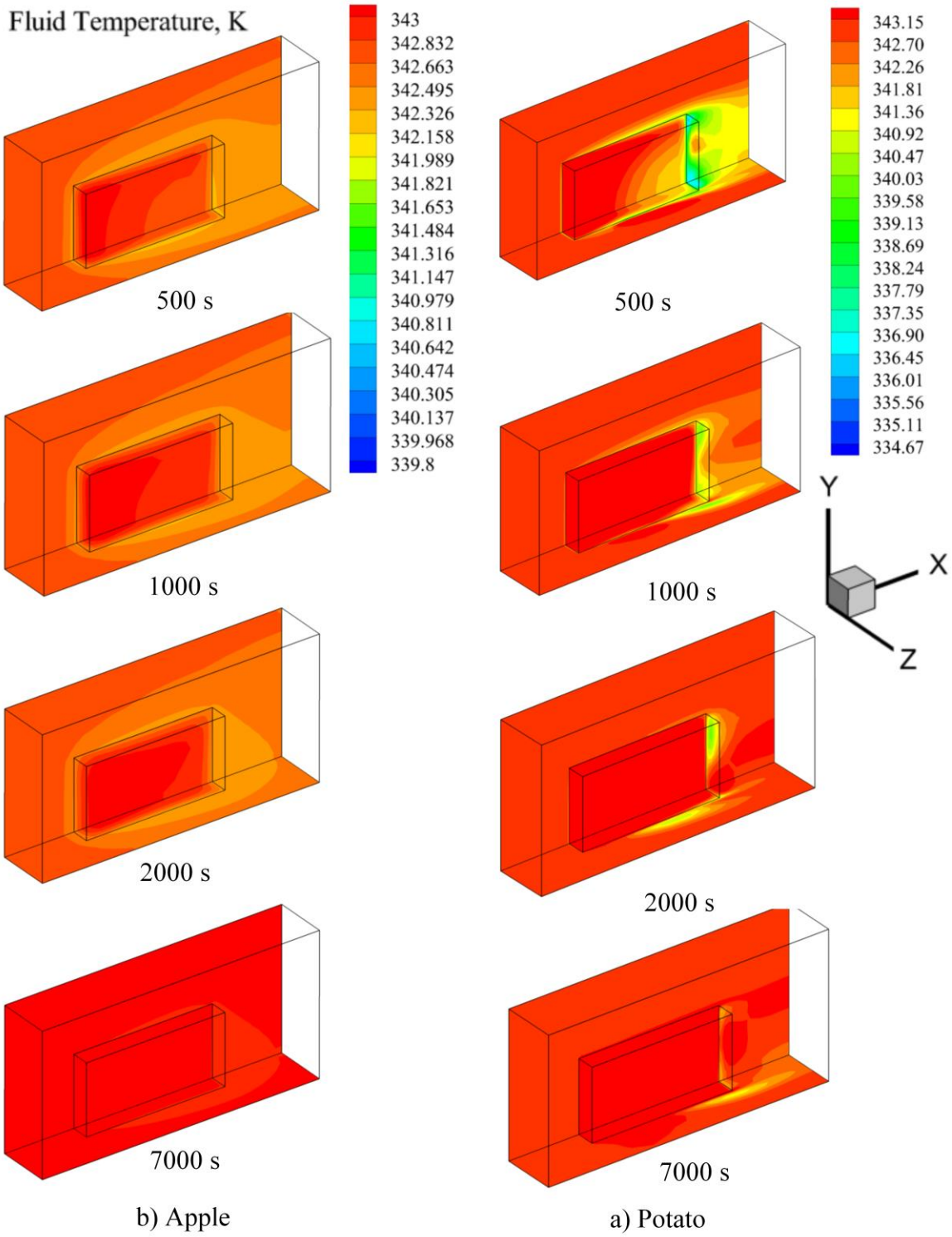

Figure 3.16: Contour plots for fluid temperature spatial variations at different time instances.

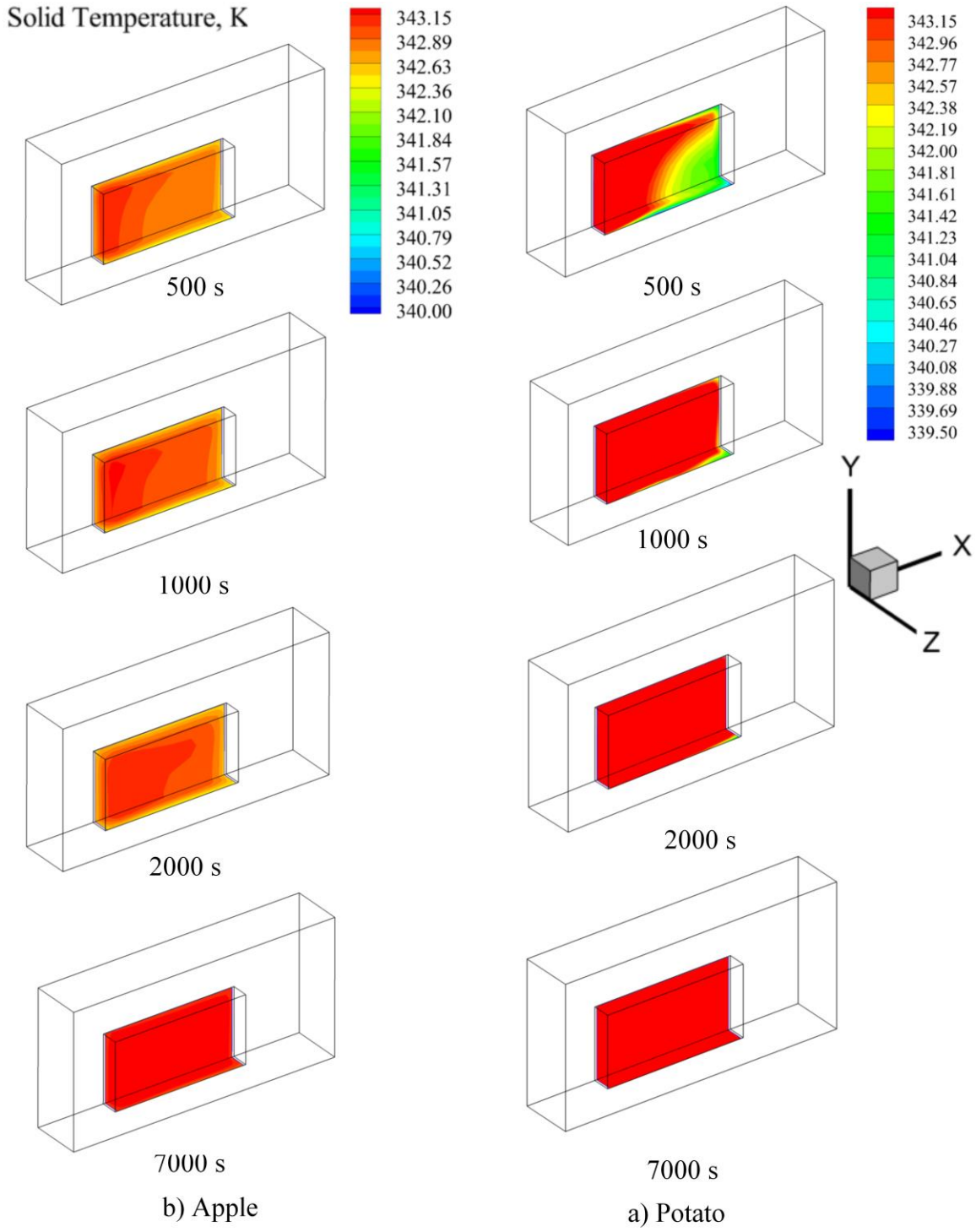

Figure 3.17: Contour plots for solid temperature spatial variations at different time instances.

- A $k-\varepsilon$ macroscopic interface coupling approach is devised that uses phase apportioning for the shear stress with intrinsic continuity of the turbulence quantities for high permeability porous media, and a novel enhanced wall-like treatment for low permeability materials. It also allows penetration/dissipation in porous media for turbulence at the macroscopic interface to evolve physically without any ad-hoc numerical switch off.
- A coupling resistance network for heat and mass transfer at the macroscopic interface is enhanced with turbulence capabilities including turbulence-modified transport diffusivities for high permeability porous media and a novel EWT heat and mass transfer treatment for low permeability porous media. The implicit coupling technique utilising the phase ratio concept for the solid leg resistance of the circuit is also modified to treat both permeability and porosity cases.

The turbulent hydrodynamics of high and low permeability interfaces is investigated using a case of a porous obstruction in a two-dimensional channel. Testing for different porous materials (potato and apple slices), and flow rates for the behavior of turbulence is carried out using the interface flux condition and investigating the effect of using an enhanced wall-like treatment. Results in terms of the velocity fields, TKE and turbulence dissipation fields indicate that the interface flux condition alone is not capable of predicting the dissipation of turbulence at the interface, which is associated with low permeability. The results for no-EWT showed an over-prediction of the turbulence field inside the porous medium, under-predicting the interface shear stress and over-predicting the amount of flow penetration to the porous obstruction. This resulted in an undersized separation bubble for the flow around the obstruction, reduced size of the back wake and different patterns of the weak flow field inside the porous material showing more penetration of the flow with an absent negative flow regions that should form near the separation bubble on the inside of the material. Utilizing an EWT depicted better physical behavior in terms of all of the above, which is more compatible with the behavior described in the literature for a wall-like obstruction. It is also shown that there is a similarity between the EWT case and the negative jump coefficient case by DeLemos [54]. Both predict a clear fluid side diffusion potential that is reduced towards the interface since the EWT follows the boundary layer

assumptions, however, they showed different clear fluid profiles for the TKE further from the interface, indicating that the EWT is not possible to be substituted with negative jump coefficients. In regards to heat and mass transfer a turbulent heat and mass transfer 3D case is simulated for turbulent convective drying of potato and apple slices. A sensitivity approach for the phase diffusivities is used for both materials to characterize the change from laminar values to turbulent ones by enhancing diffusion. The results presented trends that are compatible with the literature-reported cases. The contours of the moisture variation with time for both produce slices showed a gradual decrease of moisture that starts from macroscopic interfaces inward. The potato slice case showed almost purely diffusive behavior with neglected effect from the outside flow unlike the apple case which showed faster drying at the upstream side due to convection and turbulence penetration effects. The phase temperatures' contours depicted a cool inside-flesh region that is formed due to the slow sensible restoration of the withdrawn moisture evaporation energy unlike the upstream part which restored the energy faster. The temperature variations smooth out with time as the slices dry up because the sensible heating overcomes the drying energy. The back wake effect on fluid temperature was highly pronounced in the potato case because of the use of an EWT while it was neglected for the apple case. The overall heat and mass transfer results were physically reasonable and qualitatively comparable to the work presented in the literature. One may conclude from the above discussion that upon supplying the accurate material properties, the model is capable of predicting the correct physics for turbulent flow, heat and mass transfer.

References

[1] Betchen, L., Straatman, A. G., & Thompson, B. E. (2006). A nonequilibrium finite-volume model for conjugate fluid/porous/solid domains. *Numerical Heat Transfer, Part A: Applications*, *49*(6), 543-565.

[2] Khan, F. A., Fischer, C., & Straatman, A. G. (2015). Numerical model for non-equilibrium heat and mass exchange in conjugate fluid/solid/porous domains with application to evaporative cooling and drying. *International Journal of Heat and Mass Transfer*, *80*, 513-528.

[3] Kaya, A., Aydın, O., & Dincer, I. (2006). Numerical modeling of heat and mass transfer during forced convection drying of rectangular moist objects. *International journal of heat and mass transfer*, *49*(17-18), 3094-3103.

[4] Khan, F. A., & Straatman, A. G. (2016). A conjugate fluid-porous approach to convective heat and mass transfer with application to produce drying. *Journal of Food Engineering*, *179*, 55-67.

[5] Mohan, V. C., & Talukdar, P. (2010). Three dimensional numerical modeling of simultaneous heat and moisture transfer in a moist object subjected to convective drying. *International Journal of Heat and Mass Transfer*, *53*(21-22), 4638-4650.

[6] Zhang, K., & You, C. (2011). Experimental and numerical investigation of lignite particle drying in a fixed bed. *Energy & Fuels*, *25*(9), 4014-4023.

[7] Lal, S., Lucci, F., Defraeye, T., Poulikakos, L. D., Partl, M. N., Derome, D., & Carmeliet, J. (2018). CFD modeling of convective scalar transport in a macroporous material for drying applications. *International Journal of Thermal Sciences*, *123*, 86-98.

[8] Elhalwagy, M. M., & Straatman, A. G. (2017). Dynamic coupling of phase-heat and mass transfer in porous media and conjugate fluid/porous domains. *International Journal of Heat and Mass Transfer*, *106*, 1270-1286.

[9] Curcio, S., Aversa, M., Calabrò, V., & Iorio, G. (2008). Simulation of food drying: FEM analysis and experimental validation. *Journal of Food Engineering*, *87*(4), 541-553.

[10] De Bonis, M. V., & Ruocco, G. (2014). Conjugate heat and mass transfer by jet impingement over a moist protrusion. *International Journal of Heat and Mass Transfer*, *70*, 192-201.

[11] Caccavale, P., De Bonis, M. V., & Ruocco, G. (2016). Conjugate heat and mass transfer in drying: A modeling review. *Journal of Food Engineering*, *176*, 28-35.

[12] Ateeque, M., Mishra, R. K., Chandramohan, V. P., & Talukdar, P. (2014). Numerical modeling of convective drying of food with spatially dependent transfer coefficient in a turbulent flow field. *International Journal of Thermal Sciences*, *78*, 145-157.

[13] Van Belleghem, M., Steeman, M., Janssen, H., Janssens, A., & De Paepe, M. (2014). Validation of a coupled heat, vapour and liquid moisture transport model for porous materials implemented in CFD. *Building and Environment*, *81*, 340-353.

[14] Defraeye, T., Verboven, P., & Nicolai, B. (2013). CFD modelling of flow and scalar exchange of spherical food products: Turbulence and boundary-layer modelling. *Journal of Food Engineering*, *114*(4), 495-504.

[15] Chourasia, M. K., & Goswami, T. K. (2007). Steady state CFD modeling of airflow, heat transfer and moisture loss in a commercial potato cold store. *International Journal of Refrigeration*, *30*(4), 672-689.

[16] Delele, M. A., Ngcobo, M. E., Opara, U. L., & Meyer, C. J. (2013). Investigating the effects of table grape package components and stacking on airflow, heat and mass transfer using 3-D CFD modelling. *Food and Bioprocess Technology*, *6*(9), 2571-2585.

[17] Ambaw, A., Verboven, P., Defraeye, T., Tijskens, E., Schenk, A., Opara, U. L., & Nicolai, B. M. (2013). Porous medium modeling and parameter sensitivity analysis of 1-MCP distribution in boxes with apple fruit. *Journal of Food Engineering*, *119*(1), 13-21.

[18] Delele, M. A., Schenk, A., Tijskens, E., Ramon, H., Nicolaï, B. M., & Verboven, P. (2009). Optimization of the humidification of cold stores by pressurized water atomizers based on a multiscale CFD model. *Journal of food engineering*, *91*(2), 228-239.

[19] Delele, M. A., Vorstermans, B., Creemers, P., Tsige, A. A., Tijskens, E., Schenk, A., ... & Verboven, P. (2012). Investigating the performance of thermonebulisation fungicide fogging system for loaded fruit storage room using CFD model. *Journal of food engineering*, *109*(1), 87-97.

[20] Tutar, M., Erdogdu, F., & Toka, B. (2009). Computational modeling of airflow patterns and heat transfer prediction through stacked layers' products in a vented box during cooling. *International Journal of refrigeration*, *32*(2), 295-306.

[21] Moureh, J., Tapsoba, M., & Flick, D. (2009). Airflow in a slot-ventilated enclosure partially filled with porous boxes: Part I–measurements and simulations in the clear region. *Computers & Fluids*, *38*(2), 194-205.

[22] ANSYS Fluent Theory Guide (2015). ANSYS Inc., Canonsburg, PA.

[23] Alvarez, G., Bournet, P. E., & Flick, D. (2003). Two-dimensional simulation of turbulent flow and transfer through stacked spheres. *International Journal of Heat and Mass Transfer*, *46*(13), 2459-2469.

[24] G. Alvarez, D. Flick, Modelling turbulent flow and heat transfer using macroporous media approach used to predict cooling kinetics of stack of food products, J. Food Eng. 80 (2) (2007) 391–401.

[25] M.J. De Lemos, Turbulence in Porous Media: Modeling and Applications, Elsevier, 2012.

[26] K. Lee, J.R. Howell, Forced convective and radiative transfer within a highly porous layer exposed to a turbulent external flow field. In: Proceedings of the 1987 ASME-JSME Thermal Engineering Joint Conf., vol. 2, 1987, pp. 377–386.

[27] H. Wang, E.S. Takle, Boundary-layer flow and turbulence near porous obstacles, Bound. Layer Meteorol. 74 (1–2) (1995) 73–88.

[28] B.V. Antohe, J.L. Lage, A general two-equation macroscopic turbulence model for incompressible flow in porous media, Int. J. Heat Mass Transfer 40 (13) (1997) 3013–3024.

[29] Getachew, D., Minkowycz, W. J., & Lage, J. L. (2000). A modified form of the κ–ε model for turbulent flows of an incompressible fluid in porous media. *International Journal of Heat and Mass Transfer*, *43*(16), 2909-2915.

[30] A. Nakayama, F. Kuwahara, A macroscopic turbulence model for flow in a porous medium, J. Fluids Eng. 121 (2) (1999) 427–433.

[31] M.H. Pedras, M.J. de Lemos, Macroscopic turbulence modeling for incompressible flow through undeformable porous media, Int. J. Heat Mass Transfer 44 (6) (2001) 1081–1093.

[32] F.E. Teruel, Rizwan-uddin, A new turbulence model for porous media flows. Part I: Constitutive equations and model closure, Int. J. Heat Mass Transfer 52 (19) (2009) 4264–4272.

[33] F.E. Teruel, Rizwan-uddin, Numerical computation of macroscopic turbulence quantities in representative elementary volumes of the porous medium, Int. J. Heat Mass Transfer 53 (23) (2010) 5190–5198.

[34] Khan, F. A., & Straatman, A. G. (2016). Closure of a macroscopic turbulence and non-equilibrium turbulent heat and mass transfer model for a porous media comprised of randomly packed spheres. *International Journal of Heat and Mass Transfer*, *101*, 1003-1015.

[35] J. Moureh, M. Tapsoba, D. Flick, Airflow in a slot-ventilated enclosure partially filled with porous boxes: Part II–Measurements and simulations within porous boxes, Comput. Fluids 38 (2) (2009) 206–220.

[36] Mößner, M., & Radespiel, R. (2015). Modelling of turbulent flow over porous media using a volume averaging approach and a Reynolds stress model. *Computers & Fluids*, *108*, 25-42.

[37] M. Drouin, O. Grégoire, O. Simonin, A consistent methodology for the derivation and calibration of a macroscopic turbulence model for flows in porous media, Int. J. Heat Mass Transfer 63 (2013) 401–413.

[38] Kuwata, Y., Suga, K., & Sakurai, Y. (2014). Development and application of a multi-scale k–ε model for turbulent porous medium flows. *International Journal of Heat and Fluid Flow*, *49*, 135-150.

[39] Y. Kuwata, K. Suga, Modelling turbulence around and inside porous media based on the second moment closure, Int. J. Heat Fluid Flow 43 (2013) 35–51.

[40] Kundu, P., Kumar, V., & Mishra, I. M. (2014). Numerical modeling of turbulent flow through isotropic porous media. *International Journal of Heat and Mass Transfer*, *75*, 40-57.

[41] Kuznetsov, A. V. (2004). Numerical modeling of turbulent flow in a composite porous/fluid duct utilizing a two-layer k–ε model to account for interface roughness. *International journal of thermal sciences*, *43*(11), 1047-1056.

[42] Kuznetsov, A. V., & Xiong, M. (2003). Development of an engineering approach to computations of turbulent flows in composite porous/fluid domains. *International journal of thermal sciences*, *42*(10), 913-919.

[43] Kuznetsov, A. V., Cheng, L., & Xiong, M. (2002). Effects of thermal dispersion and turbulence in forced convection in a composite parallel-plate channel: investigation of constant wall heat flux and constant wall temperature cases. *Numerical Heat Transfer: Part A: Applications*, *42*(4), 365-383.

[44] Suga, K., & Nishiguchi, S. (2009). Computation of turbulent flows over porous/fluid interfaces. *Fluid dynamics research*, *41*(1), 012401.

[45] Fetzer, T., Smits, K. M., & Helmig, R. (2016). Effect of turbulence and roughness on coupled porous-medium/free-flow exchange processes. *Transport in Porous Media*, *114*(2), 395-424.

[46] Beyhaghi, S., Xu, Z., & Pillai, K. M. (2016). Achieving the Inside–Outside Coupling During Network Simulation of Isothermal Drying of a Porous Medium in a Turbulent Flow. *Transport in Porous Media*, *114*(3), 823-842.

[47] Prinos, P., Sofialidis, D., & Keramaris, E. (2003). Turbulent flow over and within a porous bed. *Journal of Hydraulic Engineering*, *129*(9), 720-733.

[48] Yang, G., Weigand, B., Terzis, A., Weishaupt, K., & Helmig, R. (2018). Numerical Simulation of Turbulent Flow and Heat Transfer in a Three-Dimensional Channel Coupled with Flow Through Porous Structures. *Transport in Porous Media*, 1-23.

[49] Jin, Y., & Kuznetsov, A. V. (2017). Turbulence modeling for flows in wall bounded porous media: An analysis based on direct numerical simulations. *Physics of Fluids*, *29*(4), 045102.

[50] Breugem, W. P., & Boersma, B. J. (2005). Direct numerical simulations of turbulent flow over a permeable wall using a direct and a continuum approach. *Physics of fluids*, *17*(2), 025103.

[51] Suga, K. (2016). Understanding and modelling turbulence over and inside porous media. *Flow, Turbulence and Combustion*, *96*(3), 717-756.

[52] Silva, R. A., & de Lemos, M. J. (2003). Turbulent flow in a channel occupied by a porous layer considering the stress jump at the interface. *International Journal of Heat and Mass Transfer*, *46*(26), 5113-5121.

[53] Ochoa-Tapia, J. A., & Whitaker, S. (1995). Momentum transfer at the boundary between a porous medium and a homogeneous fluid—I. Theoretical development. *International Journal of Heat and Mass Transfer*, *38*(14), 2635-2646.

[54] De Lemos, M. J. (2009). Turbulent flow around fluid–porous interfaces computed with a diffusion-jump model for k and ε transport equations. *Transport in porous media*, *78*(3), 331-346.

[55] D.C. Wilcox, Turbulence Modeling for CFD, vol. 2, DCW industries, La Canada, CA, 1998. pp. 103–217.

[56] Whitaker, S. (1977). A Theory of drying. *Advances in heat transfer*, *13*, 119-203.

[57] Craft, T. J., Gant, S. E., Gerasimov, A. V., Iacovides, H., & Launder, B. E. (2006). Development and application of wall-function treatments for turbulent forced and mixed convection flows. *Fluid Dynamics Research*, *38*(2-3), 127-144.

[58] Kader, B. A. (1981). Temperature and concentration profiles in fully turbulent boundary layers. *International journal of heat and mass transfer*, *24*(9), 1541-1544.

[59] Craft, T. J., Gerasimov, A. V., Iacovides, H. E. L. B., & Launder, B. E. (2002). Progress in the generalization of wall-function treatments. *International Journal of Heat and Fluid Flow*, *23*(2), 148-160

[60] Srikiatden, J., & Roberts, J. S. (2008). Predicting moisture profiles in potato and carrot during convective hot air drying using isothermally measured effective diffusivity. *Journal of Food Engineering*, *84*(4), 516-525.

[61] Krokida, M. K., & Maroulis, Z. B. (2001). Structural properties of dehydrated products during rehydration. *International journal of food science & technology*, *36*(5), 529-538.

[62] Feng, H., Tang, J., Plumb, O. A., & Cavalieri, R. P. (2004). Intrinsic and relative permeability for flow of humid air in unsaturated apple tissues. *Journal of Food Engineering*, *62*(2), 185-192.

[63] Gancarz, M., Konstankiewicz, K., & Zgórska, K. (2014). Cell orientation in potato tuber parenchyma tissue. *International Agrophysics*, *28*(1), 15-22.

[64] Q. Yu, B.E. Thompson, A.G. Straatman, A unit cube-based model for heat transfer and fluid flow in porous carbon foam, J. Heat Transfer 128 (4) (2006) 352–360.

[65] Menter, F. R. (1994). Two-equation eddy-viscosity turbulence models for engineering applications. *AIAA journal*, *32*(8), 1598-1605.

[66] Liu, G., Chen, J., Liu, M., & Wan, X. (2012). Shrinkage, porosity and density behavior during convective drying of bio-porous material. *Procedia Engineering*, *31*, 634-640.

[67] Srikiatden, J., & Roberts, J. S. (2006). Measuring moisture diffusivity of potato and carrot (core and cortex) during convective hot air and isothermal drying. *Journal of Food Engineering*, *74*(1), 143-152.

[68] Defraeye, T., Blocken, B., & Carmeliet, J. (2013). Influence of uncertainty in heat–moisture transport properties on convective drying of porous materials by numerical modelling. *Chemical engineering research and design*, *91*(1), 36-42.

[69] Defraeye, T., & Verboven, P. (2017). Convective drying of fruit: role and impact of moisture transport properties in modelling. *Journal of Food Engineering*, *193*, 95-107.

Chapter 4

4 Thesis summary

This chapter presents summary of the work done in this thesis, the original research contributions and recommendations for future work in this line of research.

4.1 Summary of chapters

This thesis presented a dynamic coupling, non-equilibrium, full flow, heat and mass transfer, conjugate fluid/porous, finite volume CFD framework for simulating moisture transport in cases of convective drying and rehydration. The model is capable of treating laminar and turbulent flows for high and low permeability porous materials. The model has shown versatility and a wide spectrum of applicability for different materials with cases of interstitial phase exchange, convectively-dominant and diffusively-dominant drying of moist porous materials. The applicability has been verified by comparison to experiments, existing models and physically reasonable trends for heat and mass transfer.

Chapter 2, described a dynamic coupling approach for CFD simulations of flow, heat and mass transfer in conjugate fluid/porous domains in which the phase-heat and mass transfer interstitially inside porous media and macroscopically across clear fluid/porous interfaces have been allowed to vary dynamically with space and time according to different modes for heat and mass transfer. The model allowed for tracking heat and mass transfer resistances in the fluid and solid phases to reactively select between different expressions for characterizing the exchanges locally (interstitially) and macroscopically (across macroscopic interfaces). Heat accompanying mass exchanges has been modelled so that the vaporization energy for moisture is withdrawn in different proportions from both phases based on a Biot number representation for the ability to conduct/convect heat in both fluid and solid constituents. A phase ratio concept has been devised to implicitly couple mass transfer across fluid/porous interfaces. Validation of the model has been carried out based on three different studies for interstitial coupling, macroscopic coupling for diffusively dominant mass transfer and macroscopic coupling for convectively dominant mass transport. Results showed very good agreement with experimental data [1-

2] and/or reported modeling [3] in the literature confirming the efficacy and robustness of the modeling approach.

Chapter 3, described the extension of the model to turbulent flows in which a two equation, double decomposition $k-\varepsilon$ model was successfully implemented inside the porous media and coupled to the free air (pure fluid) region. The turbulence effects on momentum, heat and mass transfer have been included successfully and the macroscopic interface coupling has been formulated to treat high and low permeability interfaces. A flux based interface treatment for turbulence is selected from the literature and adapted to the implementation framework herein that successfully represents a high permeability interface. A novel enhanced wall-like treatment for macroscopic fluid/porous interfaces is devised for low permeability porous interfaces that allows a smooth turbulence coupling between the fluid and porous regions and allows, with the use of a flux based condition, a physically correct and numerically robust treatment. An extension to this enhanced wall-like approach to heat and mass transfer is devised to allow coupling with the dynamic coupling framework. Verification is achieved by analyzing the hydrodynamics of the high and low permeability interfaces and comparing them to the jump coefficient version developed by De Lemos [4] for a 2D channel flow with porous obstruction. A full flow, heat and mass transfer for both high and low permeabilities' verification is carried out using the turbulent convective drying cases of potato and apple slices. Results show evidence that the model is numerically and physically robust and given the correct material diffusivities is capable of representing a reliable discrete CFD solution for flow, heat and mass transfer.

One may conclude based on this summary that a formulation for dynamic coupling of flow, heat and mass transfer was successfully developed, providing the framework necessary for further development. The model is generic, of minimum calibration and a suitable compromise between detailed physics, empiricism and short computational time. The wide applicability for different materials, flows and modes of flow, heat and mass transfer have been considered. The model is also possible to extend to different areas of heat and mass transfer and may easily be extended to include the effects of variable porosity and shrinkage.

4.2 Novel contributions

- The first and most original contribution in this thesis is the development of a dynamic coupling model for flow, heat and mass transfer in conjugate fluid/porous domains that was presented in Chapter 2 and enhanced to include turbulence in Chapter 3. Throughout the literature, this capability was missing. The model is generic, three dimensional and conjugate. It treats the fluid and porous regions implicitly and simultaneously. Heat and mas transfer is modeled in it with non-equilibrium and it is equally capable of characterizing microscopic (interstitial) phase coupling and macroscopic coupling (at fluid/porous interfaces). The most significant feature in it is that it is physically dynamic; i.e., it tracks local and global heat and mass transfer resistances and dynamically reacts to them by using physically formulated expressions rather than empirical formulae, which removes the need for ad-hoc empirical coefficients and almost eliminates case-to-case calibration. The model also represents a compromise between empiricism, physical detailing and computational time. The developed framework herein presents a basic step towards further research in dynamic coupling. It is also efficiently and reliably applicable to a wide spectrum of physical flow, heat and mass transfer processes and materials as shown in Chapters 2 and 3.

- In Chapter 2, a generic vaporization energy apportioning technique was developed that is equally capable for problems of evaporative cooling [5] and drying [5-6]. The technique is applicable interstitially and between fluid and porous regions where the apportioning depends on a comparison between the different phases capability to conduct/convect heat characterized by a local Biot number estimate.

- A novel phase ratio concept was developed in Chapter 2, where a ratio between the solid phase moisture presence and the fluid phase is calculated and chosen to include diffusion coefficients and densities to control its order of magnitude and variation. This technique enabled an implicit implementation for macroscopic interface mass transfer coupling that required no calibration, unlike other techniques in the literature [6].

- A novel enhanced wall-like treatment (EWT) was formulated for low permeability porous materials in Chapter 3, that allowed a two sided coupling for turbulence at the fluid/porous interface and allowed for turbulence to evolve in a wall-like, boundary-layer manner. The technique proved to not allow turbulence penetration inside the porous material without any ad-hoc switch off. It also proves to predict the unique low-permeability interface behavior that may not be arrived at by using different turbulent interface jump coefficients [4, 7].

- A coupling technique between turbulence and heat and mass transfer at the macroscopic interface is developed in Chapter 3, where variable diffusivities and conductivities were inserted in a resistance network approach for coupling at the interface. The values were calculated based on turbulent Prandtl and Schmidt numbers for high permeability porous media and were based on a novel enhanced wall-like treatment approach for heat and mass transfer for low permeability porous media.

4.3 Recommendations for future work

Based on the work presented in this thesis, the following points were found to be important to consider for future enhancements to the present model.

1- The present modeling approach was implemented in an orthogonal structured CFD framework. While the current version is applicable to a wide class of problems, to be able to treat an irregular exterior of a porous material or a simulation domain that is not Cartesian or orthogonal in shape, the use of an unstructured CFD framework [8] is important. Hence, it is a recommendation for future work to utilize the present modelling approach on an unstructured technique, developing the necessary higher order additions in the numerical discretization and build on the interface coupling techniques herein to develop counterparts that are applicable in the absence of line structures.

2- In this thesis, the volume averaged equations of porous media were derived and used on the basis that the porosity is fixed in space and time. In many cases the

variation in porosity is negligible, however, other cases have considerable variations and consequently the solid material shrinks as well due to moisture departure. A further generic approach may be developed when building on the present one with adding additional terms in the equations to characterize variation in porosity and volumetric shrinkage and formulating their effects on the coupling processes at micro- and macroscopic interfaces.

3- The current modeling approach, while capable of treating convectively dominant and diffusively dominant mass transfer, has been tested for cases where deviation from one mode to the other is neglected. A future study that considers transitioning between both modes of mass transfer would be of potential novelty.

4- The enhanced wall-like treatment of low permeability macroscopic interfaces that is developed in Chapter 3 assumes a smooth interface surface. A more generic version may be developed with including the effect of roughness for the development of the interface boundary layer.

5- It is expected as mentioned in Chapter 3 that while a high permeability interface treatment is suitable for higher porosity ranges and low permeability enhanced wall-like treatment enables a physical results for a low porosity porous media, a middle range of porosities may need a hybridization of both techniques to behave accurately. An investigation of this aspect may also be of potential novelty.

6- It is of research interest to move the present dynamic coupling framework to the area of reactive flows. Combustion, Catalysis and Biological reactive flows are within the same class of problems considered herein and hence multiple aspects of the present model will be useful for characterizing them and a definite research novelty may be achieved.

References

[1] M. Stakic´, E. Tsotsas, Modeling and numerical analysis of an atypical convective coal drying process, Drying Technol. 22 (10) (2004) 2351–2373.

[2] D. Velic´, M. Planinic´, S. Tomas, M. Bilic´, Influence of airflow velocity on kinetics of convection apple drying, J. Food Eng. 64 (1) (2004) 97–102.

[3] T. Defraeye, B. Blocken, J. Carmeliet, Analysis of convective heat and mass transfer coefficients for convective drying of a porous flat plate by conjugate modelling, Int. J. Heat Mass Transfer 55 (1) (2012) 112–124.

[4] De Lemos, M. J. (2009). Turbulent flow around fluid–porous interfaces computed with a diffusion-jump model for k and ε transport equations. *Transport in porous media*, *78*(3), 331-346.

[5] Khan, F. A., Fischer, C., & Straatman, A. G. (2015). Numerical model for non-equilibrium heat and mass exchange in conjugate fluid/solid/porous domains with application to evaporative cooling and drying. *International Journal of Heat and Mass Transfer*, *80*, 513-528.

[6] Khan, F. A., & Straatman, A. G. (2016). A conjugate fluid-porous approach to convective heat and mass transfer with application to produce drying. *Journal of Food Engineering*, *179*, 55-67.

[7] Silva, R. A., & De Lemos, M. J. (2003). Turbulent flow in a channel occupied by a porous layer considering the stress jump at the interface. *International Journal of Heat and Mass Transfer*, *46*(26), 5113-5121.

[8] DeGroot, C. T., & Straatman, A. G. (2011). A finite-volume model for fluid flow and non-equilibrium heat transfer in conjugate fluid-porous domains using general unstructured grids. *Numerical Heat Transfer, Part B: Fundamentals*, *60*(4), 252-277.

Curriculum Vitae

Name: Mahmoud Mohamed Mostafa Elhalwagy

Post-secondary Education and Degrees:

Cairo University
Cairo, Egypt
2002-2007 B.E.Sc

Cairo University
Cairo, Egypt
2007-2010 M.E.Sc.

Western University
London, Ontario, Canada
2012-2018 Ph.D.

Related Work Experience

Teaching and Research Assistant
Western University
2012-2018

Publications:

Elhalwagy, M. M., & Straatman, A. G. (2017). Dynamic coupling of phase-heat and mass transfer in porous media and conjugate fluid/porous domains. *International Journal of Heat and Mass Transfer*, *106*, 1270-1286.

Elhalwagy, M. M., & Straatman, A. G. (2018). Dynamics of turbulent flow, heat and mass transfer in porous media and conjugate fluid/porous interfaces. *Prepared for submission to a journal in the area of heat and mass transfer*.

Elhalwagy, M., Straatman, A. G. (2018). A turbulent interface treatment for conjugate fluid/porous interfaces of low-permeability. *Proceedings of the 26th. annual conference of the CFD society of Canada*, Winnipeg, Canada.

Elhalwagy, M., Dyck, N. & Straatman, A. (2017). Numerical simulation of gas respiration in produce processing and storage applications. *Proceedings of the 25th. annual conference of the CFD society of Canada*, Windsor, Canada.

Elhalwagy, M., Straatman, A. G. (2017). Extension of the dynamic heat/mass coupling approach for conjugate fluid/porous domains to unstructured CFD frameworks. *Proceedings of the 25th. annual conference of the CFD society of Canada*, Windsor, Canada.

Elhalwagy, M., Straatman, A. G. (2016). Towards a Dynamically Coupled-Phase Heat and Mass Exchange in Porous Media. *Proceedings of the 24th. annual conference of the CFD society of Canada*, Kelowna, Canada.

Elhalwagy, M., and Zhang, C. (2015). Modified Biodiesel Chemical Kinetics Based on Numerical Simulation in an Ignition Quality Tester. *Proceedings of the 25th. Canadian Congress of Applied Mechanics (CANCAM)*, London, Canada.